

**Orogenic Gold mineralization at 3Ace and Geochemical Characteristics of Quartz
Monzonite Dikes at Sprogge, South-east Yukon**

by

Shaunaugh C. Whelan

A thesis submitted in partial fulfillment of the requirements for the degree of

Master of Science

Department of Earth and Atmospheric Sciences

University of Alberta

© Shaunaugh C. Whelan, 2014

ABSTRACT

3Ace and Sprogge are two Au occurrences in the southeast Yukon, Selwyn Basin. Gold mineralization at 3Ace was previously believed to be intrusion-related, however, recent petrography and geochemical analysis show mineralization to be associated with mid-Cretaceous orogenesis. Gold occurs along fractures within quartz veins hosted in meta-sediments of the Neoproterozoic Yusezyu Formation of the Selwyn Basin, and precipitated from low salinity, CO₂-rich acidic fluids at temperatures around 300°C. Stable isotopes show evidence of fluid mixing and a significant meteoric water component in the system, but a magmatic contribution cannot be ruled out. X-ray diffraction was used to define alteration assemblages associated with Au. Geochemical analysis was also carried out at Sprogge to garner a better understanding of the regional geology and potential for mineralization. Radiogenic isotopic compositions of quartz monzonite dikes at Sprogge yielded estimated ages between 95.7 ± 2.0 Ma and 103.5 ± 1.2 Ma. Whole rock geochemical analyses indicate the quartz monzonite dikes were produced from similar petrogenetic processes to the Hyland and Tungsten plutonic suites.

ACKNOWLEDGEMENTS

I would like to thank Northern Tiger Resources for their generous support in partially funding the project, as well as allowing full access to their drill core. I would especially like to thank Chris Buchanan, Dennis Ouellette, and Bonnie Spence for their help during the field season in addition to many resourceful and helpful discussions.

Radiogenic dating of quartz monazite dikes at Sprogge was made possible through a Society of Economic Geologists Canada Foundation Graduate Research Grant. I would also like to thank them for their generous financial support in helping me to attend the SEG Discovery Conference.

This project would not have been possible without generous support, encouragement and supervision from Dr. Sarah Gleeson. Funding from Dr. Sarah Gleeson's NSERC CRD and Discovery grants are also most appreciated and made the project possible. Major support was also provided by many patient Faculty and support staff to whom I owe many thanks: Jeremy Richards, John Waldron, Karlis Muehlenbachs, Judy Schultz, Richard Stern, Andy Dufrane, Sergei Matveev, Andrew Locock, Rob Creaser, Mark Labbe, Diane Caird, Robert Dokken, and Martin Von Dollen from the University of Alberta, as well as Steve Taylor from the University of Calgary.

Preface

The author created the detailed geological map for the Main Zone, and collaborated with Emily Miller (Northern Tiger Resources) in the mapping of Sprogge. With the exception of sample F300, all samples were collected and recorded by the author. Rock sawing, crushing, and mineral separation were conducted by the author. Thin sections and fluid inclusion wafers were processed by Vancouver Petrographics, as well as the University of Alberta Thin Section Lab. Stable isotope analyses of carbonate and sulfide mineral separates were carried out by Steve Taylor at the Stable Isotope lab at the University of Calgary. Bulk oxygen isotopes in quartz were analysed at the University of Alberta Stable Isotope lab by Dr. Karlis Muehlenbachs and Olga Levner. Sample preparation and thin section drilling, and spot selection were carried out by the author at the CCIM preparation lab at the University of Alberta for SIMS O in-situ O isotope analyses. The Au-coated epoxy mount was created by Dr. Richard Stern, who also guided the SIMS analysis. XRD analyses were carried out by Diane Caird at the University of Alberta X-ray diffraction lab. Thin section coating and electron microprobe work were carried out by the author with the guidance of Dr. Sergei Matveev and Dr. Andrew Locock at the University of Alberta Electron Microprobe lab. Lead isotopes were analysed by MC-ICP-MS by Dr. Robert Creaser at the University of Alberta Radiogenic Isotope Facility. Mineral separation and mount preparation for U-Pb analyses of zircons were carried out by the author with the help of Robert Dokken. SEM-CL images of zircons were obtained at the University of Alberta CCIM lab by the author under the supervision of Anna Oh. Measurement and data analysis using LA-MC-ICP-MS were guided by Dr. Andy Dufrane. Microthermometry measurements were carried out by the author in Dr. Jeremy Richards' Fluid Inclusion Lab at the University of Alberta. Whole rock major and trace element analyses were measured from rocks prepared and analysed by ACME analytical laboratories in Vancouver, British Columbia. Desktop cathodoluminescence studies were carried out by the author under direction from Judy Schultz at the University of Alberta.

Table of Contents

CHAPTER 1: INTRODUCTION, GEOLOGY, AND ANALYTICAL METHODS

1.1 Introduction	1
1.2 Regional Geology and Tectonic Setting	5
1.2.1 Selwyn Basin	5
1.2.2 Cretaceous Plutonism and the Tombstone Gold Belt	7
1.2.3 Structural Evolution of the Selwyn Basin	9
1.3 Deposit Geology	10
1.3.1 Geology of the Sprogge Property	10
1.3.2 Geology of the 3Ace Property	11
1.4 Analytical Methods	14
1.4.1 EPMA and EDS	14
1.4.2 XRD	15
1.4.3 Desktop CL	15
1.4.4 BrF₅ Method for Oxygen Isotopes	15
1.4.5 SIMS and SEM-CL	16
1.4.6 Carbon and Oxygen Stable Isotopes in Carbonates	17
1.4.7 Sulfur Stable Isotopes in Sulfides	17
1.4.8 Radiogenic Isotope Analysis of Galena by MC-ICP-MS	18
1.4.9 Radiogenic Dating of Zircons and Monazites by LA-MC-ICP-MS	18
1.4.10 Microthermometry	19
1.4.11 Whole-Rock Major and Trace Element Analysis	20

CHAPTER 2: RESULTS

2.1 The Sprogge Property	21
2.1.1 Field Results and Petrography	21
2.1.2 Radiogenic Isotope Results	24

2.1.3	Sulfur Isotopes and Whole Rock Major and Trace Elements	25
2.2	The 3Ace Claim Block	25
2.2.1	Summarized Field Results	26
2.2.2	Host Rock Petrography.....	29
2.2.3	Petrography and Paragenesis.....	32
2.2.4	Oxygen Stable Isotopes from Quartz.....	42
2.2.5	Carbon and Oxygen Stable Isotopes from Carbonates	43
2.2.6	Sulfur Stable Isotopes from Sulfides	44
2.2.7	Pb-Pb Isotopes from Galena	46
2.2.8	Geochronology	46
2.2.9	Fluid Inclusions and Microthermometry	48
2.2.10	XRD and Wall-rock Alteration	55
CHAPTER 3:	DISCUSSION	59
3.1	Sprogge Property	59
3.1.1	Age of Quartz Monzonite Dikes	59
3.1.2	Whole Rock Geochemistry and Implications for Mineral Potential.....	59
3.2	The 3Ace Claim Block	64
3.2.1	Wall-rock and Pre-Au Mineralization	64
3.2.2	Quartz Vein Development and Mineralization	65
3.2.3	Post-Au Mineralization and Relative Timing of Vein Formation	76
3.2.4	Fluid Source and Genetic Model	79
CHAPTER 4:	CONCLUSIONS.....	88
4.1	Sprogge	88
4.2	3Ace Au mineralization.....	88
4.3	Implications for Exploration	89
References	90

Appendices

Appendix A	106
Appendix B	109
Appendix C	136
Appendix D	143
Appendix E	145
Appendix F	152
Appendix G	174

List of Tables

Table 1. Sprogge geochronology.....	25
Table 2. Summary of oxygen isotopic data from quartz.....	42
Table 3. Summary of carbon and oxygen stable isotope data.....	44
Table 4. Summary of sulfur stable isotope data	45
Table 5. Pb-Pb isotope data from galena.....	46
Table 6. U-Pb isotope data from monazite.....	47
Table 7. Summary of microthermometric data	48
Table 8. Calculated fluid inclusion pressures.....	50

List of Figures

Figure 1. Regional geological map	2
Figure 2. Geological map of the deposit area	4
Figure 3. Stratigraphic sequence of the deposit area.....	12
Figure 4. Map of Sprogge.....	see map in cover pocket
Figure 5. Photomicrographs of quartz monzonite dikes	22, 23
Figure 6. Main zone 1:50 map	27
Figure 7. Sleeping giant fault summary plots	28
Figure 8. Wall-rock photomicrographs	31
Figure 9. Paragenetic sequence chart	33
Figure 10. Quartz vein and sulfide photomicrographs	36
Figure 11. Photomicrographs of Au and arsenopyrite mineralization	38
Figure 12. Photomicrographs of post-Au mineralization	40
Figure 13. Bar graph of oxygen stable isotope composition (quartz)	43
Figure 14. Photomicrographs of fluid inclusions in quartz.....	51, 52
Figure 15. Fluid inclusion homogenization temperature and salinity diagrams.....	53, 54
Figure 16. Stratigraphy and XRD data of hole 3A-11-11	55, 56
Figure 17. XRD data and Au mineralization of hole 3A-11-11	57
Figure 18. XRD data and Au mineralization of hole 3A-10-03	58
Figure 19. Geochemical plots for samples from Sprogge	60
Figure 20. REE and LILE multi-element variant plots	62
Figure 21. Ferrous/Ferric iron ratio plot	63
Figure 22. Shale curve for Pb-Pb isotopes.....	69
Figure 23. Plot of carbon and oxygen isotopes from carbonates.....	71
Figure 24. Bar graphs of carbon and oxygen stable isotopes from carbonates	72
Figure 25. Tera-Wasserburg plot of monazite U-Pb data	77
Figure 26. Deuterium and Oxygen Stable Isotope Plot	81
Figure 27. Deposit Structural Model	86, 87

CHAPTER 1: INTRODUCTION, GEOLOGY, AND ANALYTICAL METHODS

1.1 Introduction

Canadian Au exports totaled over \$15.6 billion in 2012 with the Yukon contributing 2.5% of total production (Statistics Canada, 2013). Despite geographic and infrastructural challenges, the Yukon continues to be an important area for mineral exploration (Burke et al., 2005; Chapman et al., 2011). Historically, Au mined from alluvial and fluvial deposits (known as placer deposits) was the focus of exploration and mining operations (Chapman et al., 2011). However, advances in exploration techniques have made it possible to track placer deposits back to source epigenetic Au deposits. Such advancements have increased the emphasis on exploration for non-placer deposits (Chapman et al., 2010).

Non-placer, epigenetic Au mineralization has been classified into several deposit types: epithermal, sediment-hosted, porphyry, skarn-type, submarine exhalative, orogenic, and intrusion-related (Groves et al., 1998). Orogenic and intrusion-related Au deposits share some geological traits, and are believed to be closely related (Groves et al., 1998). In both deposit types, Au occurs within hydrothermal quartz veins and is commonly associated with the occurrence of minor base-metal sulfides including pyrite and arsenopyrite. The hydrothermal quartz veins hosting the Au in these deposits formed from fluids which were sourced from and/or heated by either metamorphic reactions at depth (as in orogenic deposits) or magmatism (as in intrusion-related deposits). The criteria for defining the two deposit types overlap (Groves et al., 2003).

Both orogenic and intrusion-related Au deposits occur in the Tintina Gold Province of central Yukon and Alaska (Stephens et al., 2004). A subdivision of this province, the Tombstone Gold Belt (TGB), is located in central and southeastern Yukon and is known to contain several Au-rich deposits associated with mid- to Late Cretaceous intrusions (Baker and Lang, 2001; Mair et al., 2006b; Selby et al., 2003; Stephens et al., 2004). Known intrusion-related Au deposits in the northwest section of

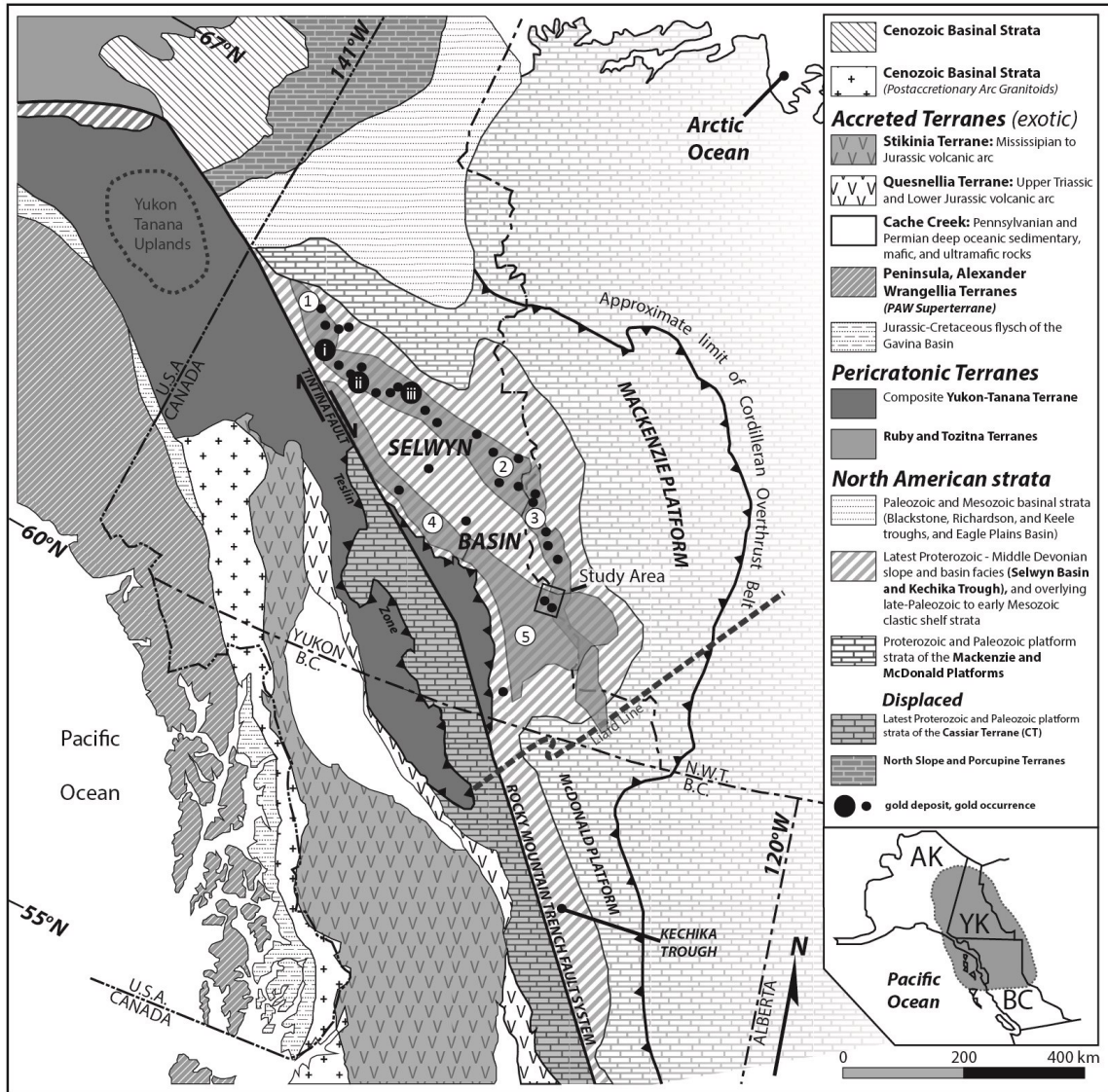


Figure 1. Geological maps of northwest North America including the Yukon (after Figure 1 in Mair et al., 2006) . Grey areas outline plutonic suites within the Selwyn Basin (1= Tombstone, 2= Mayo, 3= Tungsten, 4= Anvil, and 5= Hyland; Hart et al., 2004b). The box labelled study area is the region represented in Figure 2. Gold deposits and occurrences are only plotted for the Selwyn Basin (Rasmussen et al., 2006). Significant deposits include: i= Brewery Creek, ii= Clear Creek, and iii= Keno Hill.

the TGB include Dublin Gulch and Brewery Creek, with reserves estimated at 4.8 mega-ounces (Moz; Victoria Gold Corp, 2013) and 0.72 Moz (America’s Bullion Royalty Corp, 2013), respectively (Mair et al., 2006b). Figure 1 shows the geology of the Yukon, along with Au occurrences and plutonic suites within the Selwyn Basin.

The 3Ace and Sprogge areas are located 160 km north of Watson Lake along the Nahanni Range Road, Yukon Territory, Canada (Figure 2). Exploration in this area has increased significantly since the discovery of the Tungsten Suite of Cretaceous intrusions, and the Cantung mine less than 65 km away by road from Northern Tiger Resources' (NTR) 3Ace base camp (Hart and Lewis, 2005). This boost in exploration led to the discovery of a 50 km long trend containing several Au occurrences in the upper Hyland River Valley of the National Topographic System (NTS) mapsheet 105H (Hart and Lewis, 2005). A more detailed exploration history and overview of regional geochemical data can be found in Hart and Lewis (2006).

In an internal report completed for NTR, Conliffe and Wilton (2010) reported results from a preliminary fluid inclusion study of several Au showings on the 3Ace property. They concluded that Au deposition resulted from fault-related pressure cycling resulting in phase separation and that mineralization is likely orogenic and not intrusion-related.

Also included in the NTR claim block is the Sprogge property approximately 10 km east of 3Ace. Sprogge, described by Hart and Lewis (2006), consists of quartz vein-Au occurrences in close proximity to quartz monzonite dikes. NTR has carried out a mapping program, regional soil sampling and bulk geochemical analysis on samples from Sprogge, but has yet to carry out a drill program there. The focus of this study is primarily on the 3Ace deposit; however geochemical analyses were also carried out on samples collected at Sprogge to add to the regional and local geology.

The goal of the study is to develop a genetic model for mineralization that will guide future exploration of the 225 km² 3Ace claim block, 90% of which remains unexplored. Petrography, stable and radiogenic isotope analyses, bulk

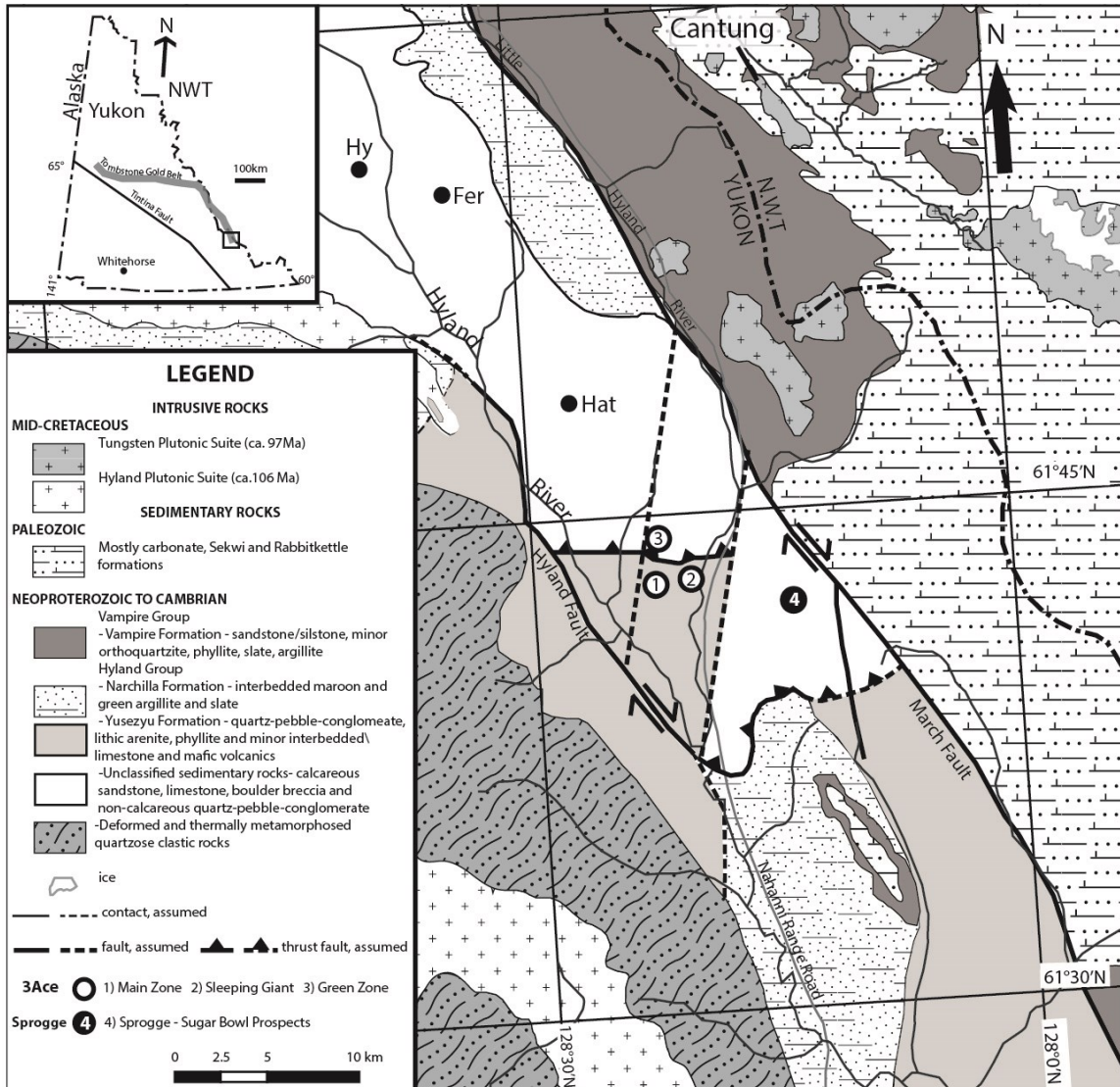


Figure 2. Geological map of the 3Ace and Sprogge areas (after Hart and Lewis, 2005).

and high-resolution geochemical analyses, X-ray diffraction, and microthermometry are used to characterize the mineralization. By understanding the genetic model, alteration phases, and regional geologic processes associated with Au, NTR will be able to focus on key geological features and minerals in order to isolate high grade zones throughout the 3Ace claim.

1.2 Regional Geology and Tectonic Setting

Both the 3Ace and Sprogge properties are hosted in Neoproterozoic to Cambrian metasediments of the Selwyn Basin (Hart and Lewis, 2005). The Selwyn Basin consists of slope to basin facies strata of Proterozoic to Paleozoic age and represents the offshore part of the Canadian Cordilleran miogeocline (Mair et al., 2006a; Falck, 2007). Late Cretaceous deformation led to formation of a complex series of orogen-parallel faults including the Tintina Fault (Mair et al., 2006a). The Tintina Gold Province and the Tombstone Gold Belt roughly follow the Tintina Fault (Mair et al., 2006b; Stephens et al., 2004). Gold mineralization in the area is believed to be genetically coincident with a series of mid to Late-Cretaceous plutonic events (Baker and Lang, 2001; Mair et al., 2006b; Selby et al., 2003; Stephens et al., 2004).

1.2.1 Selwyn Basin

Sediments of the Selwyn basin overlie a basement consisting of terranes accreted to the Canadian Shield since about 2.1 Ga (Falck, 2007). Prior to basin formation, North America was part of the Nuna supercontinent. Towards the end of the Mesoproterozoic, the Nuna supercontinent began to rift, thereby establishing the Pacific margin of North America (Falck, 2007; Gabrielse and Yorath, 1992; Sears and Price, 2000).

The onset of post-rift thermal contraction sometime between the Late Neoproterozoic and Earliest Cambrian time resulted from the spreading of the proto-Pacific Ocean (Bond and Kominz, 1984). The extensional event led to the formation of two facies belts (Gordey and Anderson, 1993). The northeast facies belt consists of shallow marine carbonates and sandstones of the Mackenzie Platform (Lenz, 1972, as referenced in Gordey and Anderson, 1993). In the southwest, the Selwyn Basin is the deeper water equivalent of these packages. Selwyn Basin strata are characterized by 'gritty', feldspathic sandstone, pebble conglomerate, maroon, red and green slate, along with phyllite, argillite, siltstone, and minor limestone (Gabrielse, 1967; Gordey and Anderson, 1993). In the late Devonian, uplift resulted in a sudden influx of marine turbiditic clastic rocks prograding to the south and east, known as the Earn Group (Falck,

2007; Gordey and Anderson, 1993; Gordey et al., 1987). Marine shelf sedimentation resumed from the mid-Mississippian to the mid-Jurassic (Gordey and Anderson, 1993), depositing mainly clastic rocks derived from the north (Gordey et al., 1987).

The oldest sediments in the Selwyn Basin are the Neoproterozoic to Cambrian Hyland Group (previously known as the "Grit Unit"; Gabrielse, 1967; Gordey and Anderson, 1993), which contains the Yusezyu and Narchilla Formations. Although the base of the unit is not exposed, the top is conformably overlain by shale of the Lower Cambrian Gull Lake Formation (Gordey and Anderson, 1993). The Yusezyu Formation is up to 3000 m thick, and consists of a succession of turbiditic quartz pebble conglomerates (formerly referred to as the 'grit' units), sandstones, and interbedded shales (Gordey and Anderson, 1993; Hart and Lewis, 2005). Unaltered quartz sandstones and quartz pebble conglomerates have a blue hue due to opalescent, blue quartz grains (Gordey and Anderson, 1993). Thin, lenticular limestone units are found near the top of the Yusezyu, and do occur rarely within the 3Ace area. Located to the northeast and coeval with the Yuzesyu Formation, the Vampire Formation comprises brown and grey siltstones and shales (Hart and Lewis, 2005).

The Narchilla formation overlies the Yusezyu Formation and occurs in some areas surrounding the 3Ace property. It consists of several hundred metres of maroon to dark blue-grey and green, recessively weathered shale, and fine grained sandstones (Hart and Lewis, 2005; Gordey and Anderson, 1993). It is in sharp contact with, and is believed to be conformably overlain by, the early Cambrian Gull Lake Formation. The Gull Lake Formation dominantly consists of blue-grey slate and siltstone that weathers buff-brown; it also contains some conglomeratic limestones near its base. It is believed to be coeval with the limestones and siliciclastics of the Sekwi Formation (Gordey and Anderson, 1993). The Gull Lake, Yusezyu, and Vampire Formations are all unconformably overlain by the Rabbitkettle Formation (Hart and Lewis, 2005). However, the contact between the Gull Lake and Rabbitkettle Formations is not observed locally, and the fact that they are very close in age may suggest a conformable contact in some areas (Gordey and Anderson, 1993).

1.2.2 Cretaceous Plutonism and the Tombstone Gold Belt

The plutonic suite classification system referred to in this paper is after Hart et al., (2004a). There are 5 Cretaceous plutonic suites within the Selwyn Basin (Figure 1).

Intrusions of the Mayo plutonic suite (MPS) are hosted within the deformed strata of the Hyland Group, and the Earn Group to the east. They form a 370 km long belt that stretches from the Tintina Fault to the eastern border of the Yukon (Hart et al., 2004b). The MPS intrusions have I-type characteristics but also have geochemical signatures consistent with a component of assimilated metasedimentary crustal material (Hart et al. 2004a; Mair et al. 2006b). The dominant lithology is quartz monzonite, occasionally with monzonitic to dioritic stocks and dikes (Hart et al. 2004a). They are believed to have formed between 95 and 92 Ma, and are associated with several types of mineralization, including Au-Bi-Te, W, As and Ag-Pb (Tab. 1 in Hart et al., 2004a, and references within). Well known mineral occurrences associated with the MPS include; Dublin Gulch, Scheelite Dome, Clear Creek, Ray Gulch, and Keno Hill (Hart et al., 2004a).

The Tombstone plutonic suite (TPS) is located in the northwest corner of the Selwyn Basin, north of the Tintina fault (Brown and Nesbitt 1987). It comprises of compositionally zoned intrusions dominated by biotite-, hornblende-, and/or pyroxene-bearing monzonite and syenite, with lesser quartz-monzonite, monzodiorite, monzogabbro, and silica-undersaturated high-K phases (Anderson 1987, as referenced in Hart et al. 2004a). The ages of the TPS plutons range from 90 to 95 Ma (Table 1 in Hart et al., 2004a, and references therein). They are considered to be magnetite-series intrusions based on their wide range of $\text{Fe}_2\text{O}_3/\text{FeO}$ and magnetic susceptibility values (Hart et al., 2004a). TPS intrusions on the Marn property contain minor Au-Ag-W-Cu mineralization associated with Bi and Te (Brown and Nesbitt, 1987).

Located to the south of the MPS and TPS is the Anvil plutonic suite (APS; Hart et al., 2004a). The APS consists of 3 different compositional phases, including: peraluminous muscovite-biotite granites, and two groups of metaluminous to

peraluminous hornblende-biotite granodiorites to granites (Hart et al. 2004a). The plutons have been dated to approximately 110-98 Ma (Pigage and Anderson 1985; Hart et al. 2004a). Mineralization associated with the TPS is zoned based on proximity to the plutons. The APS is most notably associated with numerous W veins and skarn showings, in some places with Mo, and distal Ag-Pb-Zn veins (Hart et al., 2004a).

The Hyland plutonic suite (HPS) is located to the east of the APS, and overlaps with the WPS (Heffernan and Mortensen 1999; Hart et al. 2004a). It consists of large heterolithic felsic and aluminous batholiths (Hart and Lewis 2006; Hart et al. 2004a). The HPS batholiths occur as flat sheets with fabric-concordant contacts within the Hyland Group, suggesting that they were emplaced at mid-crustal levels (approximately 10-15 km depth; Hart and Lewis, 2005). Uranium-Pb isotopes indicate a crystallization age around 106-96 Ma (Hart et al., 2004a). Mineralization believed to be associated with the HPS includes Au (Hart et al., 2004a), and W-Cu bearing skarns (Deklerk, 2003, as referenced in Table 3 of Hart et al., 2004a).

The Tungsten plutonic suite (WPS) is located in the southeast corner of the Selwyn Basin and is associated with world-class W occurrences including Mactung and Cantung (Hart et al., 2004a, and references therein). Compositionally, it is dominated by biotite granites, monzogranites, and quartz monzonites (Gordey and Anderson, 1993; Hart et al., 2004a). Several plutons of the WPS have been dated to 97-94 Ma, making them the youngest in the Selwyn Basin (Gordey and Anderson, 1993; Hart et al., 2004a,b). Mineralization associated with the WPS is almost exclusively W (Hart et al., 2004a and references therein), including the Mactung deposit, which is defined as a W-Cu-(Zn) skarn deposit (Dick and Hodgson, 1982).

The Tombstone Gold Belt is a subdivision of the Tintina Gold Province. It consists of intrusion-related mineralization associated with the Tombstone, Mayo, Tungsten and Hyland plutonic suites (Hart et al. 2004a; Stephens et al. 2004). These deposits are most notably characterized by sheeted mineralized veins within granitoid bodies and fault-hosted veins, in addition to breccias, skarns, and replacement type mineralization within the country rocks (Stephens et al., 2004).

1.2.3 Structural Evolution of the Selwyn Basin

The Selwyn Basin is located within the Omineca Belt of Cordilleran deformation (Gabrielse and Yorath, 1992). It is an area of regional uplift that is underlain by metamorphic and granitic rocks (Gabrielse and Yorath, 1992). High grade metamorphic rocks within the belt are the earliest known record of continental accretion in the Selwyn Basin (Gabrielse and Yorath, 1992). The Selwyn Fold Belt consists of northwest-trending, open to locally tight folds and associated axial-planar slaty cleavage (Gordey and Anderson, 1993). Mesozoic deformation directed easterly towards the craton resulted in an imbricated succession of folded thrust sheets, with more penetrative deformation than rocks of adjacent belts to the west (Gabrielse and Yorath, 1992). Intense imbrication of Paleozoic strata indicates pre-Cretaceous contraction of at least 50% in the Selwyn Mountains (Gabrielse and Yorath, 1992).

The area is highly faulted with both dextral, strike-slip faults and steeply dipping reverse faults that are believed to be associated with thrust faults at depth (Hart and Lewis, 2005). Faults throughout the Selwyn Fold Belt are diverse in trend and mostly steeply dipping. There are, however, two prominent fault trends (Gordey and Anderson, 1993). One strikes north to northeast and occurs oblique to the fold trend (Gordey and Anderson, 1993). These are smaller faults with less than 10 km offset and limited vertical movement (Gordey and Anderson, 1993). The second dominant strike is northwest, parallel to the fold trends, and consists of dextral, strike-slip faults and thrust faults (Gordey and Anderson, 1993). Northwest striking dextral faults, similar to the Tintina Fault, began propagating throughout the Omineca belt in the Late Cretaceous and Early Tertiary (Gabrielse and Yorath, 1992). The strike-slip faults have strike lengths up to 18 km, and throws of up to 600 m (Gordey and Anderson, 1993).

Contraction within the Selwyn Basin occurred during the Mesozoic, but cannot be determined more precisely than pre-Late Cretaceous and post-mid-Triassic in most areas (Gordey and Anderson, 1993). Using ^{40}Ar - ^{39}Ar data, fold and thrust style deformation can be further constrained to Late Jurassic to Early Cretaceous in the

northwestern area of the Selwyn Basin (Mair et al., 2006b). Mid-Cretaceous plutons cross-cut most folds within the Selwyn Mountains (Gordey and Anderson, 1993). Thrust faults are believed to have occurred coevally with folding (Gordey and Anderson, 1993). In general, northwest-trending folds and thrust faults formed as the result of north-easterly directed, horizontal compression (Gordey and Anderson, 1993), and can be explained in terms of a “thin-skinned” detachment model (Norris, 1972, as referenced in Gordey and Anderson, 1993).

1.3 Deposit Geology

The 3Ace mineral claim itself extends over 200 km² and is mainly centered between NTS map sheets 105H09 and 105H16. Both the 3Ace and Sprogge showings are hosted within the siliciclastic units of the Selwyn Basin.

1.3.1 Geology of the Sprogge Property

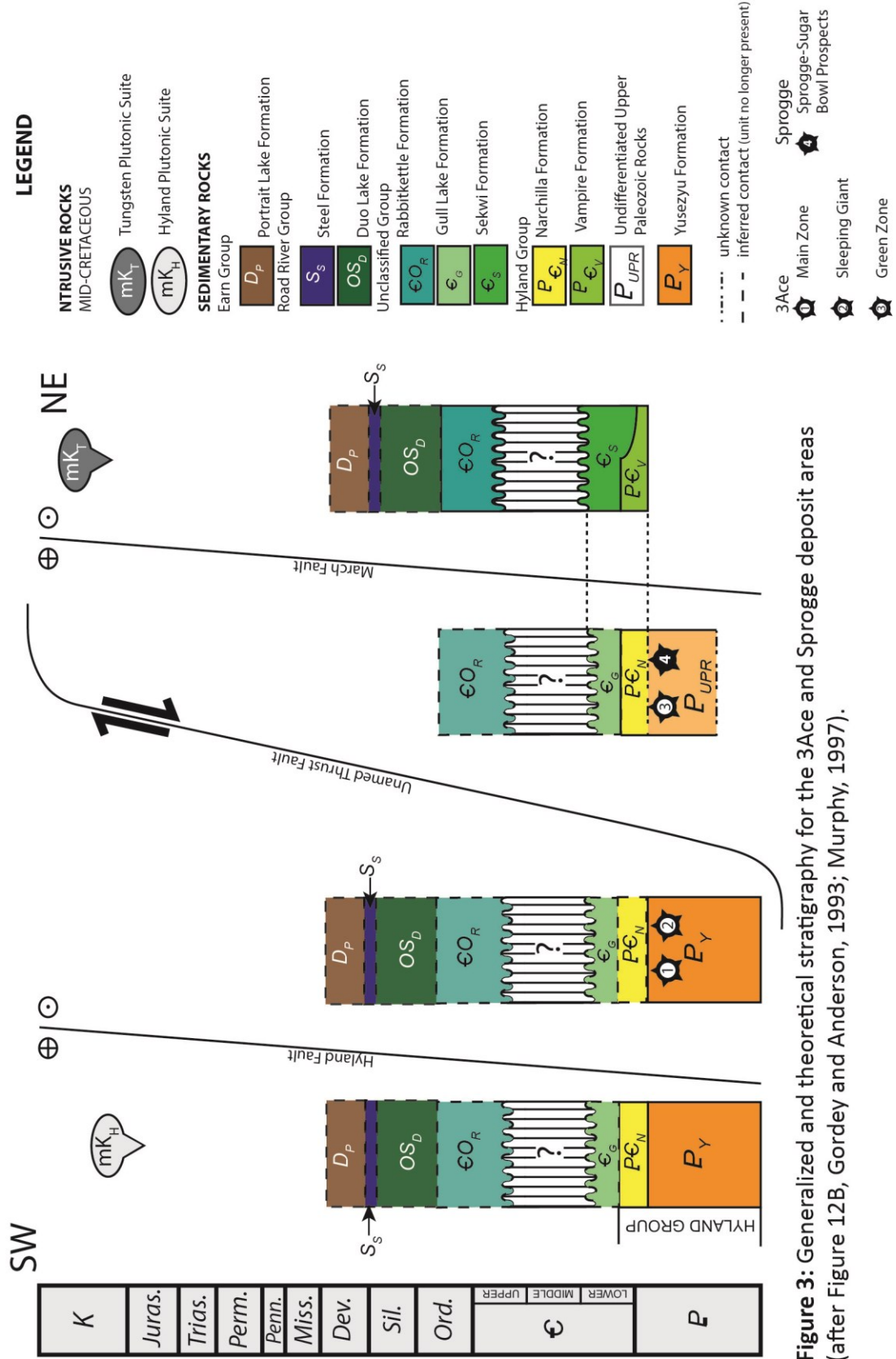
Sprogge is located approximately 10 km east of 3Ace. Detailed field mapping and sample collection began at Sprogge after a 1996 soil sampling program yielded anomalous Au values in several zones (Scott, 1999; Hart and Lewis, 2005). Mapping and sampling carried out in 2011 by NTR focussed on the Sugar Bowl prospects including the Matilda vein and Meadows zone. Previous work shows the area contains promising Au anomalies, with Au in soil values averaging more than 200 ppb (Hart and Lewis, 2005). Mineralization is believed to be associated with a 2400 m by 1200 m Sugar Bowl Alteration Zone, defined by Au, Bi, As, and Sb surface anomalies (Brownlee and Johnson, 2001). Abundant arsenopyrite occurs in biotite-quartz monzonite dikes. Intrusions and quartz veins occur within coarse clastic sediments, siltstones, shales, and silty limestones. As drill core is not available for Sprogge, this study focuses on providing a better understanding of the regional geology with respect to the nature and age of the biotite-quartz monzonite intrusions and their potential for intrusion-related mineralization.

1.3.2 Geology of the 3Ace Property

In the 3Ace property, the quartz veins are hosted within a quartz-pebble-conglomerate (QPC) package containing interbedded phyllites and lithic arenites assigned to the Yusezyu Formation (Hart and Lewis, 2005; Mair et al., 2006a). Mineralized veins strike approximately north to south, and are constrained by the Hyland and March Faults. The March Fault (Figure 2) is believed to underlie a 40 km stretch of the north-northwest trending Little Hyland River Valley (Hart and Lewis, 2005; Gordey and Anderson, 1993). Movement along the fault is largely strike-slip but facies variations on either side indicate ancient vertical motion (Hart and Lewis, 2005). The Hyland Fault on the western side of 3Ace is poorly constrained but generally underlies the Hyland River Valley.

While there are no major intrusions near the Au occurrences of 3Ace, there are two Mid-Cretaceous plutonic suites located in the area. The felsic intrusions of the Hyland plutonic suite are located 17 km to the southwest of 3Ace, on the far side of the Hyland Fault (Figure 2). They occur as thick, flat sheets emplaced at mid crustal levels, concordant with the fabric of the Hyland Group (Hart and Lewis, 2005). The second is the Tungsten plutonic suite located 10 km to the east of 3Ace on the far side of the March Fault (Figure 2). The Tungsten Plutonic suite is well known for its association with W mineralization at Cantung (Hart and Lewis 2006). The Cantung W mine is located approximately 65 km NE of the 3Ace area along the Nahanni Range road.

The 3Ace claim area consists of 4 zones, of which 3 were sampled; the Main Zone, Sleeping Giant and Green Zone. Gold mineralization is most abundant at the Main Zone and, therefore, it was the focus of this study. Au mineralization occurs along fractures and as an open-space fill within steeply dipping quartz veins that are believed to be the product of fault-related pressure cycling during orogenesis (Conliffe and Wilton, 2010). The general stratigraphy of metasediments at the Main Zone is shown in Figure 3.



Gold mineralization is believed to pre-date emplacement of the Hyland plutonic suite, but formed after peak metamorphism (Hart and Lewis, 2005). This is based on cross-cutting relationships where mineralized veins cross-cut barren veins, and a lack of evidence for plutonic activity at the Main Zone (Hart and Lewis, 2005). The 2011 NTR drill program shows that mineralization is focused along a steeply-northeast dipping ore shoot. A structural report prepared for NTR by Buchanan (2010) corroborates the idea that mineralized veins formed after peak metamorphism. He also pointed out that mineralized veins correlate strongly with large-scale structural controls, including the Hyland and March faults.

The Sleeping Giant Au occurrence is located ~1.3 km east of the Main Zone. It consists of several north-south striking quartz veins up to 25 m in width, with 2-4% fracture hosted arsenopyrite which occasionally also hosts visible Au (Schulze and Buchanan, 2010). A previous diamond drill hole about 150 m northeast of Sleeping Giant did not return significant gold values (Schulze and Buchanan, 2010). Northern Tiger Resources drilled 6 holes at Sleeping Giant between 2010 and 2011. While the drill program did intercept several Au mineralized quartz vein with grades as high as 5.05 grams per tonne (gpt) Au over 1.0 m, it failed to yield results comparable to Au grades at the Main Zone (Buchanan et al. 2012).

The Green Zone is located ~2.5 km north of the Main Zone and consists of brecciated quartz veins with abundant arsenopyrite and scorodite mineralization (Schulze and Buchanan, 2010). It shows significantly higher degrees of deformation than the other showings. Most diamond drill holes have failed to yield favourable Au results despite promising chip samples. The exceptions are 4 holes drilled across a steeply dipping shear zone which indicate that these structures control the mineralization. Drilling has revealed much thicker beds of phyllite (over 90 m) at the Green Zone compared to other areas. Buchanan (2010) also suggested intersecting faults and areas of intense brecciation resulted in fluid mixing possibly responsible for mineral precipitation.

One quartz vein field sample, SCW11 F300, was collected by a consulting NTR prospector 11 km north-northeast of the Main Zone near an area known as the Hat prospect (Hart and Lewis, 2006). This area is located at the edge of an aeromagnetic low, which in the past was believed to represent an unroofed low-magnetite intrusion; however these aeromagnetic lows may also be the result of thick QPC units (Hart and Lewis, 2006). The quartz vein contains a bleb of galena which was analysed to compare S isotopes at a site proximal to a possible intrusion but at a distance from the Au occurrences.

1.4 Analytical Methods

Precision and accuracy are reported as 2σ for each analytical technique.

1.4.1 EPMA and EDS

Electron probe microanalysis (EPMA) was carried out at the University of Alberta Electron Microprobe lab using the Cameca SX100 under the supervision of Dr. Sergei Matveev, and JEOL 8900 with Dr. Andrew Locock. Both microprobes are equipped with wavelength and energy dispersive spectrometers (WDS and EDS, respectively). Analyses were carried out in secondary and backscattered electron (BSE) modes using a beam width of 1 μm and an accelerating voltage of 20kV.

Backscattered electron images were taken of each grain prior to quantitative analysis. The Cameca SX100 was used for quantitative analysis of silicate and sulfide minerals from 3Ace and Sprogge. The Na, Mg, Al, Si, Ca, Ti, Mn, Fe, Cr, K, As, S, and P compositions of silicates were analysed, whereas sulfides were analyzed for Bi, Sb, Sn, W, S, Fe, Zn, As, Ag, Pb, Cu, Ni, and Au. The JEOL 8900 was used for both quantitative and qualitative analyses. Electron dispersive spectrometry allowed for a quick way to approximate mineral compositions for identification, as well as to determine U and Th contents in apatites, zircons, and monazites in thin section.

1.4.2 XRD

X-ray diffraction (XRD) studies were carried out at the University of Alberta X-Ray Diffraction Lab by Diane Caird using a Rigaku Geigerflex powder diffractometer equipped with a Co tube, graphite monochromator, and scintillation detector. Samples analyzed by XRD were first crushed to a ≈ 20 μm powder using a tungsten ball mill and, as needed, an agate mortar and pestle. X-ray diffraction was used to identify minerals in bulk rock samples for bulk lithology and alteration studies (e.g. Waseda et al. 2011). Only minerals with an abundance of approximately 1% or more within the crushed sample are detected by XRD.

1.4.3 Desktop Cathodoluminescence

Desktop Cathodoluminescence (D-CL) is a relatively inexpensive technique for determining structural and chemical heterogeneities and cross-cutting relationships at a microscopic level that may not be obvious from using regular microscopes or with the use of EPMA. It was also useful for finding radioactive rims surrounding radiogenic minerals that were not easily identified using a microscope, such as monazite. The Reliotron desktop CL microscope is located within the U-Pb geochronology lab at the University of Alberta, and work was completed with guidance from Judy Schultz. It consists of a microscope fitted with a vacuum chamber connected to a cathode ray tube. The microscope assemblage is fitted with a Canon DSLR and located within a dark room in order to properly capture the digital images.

1.4.4 BrF₅ method for Oxygen Isotopes

Oxygen isotope analysis using BrF₅ was carried out prior to the ion microprobe isotope analysis. Samples analysed from the Main Zone, Green Zone and Sleeping Giant, were chosen from the least altered and fractured quartz veins for analyses. Quartz generations were determined by identifying cross-cutting relationships between the veins and other quartz veins or faults (e.g. young vs old quartz). The quartz samples were separated from the host rock and then powdered using a steel mortar and pestle.

The oxygen was extracted using the method of Clayton and Mayeda (1963) in Dr. Karlis Muehlenbachs' Stable Isotope Lab at the University of Alberta with the help of Olga Levner. First, the powdered quartz was reacted with BrF_5 at 100°C within Ni reaction tubes to remove any impurities. Then the samples were reacted with BrF_5 at 600°C overnight. Once the reaction was complete, the resulting $\text{O}_{2(\text{g})}$ was passed through first a monel coil and then a glass coil 'sink' cooled by liquid nitrogen to freeze out remaining impurities. The oxygen was then passed against a graphite rod heated to 1400°C , converting the $\text{O}_{2(\text{g})}$ to $\text{CO}_{2(\text{g})}$. The collected CO_2 was then passed through a Finnigan MAT-252 Mass Spectrometer. The isotope results were measured relative to the National Bureau of Standards (NBS) 28 standard (Friedman and Gleason, 1973) and results are represented as $\delta^{18}\text{O}_{\text{SMOW}}$ and have an uncertainty of $\pm 0.1\%$.

1.4.5 SIMS and SEM-CL

Secondary Ion Mass Spectrometry (SIMS) and Scanning Electron Microscope – Cathodoluminescence (SEM-CL) analyses were carried out at the Canadian Centre for Isotopic Microanalysis (CCIM) at the University of Alberta by the author and Dr. Richard Stern. This technique was used to determine the $\delta^{18}\text{O}_{\text{VSMOW}}$ values for different generations of quartz at high spatial resolutions. Extensive petrography and CL work was carried out prior to SIMS analysis and the area of interest was then drilled out of the thin section in ~ 5 mm circles and mounted in epoxy. SEM-CL was carried out on a Zeiss EVO 15 scanning electron microscope equipped with secondary electron and backscatter electron detectors, electron dispersive spectrometer (EDS), a wide spectrum CL detector, and a Gatan Chroma CL detector. The wide spectrum CL and chroma CL detect structural heterogeneities in the rock, and were used to obtain clear images of the different quartz generations surrounding vugs or minerals of interest. These photos were then used as guides for the SIMS work in order to accurately sample each quartz generation. The SIMS analytical technique was carried out using a Cameca IMS 1280 ion microprobe. The Cs^+ beam excavated and ionized the quartz in $20\ \mu\text{m}$ circles. Pit depths at this size are $< 5\ \mu\text{m}$ making it an ideal in-situ technique for thin sections. The

secondary ions were then extracted and analysed by a mass spectrometer which determined the abundances of ^{18}O and ^{16}O to obtain $\delta^{18}\text{O}$ with a precision of $\pm 0.2\text{‰}$, or better, relative to the Vienna Standard Mean Ocean Water (VSMOW) standard.

1.4.6 Carbon and Oxygen Stable Isotopes in Carbonates

Calcite, dolomite, ankerite, and siderite were mechanically separated from the host rocks using a Dremel hand drill. The mineral separate was then crushed to a $<50\ \mu\text{m}$ mesh size. Analysis was carried out by Steve Taylor at the University of Calgary Stable Isotope Lab. There, they digested the calcite samples with anhydrous phosphoric acid in a Y-tube reaction vessel at 25°C . Dolomite, ankerite, and siderite samples were reacted with anhydrous phosphoric acid at 150°C for 2 hours similar to the technique of Rosenbaum and Sheppard (1986). The CO_2 gas was then cryogenically distilled from the reaction vessel into a 6mm Pyrex tube and flame sealed. The composition of the CO_2 gas was analysed using a VG903 stable isotope ratio mass spectrometer (IRMS) and analysed for $\delta^{13}\text{C}$ and $\delta^{18}\text{O}$ ratios relative to the Pee Dee Belemnite Standard (PDB). The precision and reproducibility for both $\delta^{13}\text{C}$ and $\delta^{18}\text{O}$ is typically better than $\pm 0.4\text{‰}$. (Coplen et al., 2002; Coplen et al., 2006)

1.4.7 Sulfur Stable Isotopes in Sulfides

Sulfur isotopes were also analysed by Steve Taylor at the University of Calgary Stable Isotope Lab. Between 400 to 500 μg of a mineral separate was placed into a tin cup, which was then dropped into a high temperature (Elemental Analyser) combustion reactor using an A128S auto-sampler running at a temperature of 1050°C . The He carrier gas then swept the resulting gases through a GC column, separating the SO_2 gas. The SO_2 was then introduced via an open interface to the ion source of a Thermo Delta XL mass spectrometer within a Carlo Erba NA 1500 elemental analyser. This technique is known as CF-EA-IRMS. Results are reproducible to within $\pm 0.6\text{‰}$ relative to the Vienna Canyon Diablo Troilite (VCDT) standard (Giesemann et al., 1994; Grassineau et al., 2001; Qi and Coplen, 2003; Poulson, 2005; Mayer and Krouse, 2004).

1.4.8 Radiogenic Isotope Analysis of Galena by MC-ICP-MS

Lead isotopes in galena were measured using multi-collector inductively coupled plasma mass spectrometry (MC-ICP-MS) at the University of Alberta Radiogenic Isotope Facility by Dr. Robert Creaser. It proved extremely difficult to separate enough galena for analysis because galena occurs as fine grained crystals inter-grown with other sulfides. As a result, only two samples were analysed. Small, pure galena cubes were dissolved into ultrapure HCl. The sample aliquots were then mixed with approximately 1.5 mL of 2% HNO₃ and 0.5 mL 5ppb Tl solution. The resulting solution was then aspirated using a cyclonic spray chamber and nebulizer. These were cooled using a Pelletier device fed into a multi-collector NuPlasma ICP-MS. This set-up is coupled to a DSN-100 introduction system. Results were measured relative to the NBS-981 Pb standards, and are presented to within a 2σ error, varying up to 0.015 for ²⁰⁸Pb/²⁰⁴Pb values, and 0.006 for ²⁰⁷Pb/²⁰⁴Pb.

1.4.9 Radiogenic Dating of Zircons and Monazites by LA-MC-ICP-MS

Zircons and monazites were analysed for U-Pb geochronology using laser ablation (LA) MC-ICP-MS at the Radiogenic Isotope Facility at the University of Alberta with the help of Dr. Andy Dufrane, following the analytical protocol and data reduction procedure outlined in Simonetti et al. (2005). Zircons were separated from field samples collected from biotite-quartz monzonite dikes at Sprogge. Samples were crushed using a jaw crusher and disc mill, and then heavy minerals were magnetically separated. Zircons were then separated from the light fractions using density-specific methylene iodide, and rinsed with acetone. Zircon grains were then handpicked using a binocular microscope and mounted in epoxy. Monazites were analysed in situ in standard polished thin sections after being identified with EPMA and CL.

A multi-collector NuPlasma ICP-MS coupled to a UP213 laser ablation system was used for the analysis. The system houses a modified collector block containing 12 Faraday cups and 3 ion counters. The laser width was set to 30 μm for zircon analysis

and 15 μm for monazite. Zircon data were standardized using in-house reference GJ1 that was initially analysed by Thermal Ionization Mass Spectrometry (TIMS; Heaman et al., unpublished). The reference zircons are from the same area in Sri Lanka as those referenced in Jackson et al. (2004); however, they are not from the same batch. Madagascar (MAD) monazite reference materials were also standardized in house (Heaman et al., unpublished). Raw U and Pb isotope data were then manipulated by Dr. Andy Dufrane using Isoplot software generated by Ludwig and the Berkeley Geochronology Centre (2012).

1.4.10 Microthermometry

Fluid inclusion wafers were processed from core and field samples at the University of Alberta Thin Section Lab and Vancouver Petrographics. Doubly polished fluid inclusion wafers were lapped down to $\sim 70 \mu\text{m}$ to increase clarity, as thicker sections were too cloudy to analyse because of the high abundance of fluid inclusions. After completing petrography to determine which quartz generations were associated with the different fluid inclusion assemblages, fluid inclusion wafers were removed from their glass backings by soaking them in acetone.

Microthermometry measurements were made using an Olympus BX50 microscope mounted with a Linkam THMSG600 heating and freezing stage in Dr. Jeremy Richards' Fluid Inclusion Lab, allowing for accuracy of $\pm 0.2^\circ\text{C}$ at temperatures below 10°C , and $\pm 2.0^\circ\text{C}$ for temperatures above 10°C . The heating and freezing stage has a working temperature range from -196°C to 600°C . Three reference quartz grains were used to calibrate the results prior to analysis and for every 3 months of analysis. Two SynFlinC standards were used to calibrate CO_2 melting at -56.6°C and heating to the 376.4°C critical point for an H_2O inclusion. A third in-house sample (AR 305) was used to calibrate the ice melting point.

Salinities were calculated using the equation from Bodnar et al. (1993) for H_2O - CO_2 -NaCl inclusions and the equation of Darling (1991) for CO_2 -rich H_2O - CO_2 -NaCl- CH_4 inclusions. Salinities are reported in weight percent NaCl equivalent (wt. % NaCl eq.).

Molar volumes were visually estimated from Figure 6 in Bakker and Diamond (2000). The molar volumes were then used to calculate fluid pressures using the software by Bakker (Computer Modelling, Fluid Inclusion Laboratory Leoben, 2014, and references therein). The Loner AP package was used to calculate fluid pressures from fluid inclusions with homogenization temperatures above 300°C, and the Loner15 (06/02) package was used for temperatures below 300°. The different packages were used as the dissociation of NaCl is substantial at homogenization temperatures below 300°C (Duan et al. 1995).

1.4.11 Whole-Rock Major and Trace Element Analysis

Seven biotite-quartz monzonite dike samples were analysed for major oxides and trace elements by ACME Analytical Laboratories in Vancouver, B.C. Samples prepared for analysis were chosen and cut down in order to analyse as much fresh rock as possible. Major element oxides were determined using their 4X01 method which uses LiBO₂ fusion followed by X-Ray fluorescence. Trace elements were analysed using the 4B02 package which employs two separate ICP-MS analyses, where rare earth and refractory elements were analysed from a lithium borate decomposition, and metals were generated from an aqua regia digestion. A single element assay was used to determine the amount of FeO from whole rock samples (method code G806). This technique roasts the sample at 1050°C, then the roasted sample was fused in a platinum-gold crucible with a commercial lithium tetraborate flux. The fused discs were then analysed by XRF. Whole rock geochemical analyses were obtained to compare the intrusions at Sprogge to other intrusive suites within the Selwyn Basin, and to attempt to evaluate their possible mineral potential.

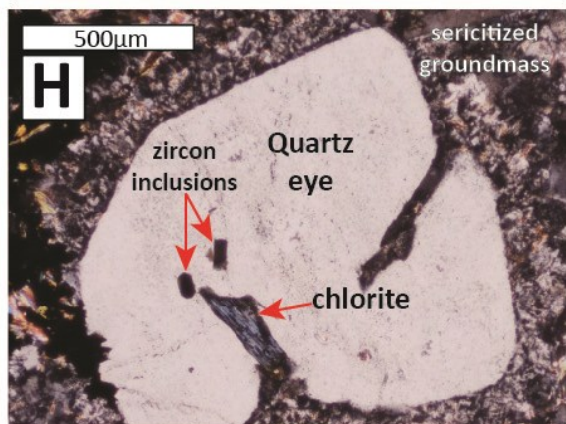
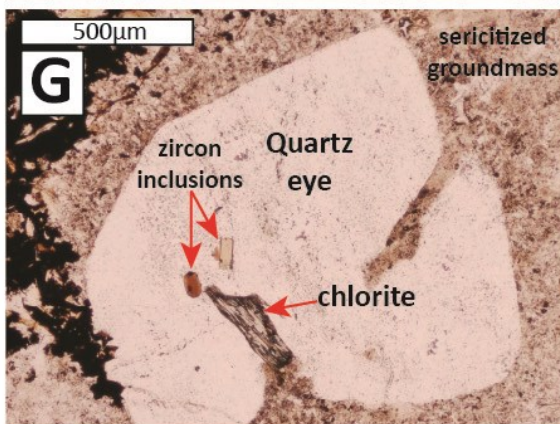
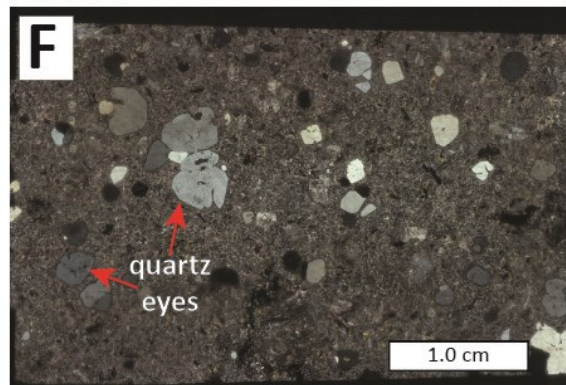
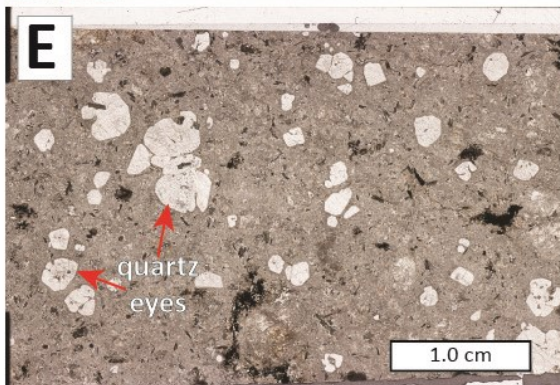
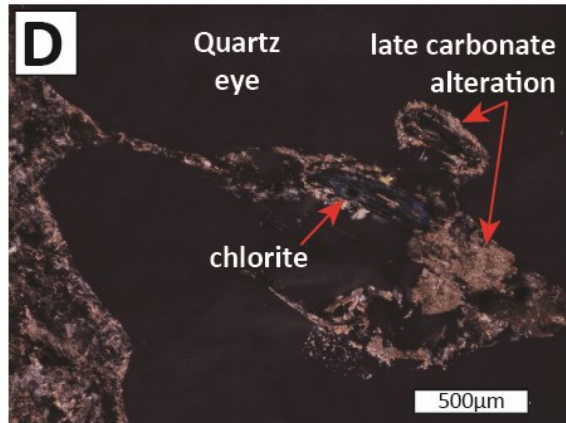
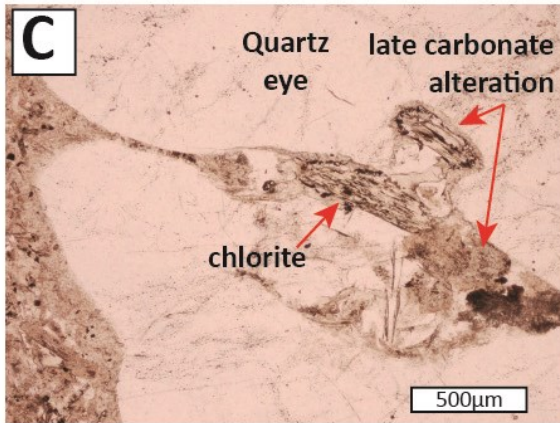
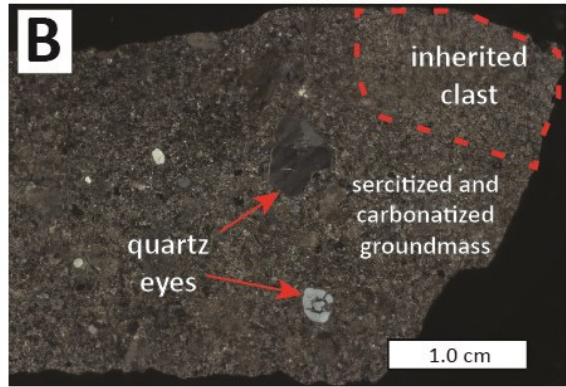
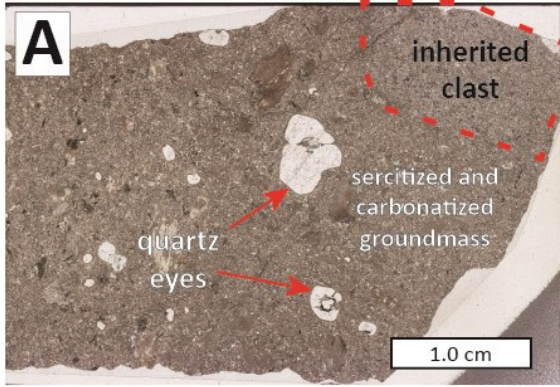
CHAPTER 2: RESULTS

2.1 Sprogge

Radiogenic isotope and geochemistry results analysed from quartz monzonite dikes at Sprogge are summarized below. Sample locations are given in Appendix A.

2.1.1 Field Results and Petrography

A map of the Sprogge property can be seen in Figure 4 (map –inside cover). Intrusive rocks were sampled as part of the mapping program in order to determine their composition. Thin section petrography was used to determine the composition of the intrusive rocks using a QAPF diagram (e.g. Figure 1, Streckeisen, 1974). Quartz occurs as subhedral to euhedral ‘quartz eye’ grains which suggest a primary magmatic origin. Euhedral quartz eyes are almost perfectly hexagonal in thin section, and are clear in PPL (plain polarized light) and isotropic in XPL (cross polarized light). Zircon and feldspar grains also occur in the matrix, but the type of feldspar was difficult to determine due to the high degree of alteration. Therefore the intrusives have been classified as quartz monzonite dikes with a porphyritic texture. While biotite contents vary from 5-20%, some biotite appears to be secondary as it cross-cuts primary quartz eye clasts. Photomicrographs of the quartz monzonite dikes are found in Figure 5. Two hand samples that stood out from the others are SCW11 F180 and F181. These samples appear to be contact breccias comprising wall-rock and chill margin fragments hosted within a quartz monzonite intrusion. They were collected from a previously unrecognized intrusion as seen in Figure 4.



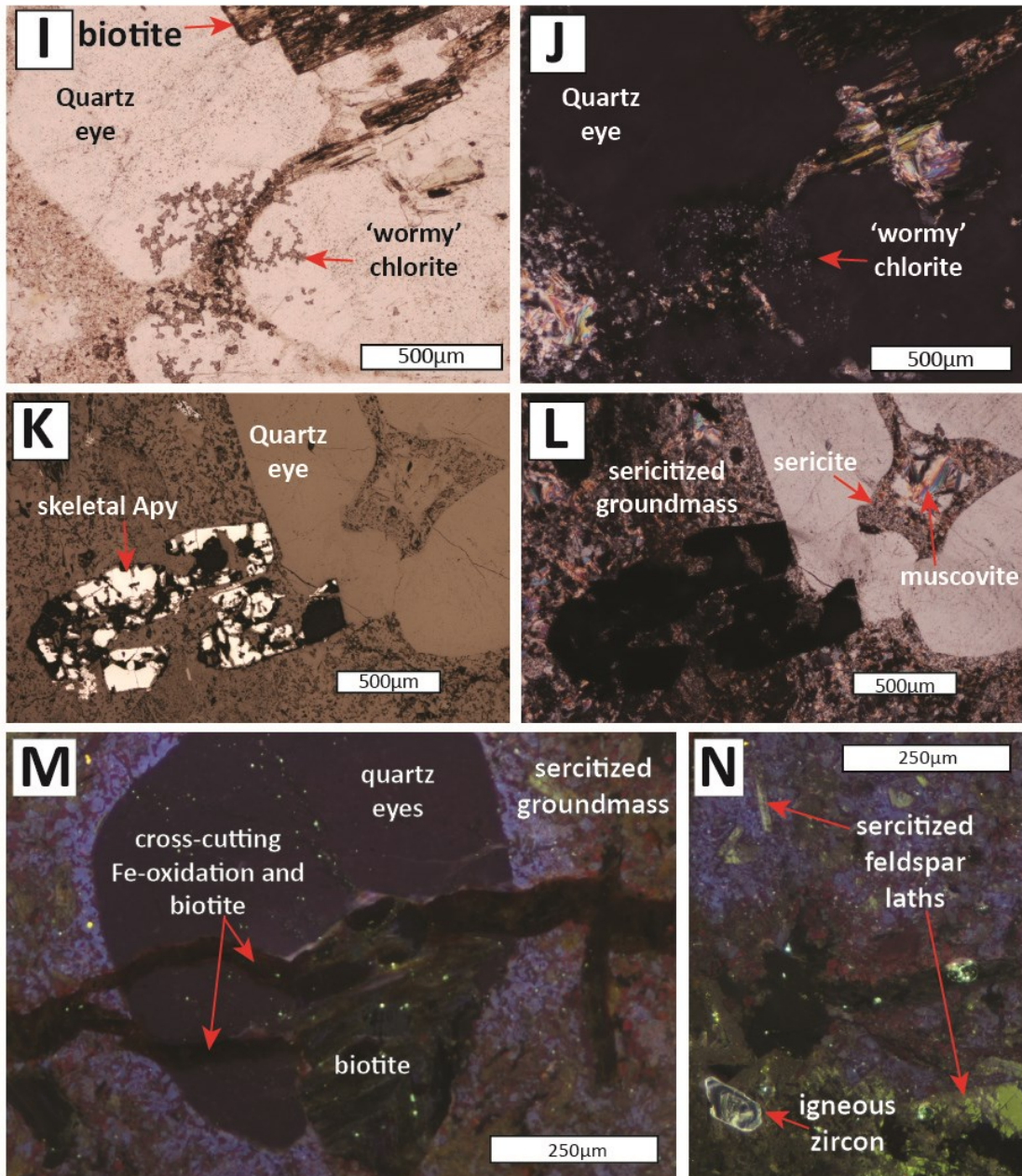


Figure 5. Thin section scans and photomicrographs of the quartz monzonite dike samples from Sprogge. Thin section scans A (PPL) and B (XPL), and photos C (PPL) and D (XPL) are of sample SCW11F 180. Scans A and B show an inherited clast within the quartz monzonite. Photos C and D show late carbonate alteration overprinting earlier chlorite alteration along fractures within a quartz eye. Thin section scans E (PPL) and F (XPL), and photos G (PPL) and H (XPL) of sample SCW 11 F215. Scans E and F show quartz eyes and opaques (weathered arsenopyrite and biotite) within the sericitized groundmass. Photos G and H show subhedral chlorite alteration along fractures in a quartz eye also containing zircon inclusions. Photos I (PPL) and J (XPL) of sample SCW11 F212 show a quartz eye that has been altered along a penetrating fracture by 'wormy' chlorite, muscovite, and biotite. Photos K (reflective PPL) and L (XPL) show sericite alteration cross-cutting skeletal arsenopyrite and hollowed out quartz eye within sample SCW11 F211. Desktop CL images M and N are from sample SCW11 F165. Photo M shows late cross-cutting features within a quartz eye. Photo N shows a pale, green-yellow, altered feldspar adjacent to an igneous zircon.

2.1.2 Radiogenic Isotope Results

Zircons were imaged using SEM-CL, revealing oscillatory growth zones and some inherited cores. In total, 163 spot analyses were carried out on zircons from 7 different Sprogge quartz monzonite dike samples. Of the spot analyses, 16 were rejected for high amounts of common Pb ($^{204}\text{Pb} > 400\text{cps}$), and 14 were rejected for ages which were >70% discordant; the majority of which were analysed from zircon cores. One other analysis was rejected because the laser ablated an older core and younger rim simultaneously. Values with high common Pb were not included in age analysis in order to increase the accuracy of the calculated age, but it should be noted that there are inherent errors with this correction which can then propagate through the age calculation (discussed in detail in Simonetti et al., 2005). Age estimates were calculated using Isoplot (Ludwig, 2003) and are summarized in Table 1.

Inverse Concordia graphs (or Tera-Wasserburg plots) were used when a Model-1 solution could be attained, yielding values with 95% confidence. When a data set did not yield Model-1 solution, a weighted average graph was used instead. Model-1 solutions assume the assigned errors are the only reason the data scatter, whereas Model-2 solutions assume other causes of scatter are involved (Ludwig, 2003). These graphs use the $^{206}\text{Pb}/^{238}\text{U}$ ages and errors to obtain an average age. Photomicrographs, SEM-CL images and a summary of the U-Pb isotope data and graphs used in age estimation can be found in Appendix F. Regression lines on the Inverse Concordia graphs were anchored at the value for common Pb, 0.86 (Stacey and Kramers, 1975; e.g. Rodionov et al., 2012).

Table 1. Summary of age determinations from U-Pb isotopes for zircons separated from Sprogge quartz monzonite dikes. With the exception of sample SCW11 F165, analyses were of the outer growth zones. Graph type refers to the graph used to calculate the estimated age (I.C.= inverse Concordia, W.A. = weighted average). Anchored refers to whether the regression line was anchored at the value of common Pb (0.86 ± 0.01).

Sample	Estimated Age (Ma \pm 2 σ)	Graph Type	Anchored (Y/N)
SCW 11 F165 outer growth zone (n=15)	98.1 \pm 2.1	I.C.	Y
SCW 11 F165 inherited core (n=2)	1063 \pm 47	I.C.	N
SCW 11 F166 (n=16)	103.5 \pm 1.2	W.A.	n.a.
SCW 11 F168 (n=11)	95.7 \pm 2.0	W.A.	n.a.
SCW 11 F172 (n=4)	102.2 \pm 1.8	I.C.	Y
SCW 11 F180 (n=6)	99.3 \pm 3.4	I.C.	Y
SCW 11 F211 (n=36)	100.8 \pm 1.1	I.C.	Y
SCW 11 F212 (n=15)	100.3 \pm 1.6	W.A.	n.a.
<i>SCW 11 F215 (n=15)</i>	<i>98.1 \pm 1.1</i>	<i>W.A.</i>	<i>n.a.</i>

2.1.3 Sulfur Isotopes and Whole Rock Major and Trace Elements

The complete set of analytical data for whole rock analysis of the quartz monzonite dikes at Sprogge can be found in Appendix G. The samples have relatively consistent major oxide compositions, with SiO₂ values ranging from 66% to 73% and K₂O+Na₂O values from 5.3% to 6.6%. Molar proportions of Al₂O₃ for all 7 samples exceed the combined molar proportions of CaO, Na₂O and K₂O indicating the intrusions are peraluminous. Barium and Sr values are relatively moderate, while Rb values are among the lowest of the TGB. The ferric/ferrous Fe contents are relatively high with all values above one, indicating the Fe in the samples is mainly oxidized. Arsenopyrite from a quartz monzonite dike (sample SCW11 F211) yielded a $\delta^{34}\text{C}_{\text{VCDT}}$ value of $8.6 \pm 0.6\%$.

2.2 The 3Ace Claim Block

3Ace consists of the Main Zone, Green Zone, and Sleeping Giant showings (Figure 2). The results presented here dominantly come from field and core samples of the Main Zone. The few results for the Green Zone and Sleeping Giant are mentioned in the results sections for the Main Zone.

2.2.1 Summarized Field Results

Drill collar and field sample locations are summarized in Appendix A. A detailed map of the Main Zone shows the discovery vein (Figure 6). Main Zone quartz veins and smaller veins are hosted in a quartz pebble conglomerate (QPC) with lithic arenite and shale interbeds. Quartz veins at the Main Zone are variably altered with Fe-oxidation and sericite growth along fractures and on the outcrop surface. Scorodite is present along fractures containing weathered arsenopyrite. Gold mineralization occurs primarily along fault surfaces within the quartz vein, which occur sub-parallel to the QPC-vein contact. These Au-bearing faults have strike/dip measurements of approximately $340^{\circ}/70^{\circ}$ with two measurements around $255^{\circ}/70^{\circ}$, suggesting the fracture surface undulates. Slickenlines along the fault surface have a trend and plunge of $054^{\circ}/52^{\circ}$. The discovery vein at the Main Zone is truncated on either side of northeast to east-northeast trending faults, seen regionally throughout the property (Hart and Lewis, 2006; Buchanan, 2010).

The Sleeping Giant area also has Au-mineralized quartz veins striking in the same direction as seen in the Main Zone. Figure 7 shows a summary of strike and dip directions for 146 fault surfaces within the quartz veins. Fault surfaces which strike north-east to south-west are well formed and cross-cut all previous fault sets. The mineralized faults at Sleeping Giant are also believed to strike north-south; the same direction as those at the Main Zone. Trenching carried out by NTR revealed anomalous Au zones with chip samples yielding grades of >45 gpt Au (Northern Tiger Resources website, 2014). Figure 7A shows the fault sets are all steeply dipping. The spread of fault strike directions likely resulted from the dextral movement of the strike-slip faults on either side of the mineralized area (Figure 2), where earlier faults would have been rotated in a counter-clockwise direction (Figure 7B).

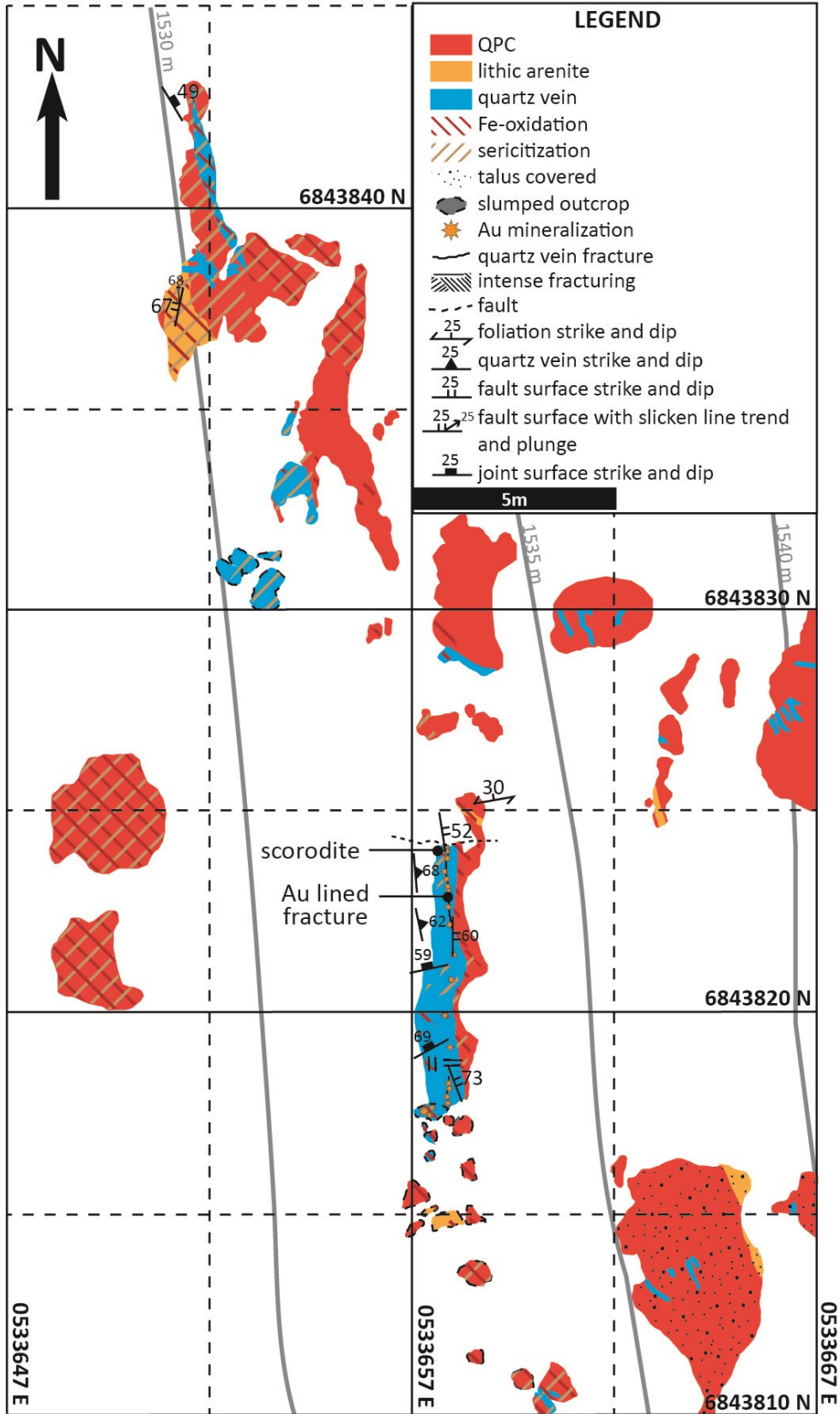


Figure 6. Detailed map of the discovery vein at the Main Zone.

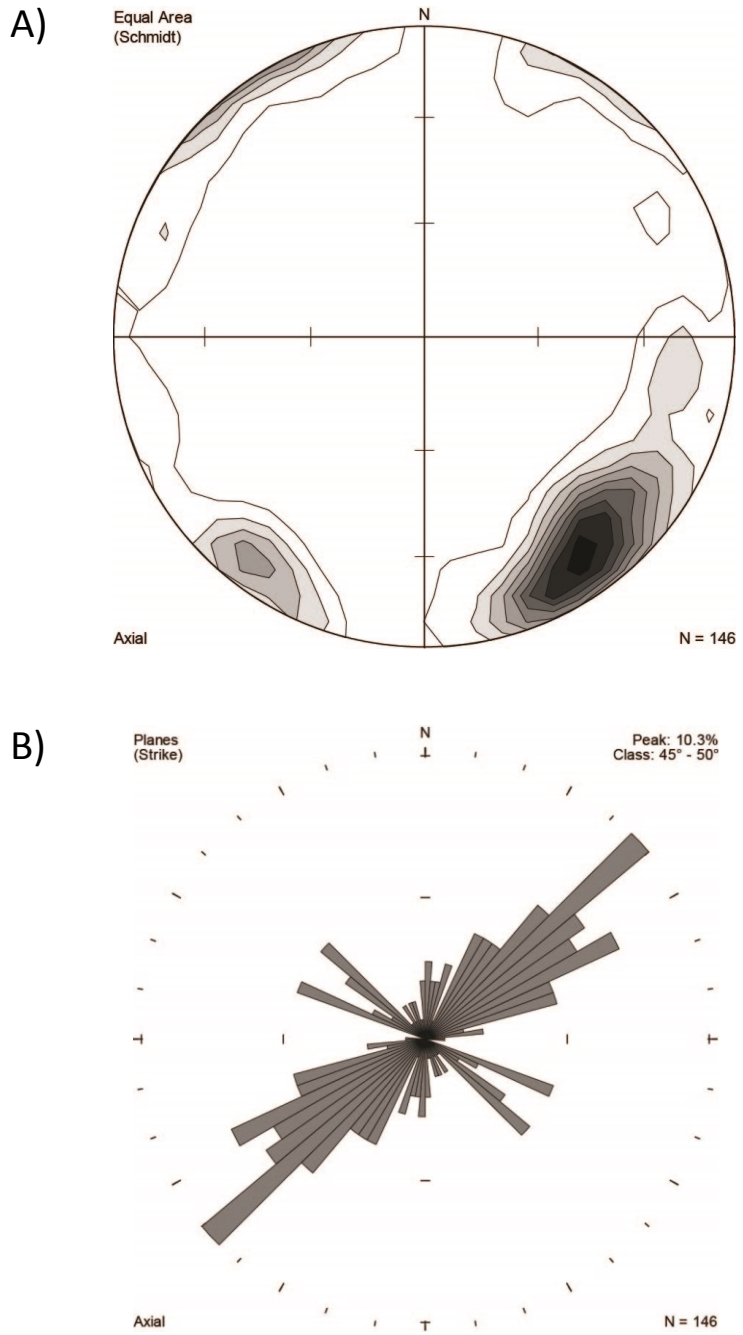


Figure 7. Plot A is an equal area projection of the poles to the fault planes that cross-cut Sleeping Giant quartz veins. Contouring intervals represent the percentage of the data within 1% of the plot area using a Gaussian (K=100) contouring method. Plot B is a rose diagram of the strike measurements of the faults.

Mapping of the talus at the Green Zone showed a north-south trending lineament, believed to be a fault that controlled fluid flow associated with alteration. In contrast to the Main Zone and Sleeping Giant, the main lithology here is limonitic and sericitically altered phyllite with lenses of QPC and lithic arenite. Quartz veins at the Green Zone are intensely brecciated, and contain up to 30% arsenopyrite mineralization and scorodite alteration, compared to <5% arsenopyrite at the Main Zone. Drilling carried out at the Green Zone showed that Au mineralization occurs within discrete lithic arenite lenses. Gold assay values from the core have an upper limit around 3 gpt; much lower than core from the Main Zone, which reached a maximum at 196 gpt.

2.2.2 Host Rock Petrography

Observations made in hand sample and thin section suggest that the mineralization is found in quartz veins hosted by the meta-sedimentary packages of the Yusezyu Formation. These sheared and fractured meta-sediments consist of quartz-pebble conglomerate (QPC), lithic arenite, and phyllite (Figure 8). The QPC is a bimodal orthoconglomerate which varies between an oligomict in less deformed areas, to a petromict in more deformed areas due to an increasing percentage of sericite in the matrix. Over 95% of the clasts are blue, opalescent, sub-rounded quartz pebbles, but clasts range in size from coarse granules to cobbles based on the Wentworth clastic sediment classification (Wentworth, 1922). Quartz clasts are elongated parallel to a foliation developed in the fine grained matrix. The remaining clasts are dominated by (variably altered) feldspars. X-ray diffraction analysis of the unit suggested that anorthite, sanidine, anorthoclase, albite, and microcline are present. The feldspars are intensely sericitized, and skeletal grains are too fine grained to distinguish from sericite in PPL and XPL. The matrix comprises up to 100% sericite, which is most prevalent along shear fractures within the QPC. Pyrite and arsenopyrite are rare and occur along microfractures following the foliation through the matrix. Biotite is visible within the matrix of meta-sediments bearing relatively high amounts of Fe-rich alteration minerals including goethite, siderite and ankerite.

Wall rock photomicrographs are seen in Figure 8. The QPC usually has a concordant, gradational contact with the lithic arenite unit. The lithic arenite comprises fine to coarse-sand sized quartz grains and granules that range from clast to matrix supported. It is very similar to the QPC in that the only discernible grains are quartz (mostly polycrystalline) and its matrix has been sericitized. Trace amounts of very fine grained (<10 µm) clinozoisite are found within the matrix of both the QPC and lithic arenite. The sericite matrix of both the QPC and lithic arenite has a foliation that is commonly emphasized by streaks of Fe-oxidation and rutile bearing muscovite stringers (see Section 2.1.4). The orientation of this foliation fabric is not consistent due to the competency variation of the QPC, but it generally has a shallow dip and an approximate east – west strike.

The phyllite units are inter-bedded in the lithic arenite and QPC along concordant or sheared contacts. The phyllites are very fine grained units with lenses that are less than 1 cm thick of fine to medium grained sandstone. Crenulation cleavage can be seen in areas of intense deformation. The earliest pyrite in the paragenesis, pyrite-1 (Py-1) occurs both within the coarser units of phyllite and within the lithic arenite matrix, along with very fine grained detrital zircons with “spongy” overgrowth rims. Pyrite-1 occurs as aggregates of cubes from 4 to 10 µm diameter and appears to have formed from recrystallized pyrite framboids; occasionally they are so abundant they can be observed in the sandstone lenses of the phyllite. Base-metal have been weathered to iron oxides in many samples.

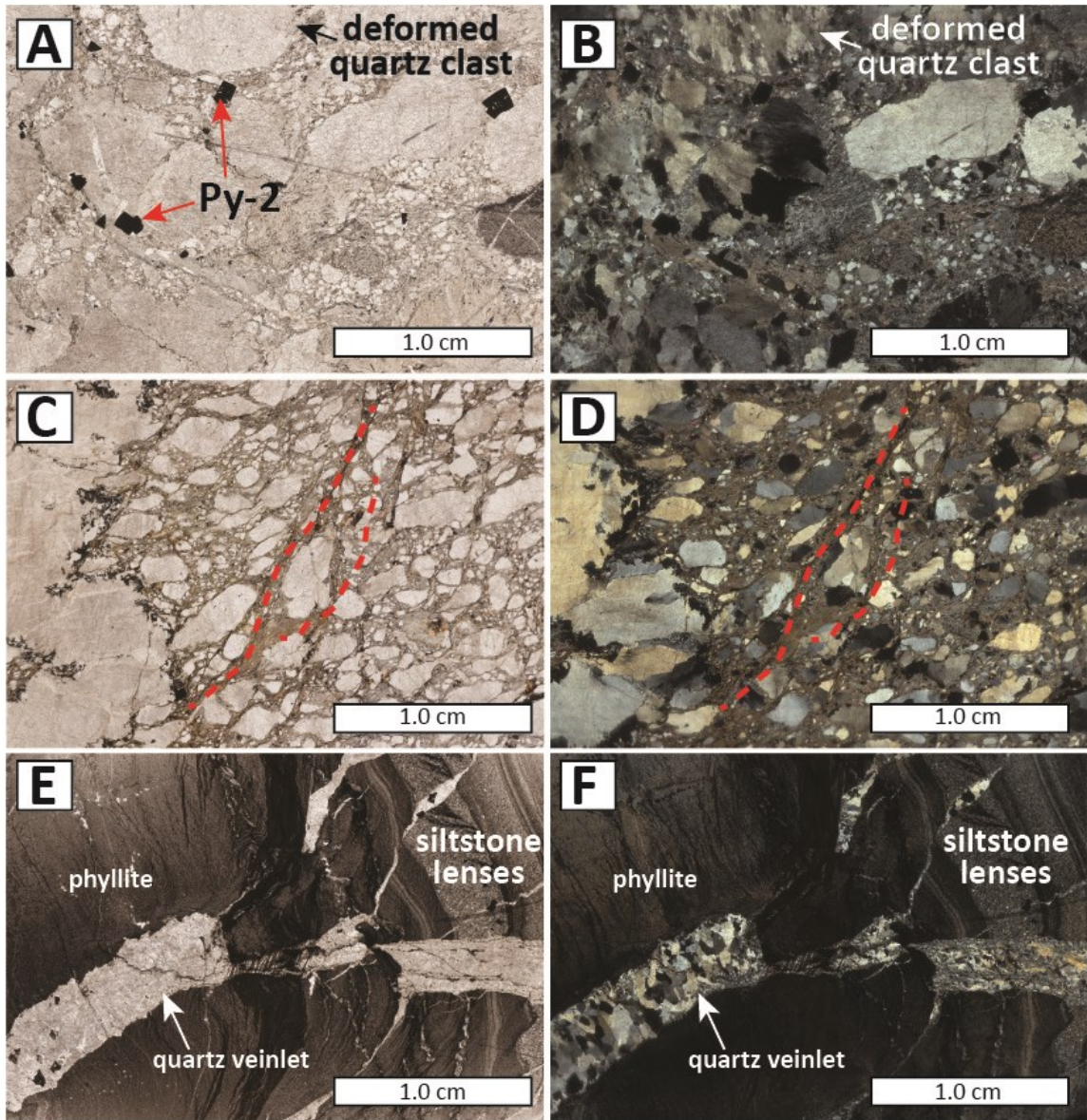


Figure 8. Thin section scans and photomicrographs of the various metasediments found at the Main Zone. Thin section scans A (PPL) and B (XPL) are of sample 3A-11-10A 78.94 comprising QPC with a sericite and Py-2 matrix. Scans C (PPL) and D (XPL) show a coarse lithic arenite from sample SCW11 F135, with a boudinaged quartz vein on the left. The red lines trace shears with abundant sericite alteration. Scans E (PPL) and F (XPL) show sheared quartz veinlets within phyllite from sample 3A-11-01 95.1.

2.2.3 Petrography and Paragenesis

Using hand sample and thin section petrography, in addition to CL, XRD, EPMA work, the different quartz vein generations and associated mineralization have been divided into several stages which are summarized in paragenetic sequence chart (Figure 9).

Quartz veins were observed in hand sample, microscopically under plane and cross polarized light, and under three cathodoluminescence (CL) systems: desktop (D-CL), SEM (SEM-CL) and SEM-chroma. At least 5 different quartz vein generations were resolved using these techniques; Q1, Q2, Q3, Q4 and Q5. Petrography showed that Q1, Q2, Q3 and Q4 are optically continuous in transmitted light and, therefore, identification of these generations is largely based on CL work. These results were then used to refine a paragenetic sequence for other minerals (Figure 9). The contents of each mineral were determined using EPMA. Due to the detection limits of EPMA, only element contents >0.1 wt. % are considered. Summaries of the data obtained by EPMA for both silicate and sulfide minerals are found in Appendix B.

Stage 1: Early quartz veins

Stage 1 is defined by the earliest quartz vein generation, Q1, along with apatite (Ap-2), albite (Ab), and pyrite (Py-2). Q1 is a composite phase of quartz veins that formed prior to the hydrothermal event responsible for Au mineralization. In hand sample Q1 is milky to opaque, white to beige quartz. BSE images show no distinction between Q1 and other quartz phases. However, Q1 has distinctive cathodic light characteristics. Under the D-CL Q1 has a dark blue-violet to blue to brown luminescence. Thin sections show that Q1 has been intensely fractured with varying degrees of recrystallization and contains abundant fluid inclusions. Euhedral apatite luminesces bright violet and is lime green along edges and fractures under the D-CL. It occurs within recrystallized quartz in a shear boundary adjacent to a coarser, later quartz vein. Pyrite (Py-2) also occurs in Q1 as fine grained, anhedral, and intensely fractured crystals. In XPL deformed pyrites are anisotropic.

Mineral	Host Rock	Stage 1	Stage 2	Stage 3	Stage 4			Stage 5	Stage 6	Stage 7
					a	b	c			
quartz (clastic) feldspars sericite apatite biotite	Qz Fsp	Ap - WR Bt				Ser				
quartz apatite calcite dolomite albite Au arsenopyrite pyrite galena sphalerite chalcopyrite pyrrhotite marcasite		Q1 Ap - QV Ab Py-1 Py-2	Q2	Q3	Q4 Cal Dol Au Apy Gn-1			Q5		Mrc
muscovite smectite kaolinite dickite zircon monazite rutile ankerite gypsum chalcedony goethite chlorite scorodite				Sme Zrn*	Ms -1 Dck	Kln	Ms -2 Sme Zrn* Mnz Rt Chl-1			Ank Gp Chal Gth Chl-2 Sc

Figure 9. Paragenetic sequence chart for the host rock and quartz veins of the Main Zone (Qz = quartz, Fsp= Feldspar, Ap= apatite, Bt= biotite, Ser= sericite, Cal= calcite, Dol= dolomite, Ab= albite, Apy= arsenopyrite, Py= pyrite, Gn= galena, Sp= sphalerite, Ccp= chalcopyrite, Po= pyrrhotite, Mrc= marcasite, Ms= muscovite, Sme= smectite, Kln= kaolinite, Dck= dickite, Zrn= zircon, Mnz= monazite, Rt= rutile, Ank= ankerite, Gp= gypsum, Chal= chalcedony, Gth= goethite, Chl= chlorite, and Sc= scorodite).

Dashed lines indicate uncertainty of mineral location in paragenetic sequence.

* zircons are inherited and have not formed from the fluids which precipitated the quartz veins

Stage 2 and 3: Later cross-cutting veins

Stage 2 comprises Q2 and no other minerals (Figure 10). Q2 both cross-cuts and occurs as overgrowths on Q1 and appears to be syngenetic with the tectonic event that led to the fracturing of earlier quartz. Q2 is volumetrically insignificant and is not visible in hand sample. In PPL, it rarely has fluid inclusions and has few fractures (but is more

fractured than Q3 and Q4). Q2 has a light brown luminescence under D-CL and predates Q3.

Stage 3 consists of Q3 which appears similar to Q2 in PPL and XPL, but it luminesces bright blue-brown to light blue under D-CL and is only visible in coarse, well zoned grains. Based on proximity to the core of the quartz crystal, the blue-brown Q3 phase is slightly earlier than the light blue Q3. While it is difficult to distinguish Q3 from Q2 using SEM-CL and SEM-Chroma CL, the two blue-brown and light blue quartz phases of Q3 are seen in D-CL, and therefore Q3 is considered to be a separate generation. In thin section 3A-11-15 240-2 a zircon fragment can be seen within a rim of Q3 surrounding a fine grained arsenopyrite (Figure 10). It is dark brown in PPL and does not show any fracturing. Cathodoluminescence shows that the zircon has irregular growth zoning.

Stage 4: Principal mineralizing events

Stage 4 consists of 3 different stages of Q4 and associated mineralization. The earliest, Q4a contains arsenopyrite (Apy), galena (Gn-1) and calcite (Cal). Q4b coincides with the only phase of Au mineralization, along with muscovite (Ms), dolomite (Dol), and calcite (Cal). Calcite continues to appear in Q4c, along with pyrite (Py-3), galena (Gn-2), sphalerite (Sp), chalcopryrite (Ccp), and pyrrhotite (Po). Q4 occurs in minor amounts as rims around late, euhedral to subhedral base-metal sulfides and vugs. Where the amount of Q4 is abundant, it appears as greyish-white, clear quartz. While it looks very similar to Q2 and Q3 in PPL and XPL, it rarely has any fluid inclusions and is less fractured. Under D-CL Q4 luminesces dark blue, and under SEM-chroma CL it is the only quartz generation that is red.

Stage 4a comprises Q4a, arsenopyrite (Apy), and galena (Gn-1). Arsenopyrite occurs as euhedral to subhedral grains along microfractures within quartz veins either as lone grains or adjacent to Au. It also occurs along microfractures within the lithic arenite or QPC wall-rock up to several meters away from quartz veins. While it only occurs in very minor amounts at the Main Zone and Sleeping Giant (<5%) it can comprise up to

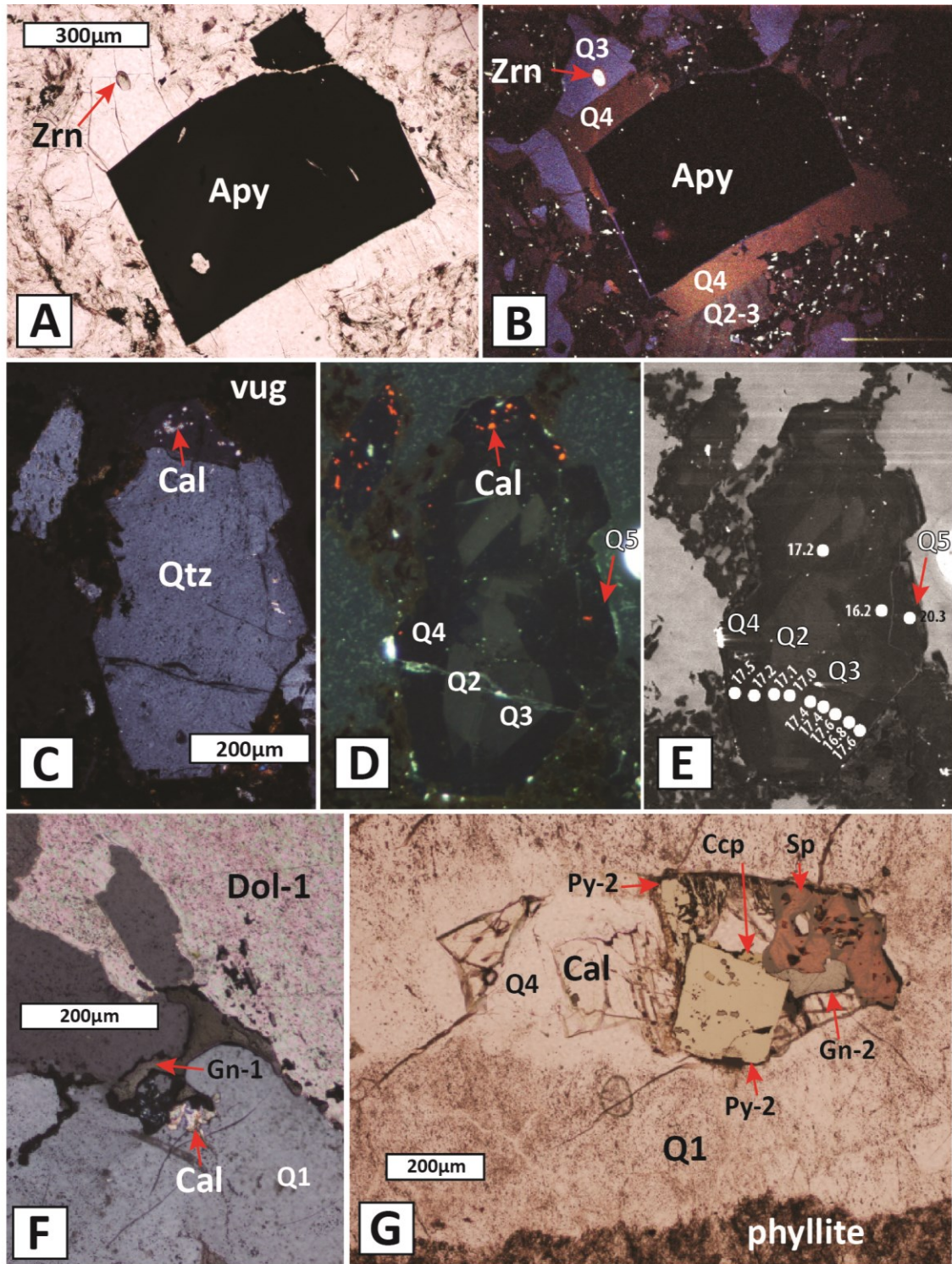


Figure 10. Photomicrographs of quartz veinlets and sulfides. Photos A (PPL) and B (XPL) are of the same arsenopyrite grain with Q4 and Q3 rims from sample 3A-11-15A 240.0. Photos C (XPL), D (D-CL), and E (SEM-CL) are of the same quartz grain terminating into a vug in sample 3A-11-11 81.94. Photo E also shows the SIMS O isotope results for each quartz generation. Photo F shows dolomite brecciating earlier quartz and galena mineralization from sample 3A-11-11 78.3. Photo G depicts the various Stage 4c sulfides within a phyllite hosted quartz veinlet in sample 3A-11-01 95.1.

~30% of brecciated quartz vein samples at the Green Zone. Arsenopyrite is most commonly rimmed by Q4, but it is also occasionally surrounded by earlier quartz or sericite. Most arsenopyrite grains show moderate to intense fracturing that is not seen in later Stage 4c sulfides, and are occasionally cross-cut by Py-3. Arsenopyrite is occasionally associated with Au, but in field samples most of the arsenopyrite has been weathered out so that only alteration phases remain. In these samples the identification of arsenopyrite was based on the shape of the weathered grains (tabular to rhombohedral) and presence of As in the alteration phases confirmed by EDS. Electron probe microanalysis of over 100 spots on arsenopyrite grains shows their compositions are consistent throughout all three Au showings, with the exception of one grain from 3A-11-11 84.49. An arsenopyrite grain located at a quartz vein contact within this thin section was coarse enough to display growth zoning. Analysis of one of the growth zones yielded Ni contents between 4.4 and 5.9%. Otherwise the arsenopyrite grains were consistently just Fe, As and S with trace amounts of Pb (<30 ppm) and Bi (<15 ppm).

In hand sample and in thin section, grains of galena tend to be rounded, anhedral blebs ranging from very fine to coarse grained; under a reflected light microscope triangular pitting is usually visible. Galena occurs in very small amounts in Main Zone samples (<2%), but comprises up to 10% of less-weathered Green Zone samples. Galena from Stage 4a (Gn-1) occurs by itself within quartz or adjacent to/as inclusions within arsenopyrite. EPMA shows that Main Zone Gn-1 occasionally contains up to 10% As, and up to 8% Fe, along with trace amounts of Bi (0.1-0.5%). Galena from Green Zone samples contains <1% of As and Fe, along with trace Bi (<0.25%) and Sb, and Sn (<0.4% for both).

Coarser grained calcite precipitated along fractures within quartz veins adjacent to Py-3 and Stage 4 quartz. It occurs as subhedral crystals that are light beige in PPL. Very fine grained, micron-sized, pale-green calcite can be found within Q3-Q4 growth zones and CO₂ rich fluid inclusions. The distinctive high birefringence and rhombohedral cleavage is visible in XPL.

Sericite is believed to have formed as a result of the alteration of host rock feldspars, muscovite, and polycrystalline quartz clasts during Stage 4 quartz veining and mineralization. X-ray diffraction analysis confirms the sericite is actually fine grained muscovite. It should be noted that while sericite has been placed in Stage 4, sericitization of the host rock may have started earlier, as microthermometry data were not obtained from Q2 or earlier.

Gold mineralization occurred during Stage 4b. In thin section, Au occurs as rounded grains in fractures, as a vug-fill occasionally with arsenopyrite (Figure 11), or as an As-Fe-Pb oxidation product. EPMA shows Au grains contain between 3% and 7.5% Ag; however, accurate readings were difficult to obtain due to the “spongy” nature of the Au. Larger grains (>400 µm) have inclusions of arsenopyrite, and are usually (but not exclusively) rimmed with Q4. There are also some examples of Au occurring within fractures with no coeval quartz generation and no other coeval minerals. In places, the Au occurs with coarse muscovite in the quartz veins. Dolomite occurs in Stage 4b but is not spatially associated with Au. Instead, drill core and the accompanying geochemistry shows it mostly forms as a vug fill within phyllite-hosted quartz veins at depths below that of common high grade Au mineralization; however, one thin section showed dolomite cross-cutting Gn-1 and Q4a.

Stage 4c is characterized by late base-metal sulfide mineralization (Figures 10 and 11). Euhedral to subhedral pyrite (Py-3) is found mainly within quartz veins or along muscovite infilled fractures. Grain sizes range from ~0.5 mm to 15 mm. EPMA shows that regardless of generation, pyrite is almost exclusively Fe and S, with As contents varying up to <5%, and trace Pb (<0.4%) and Bi (<0.25%). Pyrrhotite occurs as anhedral, dark yellow inclusions ~5-10 µm wide within subhedral pyrite (Py-3). Stage 4c galena (Gn-2) occurs adjacent to or as inclusions in pyrite (Py-3), and adjacent to fine grained chalcopyrite. Chalcopyrite occurs very rarely within the samples, and is seen only in muscovite stringers containing euhedral Py-3, or as very fine grained inclusions along

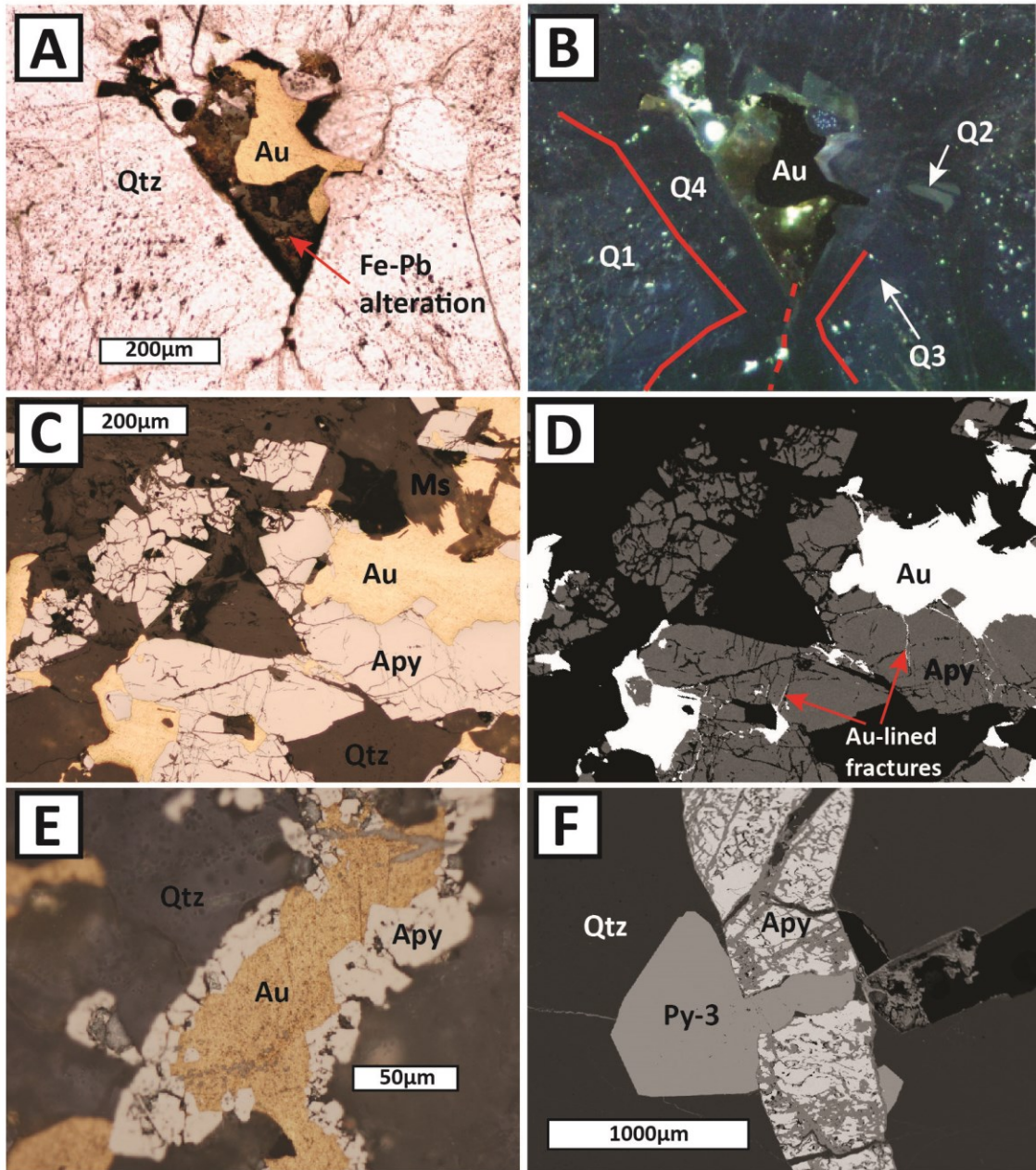


Figure 11. Photomicrographs of Au mineralization. Photo A (PPL) and B (D-CL) show Au surrounded by Fe-Pb alteration within a quartz vug from sample SCW11 F027. Photo B shows the different quartz generations as different shades of blue. The red lines outline the Q4 rim surrounding the vug and microfracture. Photo C (PPL) and image D (BSE) show Au lining the fractures of an earlier Apy grain from sample SCW11 F035. Photo C also shows the equilibrium texture between muscovite and Au. Photo E (PPL) shows euhedral Apy terminations into a vug that was later infilled with Au from sample 3A-11-11 81.75. Photo F (BSE) shows Py-3 cross-cutting earlier Apy in sample SCW11 F141.

fractures and grain boundaries of Py-3. Under reflected light microscopy, chalcopyrite is visible as anhedral, yellow blebs too fine grained to see in hand specimen. Sphalerite occurs as coarse, anhedral grains adjacent to Py-3. In hand sample the sphalerite is red to dark-greyish brown. Under a reflective light microscope triangular internal reflections can be seen. EPMA results indicate that sphalerite composition is consistently Zn, Fe and S with trace Pb (<0.3%) and Bi (<0.2%). Cathodoluminescence studies show that Py-3 and sphalerite are surrounded by rims of Q4.

Stage 5: Post-Au muscovite stringers

Stage 5 is comprised of muscovite stringers containing calcite (Cal), chlorite (Chl-1), rutile (Rt), and monazite (Mnz). These stringers cross-cut all previous stages of mineralization, including the host rock, and are characterized by medium to coarse grained muscovite. The calcite occurs along the contacts of the muscovite stringers. Euhedral blades of very fine grained chlorite (Chl-1) occur within the smaller, muscovite filled fractures, and appear light green in PPL. These muscovite stringers also contain abundant rutile occurring as anhedral grains, too fine grained for identification in hand sample. In thin section, rutile is almost opaque in transmitted light and has a very low, irregular reflectance in reflected light (Figure 12).

Monazite appears as anhedral to subhedral, very fine grains within the matrix of QPC and lithic arenite along fractures and muscovite stringers. It is not coarse grained enough to view in hand sample, and is barely recognizable in thin section without BSE imaging. In plane polarized light, coarser grains are clear to light brown in colour and blend in with surrounding Fe-oxidation when within the matrix. Cathodoluminescence studies show a red radiation halo around the monazite grains, but the monazite itself does not luminesce. High magnification optical and BSE images show the monazites are quite fractured and skeletal. Inherited zircon fragments are found abundantly within the muscovite stringers, but are only visible in thin section. The zircons are fractured and exhibit growth zoning. At least two coarser zircons do have recrystallized rims in CL; however they are too thin to analyze.

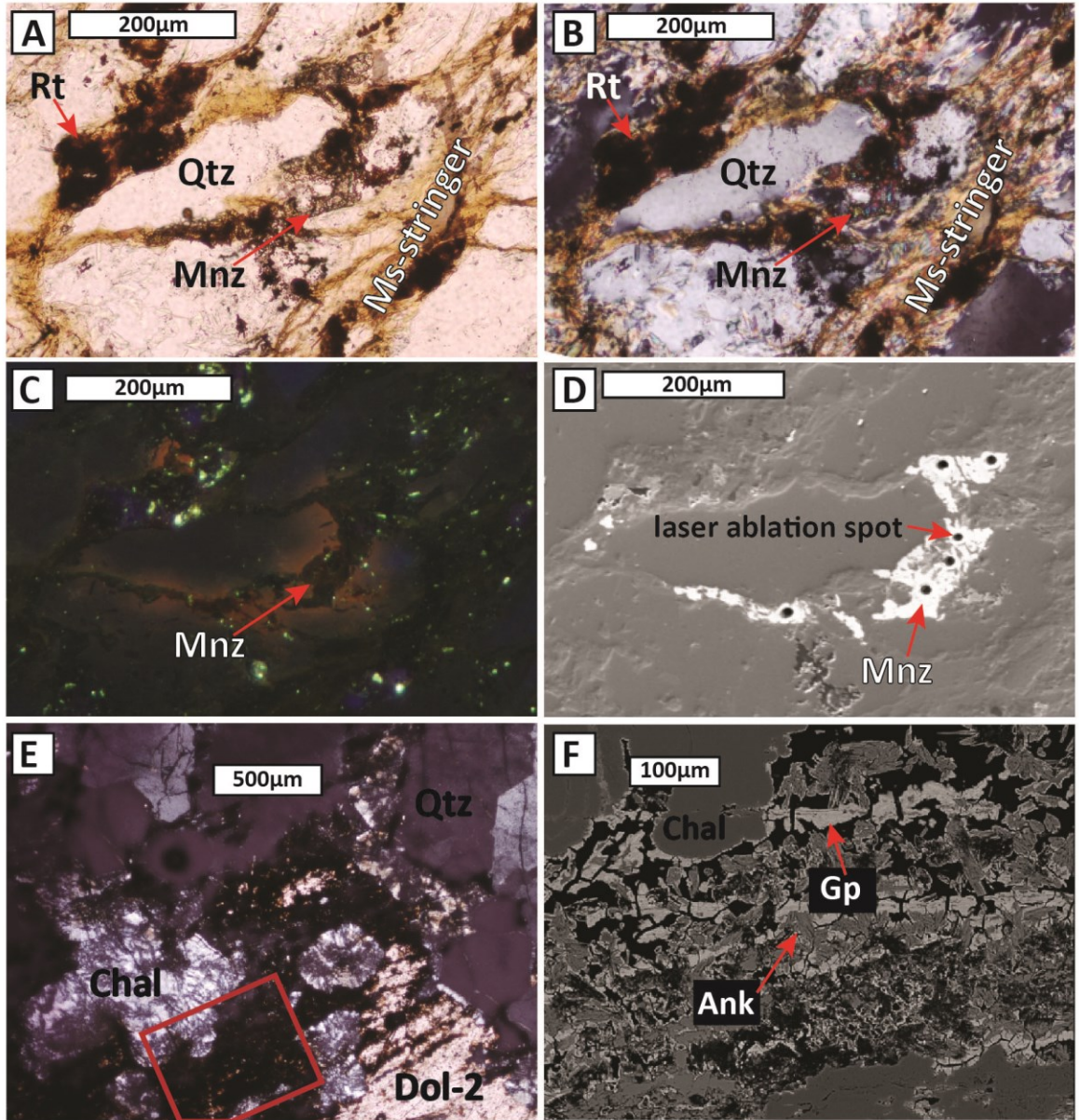


Figure 12. Photomicrographs of Stage 6 and 7 mineralization: Photos A (PPL), B (XPL), C (D-CL), and image D (SEM) show the same monazite grain along foliations within the matrix of QPC of sample 3A-11-11 81.6. Photos A and B show opaque rutile occurring along microfractures infilled with muscovite and monazite. Photo C shows an orange, radioactive alteration rim around the monazite grain. Black spots in photo D are ablation spots where the grain was analyzed by LA-MC-ICP-MS (Qtz= quartz clast; Ms stringer = muscovite stringer). Photo E (XPL) and image F (BSE) show a chalcedony lined vug within a quartz vein that has been infilled with ankerite, gypsum and dolomite in sample 3A-11-10A 45.55.

Stage 6: Post-Au quartz mineralization

Stage 6 consists of the later phases of quartz that have been grouped into Q5 (Figure 10). These are not visible in hand sample and are barely discernible in thin section without CL. They appear as small, thin quartz veinlets that cross-cut all previous quartz generations and are brown to dark brown under D-CL. SEM–Chroma CL also resolved small amounts of Q5 as overgrowths on Q4 quartz within vugs.

Stage 7: Late alteration assemblages and vug filling minerals

Stage 7 comprises chlorite (Chl-2), ankerite (Ank), goethite (Gth), gypsum (Gp), chalcedony (Chal), marcasite (Mrc) and calcite (Cal). Chlorite (Chl-2) occurs as a rim of alteration around biotite within the host rock. Marcasite occurs as a rare, colloidal vug-fill surrounding fragments of Py-3. Gypsum (Gp) and chalcedony (Chal; Figure 12) are also vug-filling minerals found within the open spaces of the quartz veins. Both are too small to identify in hand sample. Gypsum was identified using EPMA and has only been found in one thin section. In plane polarized light, gypsum has a blocky or bladed crystal habit and is light brown in colour. It appears to occur as a vug fill along with Fe-oxidation and chalcedony. Under desktop CL, the gypsum does not luminesce. In XPL the chalcedony clearly shows growth zonation, and has a colloform texture. Based on EDS and XRD analysis, Fe-rich sulfides and other Fe-rich minerals form goethite (Gth), occurring as dark red-brown to light yellowish-brown crusty or earthy films along foliations and fracture surfaces. Goethite occurs both within quartz veins and within the meta-sediments. Carbonates also occur within the matrix of the wall-rock in some areas, but are too fine grained to distinguish the exact mineralogy. Ankerite and siderite tend to occur within the alteration envelopes of the mineralized veins, and in areas of intense sericitization.

2.2.4 Oxygen Isotopes in Quartz

Results of $\delta^{18}\text{O}_{\text{qtz}}$ analysis using the BrF_5 method (Clayton and Mayeda, 1963) are presented in Table 2 along with the corresponding field relationships. SIMS and SEM-CL allowed analysis at much higher spatial resolutions, and therefore results were obtained for quartz generations Q2, Q3, Q4 and Q5 in 4 thin sections from the Main Zone. SIMS oxygen isotope results are tabulated in Appendix D.

Table 2: Oxygen isotope results obtained by the BrF_5 method

Sample ID	Map Area	Vein Description	$\delta^{18}\text{O}_{\text{SMOW}}$ (‰)
Field Samples			
SCW11 F152-1	Green Zone	younger' grey quartz vein within sericitized QPC, cross-cuts vein sample SCW11 F152-2	23.0
SCW11 F152-2	Green Zone	older' white quartz vein within QPC, cross-cut by vein sample SCW11 F152-1	16.4
SCW11 F160	(West) Green Zone	quartz veinlet within brecciated QPC, intense scorodite alteration within matrix surrounding vein	14.1
SCW11 F144	Sleeping Giant	deformed quartz vein with sericitized QPC, adjacent to arsenopyrite	16.6
SCW11 F037	Main Zone	white, cloudy quartz vein with visible Au on fault surface	17.5
Core Samples			
3A-11-10A 34.8	Main Zone	white quartz vein within QPC, Fe-oxidation along fractures	23.9
3A-11-10A 58.45	Main Zone	white, cloudy and vuggy quartz vein within quartz arenite, Fe-oxidation along fractures	20.0
3A-11-10A 114.83	Main Zone	white quartz vein within brecciated phyllite, Fe-oxidation within fractures/wall-rock contacts	16.4
3A-11-10A 118.51	Main Zone	grey quartz vein within phyllite and fine grained arenite, vein is deformed and cross-cut by shear fabric	7.0
3A-11-11 252-1	Main Zone	younger' white, cloudy vein with sharp contact within quartz arenite, pyrite and vugs occur along contact, corss cuts vein in sample 3A-11-11 252-2	25.5
3A-11-11 252-2	Main Zone	older' white, quartz vein which has a diffuse contact with the host arenite, no associated sulfides, cross-cut by vein sample 3A-11-11 252-1	9.2
3A-11-11 256.95	Main Zone	white, cloudy quartz vein within the arenite	21.9

The isotopic compositions of Q1 to Q5 from SIMS analysis are displayed in Figure 13. The $\delta^{18}\text{O}_{\text{SMOW}}$ values in Q2 ranged from $16.3\text{‰} \pm 0.2$ to $18.1\text{‰} \pm 0.2$ (n=34). Quartz generations Q3 and Q4 had $\delta^{18}\text{O}_{\text{SMOW}}$ values that ranged from $16.7\text{‰} \pm 0.2$ to $18.0\text{‰} \pm 0.2$ (n=22) and $16.2\text{‰} \pm 0.2$ to $18.2\text{‰} \pm 0.2$ (n=49), respectively. The latest quartz generation was only found in one thin section, and yielded a value for Q5 of $20.3\text{‰} \pm 0.1$ (n=1).

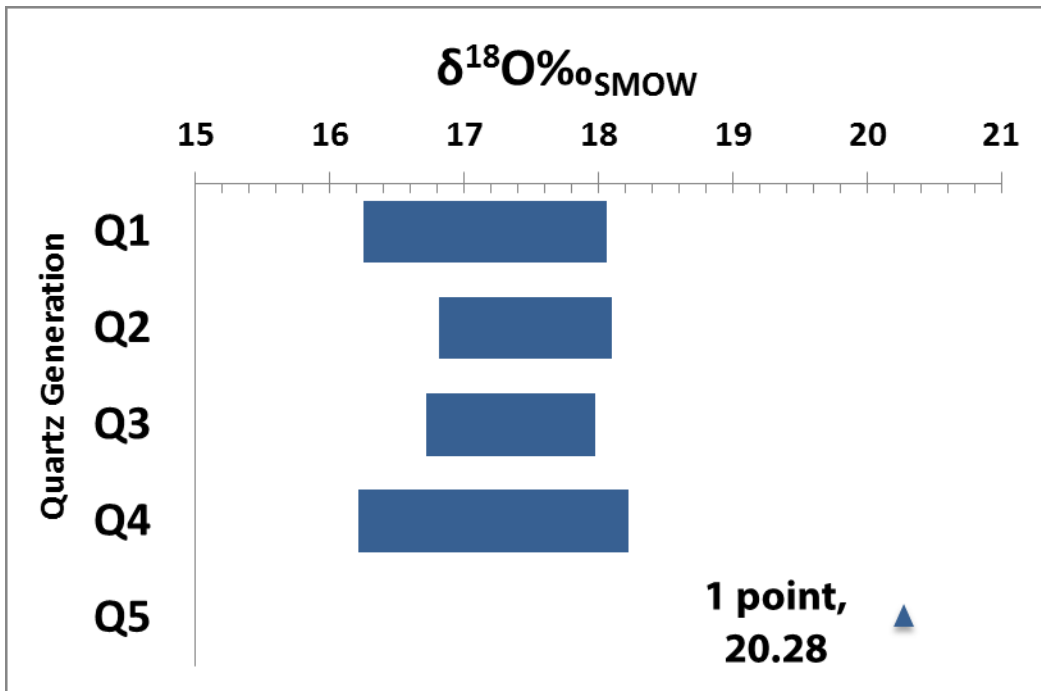


Figure 13. Bar graph of O isotopic data for all samples analyzed by SIMS.

2.2.5 Carbon and Oxygen Isotopes from Carbonates

Isotope ratio mass spectrometry was carried out on 4 different carbonate minerals; ankerite, dolomite, siderite and calcite from the Main Zone. Both $\delta^{13}\text{C}_{\text{PDB}}$ and $\delta^{18}\text{O}_{\text{PDB}}$ values vary widely from -0.3‰ to -10.4‰ , and from -14.2‰ to -23.7‰ , respectively. The results for each are tabulated by mineral in Table 3.

Table 3. Summary of C and O stable isotope data from carbonates. Abbreviations are Ank=ankerite, Cal=calcite, Dol=dolomite, and Sd=siderite.

Sample ID	$\delta^{13}\text{C}_{\text{PDB}}$ (‰)	$\delta^{18}\text{O}_{\text{SMOW}}$ (‰)	Sample ID	$\delta^{13}\text{C}_{\text{PDB}}$ (‰)	$\delta^{18}\text{O}_{\text{SMOW}}$ (‰)
3A-11-10A 45.55 Ank	-5.9	13.0	3A-11-14 135.95 Cal	-9.7	15.0
3A-11-10A 49.42 Ank	-7.2	14.9	3A-11-11 209.6 Dol	-0.9	5.6
3A-11-10A 74.65 Ank	-5.4	13.4	3A-11-11 264.35-3 Dol	-5.6	14.9
3A-11-10A 170.67 Ank	-0.3	8.0	3A-11-11 264.15 Dol	-0.9	6.7
3A-11-11 172.9 Ank	-10.4	15.2	3A-11-16 100.13 Dol	-6.9	15.3
3A-11-10A 182.5 Cal	-6.2	6.7	3A-10-01 29.75 Sd	-4.5	10.2

2.2.6 Sulfur Isotopes from Sulfides

Isotope ratio mass spectrometry was also used to analyse stable isotopes from sulfides. The analyses in Table 4 are from pyrite and arsenopyrite of the main zone. Unlike host rocks from the Main Zone, samples from the Green Zone are intensely brecciated and weathered. As a result, it was difficult to obtain fresh samples for sulfur isotope analysis. The $\delta^{34}\text{S}_{\text{VCDT}}$ values for arsenopyrite at the Main Zone occur over a relatively narrow range, from $15\text{‰} \pm 0.6$ to $17.7\text{‰} \pm 0.6$ (n=4): a difference of 2.7‰. Pyrite, however, yielded $\delta^{34}\text{S}_{\text{VCDT}}$ values ranging from $5.6\text{‰} \pm 0.6$ to $26.8\text{‰} \pm 0.6$ (n=18), a much larger difference of 21.2‰. A single arsenopyrite sample from the Green Zone yielded a $\delta^{34}\text{S}_{\text{VCDT}}$ result of $9.1\text{‰} \pm 0.6$ (n=1).

One sample of galena hosted within a quartz vein, SCW11 F300, was analysed from outside of the mineralized area near the Hat occurrence. It was analysed using the same technique, and yielded a $\delta^{34}\text{S}_{\text{VCDT}}$ value of $4.9\text{‰} \pm 0.6$ (n=1).

Table 4. Summary of S stable isotope data, including the sample location and paragenetic phase.

Abbreviations for location are MZ= Main Zone, and GZ=Green Zone. 3Ace represents a location within the 3Ace claim block but not within a specific zone. Abbreviations for minerals are Apy=arsenopyrite, Py=pyrite, and Gn = galena.

Location	Sample ID	$\delta^{34}\text{S}_{\text{CDT}}$ (‰)	Phase
MZ	3A-11-10A 102.95 ASP	15.6	Apy
MZ	3A-11-11 75.5 ASP	17.3	Apy
MZ	3A-11-11 78.3 ASP	16.7	Apy
MZ	3A-11-11 79.9 ASP	16.8	Apy
MZ	3A-11-11 84.49 ASP	15.0	Apy
MZ	3A-11-15A 227.75-2 ASP	17.2	Apy
MZ	3A-11-15 240-2 ASP	15.5	Apy
MZ	3A-11-16 104.88 ASP	17.7	Apy
MZ	3A-11-11 207.15 PY2	20.0	Py-1
MZ	2A-11-11 256.95 PY1	12.8	Py-2
MZ	3A-11-11 264.15 PY	26.8	Py-2
MZ	3A-11-11 75.5 PY	18.9	Py-2
MZ	3A-11-15 290.4 PY	10.6	Py-2
MZ	3A-11-15A 198 PY	13.4	Py-2
MZ	3A-11-15A 226.95 PY	7.8	Py-2
MZ	3A-11-15A 227.75-2 PY	6.2	Py-2
MZ	3A-11-10A 106.7 PY	13.0	Py-3
MZ	3A-11-11 207.15 PY1	5.6	Py-3
MZ	3A-11-11 256.95 PY2	9.2	Py-3
MZ	3A-11-14 135.95 PY	6.4	Py-3
MZ	3A-11-14 136.17 PY	9.7	Py-3
MZ	3A-11-15 240-1 PY	7.2	Py-3
MZ	3A-11-16 100.13 PY	13.8	Py-3
GZ	3A-11-23 153.12 ASP	9.1	Apy
GZ	3A-11-23 153.12 PY	9.9	Py-?
3Ace/Hat	SCW-11-F300 GN	4.9	Gn

2.2.7 Pb-Pb Isotopes from Galena

Lead isotopes from galena were analysed using MC-ICP-MS. Only two samples were found to contain coarse enough, unweathered grains of galena for the isotopic analysis; F300 and 3A-11-15A 226.95. Detailed results for both samples are tabulated in Table 5.

Table 5. Pb-Pb isotope data for samples SCW11-F300 and 3A-11-15A 226.95.

Sample ID	$^{208}\text{Pb}/^{204}\text{Pb}$	2σ	$^{207}\text{Pb}/^{204}\text{Pb}$	2σ	$^{206}\text{Pb}/^{204}\text{Pb}$	2σ
SCW 11 F300	39.992	0.015	15.662	0.006	19.004	0.006
3A-11-15A 226.95	39.170	0.009	15.708	0.004	19.166	0.003

2.2.8 Geochronology

Monazites were dated by analysing U-Pb isotopic compositions using LA-MC-ICP-MS. In total four monazites crystals from Stage 5 were analysed. For complete U-Pb isotope data, monazite images, and EDS spectra, refer to Appendix E. Long-exposure EDS was used to confirm the monazite's composition. BSE imaging, EDS, and microphotography were used to determine the best areas for laser analysis. A summary of these data can be found in Table 6. A definitive age cannot be determined from the data. A model-1 solution ($\pm 95\%$ confidence) using all 18 points and anchored at common Pb ($^{207}\text{Pb}/^{206}\text{Pb} = 0.86 \pm 0.6$), yielded a lower intercept age of 151.2 ± 6.1 Ma, however, due to fracturing and their anhedral crystal habit, resulting in low ^{206}Pb counts or most spots (<40 000) and discordant ages, the calculated age is not robust.

Table 6. U-Pb isotope data for Main Zone samples 3A-11-11 81.6, 3A-11-15A 227.75, 3A-10-03 3.95, and 3A-11-10A 78.94.

Spot ID	²⁰⁶ Pb (cps)	²⁰⁴ Pb (cps)	²⁰⁷ Pb/ ²⁰⁶ Pb	2σ	²⁰⁷ Pb/ ²³⁵ U	2σ	²⁰⁶ Pb/ ²³⁸ U	2σ
81.6-1A	3965	142	0.352	0.019	2.070	0.210	0.043	0.004
81.6-1B	14093	155	0.105	0.015	0.383	0.058	0.027	0.002
81.6-1C	12157	201	0.164	0.024	0.591	0.094	0.026	0.002
81.6-1D	4774	175	0.224	0.035	0.937	0.167	0.030	0.003
81.6-1E	13474	543	0.502	0.075	4.129	1.004	0.060	0.011
81.6-1F	16346	301	0.155	0.021	0.565	0.100	0.026	0.003
227.75-1A	152499	10170	0.811	0.011	40.167	3.042	0.359	0.027
227.75-1B	193792	11474	0.823	0.014	51.725	7.575	0.456	0.066
227.75-1C	182180	11913	0.824	0.011	43.184	7.344	0.380	0.064
3.95-1A	16894	570	0.470	0.015	3.286	0.213	0.051	0.003
3.95-1B	11184	381	0.409	0.023	2.519	0.245	0.045	0.004
3.95-1C	8349	141	0.129	0.018	0.448	0.067	0.025	0.002
3.95-1D	15557	434	0.383	0.017	2.113	0.152	0.040	0.002
3.95-1E	13827	283	0.281	0.020	1.196	0.128	0.031	0.003
3.95-1F	7910	104	0.193	0.023	0.722	0.095	0.027	0.001
3.95-1G	1490	118	0.576	0.075	7.549	2.163	0.095	0.024
78.94-1A	46748	2545	0.794	0.013	16.964	2.783	0.155	0.025
78.94-1B	19068	1061	0.784	0.013	24.493	2.663	0.226	0.024

2.2.9 Fluid Inclusions and Microthermometry

Quartz samples from the Green Zone, Sleeping Giant and from the Main Zone were targeted for the fluid inclusion study. Temperature and salinity results are summarized in Table 7. Calculated fluid pressures and associated data are found in Table 8. All fluid inclusion data can be found in Appendix C. Fluid inclusion assemblages (FIA) were classified as primary, secondary, and pseudosecondary based on their appearance at room temperature and relationship with the CL zones in the quartz (Roedder, 1984).

Table 7. Summary of Microthermometric Data (MZ= Main Zone, SG= Sleeping Giant, GZ= Green Zone)

	Type I	Type II	Type III
Degree of fill*			
Main Zone	0.6 to 0.9 (0.7)	0.45 to 0.8 (0.58)	0.6 to 0.95 (.86)
Sleeping Giant	0.7	0.5-0.7 (0.61)	0.9
Green Zone	0.5 to 0.75 (0.62)	0.5 to 0.65 (0.52)	n.d.
CO₂ melting (°C)			
Main Zone	n.o.	-74 to -56.6 (-58.6)	-78.8 to -57.1 (-64.3)
Sleeping Giant	n.o.	-58.0 to -68.1 (-58.7)	n.o.
Green Zone	n.o.	-57.2 to -58.2 (-57.7)	n.o.
Ice melting (°C)			
Main Zone	-4.8 to 0.2 (-2.0)	-2.9 to -0.9 (-1.4)	-4.5 to 0.0 (-2.4)
Sleeping Giant	-0.4	-1.8	-2.9
Green Zone	-1.4 to -2.1 (-1.8)	n.o.	0.65 to 0.8 (0.69)
Clathrate melting (°C)			
Main Zone	7.2 to 10.8 (9.8)	8.5 to 11 (9.7)	0.6 to 10.7 (8.2)
Sleeping Giant	n.o.	7.8 to 10.6 (10.1)	n.o.
Green Zone	n.o.	7.6 to 9.8 (9.3)	n.o.
Salinity† (wt% NaCl)			
Main Zone	0.4 to 7.6 (3.4)	0.0 to 3.0 (0.8)	0.0 to 7.2 (4.0)
Sleeping Giant	0.7	0.0 to 4.3 (0.6)	4.8
Green Zone	2.4 to 3.5 (3.0)	0.4 to 4.7 (1.4)	0.4 to 4.6 (1.9)
CO₂ homogenization (°C)			
Main Zone	n.o.	12.5 to 26.0 (21.7)	n.o.
Sleeping Giant	n.o.	15.1 to 20.7 (17.7)	n.o.
Green Zone	n.o.	23.3 to 24.9 (24.1)	n.o.
Total homogenization (°C)			
Main Zone	201 to 265 (235)	247 to 311 (294)	140 to 247 (205)
Sleeping Giant	358	246 to 306 (292)	188 to 199 (194)
Green Zone	218 to 351 (266)	276 to 310 (289)	196 to 236 (226)

Note: Mean values shown in brackets; n.o.= not observed, n.d.= not determined

* Degree of fill (proportion of aqueous phase) estimated from the charts of Shepherd et al., 1985

† Salinities estimated from clathrate melting temperature for Type II inclusions using the equation from Darling (1981), and using ice melting temperatures for Type I and III inclusions using the equation from Bodnar (1993)

Photos of several representative FIA's can be found in Figure 14. Microthermometric measurements could not be obtained from quartz generations prior to Stage 3 (Figure 9). The earliest measured fluid inclusions, Type I, are associated with Stages 3 and 4a quartz where they most commonly occur as pseudo-secondary inclusions in Q3, or as primary inclusions in Q4a. They consist of 2-phase, euhedral to subhedral, hexagonal to rounded, low salinity $\text{H}_2\text{O}-\text{CO}_2-\text{NaCl} \pm \text{CH}_4$ inclusions. Type II fluid inclusions are associated with Q4b and Q4c, and occur as secondary and pseudosecondary FIA that cross-cut Type I inclusions in earlier quartz. They consist of 3-phase, subhedral cusped to rounded, low salinity, CO_2 -rich $\text{H}_2\text{O}-\text{CO}_2-\text{CH}_4-\text{NaCl}$ inclusions. Type III fluid inclusions are associated with Q5 and Stage 6, and occur as secondary inclusions in all previous quartz generations. These are all 2-phase subhedral to anhedral, rounded-elongate, low to moderate salinity inclusions consisting of $\text{H}_2\text{O}-\text{CO}_2-\text{NaCl}$.

Fluid pressures (Table 8) were calculated using fluid inclusion data and fluid inclusion data modelling software from the Fluid Inclusions Laboratory Leoben website (2014). The modelling programs required the molar fraction of CO_2 (visually estimated using the charts of Shepherd, 1985), molar volume and total homogenization temperatures as inputs in order to calculate the fluid pressure. The molar volumes were visually estimated from Figure 6 of Bakker and Diamond (2000) using the mole fraction of CO_2 and the total homogenization temperatures for Type I and III fluid inclusions, or using the temperature at which the two CO_2 phases homogenized for Type II inclusions. The molar fractions of NaCl were calculated using the Loner AP package. Further details, including the program names, can be found in Section 1.4.10. Table 8 contains representative data for each fluid inclusion type at each of the 3Ace areas. Quartz generations for the Green Zone are not listed as petrography and cathodoluminescence studies did not clearly show a quartz vein paragenetic sequence that could be associated with Stages 2 through 4, however, the quartz was discernible from Q1- and Q5-like generations. Fluid inclusion types at the Green Zone were classified based on their appearance relative to those at the Main Zone.

Table 8. Calculated fluid pressures and associated fluid inclusion data for representative low and high temperature data end-members for each map area and fluid inclusion type (MZ = Main Zone, SG = Sleeping Giant, and GZ = Green Zone).

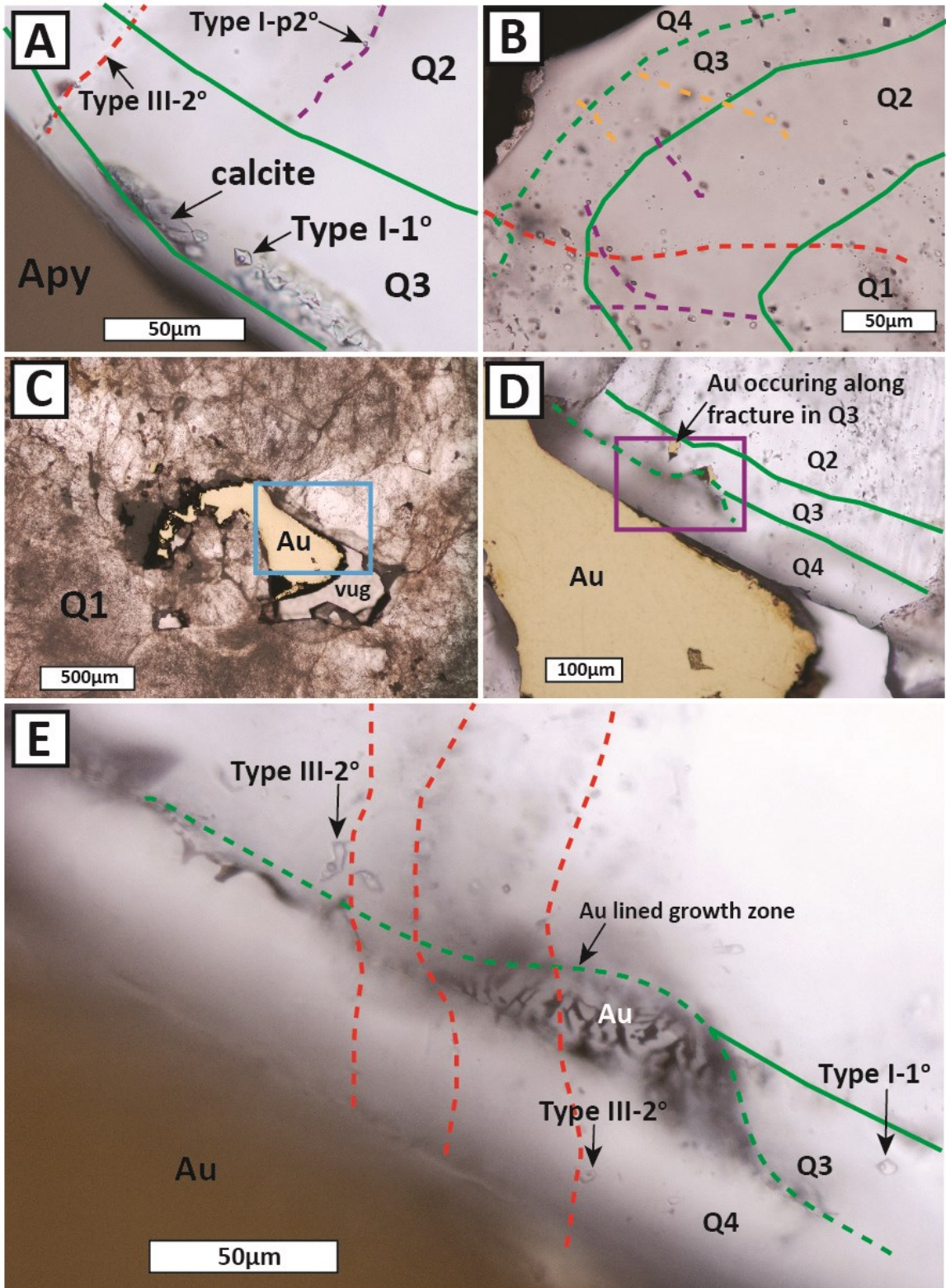
Map Area	Quartz Generation	Fluid Inclusion Type	$X_{H_2O}^*$ (%)	$X_{CO_2}^*$ (%)	$X_{NaCl}^{*\dagger}$ (%)	T_h Total [◊] (°C)	T_h CO ₂ [‡] (°C)	Estimated Molar Volume (cc/mol)	Fluid Pressure (MPa)
MZ	Q3/Q4a	I	60	40		265		29.5	290.2
MZ	Q4bc	II	70	29.8	0.2	270	24	30.0	178.2
MZ	Q4bc	II	60	40		311	13	31.5	299.9
MZ	Q5	III	90	10		247		24.5	108.7
SG	Q4bc	II	60	40		292	19	32.8	200.9
SG	Q4bc	II	70	30		306	18	28.8	299.6
GZ		I	75	24	1.0	351		28.5	219.2
GZ		II	50	47.5	2.5	276	24	39.0	125.2
GZ		II	50	49.8	0.2	303	24	39.0	173.4

* X indicates molar fraction of that component

† Most salinities were too low to determine X_{NaCl}

◊ Total Homogenization Temperature

‡ CO₂ Homogenization Temperature



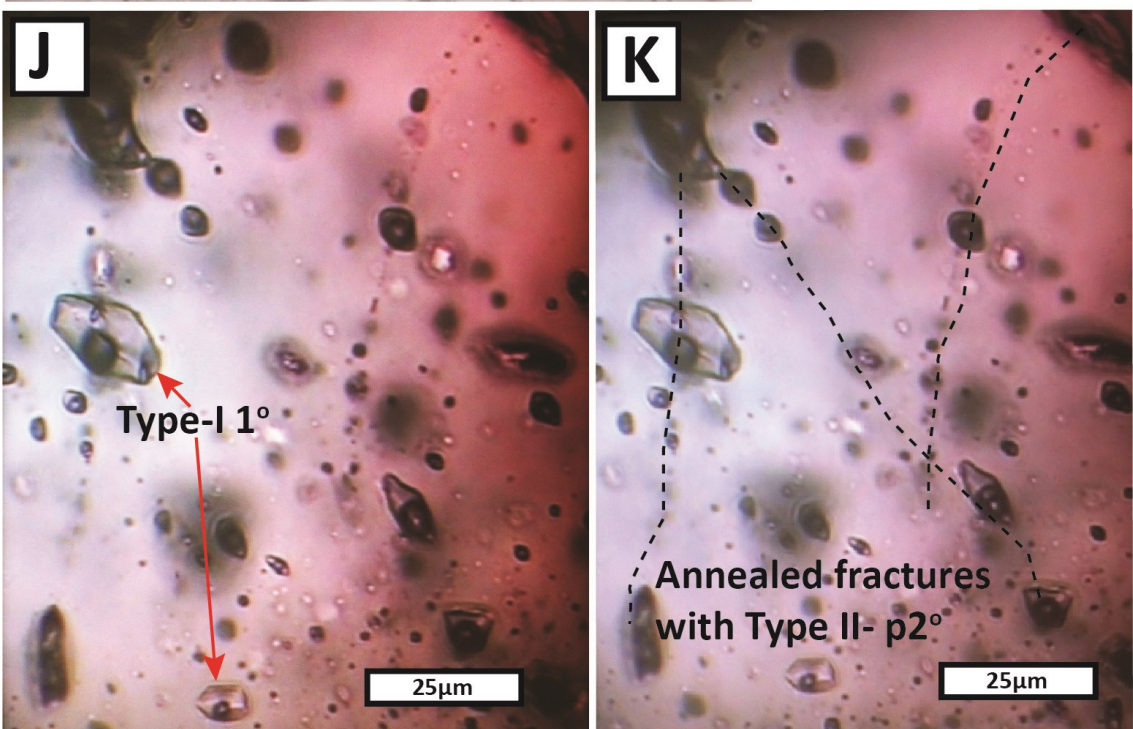
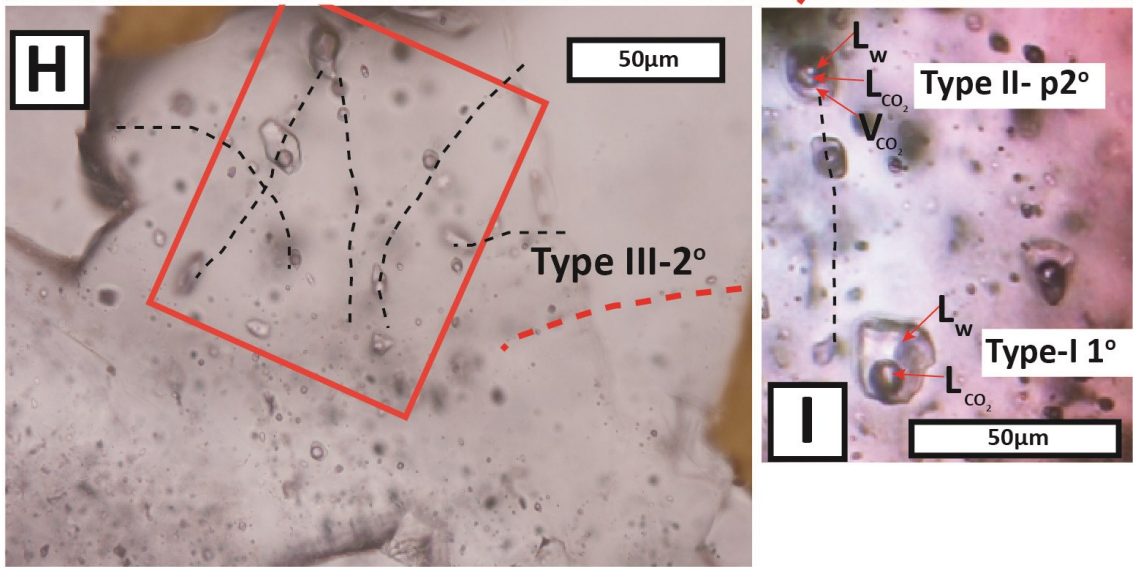
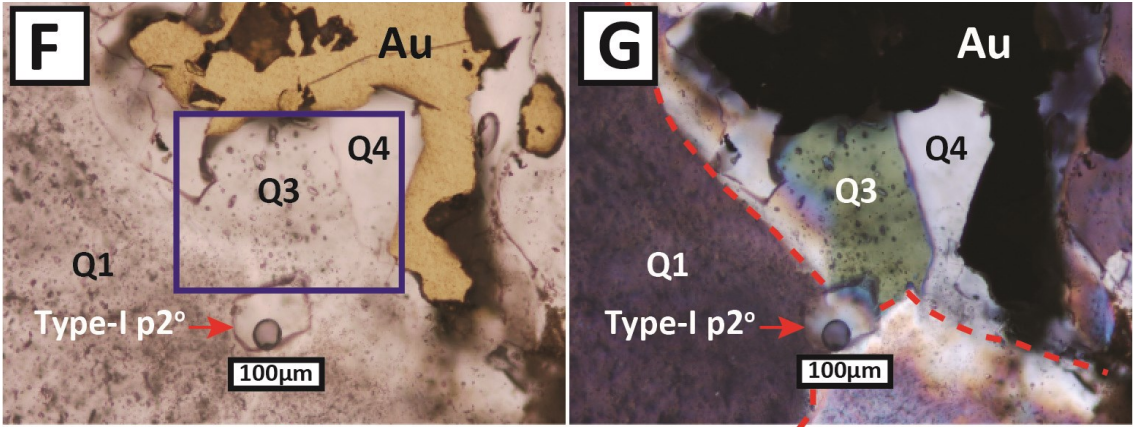
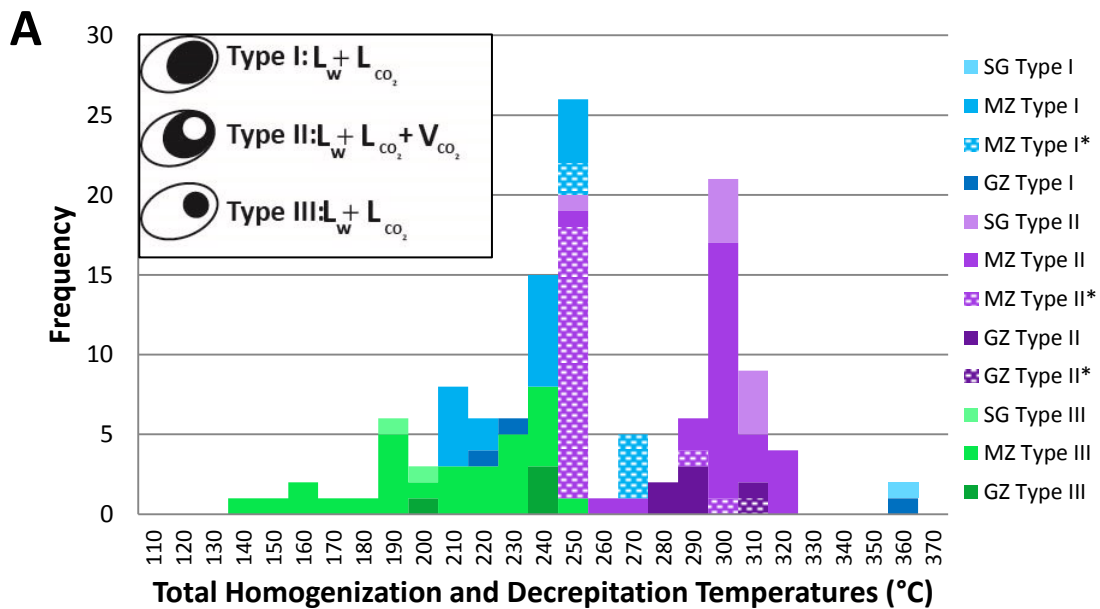


Figure 14. Photomicrographs of fluid inclusions within quartz showing the different relationships between FIA's and quartz generation [green lines = growth zones, purple lines = Type I pseudo-secondary ($p2^\circ$), yellow lines = Type II $p2^\circ$, and red lines = Type III secondary (2°)]. Photo A shows a primary (1°) Type I fluid inclusion within a calcite mineralized growth zone with Q4 rimming arsenopyrite, from sample 3A-10-03 99.66. Photo B is of quartz forming adjacent to Au from sample SCW11 F030-1. Photos C, D and E are of Au bearing quartz from sample SCW11 F028-1. The blue box in C outlines the area of photo D, and the purple box in D outlines the photo area of E. Photos F through K are of the same area of quartz surrounding Au mineralization in sample SCW11 F030-2. The blue box in photo F outlines the area for photos H, while the red box in photo H outlines the area in photos I, J and K. These photos vary as they were taken at different depths within the quartz grain.

Total homogenization temperatures are highest in Type II inclusions which are associated with the Au mineralization. The bimodal distribution on Figure 15A is the result of a high number of minimum decrepitation temperatures between 250°C and 265°C. Type II and then Type III fluid inclusions have lower T_h values. Conversely Figure 15B shows that Type I and III fluid inclusions have higher salinities than Type II inclusions overall. The negative slopes on the regression lines in Figure 15C indicate increasing salinity with decreasing temperature. This trend is more pronounced in Type I and III fluid inclusions. Not enough Sleeping Giant fluid inclusions were analysed to determine a reliable trend in T_h or salinity. Green Zone fluid inclusions occur within the higher end of the overall T_h ranges.



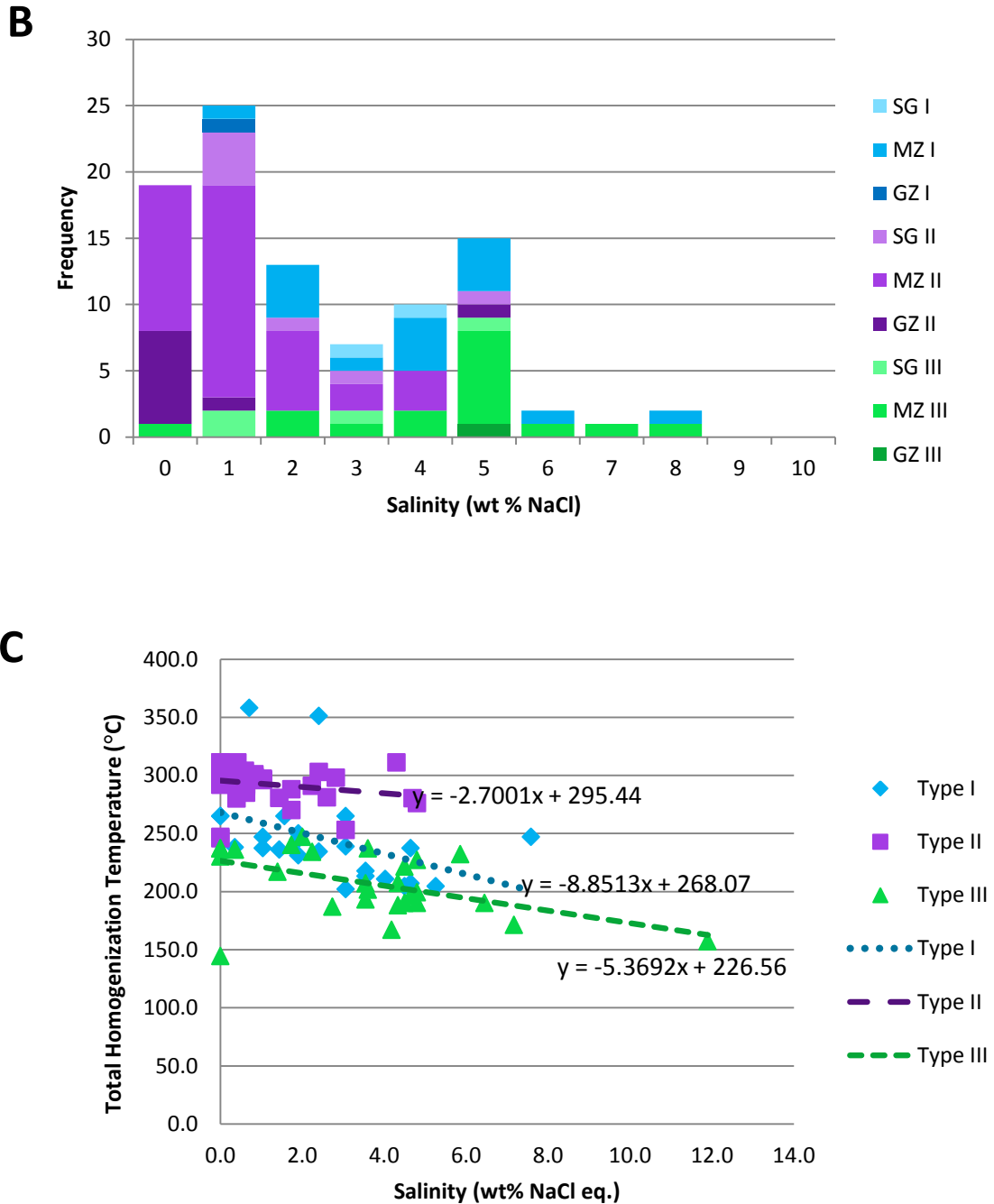


Figure 15. Fluid inclusion summary for Type I, II and III inclusions based on deposit area (SG = Sleeping Giant, MZ = Main Zone, and GZ = Green Zone). Histogram A shows the distribution of homogenization and decrepitation temperatures. Histogram B displays the frequency of calculated salinities in wt. % NaCl eq. for each inclusion type. Graph C displays the total homogenization temperature vs. the salinity in wt % NaCl eq. for each fluid inclusion type. Dotted lines for each group are the linear regressions of the data with the relevant equations displayed adjacent to the lines.

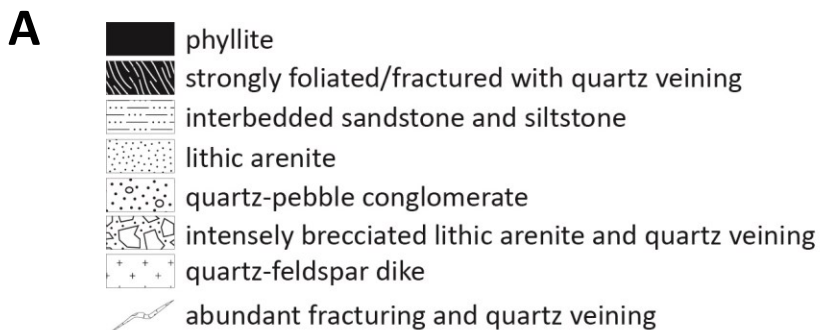
*minimum decrepitation temperatures

2.2.10 XRD and Wall-rock Alteration

Samples were collected from several drill holes, with sampling focused on holes 3A-11-11 (Figures 10 and 11) and 3A-10-01 (Figure 18), which are ~25 m away from each other. Figures 10, 11 and 12 show the XRD results relative to depth and Au grade. Au grades stated in the figures were obtained by fire assay from NTR. The lithologies in Figure 16 are based on core logging work completed by NTR. Minerals within the powdered samples were determined by XRD.

Based on detailed petrography and XRD analysis quartz, muscovite (as sericite), and pyrite occur throughout the drill holes and are found in quartz pebble conglomerate, lithic arenite and phyllite units. Kaolinite occurs within 10 m of high grade Au zones (>0.1 gpt, within 25 m of >0.01 gpt Au). Figures 11 and 12 show how ankerite occurs primarily within high grade zones, and up to 15 m away. Also occurring within 15 m of the mineralized system are calcite, albite, goethite and birnessite (Mn-oxide). Chamosite (Fe-rich chlorite) and clinocllore occur up to a minimum of 25 m away from >0.1 gpt zones, but only clinocllore consistently occurs within the high grade zones.

With the exception of one sample from hole 3A-10-01 (Figure 18), dolomite occurs within higher grade zones in addition to rutile, microcline, scorodite, apatite, smectites (nontronite and montmorillonite), dickite, magnesite (Mg-carbonate), and hematite. Application and significance of the results for exploration are discussed in section 3.1.3.



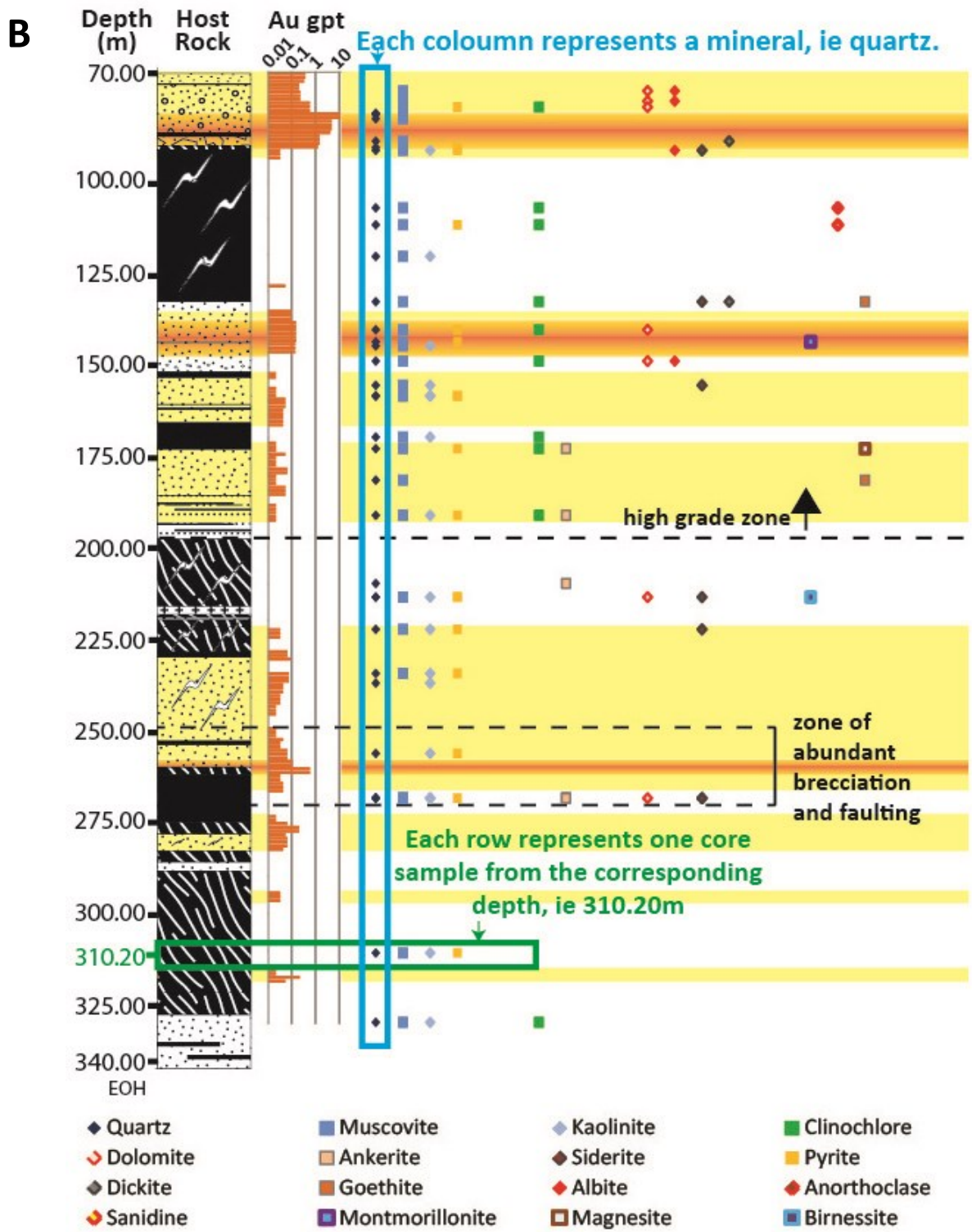


Figure 16. XRD data and Au grade with lithology for hole 3A-11-11. Part A is the legend for the host rock drill core log in part B. Part B explains how to read Figures 17 and 18.

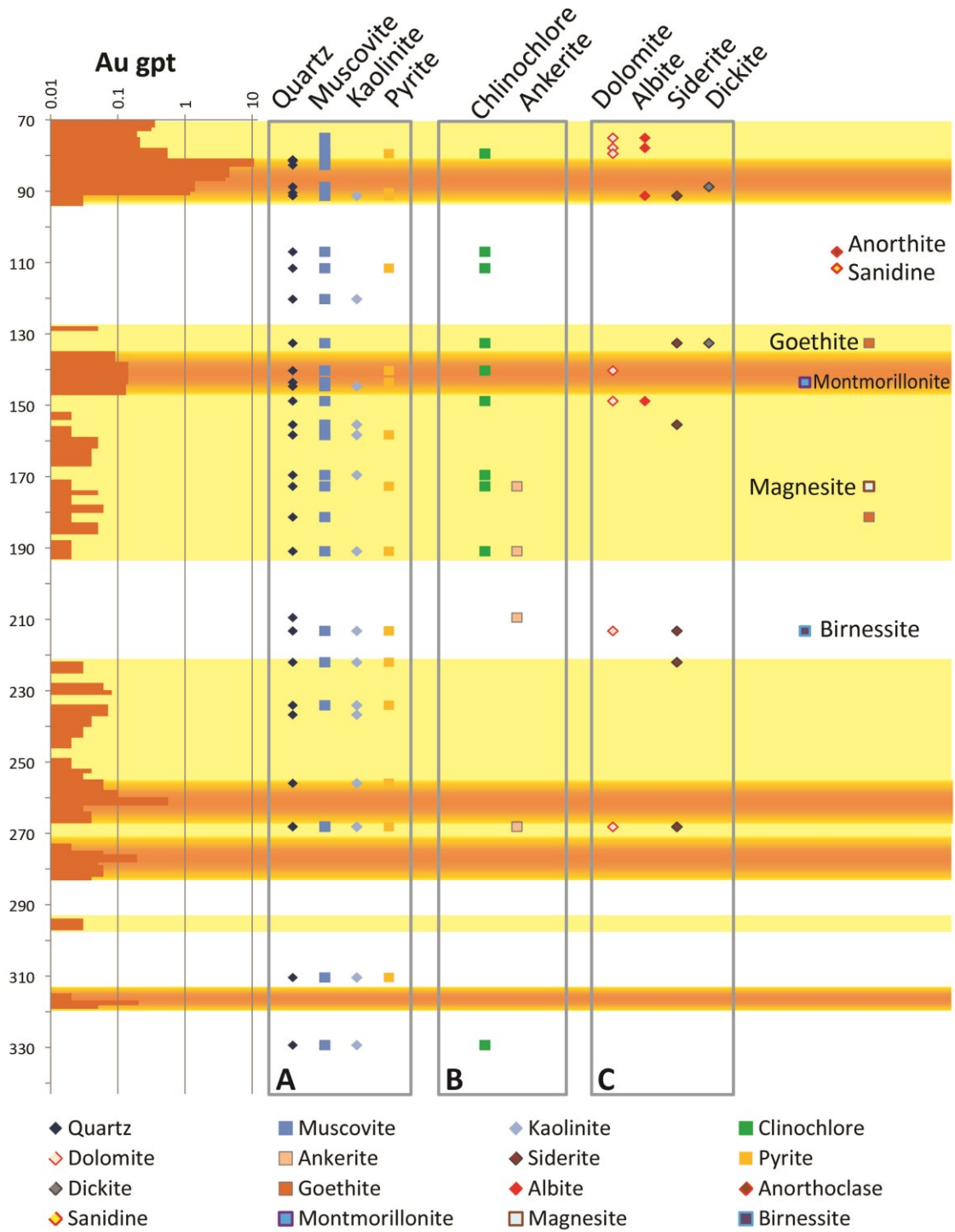


Figure 17. XRD and Au grade for hole 3A-11-11. This chart shows the XRD results relative to zones of higher Au grades (>0.1 gpt) as grouped into series. Series A represents minerals occurring throughout the length of the drill hole. Series B outlines minerals within approximately 25 m of high-grade zones, and the final box, series C, outlines minerals which occur within ~15 m of mineralization.

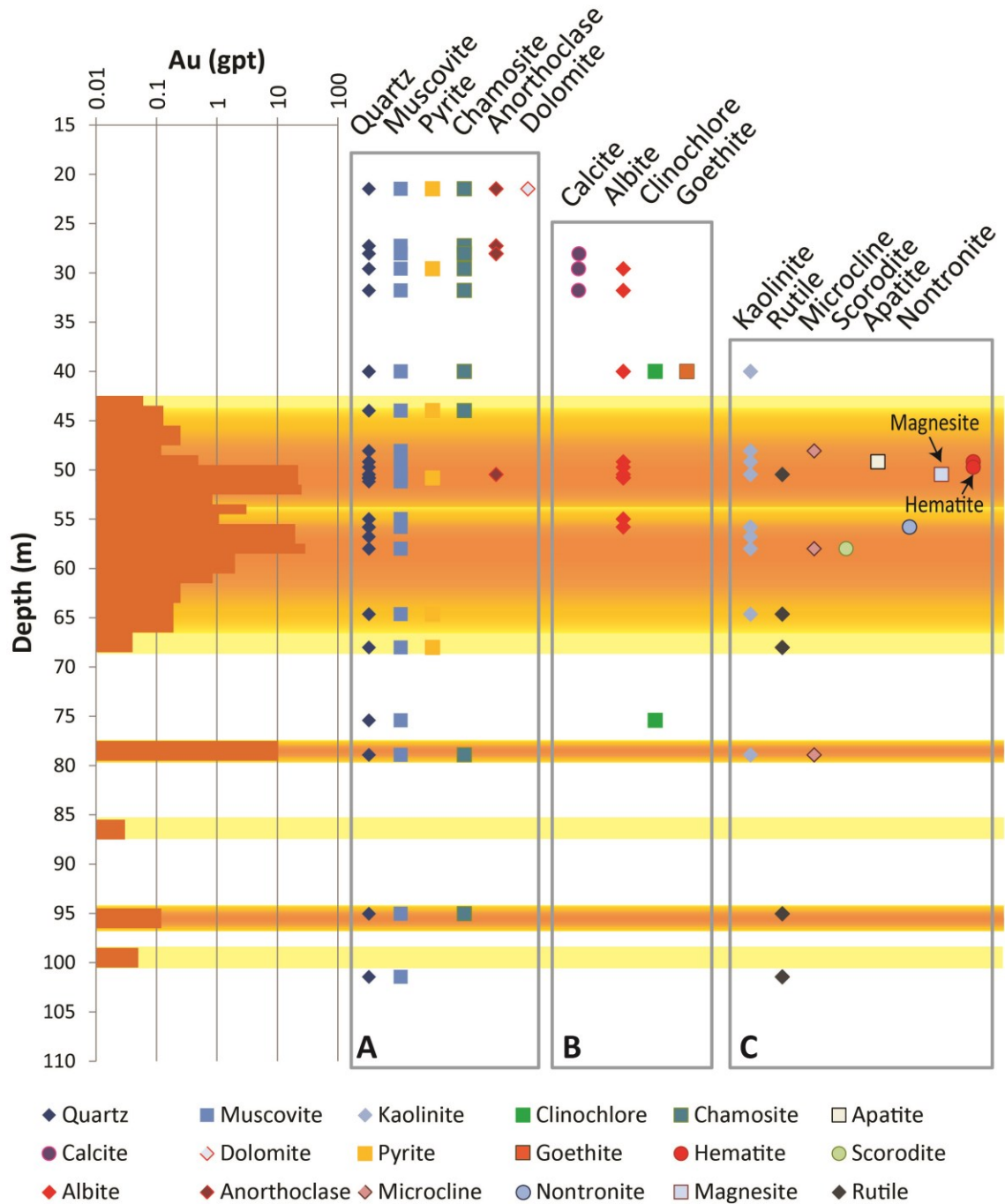


Figure 18. XRD and Au grade for hole 3A-10-03. This chart shows the XRD results relative to zones of higher Au grades (>0.1 gpt) as three series. The first box, series A represents minerals occurring throughout the length of the drill hole. Series B outlines minerals within approximately 25 m of high-grade zones, and the final box, series C, outlines minerals which occur within ~15 m of mineralization.

CHAPTER 3: DISCUSSION

3.1 Sprogge

3.1.1 Age of Quartz Monzonite Dikes

The estimated ages obtained from radiogenic isotopic compositions of zircons occur over a relatively small range, with the exception of inherited cores. An age of 1063 ± 47 Ma for the cores of zircons in sample SCW 11 F165 (see Table 1) indicate they were likely inherited from the surrounding Proterozoic meta-sediments which were derived in part from the weathering of the Grenville structural province (Rainbird et al., 1997). Estimated ages for the igneous growth rims on zircons fall within the ranges of other Selwyn Basin plutonic suites. The two adjacent suites, the HPS and WPS, have age ranges of 106 to 96 Ma, and 98 to 94 Ma, respectively (Hart et al., 2004b). These plutonic suites overlap in the sample area (Figure 4). Sprogge samples yielded ages ranging from 95.7 to 103.5 Ma. These ages are most similar to those of the HPS, but the younger ages still fall within the range for the WPS.

3.1.2 Whole Rock Geochemistry and Implications for Mineral Potential

Each plutonic suite within the Selwyn Basin has a distinctive petrogenesis, and as a result, associated metallogeny (Hart et al., 2004b). Different major oxide and trace element suites can be used to compare the plutons and the chemical characteristics associated with mineralization (Figure 19). Figures 19 A, B and C show that the Sprogge samples tend to group closely to those of the WPS, APS and HPS for $\text{Na}_2\text{O} + \text{K}_2\text{O}$ and MgO contents. Sprogge ASI (aluminum-saturation index) values are generally higher than those of the TPS, MPS, and WPS. The ASI value refers to the molar ratio of $\text{Al}_2\text{O}_3 / (\text{CaO} + \text{Na}_2\text{O} + \text{K}_2\text{O})$. Figures 19D and E show Ba and Sr values from Sprogge tend to cluster around those of the WPS, APS, and HPS intrusives. These elements are very mobile, and if expressed over a wider range, such as those of the TPS, would indicate greater degrees of melt fractionation (Winter, 2010). Highly fractionated parts of the TPS are associated with Au, Cu and Bi mineralization (Hart et al., 2004a).

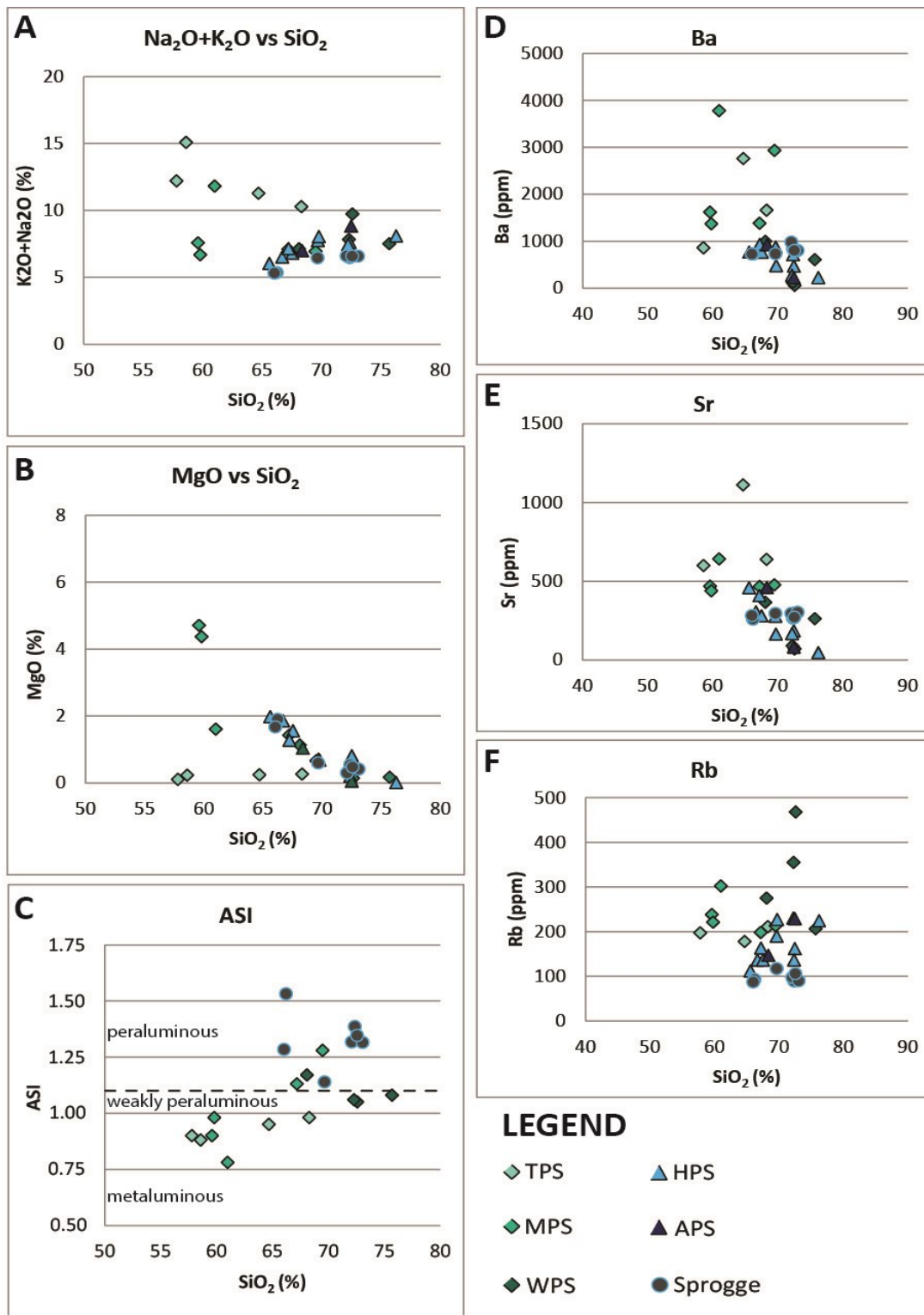


Figure 19. Geochemical plots comparing the values obtained from quartz monzonite dikes at Sprogge to those of other Selwyn basin plutonic suites using data from Hart et al. (2004a) and Heffernan (2004): TPS= Tombstone plutonic suite, MPS= Mayo plutonic suite, WPS= Tungsten plutonic suite, HPS = Hyland plutonic suite, and APS = Anvil plutonic suite. ASI criteria are from Chappell and White (2001).

With the exception of Cs and Th, trace element analyses (Figure 20) of Sprogge samples show they are almost as enriched in large ion lithophile elements (LILE) as the MPS and HPS (Hart et al. 2004a). Cesium values from Sprogge were slightly lower than those of the other plutonic suites. Rare earth elements were generally lower at Sprogge than the values reported for other plutonic suites. While the Ba, Sr and Rb values do not indicate high degrees of fractionation in the MPS and TPS, negative europium anomalies (Figure 20 B) are indicative of more fractionated intrusions of the WPS (Hart et al., 2004a). The APS and HPS show larger negative Eu anomalies, whereas the Sprogge samples have relatively smaller negative Au anomalies, and low Ba, Sr, and Rb. The intrusions at Sprogge therefore do not indicate melt fractionation to the same degree as other plutonic suites.

Oxygen fugacity and redox state of granitic magmas are important controls on ore deposition (Ishihara, 1981, as referenced by Hart et al., 2004a; Blevin and Chappell, 1992). One indicator of redox state is the whole rock ferric:ferrous ratio (Hart et al., 2004a). According to Figure 21, Sprogge intrusives are relatively more oxidised than the other plutonic suite, and overlap the range of ferrous/ferric iron ratios of the TPS. While Figure 21 indicates the HPS values are much lower, Table 1 of Hart et al. (2004a) gives data that overlap with Sprogge, indicating they formed from magmas with similar redox states (Hart et al., 2004b). These higher values may also be the result of surface weathering processes and interaction of the Fe-sulfides with meteoric water, resulting in hematite precipitation. While the role that redox state plays in generating Au-rich magmas is not fully understood, it is likely that magmas which are more oxidized are more efficient at concentrating Au during fractionation as they are too oxidized to precipitate sulfide minerals (Candela, 1989, as referenced in Hart et al., 2004a). Of the TPS, WPS and MPS, Cu and Au mineralization are strongly associated with intrusions which are relatively more oxidized (Hart et al., 2004b). As previously discussed, intrusions of the HPS are also associated with Au and Cu mineralization.

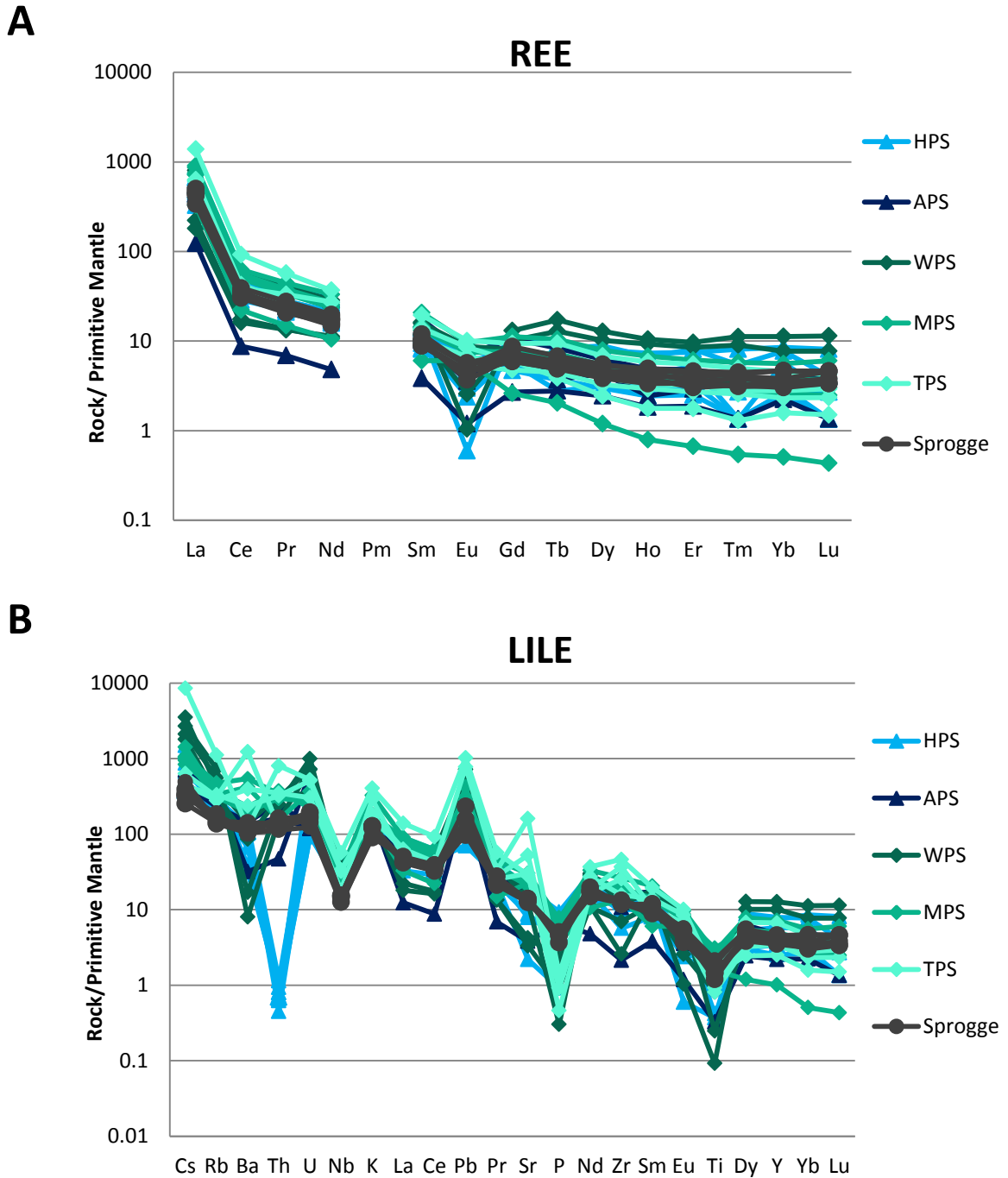


Figure 20. LILE (A) and REE (B) multi-element variation diagrams using normalized geochemical data from Hart et al. (2004a) and Heffernan (2004), and the primitive mantle data of Sun and McDonough (1989): TPS= Tombstone plutonic suite, MPS= Mayo plutonic suite, WPS= Tungsten plutonic suite, HPS = Hyland plutonic suite, and APS = Anvil plutonic suite. Sprogge data are from this study.

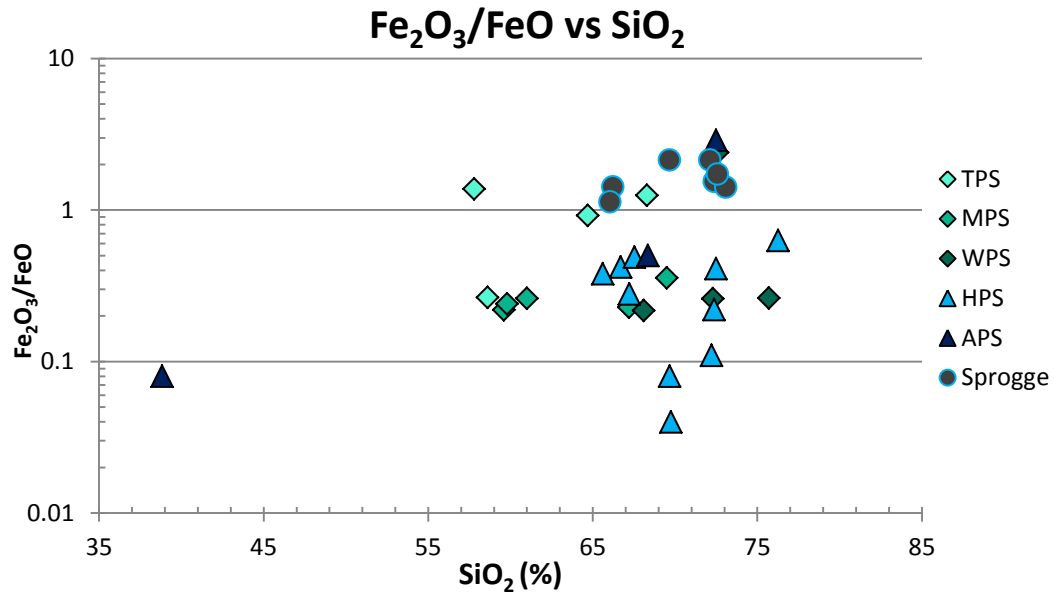


Figure 21. Ferric/ferrous iron plot vs. SiO_2 comparing values from Sprogge with other plutonic suites using data from Hart et al. (2004a) and Heffernan (2004): TPS= Tombstone plutonic suite, MPS= Mayo plutonic suite, WPS= Tungsten plutonic suite, HPS = Hyland plutonic suite, and APS = Anvil plutonic suite.

The whole-rock geochemical characteristics for samples at Sprogge match those of fractionated MPS and WPS plutonic rocks, and also share common ages and redox states with the HPS. These results are promising for exploration and indicate that the quartz monzonite dikes at Sprogge formed under the same conditions as other mineralized plutons in the TGB. Mineralization styles between occurrences of the HPS and WPS vary. The Sprogge exploration target may be associated with intrusions of either suite. This should be taken into account when exploring for mineralization further, including focusing on both disseminated and vein-hosted occurrences (as commonly seen in HPS deposits), or on metasomatism with calcareous wall-rock which may result in a mineralized skarn (as seen in WPS deposits).

3.2 The 3Ace Claim block

3.2.1 Wall-rock and Pre-Au Mineralization

Drill core and assay results from NTR have shown approximately 65% of Au mineralization is hosted in quartz veins in QPC and lithic arenite units, with the rest occurring in intensely brecciated zones in phyllite and fault gouge. The wall-rock is therefore important for understanding the controls on vein development and mineralization. There is limited mineralization within the wall-rock with the exception of foliation-discordant faults and dilational fractures.

Sericite dominates the matrix within the QPC and lithic arenite, and occurs concentrated along foliation discordant fractures. Alteration tends to be concentrated to within 10's of meters of the mineralized veins. The presence of sericite alteration along shears may indicate strain-softening. The presence of strain softening and quartz-veining may indicate mineralization took place within a shear zone at a depth within the brittle-ductile transition zone, which is characteristic of Au mineralized mesothermal veins (Kerrick and Feng 1992).

Based on the presence of pyrrhotite, temperatures between 247-311°C (from fluid inclusion data), and intense host-rock sericitization suggestive of acidic fluids, it can be assumed that $\delta^{34}\text{S}_{\text{mineral}} \approx \delta^{34}\text{S}_{\text{H}_2\text{S}} \approx \delta^{34}\text{S}_{\text{fluids}}$ (Ohmoto and Goldhaber, 1997). Recrystallized pyrite framboids within silty lenses of the phyllite unit have a $\delta^{34}\text{S}_{\text{CDT}}$ value of $20\text{‰} \pm 0.6$. Replacement appears to have occurred by hydrothermal fluids associated with Stage 2 quartz veining, as these veins are associated with euhedral pyrite within phyllite (see below). The pyrite framboids probably formed by biogenic sulfate reduction, and likely had an original isotope composition ($\delta^{34}\text{S}_{\text{VCDT}}$) values below 0‰ (Ohmoto and Goldhaber, 1997; Kohn et al., 1998). The 20‰ value reflects reduction of sea water sulfate and a marine S source (Rye and Ohmoto, 1974; Kerridge et al., 1983; Ohmoto and Goldhaber, 1997).

3.2.2 Quartz Vein Development and Mineralization

The quartz vein paragenesis is summarized in Figure 9. Stage 1 and Q1 represent quartz veining prior to the event associated with Au mineralization. Stages 2 through 4 are believed to have occurred from similar fluid sources based on similar O isotopes of the vein quartz (see below). These quartz vein stages are cross-cut by muscovite stringers, which are in turn cross-cut by Q5. The nature of the mineralization and fluid sources associated with each stage are discussed below.

Stage 1: Early Quartz Veining – Stage 1 is associated with Q1 containing apatite, albite and pyrite (Py-2) formation. $\delta^{18}\text{O}_{\text{VSMOW}}$ values range from $16.3\text{‰} \pm 0.2$ to $18.1\text{‰} \pm 0.2$. These values fall within the range of low-grade metamorphic foreland basin sediments, which are remarkably uniform in isotopic compositions ($\delta^{18}\text{O}_{\text{VSMOW}} = 14$ to 18‰ ; Burt and Taylor, 1993, as referenced in Taylor, 1997). They are also close to the range of unaltered metasedimentary rocks of the Hyland Group found near the Scheelite Dome deposit (Mair et al., 2006b). The wall-rock there also comprises quartz and muscovite and has a slightly lower isotopic range ($\delta^{18}\text{O}_{\text{VSMOW}} = 13.8$ to 16.5‰ ; Table 5, Mair et al., 2006b). Beige Q1 has undergone high degrees of recrystallization to polycrystalline quartz. Due to intense deformation, fluid inclusion measurements could not be obtained from Q1.

Pyrite (Py-2) is also intensely deformed to the extent that it shows anisotropic extinction. The S isotope composition of one Py-2 sample ($\delta^{34}\text{S}_{\text{VCDT}} = 26.8\text{‰} \pm 0.6$) suggests the S was derived from reduction of seawater sulfate. Highly positive sulfur isotope values above are likely derived from seawater sulfate or evaporates; a $\delta^{34}\text{S}_{\text{VCDT}}$ value of 26.8‰ could be derived from Neoproterozoic, Cambrian or Ordovician seawater or evaporates (Figure 5, Bottrell and Newton, 2006, modified from Claypool et al., 1980). None of the currently exposed host rocks contain sulfate units, and sulfates have not been observed in local limestones. A possible source for the sulfate is the barite unit within the regionally extensive, Mid-Devonian Portrait Lake Formation of the Earn Group. This unit is believed to represent the first indication of tectonic instability

due to the sudden change from low clastic input and siliceous chert deposition to sedimentary gravity flows and the position of chert-pebble conglomerates and bedded barite (Godey and Anderson, 1993). However, it still predates orogenesis, which did not occur until the Mid-Triassic at the earliest (Gordey and Anderson, 1993). According to Figure 5 of Bottrell and Newton (2006, modified from Clayton et al., 1980), the S isotopic compositions for evaporites during the Devonian range from ~17‰ to 24‰, and the range for O isotopes from marine sulfate occurs between 15‰ and 16.5‰. The observed S isotope values indicate 3 possible sources for S and O from the fluids associated with quartz vein formation:

1. Fluids interacted with overlying sulfate-bearing sedimentary units (e.g. Portrait Lake Formation) prior to orogenesis and then travelled to depth along crustal faults;
2. The Yusezyu Formation was thrust over sediments as young as the Portrait Lake Formation, where fluids then interacted with evaporites already at depth;
3. Sulfur is derived from an unknown sulfate unit at depth possibly derived from Neoproterozoic or early Cambrian evaporites, or from ancient seawater within Hyland Group Sediments.

According to Bottrell and Newton (2006), the O isotopes of the evaporite-derived sulfate are <15‰, lower than that of Q1. However, there is a significant amount of uncertainty (~3-5‰) of both isotope age curves (Bottrell and Newton, 2006); therefore a Neoproterozoic sulfate source cannot be ruled out, and the S and O for Py-2 and Q1, respectively were likely derived from the same sulfate source.

Stage 2: A new hydrothermal event – Stage 2 is associated with Q2, which is only visible under a microscope and cathodic light. $\delta^{18}\text{O}_{\text{VSMOW}}$ values for Q2 range from 16.8‰ ±.2 to 18.1‰ ±.2 and fall within the same range as Q1. Stage 2 fluid inclusions are rare and too small to obtain microthermometric measurements. While the isotopic values are

higher than those for typical igneous rocks, the oxygen isotope composition of the fluids cannot be determined without microthermometric data.

Stage 3 and 4a – Pre-Au mineralization: These stages are grouped together as they are both associated with Type 1 fluid inclusions (Table 1). Stage 3 comprises just Q3, and Stage 4a comprises Q4a, arsenopyrite (Apy), and galena (Gn-1). The isotopic composition of Q3 has a similar range to Q1 and Q2 ($\delta^{18}\text{O}_{\text{VSMOW}} = 16.7 \text{‰} \pm 0.2$ to $18.0 \text{‰} \pm 0.2$). Microthermometry carried out on primary Q3 fluid inclusions, and pseudo-secondary inclusions associated with Q4a, suggest the quartz-forming fluids at the Main Zone had relatively low salinities (an average of 3.4 wt.% NaCl; Table 1). Homogenization temperatures (T_h) of Type I inclusions suggest the minimum trapping temperature was in the range of 201°C to 265°C for Q3 and Q4a at the Main Zone at pressures of ~290 MPa (Table 8). Using the oxygen isotope of Q3, the T_h values of Type I inclusions, and the fractionation constants determined by Matsuhisa et al. (1979), the calculated $\delta^{18}\text{O}_{\text{fluid}}$ which precipitated Q3 ranges from 5.2 ‰ to 6.5 ‰ for fluids at 201°C, and from 8.5 ‰ to 9.8 ‰ for fluids at 265°C.

Fluid temperatures were higher at Sleeping Giant, where the only Type I fluid inclusion yielded a T_h value of 358°C and a salinity of 0.7 wt.% NaCl. Assuming similar $\delta^{18}\text{O}_{\text{quartz}}$ values as the Main Zone, the calculated $\delta^{18}\text{O}_{\text{fluid}}$ values at Sleeping Giant would be from 11.6 ‰ to 12.9 ‰. Type I inclusions at the Green Zone yield slightly higher T_h values from 218°C to 351°C, as well as a narrow salinity range from 2.4 to 3.5 wt.% NaCl, and a pressure of ~219 MPa. The BrF_5 method for O isotopes yielded a $\delta^{18}\text{O}_{\text{quartz}}$ value of 16.4 ‰ at the Green Zone for quartz believed to be associated with arsenopyrite mineralization. Based on this value, the calculated $\delta^{18}\text{O}_{\text{fluid}}$ values are 5.9 ‰ for fluids at 218°C, and 11.1 ‰ at 351°C. Using the criteria of Ramboz et al. (1982), fluid inclusions at 3Ace do not show signs of fluid immiscibility.

Sulfur isotopes for Apy both within the host rock and quartz vein have a narrow range of $\delta^{34}\text{S}_{\text{VCDT}} = 15.0\text{‰} \pm 0.6$ (wall-rock sample) to $17.7\text{‰} \pm 0.6$ (quartz vein sample). The narrow range in values indicates that arsenopyrite precipitated from fluids with a

common S source. These values are lower than those discussed previously. According to Bottrell and Newton (2006), seawater sulfate sources with average S isotopes in the range of Apy formed during 3 time periods: Carboniferous (Pennsylvanian), Mid-Triassic, and Early Cretaceous. In the Nahanni map area, one unit found in the Selwyn Mountains that has been dated to be Late Mississippian to Permian in age is the Mount Christie Formation, which contains abundant barite nodules (Gordey and Anderson, 1993), but this unit has not been found within the map area. The possible sources of S for Apy are likely similar to those of Py-2, but the seawater sulfate would have to be Carboniferous in age instead of Neoproterozoic, and could be sourced from seawater sulfate in the pore-waters or from sulfate units. Variations of S isotopes between the different generations of sulfides may also be the result of different degrees of wall-rock and fluid interaction (Ohmoto and Goldhaber, 1997).

Another way to produce sulfides with lower isotopic compositions is by thermochemical S reduction (TSR) when sulfate is reduced during sulfide precipitation ($\text{SO}_4^{2-} \rightarrow \text{S}^{2-}$; Machel et al. 1995). At 200°C, TSR results in a negative shift of 10‰ from the original sulfate composition, but the shift decreases with increasing fluid temperatures (Machel et al. 1995). If seawater sulfate compositions were between 25‰ and 30‰ during the Neoproterozoic (Bottrell and Newton, 2006), then the S isotope compositions in Apy and later sulfides could have resulted by TSR whereby fractionation during reduction resulted in a negative shift in $\delta^{34}\text{S}$ values by 10‰ or less. A reductant, commonly organic matter, is necessary for TSR to take place and there is typically an associated carbon isotope fractionation. At 3Ace, there is a lack of organic material and the C isotopic signature of the carbonate minerals indicate that TSR did not occur locally to the deposit (Machel et al. 1995). Therefore, we infer that TSR may have generated H_2S elsewhere in the host-rock package and then the reduced S was transported by the mineralizing fluids and incorporated into the base-metal sulfide minerals at 3Ace.

Unfortunately Pb isotopes were only analysed from the quartz vein galena of 2 samples, the 3Ace sample collected near the Hat prospect (SCW11 F300) and Main Zone core sample 3A-11-15A 226.95. The latter is believed to be Gn-1 which formed during

Stage 4a. Figure 22 shows how the Pb-Pb isotope results compare to the Shale Curve of Godwin and Sinclair (1982), as well as compared to mixing isochrons between the Shale Curve and the Bluebell Curve (Andrew et al. 1984). One sample sits directly on the shale curve, which indicates the Pb was derived from an upper crustal source (Godwin and Sinclair, 1982) and has a model age of ~189 Ma (Figure 22; from Equation 1 in Godwin and Sinclair, 1982). In contrast, the second sample lies along a 100 Ma mixing isochron between the two curves, indicating Pb was likely derived from two sources including the upper crust and the lower crust or upper mantle (Andrew et al. 1984).

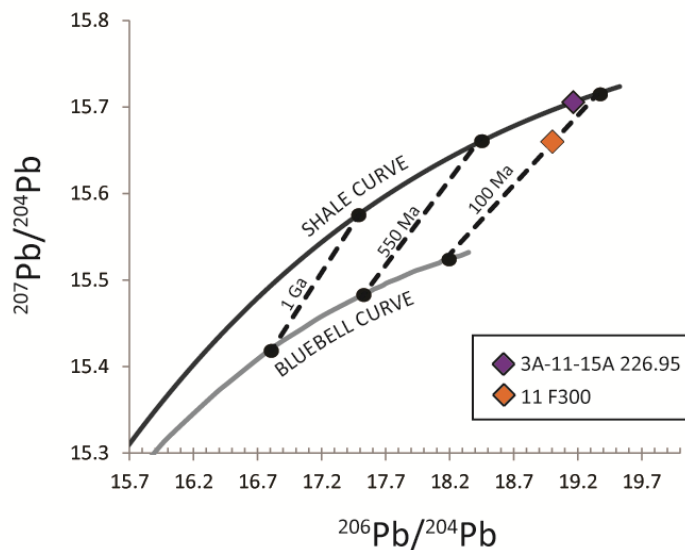


Figure 22. Pb-Pb isotope results for samples 11 F300 (3Ace) and 3A-11-15A 226.95 (Main Zone). The Shale Curve was plotted using the data from Godwin and Sinclair (1982), and the Bluebell Curve and mixing isochrons were plotted using data from Andrew et al. (1984).

The model age of 100 Ma correlates well with the emplacement of the Hyland and Tungsten plutonic suites, which as previously discussed, could possibly underlie the area near the sample location for 11 F300. Although the sample's placement relative to the Shale Curve may indicate that sample 3A-11-15A 226.95 is slightly older, the error on these curves is too large to estimate a meaningful age. Furthermore the error on age

determination using the mixing isochrons may be as large as 100 Ma (Andrew et al., 1984).

Stage 4b and 4c: Au and base-metal sulfide mineralization - Stage 4b is most notably defined by Au mineralization, along with coarse muscovite (Ms-1), euhedral calcite (Cal) and dolomite (Dol). As seen in Figure 11, Au post-dates arsenopyrite and is not coeval with sulfide mineralization. Microthermometry indicates Type II fluid inclusions (Table 1) associated with Au mineralization at the Main Zone were trapped at temperatures between 247°C and 311°C, and at pressures ranging from 165 to 300 MPa (Table 8). Such a range in pressures likely indicates depressurization during vein formation. The higher pressures also explain why fluid inclusions within Q1 were completely decrepitated (Goldfarb, 1993). The ion microprobe yielded isotopic compositions ($\delta^{18}\text{O}_{\text{VSMOW}}$) of Q4 between $16.2\text{‰} \pm 0.2$ and $18.2\text{‰} \pm 0.2$. The calculated $\delta^{18}\text{O}_{\text{fluid}}$ from a Q4 trapping temperature of 247°C are 7.2 ‰ and 9.2 ‰, whereas fluids at 311°C have values from 9.7 ‰ to 11.7 ‰. Trapping temperatures at Sleeping Giant range from 246°C to 306°, yielding calculated fluid pressures from 201 to 300 MPa. Using the same $\delta^{18}\text{O}_{\text{quartz}}$ values as Main Zone Q4, calculated $\delta^{18}\text{O}_{\text{fluid}}$ values are between 7.1 ‰ and 9.1 ‰ for fluids at 246°C, and from 9.6 ‰ to 11.6 ‰ for fluids at 306°C. Oxygen isotopes and T_{h} values at the Green Zone also fall within the same range, and therefore so do the $\delta^{18}\text{O}_{\text{fluid}}$ values. The calculated fluid pressures are much lower at the Green Zone for Type II inclusions, and range from 125 to 173 MPa.

Microthermometric data shows that the Au mineralizing fluids had the highest temperatures. Pre- and post-ore fluids were cooler, but have a small overlap in temperatures with Stage 4b, indicating fluids leading up to mineralization were increasing in temperature up until Au precipitation, and then decreased in temperature afterwards. The calculated fluid pressures (Table 8) indicate fluid pressures were highest prior to Au-mineralization, then decreased with decreasing temperature at the Main Zone and Sleeping Giant. The decrease in fluid pressures from Q3 to Q4b may also explain why there is earlier arsenopyrite mineralization in the wall-rock surrounding the

quartz veins, but no Au, since fluids associated with Q4b were no longer adequately pressurized to fracture the surrounding quartz vein into the wall-rock.

Pale-green, very fine grained calcite occurs as micron-sized ‘flecks’ in Type I and Type II fluid inclusions, as well as within Q3 and Q4 growth zones surrounding arsenopyrite or Au mineralization. Coarser, beige calcite also occurs along fractures within the quartz veins. Figure 23 shows the range of C and O isotopes from calcite, siderite, dolomite, and ankerite compared to other common carbonate sources.

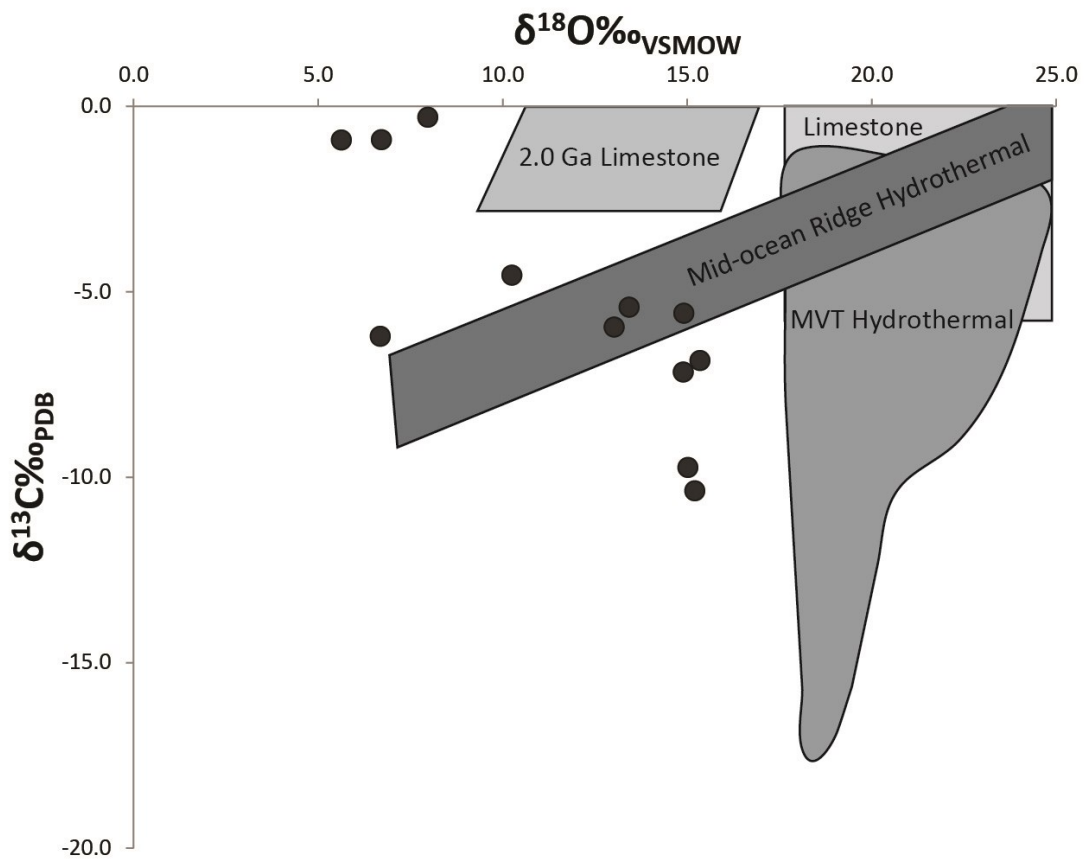


Figure 23. A cross plot of $\delta^{13}\text{C}_{\text{PDB}}$ and $\delta^{18}\text{O}_{\text{VSMOW}}$ values of Main Zone carbonate samples relative to several carbonate sources (MVT = Mississippi Valley Type deposit; after Figure 7.19 of Rollinson et al. 1993, and references therein).

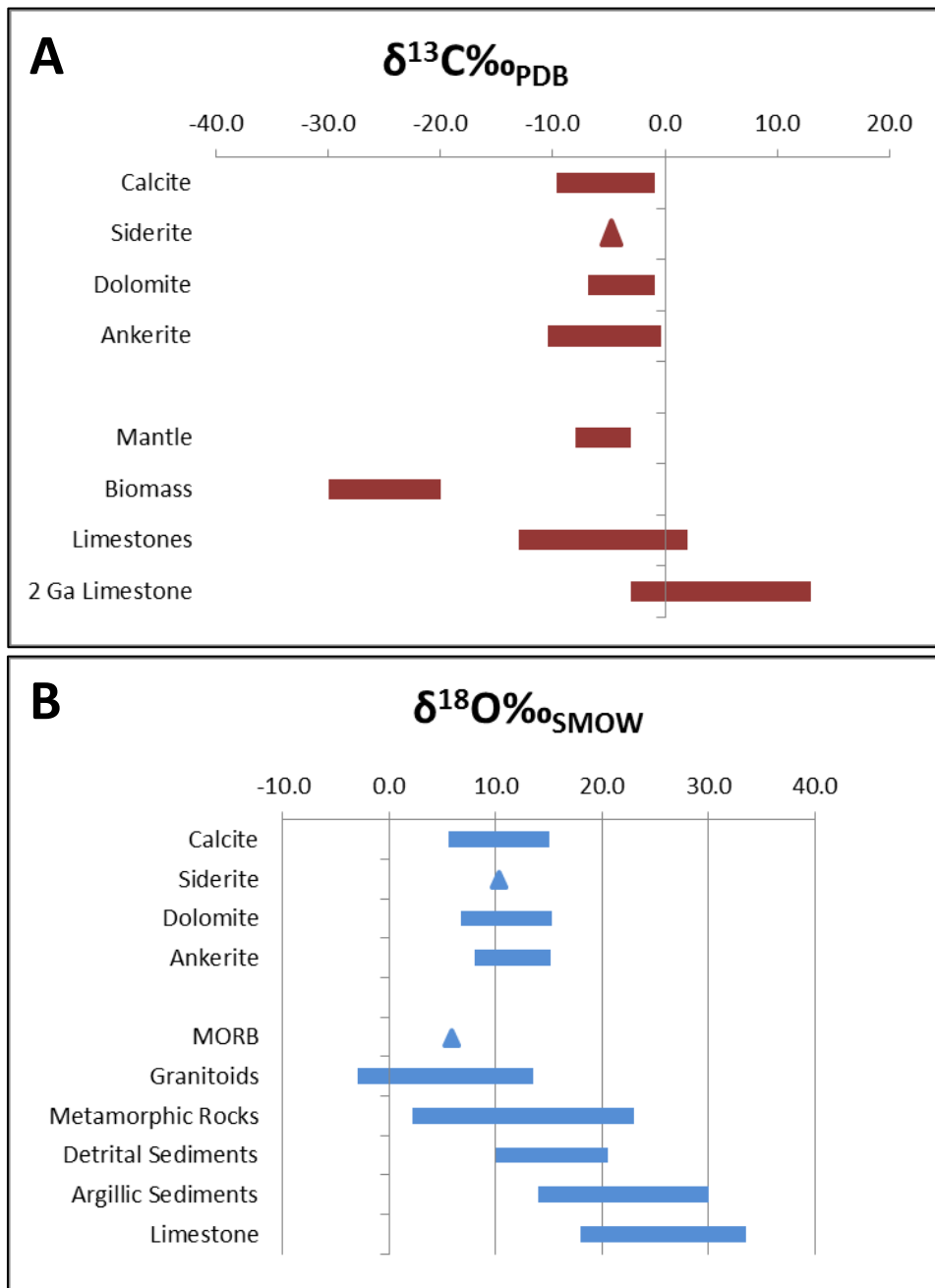


Figure 24. Bar graph A shows the distribution of $\delta^{13}\text{C}_{\text{PDB}}$ values for calcite, siderite, dolomite, and ankerite from Main Zone samples relative to different source rocks (after Figure 7.17 of Rollinson et al., 1993, and references therein). Bar graph B shows the range of $\delta^{18}\text{O}_{\text{VSMOW}}$ values for calcite, siderite, dolomite and ankerite relative to different source rocks (MORB=Mid-oceanic ridge basalts; after Figure 7.1 of Rollinson et al. 1993, and references therein)

The samples, however, do not correlate with another rock type. Figure 23A shows that the isotopic composition of all four phases indicates limestone to be the most likely source of C ($\delta^{13}\text{C}_{\text{PDB}} = -0.3\text{‰}$ to -10.4‰). In contrast, the O isotopic compositions of the same carbonate samples indicate a different O reservoir. The results presented in Figure 24B indicate the O within the fluids could have been likely derived from granitoid rocks, metamorphic rocks, detrital sediments, or a fluid which has equilibrated with any of these. There are two possible explanations for the difference in source reservoirs for the O and C in the carbonate: they either precipitated from a fluid produced by the mixing of two different fluids that had equilibrated with different wall-rocks, or the C within the fluid was not modified by water-rock interaction with the host rocks whereas the O was.

Stage 4c contains post-Au base-metal sulfide mineralization, dominated by pyrite (Py-3) with minor galena (Gn-2), sphalerite (Sp), chalcopyrite (Ccp), and pyrrhotite (Po). Goethite forms as the weathering product of these base-metal sulfides. The $\delta^{34}\text{S}_{\text{VCDT}}$ values of Py-3 have a large range, from $5.6\text{‰} \pm 0.6$ to $18.9\text{‰} \pm 0.6$. Py-3 that cross-cuts arsenopyrite yielded $\delta^{34}\text{S}_{\text{VCDT}}$ values of $10.6\text{‰} \pm 0.6$ and $18.9\text{‰} \pm 0.6$. Py-3 is always euhedral and barely deformed and occurs in a variety of settings; it is observed on fracture surfaces in phyllite and lithic arenite, along wall-rock foliations, and also within quartz veins and near quartz vein contacts. Thermochemical S reduction could account for the range of S compositions as microthermometric data confirm decreasing temperatures during Q4b and c, which in turn would increase the negative shift in $\delta^{34}\text{S}$ values by as much as 20‰ at 100°C (Machel et al., 1995).

The wide range of $\delta^{34}\text{S}_{\text{VCDT}}$ could also indicate there is more than one S source, and suggests that the mineralizing fluids integrated S from different sources. Most notable are the lowest values (under 9‰) as these values can be indicative of S from a magmatic or basaltic source (Ohmoto and Goldhaber, 1997; Kerridge et al., 1983; Rye and Ohmoto, 1974). Another possibility, however, is that reduced S was sourced from a partially closed system with respect to SO_4^{2-} . Pyrite that mineralizes in a closed system, and to some degree a partially closed system, is subject to Rayleigh isotopic

fractionation (Ohmoto and Goldhaber, 1997), whereby $\delta^{34}\text{S}$ for sulfides continuously changes from strongly skewed towards less positive values to strongly skewed towards more positive values relative to values for MORB (Ohmoto and Felder, 1987). Of the five samples with values $<9\text{‰}$, four occur below a depth of 200 m and are primarily hosted by phyllitic units. In the absence of bioturbation, Rayleigh isotopic fractionation can lead to a large range of $\delta^{34}\text{S}_{\text{sulfide}}$ values (Ohmoto and Felder, 1987; Ohmoto and Goldhaber, 1997).

The presence of arsenopyrite, pyrite and pyrrhotite indicates acidic, reducing fluid conditions prior to, and following, Au mineralization (Ohmoto and Goldhaber, 1997) based on the low oxidation state of the S in the sulfides (Ohmoto, 1972). Under these conditions and in low salinity fluids, Au was therefore transported in solution by H_2S as $\text{Au}(\text{HS})_2^-$ (Shenberger and Barnes 1989), or as $\text{Au}(\text{HS})^0$ (Benning and Seward 1996) at relatively high temperatures and pressures (Benning and Seward 1996). Precipitation of Au out of solution appears to have occurred as the result of at least 3 processes: 1) oxidation of the Au-bearing fluid by cooler, wall-rock equilibrated fluid, 2) destabilization of the gold-transporting complex by earlier precipitation of arsenopyrite resulting in a decrease of H_2S , and 3) depressurization resulting in reduced Au solubility of the acidic fluid (Seward, 1993; Benning and Seward, 1996; Alm et al., 2003).

While homogenization temperatures were consistent across all 3 deposits, pressure estimations vary (Table 8). Similar pressure conditions existed between the Main Zone and Sleeping Giant; however pressure estimates are much lower at the Green Zone. In acidic fluids, lower pressures would result in lower Au solubilities (Benning and Seward, 1996), which may be the case at the Green Zone as evidenced by markedly lower Au concentrations; however further work is warranted to confirm such a conclusion. The remaining sulfides and calcite continued to be deposited within the quartz vein as open space fillings following Au mineralization by fluids with similar compositions at lower temperatures and pressures. Similar calcite mineralization to that observed at the main zone has been observed in orogenic gold deposits where it is believed calcite precipitated due to pressure changes of a CO_2 rich aqueous fluid (Alm et

al., 2003). Experiments have shown that the solubility of calcite decreases with decreasing pressure (Fein and Walther 1987, as referenced in Alm et al., 2003) due to a proportionate decrease in fugacity (f_{CO_2} ; Segnit et al. 1962). This supports a structural regime where CO_2 rich fluids were depressurized during pressure cycling and vein formation. Interaction with metasediments in the wall-rock can also result in the reduction of H^+ in solution, thereby increasing the CO_3^{2-} concentration at a given total carbon species concentration and resulting in calcite precipitation (Holland and Malinin, 1979). Calcite precipitation at 3Ace was likely the result of a combination of wall-rock interaction and sudden depressurization of the CO_2 bearing fluid.

Most alteration minerals associated with Stage 4 were not discernible in thin section due to their fine grained nature or relatively low abundance. Quartz, muscovite, pyrite and clinocllore represent sericitization of the host rock (Reed, 1997), which is an expected alteration assemblage for orogenic Au deposits occurring in clastic sedimentary units (Nesbitt et al., 1989; Groves et al., 1998). Figures 11 and 12 show kaolinite occurring throughout much of hole 3A-11-11 including high grade Au zones, but it is more focused in high grade zones in hole 3A-10-01. One sample also near the high grade zones contained the smectite montmorillonite. Together, these minerals likely represent an intermediate argillic alteration assemblage (Reed, 1997; Evans, 1993) that formed alteration envelopes within the wall-rock around mineralized veins, as the result of either the pre- or post-Au fluids altering the metasediments, but not during Stage 4b when fluid temperatures would have been too high. The smectites indicate that sericitization locally transitions into a lower grade intermediate argillic alteration assemblage (Evans, 1993). As previously discussed, minimum trapping temperatures for fluids associated with Au mineralization, Type II, range between 247°C and 311°C at the Main Zone. Smectites are associated with intermediate argillic alteration at temperatures between 200-250°C, as higher temperatures do not kinetically favour smectite formation. In terms of the timing of their formation, smectites could have formed at lower temperatures earlier in quartz vein development prior to Au

mineralization and persisted due to self-made metastability whereby occlusion of pore spaces prevented fluid flow, and thereby also prevented their dissolution (Reed, 1997).

Sericitization can also grade into the higher temperature advanced argillic alteration. This alteration assemblage usually consists of dickite, kaolinite, pyrophyllite and quartz at temperatures around 350°C (Evans 1993), and is characteristic of magmatic fluids interacting with felsic rocks or sediments. Only one fluid inclusion at Sleeping Giant had a minimum trapping temperature above 350°C, but dickite has been found in a couple of samples near high grade Au zones in hole 3A-11-11 (Figure 11). Although dickite is a higher temperature polymorph of kaolinite, pre-existing kaolinite is not necessary for its formation, as dickite can be precipitated directly by hydrothermal fluids at temperatures ranging from 150°C to 270°C (Zotov 1998). This indicates that high temperature fluids associated with Au mineralization did penetrate and alter wall-rock adjacent to veins. Also forming at high temperatures near the high grade Au zones is albite, which likely occurred by albitization of plagioclase grains and clasts within the lithic arenite or QPC wall-rock. Albitization is also a common alteration product of orogenic Au deposits (Nesbitt et al. 1989; Groves et al. 1998).

3.2.3 Post-Au mineralization and relative timing of vein formation

Stage 5: Muscovite stringers - Stage 5 is defined by muscovite stringers associated with a fluid that remobilized the margins of base-metal sulfides and in some instances Au. It was not possible to obtain information on the fluid responsible for muscovite precipitation due to the absence of quartz or other fluid-inclusion bearing minerals. One can only speculate that at some point following Au deposition, a later and relatively high-temperature acidic fluid took advantage of pre-existing fractures and the increased porosity of the wall-rock that occurred as the result of the Stage 3 and 4 mineralization. This fluid dissolved and remobilized sulfides and Au along micro-fractures, as well as within the foliations and fractures of the wall-rock surrounding the veins. In addition to muscovite, this post-Au fluid also precipitated monazite (Mnz), rutile (Rt; as identified by XRD), blue-green chlorite (Chl-1), and entrained inherited zircons (Zrn).

Cathodoluminescence studies show that the zircon fragments have growth zoning and do not have metamorphic rims, suggesting they are magmatic in origin and possibly indicate a pluton at depth.

An attempt was made to analyse the U-Pb contents and date the monazites using LA-MC-ICP-MS; however, due to the fractured and anhedral nature of the grains, ^{207}Pb counts were too low to yield concordant results. Of the 18 spot analyses, only 2 did not lie along a linear regression anchored at the value for common Pb (0.86; Stacey and Kramers, 1975) on an Inverse Concordia, or *Tera-Wasserburg* plot (Tera and Wasserburg, 1972), as seen in Figure 25. This regression line yields an intercept age of 151.2 ± 6.1 Ma. Although there is a lot of uncertainty to this age due to low Th contents and low Pb counts, it warrants further research.

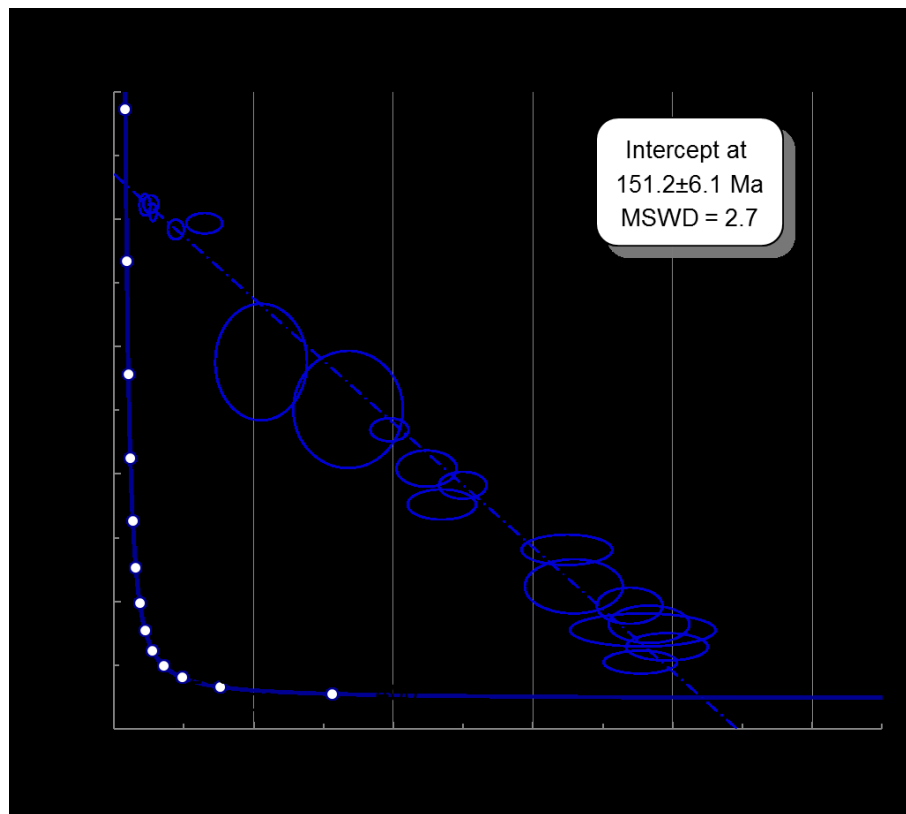


Figure 25. Inverse Concordia or Tera-Wasserburg plot for hydrothermal monazite U-Pb data from the Main Zone (Ludwig, 2012).

These stringers are small and generally rare. They also do not appear to have occurred on a broad scale, or at sufficiently high volumes to remobilize significant Au and greatly alter the grade of the deposit. The minerals monazite and rutile generally form at high pressures and temperatures relative to those involved with low grade metamorphism and orogenesis (Dachille et al., 1968; Schandl and Gorton, 2004). While the minerals appear to be hydrothermal, as supported by the low ThO₂ contents of the monazites (Schandl and Gorton, 2004), they may have been precipitated from a REE rich magmatic fluid that originated from an intrusion that post-dated Au mineralization.

Stage 6: Post-Au quartz veining - Q5 cross-cuts all previous paragenetic stages, and occurs as <2 mm veinlets within previous quartz veins and surrounding wall-rocks, or as a <2 mm rim around euhedral quartz terminations in vugs (Figure 6). Type III fluid inclusions associated with Q5 are always secondary. Homogenization temperatures for Q5 range from 140°C to 237°C, which likely reflects a cooling hydrothermal fluid system. One Main Zone Type III fluid inclusion yielded a calculated pressure of 109 MPa. Q5 had a $\delta^{18}\text{O}_{\text{VSMOW}}$ value of 20.3‰ ± 0.1. Using the $\delta^{18}\text{O}_{\text{qtz}}$ value of 20.3‰, the calculated $\delta^{18}\text{O}_{\text{fluid}}$ values for Q5 from 140°C to 237°C range between 4.0 ‰ and 11.3 ‰, respectively. The value of 11.3‰ for the higher temperature fluid falls within the same range as the Q4 fluid. This indicates the fluids initially involved with Q5 vein formation were likely from a similar reservoir as Q4, and as the fluids cooled they incorporated a meteoric fluid with a lower isotopic composition, that in general range from -40‰ to +0‰ (Craig, 1961).

Homogenization temperatures, salinities and stable isotopes for Q5 show the fluids which formed it were cooler, and had a larger meteoric component than the Stage 4 ore fluids. These fluids most likely represent the cooling stage following mineralization towards the waning of orogenesis and metamorphism. At this point fluids were no longer under high enough pressures or temperatures to carry dissolved metals, and as such are not associated with mineralization. The extensive Fe-oxidation of sulfides is

believed to be associated with oxidized meteoric fluids which propagated along late fractures within the QPC and lithic arenite host rocks, as well as within the quartz veins.

Stage 7: Post-ore Alteration - Stage 7 mineralization consists of low temperature alteration assemblages, which mainly occur along fractures or as vug fills. Chalcedony represents the lowest temperature end-member of the fluids that precipitated Q5. The presence of gypsum, which although minor and rare, supports a sulfate bearing fluid at the waning stages of mineralization and either a sulfate or oxidized sulfide source for the O associated with Q5. Other minerals occurring close to high grade Au zones in Figures 17 and 18 include carbonates such as calcite, dolomite, siderite and ankerite, as well as goethite, rutile, scorodite, magnesite, and hematite. These minerals have been identified by petrography and are not part of hydrothermal alteration assemblages. Instead, they represent different stages of the paragenesis. They can still, however, be used as indicators for certain processes which commonly occur adjacent to, or within, mineralized veins. Siderite and ankerite are alteration products associated with late, oxidizing, Fe-rich fluids which likely altered pre-existing calcite and dolomite, respectively. Similar fluids were also involved in sulfide alteration resulting in goethite, scorodite and hematite.

3.2.4 Fluid Source and Genetic Model

The stable isotope results do not definitely point to a single fluid source. According to Figure 26, there are several possible O sources for the fluids associated with quartz vein formation. While S stable isotopes indicate a seawater sulfate source that may have been reduced in a partially closed environment and have a possible magmatic input, C and O stable isotopes from carbonates indicate both a limestone (where more negative suggest an organic input), and the same sources as quartz for O. There could be two reasons for separate sources in carbonates: either the fluid equilibrated with a limestone unit first then with a lithic unit poor in C, or the isotopic signature resulted from the mixing of two fluids that equilibrated with different wall-rocks.

As previously determined, the pre-Au mineralizing fluids had an overall $\delta^{18}\text{O}_{\text{fluid}}$ range from 4.7‰ to 9.3‰ at the Main Zone. Fluids at Sleeping Giant and the Green Zone have slightly higher ranges up to 12.6‰ and 10.6‰, respectively. Figure 25 shows these values lie within the ranges of either magmatic, metamorphic, and mother lode ore fluids (which involved a large meteoric water component). The $\delta^{18}\text{O}_{\text{fluid}}$ values from Type II inclusions and Q4 lie within a similar range. Here, possible fluid sources could include the following, or a combination thereof:

1. Connate seawater buried at depth was tapped during orogenesis and focused along crustal faults where it mixed with other fluids;
2. Metamorphism at depth resulted in the formation of heated, metamorphic fluids which equilibrated with multiple wall-rocks;
3. Magmatic fluids below the seismogenic zone were focused along faults where they mixed with fluids from above the seismogenic zone.
4. Meteoric fluids that have equilibrated with the sedimentary host rocks at temperatures around 300°C.

While the stable isotope evidence is not definitive, there are other geological characteristics that can be used to constrain a deposit model. Intrusion-related Au deposits (IRGD) have many characteristics in common with orogenic Au deposits, including similar wall-rock alteration assemblages, fluid characteristics, metal associations, and even structural controls on fluid flow (Groves et al. 2003). Both deposit types are associated with sub-greenschist facies metamorphism, compressional tectonic settings, lamprophyre dikes, and sheeted veins that formed after peak metamorphism at 1.5 kbars from CO_2 -rich fluids with trapping temperatures between 200°C and 400°C, in addition to mica-carbonate-Fe sulfide alteration at depths of around (Groves et al., 2003; Baker and Lang 2001). All these characteristics can be used in some way to describe mineralization at all three Au occurrences at 3Ace.

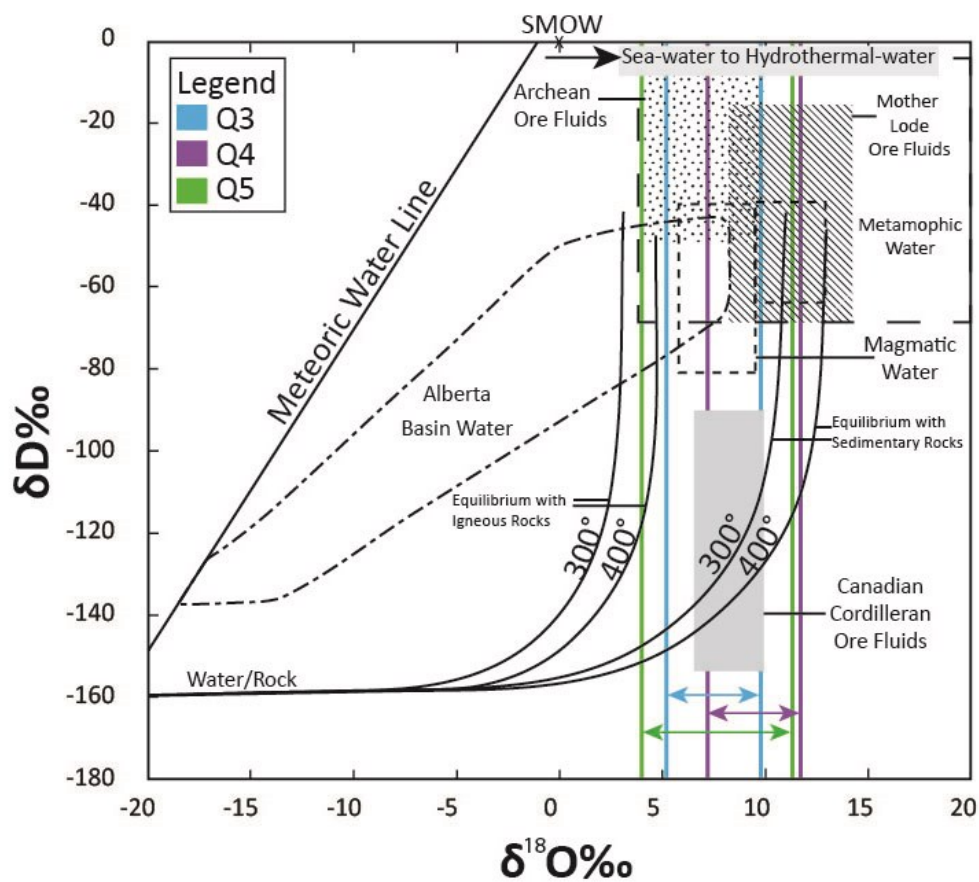


Figure 26. A H and O stable isotope plot with outlined values for common hydrothermal Au fluid sources (after Figure 10 of Nesbitt et al., 1989, and references therein; Figures 4 and 6 in Sheppard, 1986, and references therein). Vertical lines and arrows display the range in Main Zone $\delta^{18}O_{\text{fluids}}$ values for Q3, Q4, and Q5.

IRGD's with similar $\delta^{18}O_{\text{qtz}}$ values Q3 and Q4 include Au bearing quartz veins associated with the South Mountain Batholith (11.7 to 17.8‰; Kontak and Kyser, 2011), and the TGB Clear Creek deposit that is associated with the Mayo plutonic suite (13‰ to 16‰; Marsh et al., 2003). Kontak and Kyser (2011) interpreted the wide range of $\delta^{18}O_{\text{qtz}}$ values to reflect a mixture of contact metamorphic fluid and magmatic fluid from the intrusion. Pegmatitic quartz from the intrusion produced a $\delta^{18}O_{\text{qtz}}$ value of 14.0‰ (Kontak and Kyser, 2011). A similar conclusion was reached for the quartz veins at Clear Creek (Marsh et al., 2003). Fluid inclusions from the Main Zone and Sleeping Giant that are associated with Au mineralization and a CO_2 -rich, low salinity fluid are most similar to deep, mesothermal sheeted veins found within IRGD's, such as the Fort Knox deposit

of Alaska (McCoy et al., 1997, as referenced in Baker, 2002). At Fort Knox, fluids were trapped at ~1.5 kbar at temperatures between 270°C and 330°C (McCoy et al., 1997, as referenced in Baker, 2002). These isotope and microthermometric similarities could support a magmatic fluid component.

Few samples were collected outside the mineralized areas. One sample, F300, was located near the Hat showing within the Yusezyu Formation near an aeromagnetic low (see Figure 2 of Hart and Lewis, 2005). Within the quartz is a coarse bleb of galena, which yielded a $\delta^{34}\text{S}_{\text{VCDT}}$ value of 4.9‰. This value falls within the range of most common ore deposits which have magmatic or volcanic derived sulfur, such as volcanogenic massive sulfides, porphyries and skarns (Ohmoto and Goldhaber, 1997). This prospect lies near the edge of an aeromagnetic low, commonly associated with intrusions of the Tungsten plutonic suite (Hart and Lewis, 2005). One Au occurrence referred to at the Fer property has been found to be best explained by an intrusion-related model (Jones and Caulfield, 2000). The data is therefore encouraging for future exploration of intrusion-related deposits; however much more work is needed to understand the style of mineralization and how it relates to other deposits within the 3Ace claim.

A major difference between IRGD's and orogenic Au deposits is the host rock. While the quartz veins of the Fort Knox deposit are located within granodiorite and granite (McCoy et al., 1997, as referenced in Baker, 2002), the mineralized veins at 3Ace are exclusively hosted within metasediments and there is no indication of contact metamorphism or zoned alteration that would be associated with an intrusion, or of an intrusion itself. Although there are small dikes within the 3Ace claim, they are not spatially related with mineralization, and their timing relative to mineralization has not been constrained. The BrF_5 method for O isotopes did yield some lower $\delta^{18}\text{O}_{\text{qtz}}$ values within the range of magmatic rock (5.5‰ to 10‰; Taylor, 1997), but these were from small quartz veinlets which cross-cut pyrite mineralized veins. These lower O isotope values may support a post-mineralization igneous event, where the igneous fluids may have also combined with isotopically lighter meteoric fluids.

The lack of evidence for a local intrusion, therefore, supports an orogenic Au genetic model. Orogenic Au deposits form as a result of diachronous consolidation and exhumation of the orogenic belt that produces crustal heating and large-scale fluid production (Bierlein et al., 2004). They often occur near second or third order compressional structures, near large scale and often transcrustal faults (Groves et al., 1998). Figure 27 shows how the generation of the faults in the 3Ace area occurred, and how they led to vein formation. One suggestion is that quartz veins formed as the result of extension fractures off Riedel shears which formed as the result of a rotating compressional regime bounded by the Hyland and March faults (Chris Buchanan, pers. comm.; Hodgson, 1989); however, the current orientation of the quartz veins does not fall within the correct orientation relative to the strike-slip faults for them to have formed this way. Therefore, we suggest that the quartz veins formed as the result of extension in the direction of the least compressive stress relative to the March and Hyland strike-slip faults. This structural regime could also account for the presence of concomitant shear and brittle fabrics, indicative of quartz vein formation within the brittle-ductile transition zone (Kerrick and Feng, 1992). These textures are also classic indicators of orogenic Au, whereas IRGD are generally associated with relatively more brittle structures (Groves et al., 2003) .

Vein formation follows what would be expected for an orogenic Au model where fluids are under pressure at depth. Sibson (2004) noted crack-seal and open-space fill textures indicate that tensile over-pressure conditions (where fluid pressures exceed the least compressive stress) were attained locally and resulted in flow through open fractures. Open space-filling textures are also found within the quartz veins of the Main Zone. In Sibson's model, fluids are over-pressured at the base of the crustal seismogenic zone which occupies the upper part of deforming crust in a sub-greenschist to mid-greenschist metamorphic environment and acts as an impermeable cap, resulting in a fault-activated 'valve' action for fluid release (Sibson, 1990). As the majority of

mineralization occurs within the more porous lithic arenites and QPC, it is also possible the phyllitic units acted as local impermeable barriers as well.

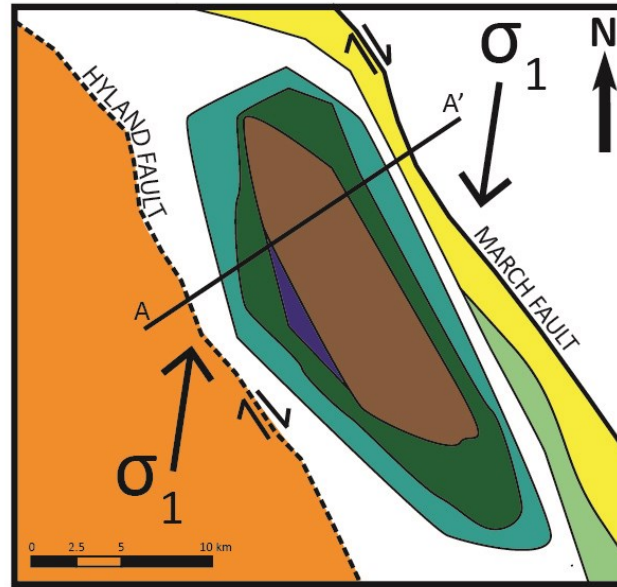
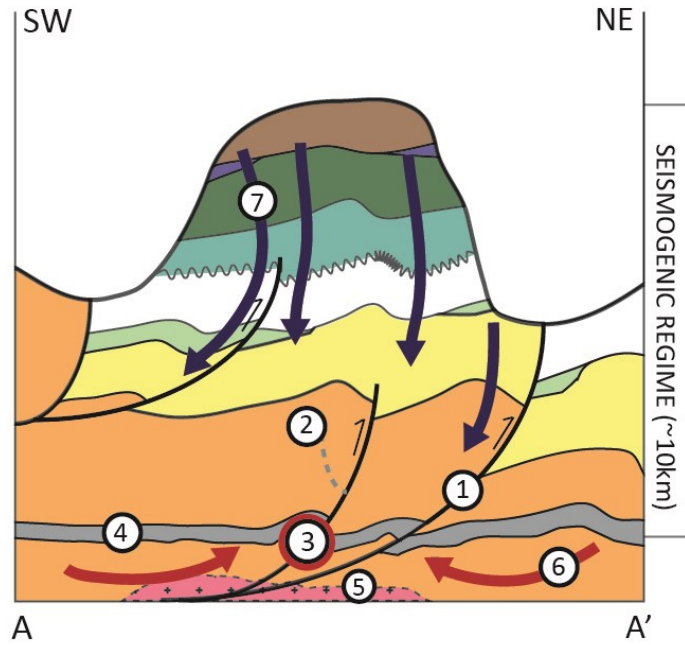
Sibson (1988) listed 5 requirements for fault-valve fluid release in orogenic terrains:

- 1) Prefailure: fluid pressure builds at depth below the seismogenic zone;
- 2) Seismogenic Fault Failure: fluid pressure exceeds lithostatic load, substantially reducing normal stress along pre-existing faults;
- 3) Postfailure Discharge: fluids under pressure at depth drain through the rupture zone and associated subsidiary fractures;
- 4) Self-Sealing: fractures are resealed by hydrothermal mineral precipitation along the rupture zone;
- 5) Repetition of Cycle: fluid pressure eventually rebuilds at depth, resulting in the repeating of the cycle.

Petrography of the quartz veins at the Main Zone shows that there were at least 2 cycles of fault-valve action, where Q1 represents cycle(s) occurring prior to Stage 2. Evidence of the first criterion, prefailure, is given by the initial high fluid pressures during Stage 4a, and declining pressures thereafter, assuming the initial pressures were higher than lithostatic pressures. The brittle-ductile transition zone occurs at depths between 8 and 12 km (Kerrick and Feng 1992). Assuming an average density of 2.7g/cm^3 for clastic sedimentary rocks (McCulloh, 1967), lithostatic pressures would range between 212 and 318 MPa at those depths. Fluid temperature, vein morphology, dominance of brittle structures, and sub-greenschist facies metamorphism indicates the veins formed at the shallow end of the brittle-ductile transition between 7.5 and 9 km depth (McCuaig and Kerrich, 1994; Groves et al., 2003). The condition of prefailure is therefore supported by several observations, as pressures at these shallower depths would have most likely been lower than the fluid pressures calculated from Type I and Type II fluid inclusions at the Main Zone and Sleeping Giant. Fault failure and the subsequent fluid discharge resulted in fracture propagation through pre-existing veins and faults, including 2nd and

3rd order splays. Mineralization occurred when pressurized and heated fluids at depth flowed through the re-opened fracture and veins, where they depressurized and mixed with meteoric fluids. There were at least 3 fluid pulses associated with the fluid release event associated with Au precipitation (Stages 4a, b and c). Fractures were then sealed by quartz precipitation and vein formation. The cycle does not appear to have repeated, at least to the same degree of stress release, after Au-mineralization. The ore-forming event resulted in extensive quartz veining and fracturing of pre-existing veins. There is no evidence of similar fracturing or wall-rock brecciation after Stage 4c. This correlates well with the Au mineralization occurring after peak metamorphism and during the waning stages of orogenic deformation.

A) Late Jurassic - Early Cretaceous



LEGEND

SEDIMENTARY ROCKS

- Earn Group
 - D_P Portrait Lake Formation
- Road River Group
 - S_S Steel Formation
 - OS_D Duo Lake Formation
- Unclassified Group
 - ϵ_{O_r} Rabbitkettle Formation
 - ϵ_G Gull Lake Formation
 - ϵ_S Sekwi Formation
- Hyland Group
 - PE_N Narchilla Formation
 - PE_V Vampire Formation
- P_{UPR} Undifferentiated Upper Paleozoic Rocks
- P_Y Yusezyu Formation

B) Mid-Cretaceous

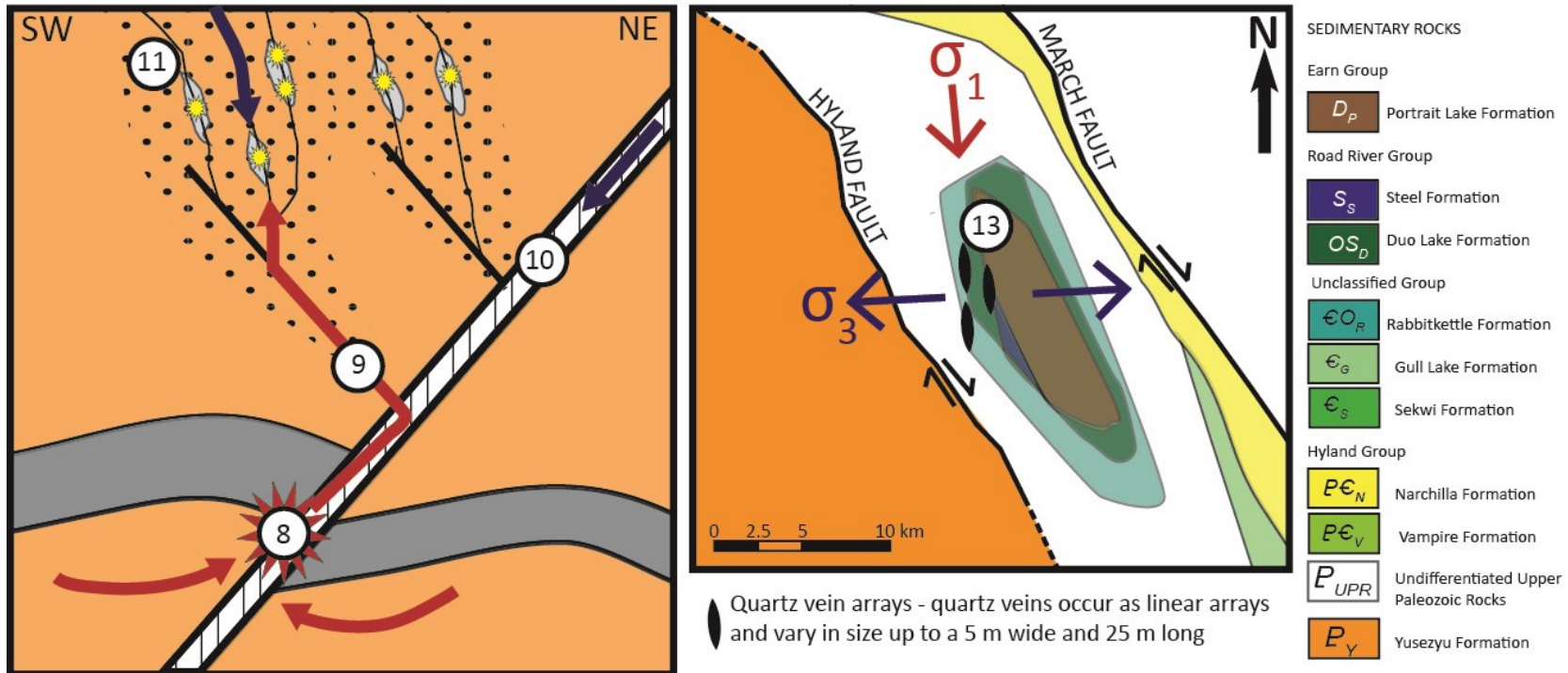


Figure 27. Diagrams of the genetic and structural models for the Main Zone area. Diagram A shows meteoric flow of water controlled in part by impermeable faults zones above the seismogenic regime, with several characteristics involved with vein formation: 1) reactivation of thrust faults as dextral faults; 2) secondary and third order splays form off the main fault zones; 3) intersection of the main fault system and the base of the seismogenic zone; 4) impermeable barrier, which possibly consists of phyllite; 5) possible pluton at depth supplied heat and/or fluid source; 6) heated and pressurized fluid flow below the impermeable barrier; and 7) connate or meteoric water interacted with wall-rock. Diagram B shows an enlarged view of the main fault rupture at the base of the seismogenic zone, where: 8) area where upwards fault propagation occurred; 9) pressurized, heated fluids then traveled upwards along the main fault, as well as secondary and third order splays; 10) fluids within the metasediments were focused downwards along the faults where they mixed with heated fluids and precipitated minerals within fractured quartz veins; and 11) alteration envelopes formed around the quartz veins as heated fluids penetrated and interacted with the wall-rock. Extension veins (12) formed parallel to the greatest compressive stress bound within the March and Hyland faults, and were eventually exposed by erosion.

CHAPTER 4: Conclusions

4.1 Sprogge

Radiogenic isotope data show the Sprogge quartz monzonite dikes range in age from 96 to 106 Ma. Whole-rock geochemical analyses indicate the quartz monzonite dikes at Sprogge are most similar to the Hyland plutonic suite (HPS) in age and oxidation state, but also they also share geochemical trace element characteristics with the Anvil plutonic suite (APS) and Tungsten plutonic suite (WPS) which indicate geochemical processes commonly associated with fertile magmas and Au mineralization. Both the HPS and WPS are present in the region. These results suggest that future exploration on the Sprogge claim blocks should focus on an intrusion-related Au model: especially in the Sugar Bowl, Matilda Vein and Meadow Zone prospects.

4.2 3Ace Au Mineralization

Au mineralization at 3Ace occurs along fractures within quartz veins hosted by sub-greenschist meta-sediments of the Yusezyu Formation. Petrography and geochemical analyses confirm that Au precipitated from acidic, low salinity, CO₂-rich fluids which consisted of a mixture of metamorphic and possible meteoric and magmatic waters at temperatures around 300°C. Estimated fluid pressures fluctuated from 300 MPa to 165 MPa at the Main Zone during the Au mineralizing stage; these variations indicate fault-valve action consistent with orogenic Au deposits. Au-mineralization at the Main Zone is not only orogenic in origin as opposed to intrusion-related; the fluids that precipitated Au likely included a significant sea-water sulfate source. A magmatic fluid contribution cannot be definitively confirmed, and as the rocks are neither hosted within, nor metamorphosed by, an igneous intrusion, the deposit is not likely to be intrusion-related.

Although a definitive age constraint could not be determined for Au mineralization, its relative timing has been determined with respect to the vein

forming events. Gold was previously thought to be coeval with arsenopyrite; however detailed petrography has shown that Au occurs along micro-fractures cross-cutting arsenopyrite. X-ray diffraction indicates alteration envelopes consist of intermediate argillic alteration and intense sericitization. The latter led to softening and increased porosity within 10-25 m of the quartz veins.

Structural controls indicate the mineralized veins opened as extensional fractures within a transpressional regime during the waning stages of orogenesis. Exploration within the area of the Main Zone should therefore be focused on quartz veins hosted by the Yusezyu Formation that have similar trends as those at the Main Zone and Sleeping Giant, instead of intrusions. Radiogenic isotope results, while not conclusive, possibly imply that mineralization at 3Ace occurred prior to the emplacement of the HPS and WPS, warranting further research. The wide range in conventional O and S isotope results suggest more than one fluid reservoir was tapped during the multiple stages of vein formation.

4.3 Implications for Exploration

Exploration at 3Ace should be based on an orogenic Au model within the Main Zone and Sleeping Giant areas. North-south striking quartz veins should be the main target as Au occurs along fractures within these veins. Fluid pressures and lithology at the Green Zone do not make it a favourable target, as fluids do not appear to have been under high enough pressure to effectively mobilize Au. The 3Ace vein sample, SCW11 F300, yielded a $\delta^{34}\text{S}$ result which was significantly lower than those of the other areas, and may yet support the existence of a pluton in the area, and therefore warrants further research. The XRD drill-hole study also shows a pattern of mineral zonation which corresponds with fluid temperature and mineralization. These results could be used along with hand-held XRF in the field or core shack as an exploration tool to isolate high grade Au mineralization.

References

Alm, E., Broman, C., Billstrom, K., Sundblad, K., & Torsander, P. (2003). Fluid characteristics and genesis of early Neoproterozoic orogenic gold-quartz veins in the Harnas area, southwestern Sweden. *Economic Geology And The Bulletin Of The Society Of Economic Geologists*, 98(7), 1311-1328.

Anderson, R. G. (1987). Plutonic rocks in the Dawson map area, Yukon Territory. *Paper - Geological Survey Of Canada*, 87-1A, 689-697.

Andrew, A., Godwin, C. I., & Sinclair, A. J. (1984). Mixing line isochrons; a new interpretation of galena lead isotope data from southeastern British Columbia. *Economic Geology And The Bulletin Of The Society Of Economic Geologists*, 79(5), 919-932.

Baker, T. (2002). Emplacement depth and carbon dioxide-rich fluid inclusions in intrusion-related gold deposits. *Economic Geology And The Bulletin Of The Society Of Economic Geologists*, 97(5), 1111-1117.

Baker, T., & Lang, J. R. (2001). Fluid inclusion characteristics of intrusion-related gold mineralization, Tombstone tungsten magmatic belt, Yukon Territory, Canada. *Mineralium Deposita*, 36(6), 563-582.

Beaudoin, G & Therrien, P. (2009) The updated web stable isotope fractionation calculator, *in Handbook of stable isotope analytical techniques*, Volume-II, ed. De Groot, P.A., Elsevier, 1120-1122.

Benning, L. G., & Seward, T. M. (1996). Hydrosulphide complexing of Au(I) in hydrothermal solutions from 150-400 degrees C and 500-1500 bar. *Geochimica Et Cosmochimica Acta*, 60(11), 1849-1871.

Bierlein, F. P., Arne, D. C., & Cartwright, I. (2004). Stable isotope (C, O, S) systematics in alteration haloes associated with orogenic gold mineralization in the Victorian gold province, SE Australia. *Geochemistry - Exploration, Environment, Analysis*, 4(3), 191-211.

Blevin, P. L., & Chappell, B. W. (1992). The role of magma sources, oxidation states and fractionation in determining the granite metallogeny of eastern Australia. *Special Paper - Geological Society Of America*, 272, 305-316.

Bodnar, R. J. (1983). A method of calculating fluid inclusion volumes based on vapor bubble diameters and P-V-T-X properties of inclusion fluids. *Economic Geology and The Bulletin of The Society of Economic Geologists*, 78(3), 535-542.

Bodnar, R. J. (1993). Revised equation and table for determining the freezing point depression of H (sub 2) O-NaCl solutions. *Geochimica Et Cosmochimica Acta*, 57(3), 683-684.

Bond, G. C., & Kominz, M. A. (1984). Construction of tectonic subsidence curves for the early Paleozoic miogeocline, southern Canadian Rocky Mountains; implications for subsidence mechanisms, age of breakup, and crustal thinning. *Geological Society Of America Bulletin*, 95(2), 155-173.

Brown, I. J., & Nesbitt, B. E. (1987). Gold-copper-bismuth mineralization in hedenbergitic skarn, Tombstone Mountains, Yukon. *Canadian Journal of Earth Science*, 24(12), 2362-2372.

Buchanan, C. (2010) *3Ace Property: summary of structural analysis*. Internal report prepared for Northern Tiger Resources

Burke, M., Hart, C. R., & Lewis, L. L. (2005). Models for epigenetic gold exploration in the northern Cordilleran Orogen, Yukon, Canada. *Proceedings Of The ... Biennial SGA Meeting, 8, Vol. 15*, 25-528.

Burt, E. A., & Taylor, H. r. (1993). Remarkably uniform bulk silicate delta (super 18) O values of terrigenous sedimentary rocks from the Central Appalachian and Ouachita geosynclines. *Abstracts With Programs - Geological Society Of America*, 25(6), 203-204.

Candela, P. A. (1989). Felsic magmas, volatiles, and metallogenesis. *Reviews In Economic Geology*, 42, 23-233.

Chapman, R. J., Mortensen, J. K., Crawford, E. C., & Lebarge, W. W. (2010). Microchemical studies of placer and lode gold in the Klondike District, Yukon, Canada; 1, Evidence for a small, gold-rich, orogenic hydrothermal system in the Bonanza and Eldorado Creek area. *Economic Geology And The Bulletin Of The Society Of Economic Geologists*, 105(8), 1369-1392.

Chapman, R., Mortensen, J., & LeBarge, W. P. (2011). Styles of lode gold mineralization contributing to the placers of the Indian River and Black Hills Creek, Yukon Territory, Canada as deduced from microchemical characterization of placer gold grains. *Mineralium Deposita*, 46(8), 881-903.

Chappell, B. W., & White, A. J. R. (2001). Two contrasting granite types: 25 years later. *Australian Journal of Earth Sciences*, 48(4), 489-499.

- Claypool, G. E., Holser, W. T., Kaplan, I. R., Sakai, H., & Zak, I. (1980). The age curves of sulfur and oxygen isotopes in marine sulfate and their mutual interpretation. *Chemical Geology*, *28*, 199-260.
- Confliffe, J., and Wilton, D. (2011) Fluid Inclusion Studies of Quartz Veins Associated with Gold Mineralization at the 3Ace Property, Southeastern Yukon, Internal Report submitted to Northern Tiger Resources by the CREAT Network, Memorial University of Newfoundland
- Coplen, T., Hopple, J., Bohlke, J., Peiser, H., Rieder, S., Krouse, H., ... & De Bievre, P. (2002) Compilation of minimum and maximum isotope ratios of selected elements in naturally occurring terrestrial materials and reagents. *US Geological Survey Water-Resources Investigations Report*, *98*, 01-4222.
- Coplen, T. B., Brand, W. A., Gehre, M., Gröning, M., Meijer, H. A., Toman, B., & Verkouteren, R. M. (2006). New guidelines for $\delta^{13}\text{C}$ measurements. *Analytical Chemistry*, *78*(7), 2439-2441.
- Corfu, F., Hanchar, J. M., Hoskin, P. O., & Kinny, P. D. (2003). Atlas of zircon textures. *Reviews In Mineralogy And Geochemistry*, *53*, 469-500.
- Craig, H. (1961). Isotopic variations in meteoric waters. *Science*, *133*(3465), 1702-1703.
- Dachille, F., Simons, P. Y., & Roy, R. (1968). Pressure-temperature studies of anatase, brookite, rutile and $\text{TiO}_2\text{-II}$. *American Mineralogist*, *53*, 1929-1939.
- Darling, R. S. (1991). An extended equation to calculate NaCl contents from final clathrate melting temperatures in $\text{H}_2\text{O-CO}_2\text{-NaCl}$ fluid inclusions;

implications for P-T isochore location. *Geochimica Et Cosmochimica Acta*, 55(12), 3869-3871.

Darling, R. S. (1991). An extended equation to calculate NaCl contents from final clathrate melting temperatures in H₂O-CO₂-NaCl fluid inclusions; implications for P-T isochore location. *Geochimica et Cosmochimica Acta*, 55(12), 3869-3871.

Deklerk, R. (compiler; 2003) Yukon MINFILE 2003 – A Database of Mineral Occurrences, Yukon Geological Survey, CDROM

Duan, Z., Moller, N., & Weare, J. W. (1995). Equation of state for the NaCl-H (sub 2) O-CO (sub 2) system; prediction of phase equilibria and volumetric properties. *Geochimica et Cosmochimica Acta*, 59(14), 2869-2882.

Evans, A. M. (1993). *Ore geology and industrial minerals; an introduction* *Geoscience texts*. United Kingdom: Blackwell Sci. Publ. : Oxford, United Kingdom.

Falck, H. H. (2007). Appendix 1, A review of the bedrock geology of the Nahanni River region and its context in the northern Cordillera. *Open-File 5344 Report - Geological Survey of Canada*, 327-365.

Fein, J. B., & Walther, J. V. (1987). Calcite solubility in supercritical CO (sub 2) -H (sub 2) O fluids. *Geochimica Et Cosmochimica Acta*, 51(6), 1665-1673.

Friedman, I., & Gleason, J. D. (1973). A new silicate reference standard for O 18 analysis. *Geochimica et Cosmochimica Acta*, 37(1), 180.

Gabrielse, H. (1967). Tectonic evolution of the northern Canadian Cordillera. *Canadian Journal of Earth Sciences*, 4(2), 271-298.

Gabrielse, H., & Yorath, C. J. (1991). Tectonic synthesis. *Geology of the Cordilleran Orogen in Canada. Edited by H. Gabrielse and CJ Yorath. Geological Survey of Canada, Geology of Canada, 4, 677-705.*

Giesemann, A., Jäger, H. J., Norman, A. L., Krouse, H. R., & Brand, W. A. (1994). Online sulfur-isotope determination using an elemental analyzer coupled to a mass spectrometer. *Analytical Chemistry, 66(18), 2816-2819.*

Godwin, C. I., & Sinclair, A. J. (1982). Average lead isotope growth curves for shale-hosted zinc-lead deposits, Canadian Cordillera. *Economic Geology And The Bulletin Of The Society Of Economic Geologists, 77(3), 675-690.*

Goldfarb, R. J., Snee, L. W., & Pickthorn, W. J. (1993). Orogenesis, high-T thermal events, and gold vein formation within metamorphic rocks of the Alaskan Cordillera. *Mineralogical Magazine, 57(388), 375-394.*

Gordey, S. P., & Anderson, R. G. (1993). Evolution of the northern Cordilleran miogeocline, Nahanni map area [105I], Yukon and Northwest Territories. *Memoir - Geological Survey Of Canada, 428*

Gordey, S. P., Abbott, J. G., Tempelman-Kluit, D. J., & Gabrielse, H. H. (1987). 'Antler' clastics in the Canadian Cordillera. *Geology, 15(2), 103-107.*

Grassineau, N. V., Matthey, D. P., & Lowry, D. (2001). Sulfur isotope analysis of sulfide and sulfate minerals by continuous flow-isotope ratio mass spectrometry. *Analytical Chemistry, 73(2), 220-225.*

Groves, D. I., Goldfarb, R. J., Gebre-Mariam, M. M., Hagemann, S. G., & Robert, F. F. (1998). Orogenic gold deposits; a proposed classification in the context of their crustal distribution and relationship to other gold deposit types. *Ore Geology Reviews*, 13(1-5), 7-27.

Groves, D. I., Goldfarb, R. J., Robert, F., & Hart, C. R. (2003). Gold deposits in metamorphic belts; overview of current understanding, outstanding problems, future research, and exploration significance. *Economic Geology and The Bulletin of The Society Of Economic Geologists*, 98(1), 1-29.

Hart, C. R., Mair, J. L., Goldfarb, R. J., & Groves, D. I. (2004a). Source and redox controls on metallogenic variations in intrusion-related ore systems, Tombstone-Tungsten Belt, Yukon Territory, Canada. *Transactions of The Royal Society of Edinburgh: Earth Sciences*, 95, 339-356.

Hart, C. J., Goldfarb, R. J., Lewis, L. L., & Mair, J. L. (2004b). The Northern Cordilleran Mid-Cretaceous Plutonic Province: Ilmenite/Magnetite-series Granitoids and Intrusion-related Mineralisation. *Resource Geology*, 54(3), 253-280.

Hart, C. J., & Lewis, L. L. (2005). Gold mineralization in the upper Hyland River area: A non-magmatic origin. In: *Yukon Exploration and Geology*, Edited by D.S. Emond, G.D. Bradshaw, L.L. Lewis and L.H. Weston, Yukon Geological Survey, 109-125.

Heffernan, S., & Mortensen, J. K. (1999). Age, geochemical and metallogenic investigations of Cretaceous intrusions in southeastern Yukon and southwestern NWT: A preliminary report. In: *Yukon Exploration and Geology 1999*, Edited by

D.S. Emond and L.H. Weston, *Exploration and Geological Services Division, Yukon, Indian and Northern Affairs Canada*, 145-149.

Heffernan, R. S. (2004). *Temporal, geochemical, isotopic, and metallogenic studies of mid-Cretaceous magmatism in the Tintina Gold Province, southeastern Yukon and southwestern Northwest Territories, Canada* (MSc dissertation, University of British Columbia).

Hodgson, C. J. (1989). The structure of shear-related, vein-type gold deposits: a review. *Ore Geology Reviews*, 4(3), 231-273.

Ishihara, S. (1977). The magnetite-series and ilmenite-series granitic rocks. *Kozan Chishitsu = Mining Geology*, 27(5), 293-305.

Jackson, S. E., Pearson, N. J., Griffin, W. L., & Belousova, E. A. (2004). The application of laser ablation-inductively coupled plasma-mass spectrometry to in situ U–Pb zircon geochronology. *Chemical Geology*, 211(1), 47-69.

Jia, Y., Kerrich, R., & Goldfarb, R. (2003). Metamorphic origin of ore-forming fluids for orogenic gold-bearing quartz vein systems in the North American Cordillera: Constraints from a reconnaissance study of $\delta^{15}\text{N}$, δD , and $\delta^{18}\text{O}$. *Economic Geology*, 98(1), 109-123.

Jones, M., & Caulfield, D. (1999). The Fer property: A plutonic-related gold property in southeastern Yukon. In: *Yukon Exploration and Geology*, Edited by D.S. Emond and L.H. Weston, *Exploration and Geological Services Division, Yukon, Indian and Northern Affairs Canada*, 229-236.

Kerrick, R. R., & Feng, R. R. (1992). Archean geodynamics and the Abitibi-Pontiac collision; implications for advection of fluids at transpressive collisional boundaries and the origin of giant quartz vein systems. *Earth-Science Reviews*, 32(1-2), 33-60.

Kerridge, J. F., Haymon, R. M., & Kastner, M. (1983). Sulfur isotope systematics at the 21 N site, East Pacific Rise. *Earth and Planetary Science Letters*, 66, 91-100.

Kohn, M. J., Riciputi, L. R., Stakes, D., & Orange, D. L. (1998). Sulfur isotope variability in biogenic pyrite: Reflections of heterogeneous bacterial colonization?. *American Mineralogist*, 83, 1454-1468.

Kontak, D. J., & Kyser, K. (2011). A fluid inclusion and isotopic study of an intrusion-related gold deposit (IRGD) setting in the 380 Ma South Mountain Batholith, Nova Scotia, Canada: evidence for multiple fluid reservoirs. *Mineralium Deposita*, 46(4), 337-363.

Lenz, A. C. (1972). Ordovician to Devonian history of northern Yukon and adjacent District of Mackenzie. *Bulletin of Canadian Petroleum Geology*, 20(2), 321-361.

Ligang, Z., Jingxiu, L., Huanbo, Z., & Zhensheng, C. (1989). Oxygen isotope fractionation in the quartz-water-salt system. *Economic Geology*, 84(6), 1643-1650.

Mair, J. L., Hart, C. J., & Stephens, J. R. (2006). Deformation history of the northwestern Selwyn Basin, Yukon, Canada: Implications for orogen evolution and mid-Cretaceous magmatism. *Geological Society of America Bulletin*, 118(3-4), 304-323.

- Mair, J. L., Goldfarb, R. J., Johnson, C. A., Hart, C. J., & Marsh, E. E. (2006). Geochemical constraints on the genesis of the Scheelite Dome intrusion-related gold deposit, Tombstone gold belt, Yukon, Canada. *Economic Geology*, *101*(3), 523-553.
- Marsh, E. E., Goldfarb, R. J., Hart, C. J., & Johnson, C. A. (2003). Geology and geochemistry of the Clear Creek intrusion-related gold occurrences, Tintina Gold Province, Yukon, Canada. *Canadian Journal of Earth Sciences*, *40*(5), 681-699.
- Matsuhisa, Y., Goldsmith, J. R., & Clayton, R. N. (1979). Oxygen isotopic fractionation in the system quartz-albite-anorthite-water. *Geochimica et cosmochimica acta*, *43*(7), 1131-1140.
- Mayer, B., & Krouse, H. R. (2004). Procedures for sulfur isotope abundance studies. *Handbook of stable isotope analytical techniques*, Edited by de Groot, P., *1*, 538-596.
- McCoy, D.T., Newberry, R.J., Layer, P.W., DiMarchi, J.J., Bakke, A., Masterman, J.S., Minehane, D.L. (1997). Mineral deposits of Alaska. *Economic Geology Monograph 9*, 151–190.
- McCulloh, T. H. (1967). *Mass properties of sedimentary rocks and gravimetric effects of petroleum and natural-gas reservoirs*. US Government Printing Office.
- Nesbitt, B. E., Muehlenbachs, K., & Murowchick, J. B. (1989). Genetic implications of stable isotope characteristics of mesothermal Au deposits and related Sb and Hg deposits in the Canadian Cordillera. *Economic Geology*, *84*(6), 1489-1506.

Ohmoto, H. (1972). Systematics of sulfur and carbon isotopes in hydrothermal ore deposits. *Economic Geology*, 67(5), 551-578.

Ohmoto, H., & Felder, R. P. (1987). Bacterial activity in the warmer, sulphate-bearing, Archaean oceans. *Nature*, 328(6127), 244-246.

Ohmoto, H., & Goldhaber, M. B. (1997). Sulfur and carbon isotopes. *Geochemistry of hydrothermal ore deposits*, 3, 517-612.

Panagapko, D. (2012). *Gold – 2012 Annual Review*. Natural Resources Canada

Pigage, L. C., & Anderson, R. G. (1985). The Anvil plutonic suite, Faro, Yukon Territory. *Canadian Journal of Earth Sciences*, 22(8), 1204-1216.

Poulson, S. R. (2005). The effect of sulfate- $\delta^{18}\text{O}$ upon on-line sulfate- $\delta^{34}\text{S}$ analysis, and implications for measurements of $\delta^{33}\text{S}$ and $\Delta^{33}\text{S}$. *Rapid communications in mass spectrometry*, 19(2), 105-107.

Qi, H. P., & Coplen, T. B. (2003). Evaluation of the $^{34}\text{S}/^{32}\text{S}$ ratio of Soufre de Lacq elemental sulfur isotopic reference material by continuous flow isotope-ratio mass spectrometry. *Chemical Geology*, 199(1-2), 183-187.

Rainbird, R. H., McNicoll, V. J., Theriault, R. J., Heaman, L. M., Abbott, J. G., Long, D. G. F., & Thorkelson, D. J. (1997). Pan-continental river system draining Grenville Orogen recorded by U-Pb and Sm-Nd geochronology of Neoproterozoic quartzarenites and mudrocks, northwestern Canada. *The Journal of Geology*, 105(1), 1-17.

Ramboz, C., Pichavant, M., & Weisbrod, A. (1982). Fluid immiscibility in natural processes: use and misuse of fluid inclusion data: II. Interpretation of fluid inclusion data in terms of immiscibility. *Chemical Geology*, 37(1), 29-48.

Rasmussen, K. L., Mortensen, J. K., & Falck, H. (2005). Geochronological and litho-geochemical studies of intrusive rocks in the Nahanni region, southwestern Northwest Territories and southeastern Yukon. *Yukon Exploration and Geology*, 2006, 287-298.

Reed, M. H. (1997). Hydrothermal alteration and its relationship to ore fluid composition. *Geochemistry of Hydrothermal Ore Deposits*, 3, 303-365.

Rodionov, N. V., Belyatsky, B. V., Antonov, A. V., Kapitonov, I. N., & Sergeev, S. A. (2012). Comparative in-situ U–Th–Pb geochronology and trace element composition of baddeleyite and low-U zircon from carbonatites of the Palaeozoic Kovdor alkaline–ultramafic complex, Kola Peninsula, Russia. *Gondwana Research*, 21(4), 728-744.

Roedder, E. (1984). Fluid inclusions. *Reviews In Mineralogy*, 12

Roedder, E., & Bodnar, R. J. (1980). Geologic pressure determinations from fluid inclusion studies. *Annual Review of Earth and Planetary Sciences*, 8, 263.

Rollinson, H. R. (1993). *Using geochemical data; evaluation, presentation, interpretation*. United Kingdom: Longman Scientific & Technical : Harlow, United Kingdom.

Rosenbaum, J., & Sheppard, S. M. F. (1986). An isotopic study of siderites, dolomites and ankerites at high temperatures. *Geochimica et Cosmochimica Acta*, 50(6), 1147-1150.

Rye, R. O., & Ohmoto, H. (1974). Sulfur and carbon isotopes and ore genesis: a review. *Economic Geology*, 69(6), 826-842.

Schandl, E. S., Gorton, M. P., & Davis, D. W. (1994). Albitization at 1700 ± 2 Ma in the Sudbury-Wanapitei Lake area, Ontario: implications for deep-seated alkalic magmatism in the Southern province. *Canadian Journal of Earth Sciences*, 31(3), 597-607.

Scott, E. (1999). *1998 Geological and Geochemical assessment report of the Sprogge Project*. Report prepared for the Yukon Geological Survey by Battle Mountain Canada Ltd.

Sears, J. W., & Price, R. A. (2000). New look at the Siberian connection: no SWEAT. *Geology*, 28(5), 423-426.

Segnit, E. R., Holland, H. D., & Biscardi, C. J. (1962). The solubility of calcite in aqueous solutions—I The solubility of calcite in water between 75° and 200° at CO₂ pressures up to 60 atm. *Geochimica et Cosmochimica Acta*, 26(12), 1301-1331.

Selby, D., Creaser, R. A., Heaman, L. M., & Hart, C. R. (2003). Re-Os and U-Pb geochronology of the Clear Creek, Dublin Gulch, and Mactung deposits, Tombstone gold belt, Yukon, Canada; absolute timing relationships between plutonism and mineralization. *Canadian Journal Of Earth Sciences = Revue Canadienne Des Sciences De La Terre*, 40(12), 1839-1852.

Seward, T. M. (1993). The hydrothermal geochemistry of gold. In *Gold metallogeny and exploration*, Edited by Foster, R.P., 34-62

Shenberger, D., & Barnes, H. L. (1989). Solubility of gold in aqueous sulfide solutions from 150 to 350 C. *Geochimica et Cosmochimica Acta*, 53(2), 269-278.

Shepherd, T. J., Rankin, A. H., & Alderton, D. H. M. (1985). *A practical guide to fluid inclusion studies*, 239, Glasgow: Blackie.

Sheppard, S. M. (1986). Characterization and isotopic variations in natural waters. *Reviews in Mineralogy and Geochemistry*, 16(1), 165-183.

Sibson, R. H. (1990). Conditions for fault-valve behaviour. *Geological Society, London, Special Publications*, 54(1), 15-28.

Sibson, R. H. (2004). Controls on maximum fluid overpressure defining conditions for mesozonal mineralisation. *Journal of Structural Geology*, 26(6), 1127-1136.

Simonetti, A., Heaman, L. M., Hartlaub, R. P., Creaser, R. A., MacHattie, T. G., & Böhm, C. (2005). U–Pb zircon dating by laser ablation-MC-ICP-MS using a new multiple ion counting Faraday collector array. *Journal of Analytical Atomic Spectrometry*, 20(8), 677-686.

Stacey, J. T., & Kramers, J. (1975). Approximation of terrestrial lead isotope evolution by a two-stage model. *Earth and Planetary Science Letters*, 26(2), 207-221.

Stephens, J. R., Mair, J. L., Oliver, N. H., Hart, C. J., & Baker, T. (2004). Structural and mechanical controls on intrusion-related deposits of the Tombstone Gold

Belt, Yukon, Canada, with comparisons to other vein-hosted ore-deposit types. *Journal of Structural Geology*, 26(6), 1025-1041.

Streckeisen, A. (1974). Classification and nomenclature of plutonic rocks recommendations of the IUGS subcommission on the systematics of Igneous Rocks. *Geologische Rundschau*, 63(2), 773-786.

Taylor Jr, H. P. (1997). Oxygen and hydrogen isotope relationships in hydrothermal mineral deposits. *Geochemistry of Hydrothermal Ore Deposits*, 3, 229-302.

Tera, F., & Wasserburg, G. J. (1972). U-Th-Pb systematics in three Apollo 14 basalts and the problem of initial Pb in lunar rocks. *Earth and Planetary Science Letters*, 14(3), 281-304.

Waseda, Y., Matsubara, E., & Shinoda, K. (2011). *X-ray diffraction crystallography: introduction, examples and solved problems*. Springer.

Wentworth, C. K. (1922). A scale of grade and class terms for clastic sediments. *Journal of Geology*, 30(5), 377-392.

Wilkinson, J. J., & Johnston, J. D. (1996). Pressure fluctuations, phase separation, and gold precipitation during seismic fracture propagation. *Geology*, 24(5), 395-398.

Winter, J. D. (2010). *Principles of igneous and metamorphic petrology* (Vol. 2). New York: Prentice Hall.

Zotov, A., Mukhamet-Galeev, A., & Schott, J. (1998). An experimental study of kaolinite and dickite relative stability at 150-300 C and the thermodynamic properties of dickite. *American Mineralogist*, 83, 516-524.

Internet Resources:

America's Bullion Royalty Corp: <http://www.aubullion.com/Brewery-Creek.html>
[December, 2013]

Berkeley Geochronology Centre: http://www.bgc.org/isoplot_etc/isoplot.html
[March, 2014]

Computer Modelling, Fluid Inclusion Laboratory Leoben:
<http://fluids.unileoben.ac.at/Computer.html> [March, 2014]

Northern Tiger Resources: <http://www.northern-tiger.com/s/3Ace.asp> [March, 2014]

Victoria Gold Corp:
http://www.vitgoldcorp.com/s/dublin_gulch.asp?ReportID=534835 [December, 2013]

APPENDIX A

Drill collar and sample locations

All coordinates are expressed within UTM NAD 83 Zone 9

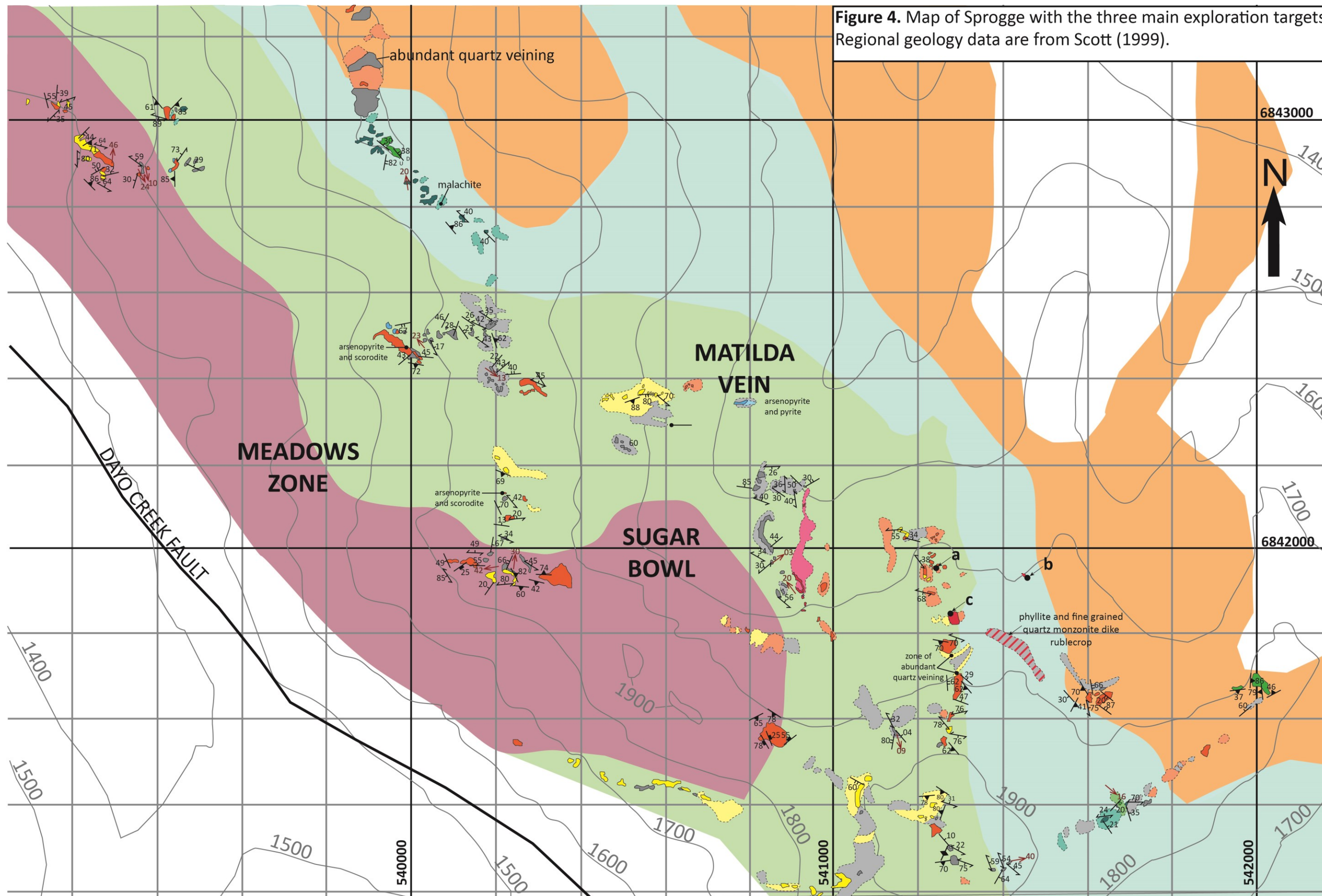


Figure 4. Map of Sprogge with the three main exploration targets. Regional geology data are from Scott (1999).

LEGEND

- Cretaceous Intrusive**
- K_{qm} - (biotite) quartz monzonite dike outcrop, inferred
- PreCambrian Unclassified Sediments**
- pC_{uc}4 - sandstone, conglomerate with minor shale, siltstone
 - pC_{uc}3 - interbedded sandstone, calcareous siltstone, limestone, and calcareous phyllite
 - pC_{uc}2 - interbedded phyllite, sandstone, and conglomerate; minor calcareous shale
 - pC_{uc}1 - quartz-pebble-conglomerate and sandstone with with siltstone, shale interbeds
- Sample locations and corresponding samples**
- a** - SCW11 F165, F166, F168
 - b** - SCW11 F180
 - c** - SCW11 F211, F212, F215
- Structural Symbols**
- bed strike and dip
 - foliation strike and dip
 - quartz vein strike and dip
 - vertical quartz vein
 - fault strike and dip
 - lateral direction of fault movement
 - vertical direction of fault movement (U=up, D=down)
 - joint strike and dip
 - Fold axis dip direction and dip
- Contours are every 100 m ASL

Drill Collar Coordinates and Elevations

Area	Hole Number	Easting (m)	Northing (m)	Elevation (m)
Main Zone	3A 10 001	0533685	6843878	1557
Main Zone	3A 10 002	0533677	6843817	1548
Main Zone	3A 10 003	0533677	6843817	1548
Main Zone	3A 11 010	0533715	6843826	1567
Main Zone	3A 11 010A	0533715	6843826	1567
Main Zone	3A 11 011	0533710	6843876	1559
Main Zone	3A 11 014	0533675	6843984	1551
Main Zone	3A 11 015A	0533723	6843902	1556
Main Zone	3A 11 016	0533723	6843902	1556
Green Zone	3A 11 022	0533366	6845919	1808
Green Zone	3A 11 023	0533366	6845919	1808

Field Sample Coordinates

Map Name	Sample ID (SCW 11 FXXX)	Easting (m)	Northing (m)	Elevation (m)
3Ace	300	0528143	6853585	2069
Main Zone	026	0533658	6843813	1525
Main Zone	027	0533658	6843813	1525
Main Zone	028	0533658	6843813	1525
Main Zone	030	0533658	6843813	1525
Main Zone	033	0533658	6843807	1525
Main Zone	034	0533658	6843807	1525
Main Zone	035	0533658	6843807	1525
Main Zone	036	0533658	6843807	1525
Main Zone	037	0533658	6843807	1525
Main Zone	038	0533658	6843807	1525
Main Zone	057	0533658	6843813	1525
Main Zone	070	0533654	6843830	-
Main Zone	081	0533654	6843833	-
Main Zone	100	0533636	6843883	-
Main Zone	133	0533657	6843810	1525
Main Zone	134	0533658	6843813	1525
Main Zone	135	0533658	6843813	1525
Main Zone	208	0533658	6843814	1525
Sleeping Giant	137	0534591	6844169	1256
Sleeping Giant	140	0534569	6844279	1286
Sleeping Giant	141	0534570	6844273	1280
Sleeping Giant	143	0534568	6844277	1284
Green Zone	152	0533294	6845893	1777
Green Zone	154	0533319	6845906	1792
Green Zone	160	0533076	6845926	1668
Sprogge	165	0541241	6841946	1719
Sprogge	166	0541241	6841946	1719
Sprogge	167	0541241	6841946	1719
Sprogge	168	0541241	6841946	1719
Sprogge	171	0541241	6841939	1718
Sprogge	172	0541241	6841939	1718
Sprogge	173	0541241	6841939	1718
Sprogge	180	0541450	6841919	1705
Sprogge	181	0541450	6841919	1705
Sprogge	211	0541266	6841839	1738
Sprogge	212	0541266	6841839	1738
Sprogge	213	0541266	6841839	1738
Sprogge	214	0541266	6841839	1738
Sprogge	215	0541266	6841839	1738

APPENDIX B

EPMA Data (all units are in %)

Note: for all samples containing considerable peaks, any reported Au values are anomalous due to a peak overlap between Zn and Au.

Silicate Data: all values are in percentages (%)

Sample ID	Al	As	Ca	Cl	Cr	F	Fe	K	Mg	Mn	Na	P	Si	S	Ti	O	Total
11-22 50.6a-1	0.11	32.76					23.66	0.01		0.01	0.01	0.33	0.04	0.19		21.41	78.50
11-22 50.6a-2	0.15	31.91					25.30	0.01		0.03	0.02	0.23	0.02	0.28		21.84	79.79
11-22 50.6a-3	0.08	24.49	0.01				20.06	0.05		0.01	0.03	0.17	14.51	0.21		32.93	91.65
11-22 50.6a-4	0.11	33.23	0.01		0.02		25.18	0.02		0.01	0.01	0.16	0.12	0.24		22.16	81.26
11-22 50.6a-5	0.11	27.46			0.02		22.06	0.02		0.01	0.02	0.58	7.50	0.24	0.01	27.94	85.97
11-22 50.6a-6	0.08	31.62	0.01				24.78	0.01		0.01	0.01	0.22	0.07	0.26	0.01	21.50	78.55
11-22 50.6a-7	18.38						0.32	6.33	0.80				22.84		0.09	44.33	92.84
11-22 50.6a-8	4.53	25.03	0.01				20.83	1.61		0.02	0.06	0.27	4.38	0.22	0.10	26.39	82.54
11-22 50.6a-9	0.31	32.24	0.01		0.01		23.42	0.11				0.24	0.29	0.33		21.67	78.62
11-22 50.6a-10	0.54	3.16	0.04		0.01		7.19	0.77			0.06	0.08	12.01	0.62	0.03	19.18	43.64
11-10 39.15a-2	0.07		37.61		0.02		0.05	0.05	0.02	0.01		17.54	0.92		0.01	38.85	95.16
11-10 39.15a-3	0.02	0.04	0.01				0.03						47.11		0.01	53.72	100.94
11-10 39.15a-4	0.04	0.03	38.36				0.05	0.03	0.02			17.80	0.05	0.01		38.45	94.85
11-10 39.15a-5	0.45		0.03				0.02	0.16	0.01		0.01		46.52		0.02	53.46	100.66
11-10 39.15a-6	19.18		0.02		0.02		0.48	5.95	0.26		0.42	0.01	21.51	0.01	0.50	43.67	91.95
11-10 39.15a-7	0.19	0.01	0.03				0.05	0.03			0.02		46.82		0.02	53.56	100.71
11-10 39.15a-8	0.06		38.64				0.04	0.11	0.01			18.28	0.12	0.01	0.10	39.32	96.64
11-10 39.15a-9	14.71		0.08		0.01		0.89	3.07	0.23	0.01	0.22	0.02	18.05		2.18	36.41	75.85
11-10 39.15a-10	14.10		10.97		0.01		0.23	2.61	0.11	0.03	0.16	4.96	15.42	0.03	0.04	41.73	90.37
11-10 39.15b-1	0.03	0.02	0.05				0.20	0.05					0.02		60.08	40.30	100.73
11-10 39.15b-2	0.24	0.06	0.07		0.02		0.51	0.05		0.01			16.61		0.48	19.41	36.83
11-10 39.15b-3	0.49	0.01	39.22		0.02		0.03	0.20	0.02	0.02		18.09	0.33	0.01	0.03	39.95	98.41
11-10 39.15b-4	14.81		0.16				0.49	4.61	0.24		0.22	0.07	26.87		0.09	45.39	92.91
11-10 39.15b-5	17.45	0.03	2.65				1.15	0.71	0.06	0.01	0.07	1.65	20.11	0.01	0.54	42.72	87.14

Silicate Data—continued

Sample ID	Al	As	Ca	Cl	Cr	F	Fe	K	Mg	Mn	Na	P	Si	S	Ti	O	Total
11-10 39.15b-6	19.93		0.03				0.55	6.05	0.29	0.01	0.28		22.19	0.01	0.12	44.86	94.23
11-10A 45.55b-1	0.06	0.02	25.24				3.14	0.01	0.01		0.02		0.06	13.78		25.30	67.63
11-10A 45.55b-2	0.07	0.04	0.01				0.03	0.01	0.01		0.01		47.11			53.77	101.05
11-10A 45.55c-1	0.18	0.08	0.13				1.44			0.03		0.55	14.00	0.54	0.05	17.95	34.52
11-10A 45.55c-2		0.08			0.03		0.08	0.01					17.11	0.01	0.01	18.38	34.36
11-10A 45.55c-3	4.02		0.02		0.02		7.41	0.28	2.01	0.05	0.01	0.01	34.77	0.04		47.84	96.47
11-10A 45.55c-4	10.74		0.29		0.03		20.59	0.01	5.37	0.18	0.03	0.01	14.95	0.08	0.04	39.30	91.62
11-10A 45.55c-5	9.30						6.13	0.27	1.22	0.02	0.60	0.05	24.80	0.22	0.01	41.50	83.64
11-10A 45.55c-6	10.39		0.02				0.03	0.02		0.01	5.66		32.21			47.94	96.27
11-10A 45.55c-7	0.03		0.01				0.26	0.01	0.01		0.01	0.01	0.06	0.01	59.92	40.29	100.62
11-10A 45.55c-8	9.19		0.02		0.05		0.45	2.77	0.26		0.20		8.96	0.05	37.05	44.20	103.11
11-10A 45.55c-9	18.86		0.04		0.01		0.87	6.55	0.38	0.01	0.36		22.31	0.01	0.07	44.33	93.66
11-10A 46.43a-1	0.04		0.14				42.70	0.02	0.27	0.52	0.04	0.01	0.88	0.05		19.77	64.18
11-10A 46.43a-2	10.29		0.05				3.45	4.53	0.48		0.33	0.01	9.21	0.02	0.09	22.48	50.53
11-10A 46.43a-3	12.77		0.05		0.01		24.89	0.01	4.74	0.10			11.01	0.02	0.02	37.82	91.44
11-10A 46.43a-4	0.02	0.06	0.02				0.20	0.01					17.16	0.02	0.01	18.49	34.60
11-10A 46.43a-5	16.28	0.07	0.10		0.01		9.49	6.35	0.24	0.11	0.23	0.03	18.05	0.02	0.36	41.07	92.40
11-10A 46.43a-6	3.90	0.03	0.08				1.00	0.90	0.06	0.03			18.31	0.01	0.04	24.52	48.19
11-10A 46.43a-7	17.92		0.09		0.04		4.53	4.67	0.41	0.06	0.26	0.01	20.40	0.01	0.13	42.60	91.00
11-10A 46.43a-8	0.03	0.02	0.02		0.01		0.05	0.01					47.36			54.00	101.47
11-10A 46.43b-1	0.03	0.03	0.03				0.25	0.04					0.03	0.02	59.68	40.09	100.19
11-10A 46.43b-2	8.75		0.06				0.59	2.89	0.35		0.23	0.01	30.81		0.05	44.06	87.67
11-10A 46.43b-3	21.25		0.06				0.24	0.05	0.08	0.01	0.02	0.01	22.85	0.01		45.16	89.72
11-10A 46.43b-4	0.62	0.04	0.49		0.03		0.51	0.11	0.05	0.01		0.17	15.18	0.04	0.04	18.48	35.34

Silicate Data—continued

Sample ID	Al	As	Ca	Cl	Cr	F	Fe	K	Mg	Mn	Na	P	Si	S	Ti	O	Total
11-10A 46.43b-5	1.74		0.01				2.70	0.11	0.55	0.01	0.01		43.15	0.01	0.01	52.19	100.25
11-10A 46.43b-6	2.89		0.08		0.05		2.73	1.09	0.13		0.11	0.02	3.91	0.02	41.63	36.47	89.12
11-10A 46.43b-7	0.26	0.03	0.06		0.09		0.23	0.07	0.01	0.01	0.01		0.54		58.44	40.10	99.86
11-10A 46.43b-8	12.31		0.01		0.01		23.22	0.01	5.66	0.20	0.04		11.42	0.01	1.26	38.61	92.77
11-10A 46.43b-9	0.12	0.01					0.01	0.04	0.01			0.01	47.07		0.01	53.74	100.99
11 F035-1_A_1	17.38		0.01		0.01	0.44	0.66	7.71	1.03	0.03	0.16		21.77		0.09	42.85	92.13
11 F035-1_A_2	17.48		0.01			0.39	0.64	6.69	0.93	0.01	0.11		22.23		0.09	43.17	91.77
11 F035-1_A_3	17.41			0.01	0.01	0.35	0.64	8.11	0.90		0.16		21.77		0.07	42.83	92.25
11 F035-1_A_4	16.64				0.03	0.51	0.90	7.88	1.04	0.02	0.10		22.20		0.09	42.78	92.18
11 F035-1_A_5	17.35		0.04	0.03		0.52	0.67	7.70	0.90	0.02	0.14		22.03		0.10	43.07	92.57
11-14 13617-3_A_1	12.27		0.13		0.02	0.28	22.75	0.01	6.02	0.22	0.02		11.90			35.09	88.71
11-14 13617-3_A_2	11.99		0.08		0.02	0.28	23.58		6.04	0.24			11.57		0.02	34.71	88.52
11-14 13617-3_A_3	11.53		0.18		0.01	0.31	22.02		6.59	0.24	0.01		11.39			34.04	86.34
11-14 13617-3_A_4	1.34		0.25	0.01	0.01	0.25	33.81	0.01	7.84	0.25	0.06		1.29			17.71	62.81
11-14 13617-3_A_5	19.63		0.07			0.12	0.42	0.07	0.12	0.03	0.01		22.05			42.86	85.39
11-14 13617-3_A_6	19.40		0.08	0.02		0.24	0.63	0.07	0.20	0.02	0.02		21.97			42.68	85.34
11-14 13617-3_A_7	20.17		0.04	0.02		0.16	0.43	0.02	0.04		0.01		22.51		0.01	43.78	87.18
11-14 13617-3_A_8	0.02		0.19		0.01	0.24	34.76	0.01	8.32	0.83	0.06		0.01		0.01	15.81	60.26
11-14 13617-3_A_9	11.91		0.02			0.30	23.70		5.93	0.18			11.69		0.02	34.69	88.45
11-14 13617-3_A_10	12.70		0.03	0.02		0.39	20.19		5.85	0.22	0.01		12.86			35.67	87.94
11-14 13617-3_A_11	11.96		0.02			0.31	24.15		5.99	0.20	0.01		11.70		0.03	34.93	89.30
11-14 13617-3_B_11	12.13					0.34	23.68		6.24	0.21			11.62		0.01	35.01	89.25
11-14 13617-3_B_12	11.78		0.03	0.01		0.35	23.73	0.01	6.08	0.20	0.02		11.49		0.01	34.46	88.17
11-11 83.08a-1	2.52	4.05	0.03				4.73	0.77			0.12	0.03	35.57	0.15	0.03	45.81	93.77

Silicate Data—continued

Sample ID	Al	As	Ca	Cl	Cr	F	Fe	K	Mg	Mn	Na	P	Si	S	Ti	O	Total
11-11 83.08a-2	1.49	0.70	0.02				0.95	0.54	0.03		0.06	0.02	42.36	0.04	0.01	50.31	96.52
11-11 83.08a-3	3.26	0.48	0.02		0.01		0.56	0.56	0.07		0.04	0.01	38.16	0.04	0.06	46.96	90.22
11-11 83.08a-4	14.29		0.02		0.10		1.33	5.99	1.13	0.01	0.27	0.01	18.34		8.24	41.55	91.04
11-11 83.08a-5	11.53	0.08	0.02		0.09		0.53	4.51	0.40		0.19	0.19	12.68	0.03	21.78	41.01	93.04
11-11 83.08a-6	9.50	4.27	0.02		0.07		4.23	3.83	0.26		0.10	0.01	11.02	2.13	9.14	32.86	77.43
11-11 83.08a-7	15.18		0.01		0.06		0.71	6.58	0.49		0.33		24.01	0.01	2.61	44.58	94.45
11-11 83.08b-8	7.79	0.01	0.01		0.01		0.53	3.62	0.35	0.01			25.86	0.11	0.21	37.52	75.74
11-11 83.08b-9	14.66	4.01	0.01		0.03		5.83	6.19	0.42		0.16		18.92	3.03	0.16	42.29	95.69
11-11 83.08b-10	7.60	0.08			0.01		0.48	3.48	0.29	0.01			30.97	0.11	0.03	43.09	86.01
11-11 83.08b-11	17.12		0.01				0.61	8.17	0.82	0.01	0.17		21.82	0.02	0.12	42.56	91.21
11-11 81.75a-12	4.76		0.01				0.33	2.38	0.25	0.01	0.07	0.01	39.63		0.04	50.18	97.62
11-11 81.75a-13	13.99	0.41	0.03		0.01		1.15	6.60	0.40		0.32	0.01	25.84		0.20	44.24	93.20
11-11 81.75a-14	7.49	1.30	0.05		0.01		2.08	3.39	0.15		0.13	0.03	33.88		0.04	47.20	95.75
11-11 81.75b-15	0.74	25.06	0.03		0.01		17.59	0.26			0.11	0.01	2.67	1.18	0.08	17.50	64.31
11-11 81.75b-16	0.11	0.07	0.01				0.04	0.06					44.86	0.01		51.25	96.37
11-11 81.75b-17	0.03	0.04	0.07				0.04	0.06	0.02		0.11	0.01	45.16	0.04		51.64	97.20
11-11 81.75b-18	0.19	16.74	2.29		0.03		16.54	0.09		0.19	0.25	0.07	16.33	0.05	0.02	29.70	81.85
11-11 81.75b-19	7.27	0.29	0.02		0.01		0.72	3.76	0.38		0.11		35.64	0.01	0.05	48.49	96.75
11 F211a-20	0.01	0.02			0.01		0.02			0.01			45.46			51.83	97.36
11 F211a-23	11.11	0.31	0.24				18.10	3.83	0.57	0.02	1.49	0.16	16.10	0.45	0.06	35.99	88.45
11 F211b-24	0.27	0.97	0.04				8.69	0.02		0.22	0.06	0.12	0.39	0.13	15.66	14.31	40.83
11 F211a-21	8.27	0.02	0.04		0.01		0.05	11.00			0.31		31.28	0.01	0.01	45.41	96.40
11 F211a-22	0.70	0.02	0.02				0.04	0.55		0.01	0.15		44.58		0.01	51.60	97.67
11 F211c-25	0.03				0.01					0.01	0.01		46.01	0.02		52.47	98.55

Silicate Data—continued

Sample ID	Al	As	Ca	Cl	Cr	F	Fe	K	Mg	Mn	Na	P	Si	S	Ti	O	Total
11 F211c-26	17.87		0.01				2.00	8.77	0.17	0.16	0.28		21.51	0.02	0.06	43.08	93.89
11 F211c-27	0.02	0.05	37.98				0.40	0.01	0.01	0.23		18.48	0.09	0.03	0.01	39.39	96.69
11 F211c-28	4.84	1.14	24.30				1.83	1.28	0.14	0.10	0.04	13.01	7.63	0.05	0.42	41.12	95.90
11 F211c-29	2.96	2.15	0.07		0.01		5.03	0.26	0.42	0.01	0.11		34.78	0.06	0.16	44.96	90.99
11 F211c-30	7.93	5.28	4.87		0.02		8.97	1.52	0.63	0.04	0.23	3.00	13.34	0.21	0.33	33.59	79.96
11 F211c-31	6.72	3.59	9.33				5.48	1.83	0.40	0.04	0.22	5.60	11.19	0.19	1.03	34.01	79.63
11-11 143.82a-32	0.01	0.04	37.96				0.01					18.54	0.01	0.01	0.01	39.13	95.67
11-11 143.82a-33	16.47		0.02				0.80	7.92	0.79	0.02	0.26		22.75	0.02	0.10	43.04	91.90
11-11 143.82a-34	13.35		0.04				0.43	6.00	0.65	0.01	0.17		27.84		0.08	45.41	93.73
11-11 143.82a-35	8.10		0.66				25.47	1.18	0.94	2.43	0.10	0.06	9.43	0.04	0.01	27.16	75.36
11-11 143.82a-36	15.18		0.17				7.18	5.63	0.63	0.92	0.25	0.02	18.11	0.03	0.06	38.21	86.17
11-11 143.82a-37	0.04		1.30				0.38	0.08	0.45	0.68	0.39	0.30	1.23	0.21		3.27	8.24
11-11 143.82a-38	0.42		0.62				39.58	0.15	2.43	1.58	0.03	0.01	0.44	0.12	0.01	14.41	58.90
11 F165a-39	0.02	0.01			0.01		0.03	0.01	0.01	0.01			46.95			53.54	100.58
11 F165a-40	11.12		0.05		0.02		23.13	0.38	5.59	0.18	0.03	0.02	13.20	0.01	0.26	35.62	89.61
11 F165a-41	16.95				0.01		2.25	8.62	1.17	0.02	0.16	0.01	21.97		0.38	43.44	94.45
11 F165a-42	8.92		0.02		0.01		16.97	6.79	4.69	0.23	0.08	0.01	16.63	0.03	1.94	37.66	93.97
11 F165a-43	3.75		23.14				3.78	0.23	0.61	0.10	0.01	10.68	5.53	0.03	0.57	34.56	82.75
11 F165a-44	8.49		0.03		0.01		15.57	5.14	3.68	0.16	0.02		18.99	0.01	1.83	38.43	92.36
11 F165a-45	0.01	0.01	38.65				0.15		0.01	0.16		18.57	0.18	0.01	0.01	39.74	97.48
11 F165a-46	9.83		0.04		0.01		0.03	12.95			0.26		29.98			45.68	98.78
11 F165a-47	6.39		0.01				14.11	0.05	3.35	0.22	0.01		27.14	0.02	0.02	42.96	94.26
11 F165a-48	0.08	0.01			0.01		0.05	0.02		0.02		0.01	47.13	0.01	0.01	53.83	101.18
11 F165a-49	11.42		0.05				23.77	0.08	5.41	0.11	0.01	0.01	12.64	0.01	0.12	35.10	88.71

Silicate Data—continued

Sample ID	Al	As	Ca	Cl	Cr	F	Fe	K	Mg	Mn	Na	P	Si	S	Ti	O	Total
11 F165c-50	11.64		0.01				22.91	0.02	6.60	0.34			11.72	0.01	0.04	34.76	88.04
11 F165c-51	16.91		0.01				3.03	8.11	1.52	0.03	0.16		21.91	0.02	0.32	43.62	94.95
11 F165c-52	0.02		38.31				0.51	0.03	0.02	0.14		18.43	0.09	0.03		39.44	97.02
11 F165d-53	1.75	0.06	0.15				44.44	0.09	0.02	0.01	0.15	0.74	10.81	0.25	0.01	27.98	86.46
11 F165d-54	0.01	0.01	0.01		0.01		0.12	0.01					47.33		0.01	53.99	101.50
11 F165d-55	16.73						3.26	8.45	1.64	0.03	0.14		21.65	0.01	0.32	43.35	94.90
11 F165d-56	17.00		0.02				3.45	7.86	1.01		0.13	0.06	21.31	0.05	0.10	42.80	93.42
11 F165d-57	0.47	0.01	0.02				0.35	0.04	0.01	0.01	0.17		46.70			53.77	101.49
11 F165d-58	1.92	0.04	0.38				44.75	0.08	0.08		0.28	1.58	7.92	0.23		26.16	83.42
11 F165e-59	0.01	0.01	38.84				0.18	0.03	0.01	0.17		18.61	0.14	0.01		39.82	97.78
11 F165e-60	11.04		0.03		0.01		24.63	0.07	5.48	0.14		0.01	11.94	0.01	0.90	34.78	89.03
11 F165e-61	0.03		38.45				0.65	0.01	0.03	0.16		18.59	0.12		0.04	39.79	97.85
11 F165e-62	11.38		0.03		0.01		23.81	0.45	5.07	0.04	0.01		12.72	0.01	0.26	35.09	88.89
11 F165e-63	17.64		0.01		0.02		1.49	7.31	0.61		0.06		23.12	0.01	0.10	44.40	94.55
11 F165e-64	11.91						20.05	0.01	8.10	0.43		0.02	12.09	0.02	0.04	35.63	88.29
11 F165f-65	3.04	0.08	0.01				49.47	0.01	0.01	0.08	0.01	0.29	1.78	0.55	0.05	19.92	75.29
11 F165f-66	0.02	0.02					0.05	0.01					47.38			54.02	101.48
11 F165f-67	1.81	0.04	0.14				45.44	0.10	0.05		0.19	1.14	9.09	0.23		26.88	85.12
11 F165f-68	10.18		0.24		0.03		19.05	0.53	2.92	0.07	0.11	0.12	14.60	0.07	3.77	36.09	87.79
10-03 3.95b-69	12.56		0.02		0.01		22.99	0.06	5.28	0.13	0.02		11.49		0.01	34.40	86.97
10-03 3.95b-70	0.17	0.03	0.01				0.09			0.01	0.09		46.88			53.64	100.91
10-03 3.95b-71		0.02					0.02						47.30			53.90	101.25
10-03 3.95b-72	12.62						25.91	0.01	4.70	0.07	0.01		11.16		0.01	34.47	88.95
10-03 3.95c-73	12.57				0.02		25.91		4.47	0.12	0.02		10.96	0.01		34.10	88.19

Silicate Data—continued

Sample ID	Al	As	Ca	Cl	Cr	F	Fe	K	Mg	Mn	Na	P	Si	S	Ti	O	Total
10-03 3.95c-74	0.02	0.01	0.01		0.03		0.25	0.07				0.01	0.04		59.62	4	100.05
10-03 75.75a-75	12.48				0.01		24.14	0.01	5.69	0.26	0.01	0.01	11.50		0.01	34.97	89.09
10-03 75.75a-76	12.22						23.81	0.01	5.92	0.28	0.01		11.30		0.02	34.54	88.09
10-03 75.75a-77	12.45		0.01				23.54		6.00	0.30	0.04		11.43	0.01	0.02	34.92	88.73
10-03 75.75a-78	19.21						0.54	7.60	0.35	0.01	0.43		22.33		0.03	44.61	94.98
10-03 75.75a-79	13.29				0.01		24.15	0.14	4.77	0.27		0.01	11.29	0.01	0.01	34.89	88.86
10-03 75.75a-80	0.02	0.03			0.02		0.02						47.37			53.99	101.41
10-03 75.75a-81	0.01	0.02					0.01						47.38			53.99	101.38
11-14 136.17-3a-82	18.99		0.02		0.03		0.79	7.60	0.47	0.01	0.32		22.31		0.10	44.54	94.99
11-14 136.17-3a-83	12.78		0.01		0.01		22.38	0.04	5.76	0.22	0.01		11.63	0.01	0.02	34.94	87.82
11-14 136.17-3a-84	0.54		0.20				31.23	0.23	9.80	0.26	0.03	0.01	0.60	0.01	0.01	16.81	59.73
11-14 136.17-3a-85	20.34		0.05				0.17	0.10	0.08	0.01	0.03	0.01	22.82	0.01		44.24	87.79
11-14 136.17-3a-86	0.54		1.64		0.01		37.11	0.01	4.10	0.44	0.03	0.01	0.55		0.01	15.25	59.70
11-14 136.17-3a-87	12.67		0.03				23.66	0.02	5.60	0.18	0.01		11.28		0.01	34.67	88.14

Sulfide Data: all values are in percentages (%), 'M' or 'ii' within the Sample ID denotes fluid inclusion wafer

Sample ID	Ag	As	Au	Bi	Cu	Fe	Ni	Pb	S	Sb	Sn	Ti	W	Zn	Total
11-11 81.6-1	0.02	5.37			0.03	45.55	0.01		0.09					0.14	51.13
11-11 81.6-2	0.01	0.01	0.03			0.17		0.07						0.01	0.29
11-11 81.6-3		5.04	0.04		0.01	44.16	0.02	0.18	0.15					0.78	50.39
11-11 81.6-4		0.07			0.01	6.92	0.01	0.07	34.04					49.51	90.59
11-11 81.6-5	0.02	0.03			96.34	0.20		0.04	0.02						96.63
11-11 81.6-6		0.05				6.53	0.01		33.38					48.66	88.52
11-11 81.6-7		42.67			0.02	35.05		0.12	21.65						99.47
11-11 81.6-8	0.03	42.22				35.35			22.17					0.01	99.68
11-11 81.6-9		42.27	0.03		0.01	35.07		0.04	22.13						99.55
11-11 81.6-10	0.02	42.81				34.96	0.01	0.01	21.42						99.20
11-11 81.6-11		0.02			0.01	0.07		86.30	13.63						99.79
11-11 81.6-12	0.01	45.19	0.01			12.66	18.35	0.03	20.54					0.01	96.79
11-11 81.6-13		42.97				11.34	21.49		19.57						95.28
11-11 81.6-14		1.02	0.01			46.26	0.01	0.09	52.94					0.01	100.29
11-11 255.9-1-15		1.33			0.01	46.16		0.15	53.07						100.64
11-11 255.9-1-16	0.02	1.10			0.01	45.99	0.01	0.17	53.02						100.29
11-11 255.9-1-17		1.63	0.01			45.62		0.16	52.72						100.13
11-11 255.9-1-18	0.04	0.13			0.02	29.60	0.03	31.77	38.97					0.03	100.53
11-11 255.9-1-19	0.02	1.56				45.88		0.16	52.69						100.27
11-11 255.9-1-20	0.03	0.48			0.01	45.83	0.03	0.11	53.13					0.01	99.61
11-11 255.9-1-21		0.06			0.02	9.14	0.01	64.40	22.78						96.22
11-11 255.9-1-22		0.02	0.02			46.40	0.02	0.24	53.93						100.59
11-11 255.9-1-23	0.02	0.11				54.10	0.03	0.15	61.85						116.23
11-11 255.9-1-24	0.03	0.04	0.01			0.19			0.01						0.15

Sulfide Data -continued

Sample ID	Ag	As	Au	Bi	Cu	Fe	Ni	Pb	S	Sb	Sn	Ti	W	Zn	Total
11-11 255.9-1-25	0.02		0.02			29.67			0.13					0.01	29.83
11-11 209.6-1 -26	0.03	0.01				46.49	0.05	0.08	53.85					0.01	100.48
11-11 209.6-1 -27		0.03			0.04	46.17	0.06	0.19	53.94						100.37
11-11 209.6-1 -28		0.01			0.04	46.38		0.12	53.92						100.41
11-11 209.6-1 -29	0.01	0.02	0.01		0.01	46.30	0.10	0.16	53.58						100.20
11-11 209.6-1 -30	0.02		0.03			46.10		0.09	53.71						99.94
11-11 209.6-1 -31		0.03	0.01		33.20	29.16		0.19	34.86						97.21
11-11 209.6-1 -32		0.06	0.06		33.80	29.44		0.03	35.28						98.46
11-11 209.6-1 -33						3.23								0.01	3.20
11-11 209.6-1 -34			0.03		0.01	1.33								0.01	1.34
11-15A 240-2 -35	0.12	0.02			0.01	0.03		0.11	18.11					0.04	18.33
11-15A 240-2 -36	0.01	0.61	0.06			46.07	0.01		53.00					0.01	99.69
11-15A 240-2 -37		43.94	0.08			34.08		0.03	20.45						98.57
11-15A 240-2 -38	0.02	40.88				35.32		0.13	22.80					0.01	99.07
11-15A 240-2 -39		0.02				46.06	0.14	0.09	53.53						99.80
11-15A 240-2 -40		40.81	0.03		0.01	34.98	0.07		22.72					0.01	98.54
11-15A 240-2 -41	0.01	41.05	0.01			34.88	0.10	0.03	22.39						98.44
11-15A 240-2 -42		41.54	0.04			34.96	0.01		22.19						98.73
11-15A 240-2 -43		42.58	0.06		0.01	34.37	0.05	0.07	21.04						98.15
11-15A 240-2 -44					0.02	23.36		0.03	0.04						22.78
11-15A 240-2 -45	0.02		0.02		0.01	34.99	0.01		2.14						36.59
11-15A 240-2 -46		0.11				45.64		0.14	52.60						98.44
11-15A 240-2 -47		0.19			0.01	39.31	0.02	0.09	46.22						85.80
11-15A 240-2 -48		0.05	20.53			0.03			0.01					0.01	20.55

Sulfide Data -continued

Sample ID	Ag	As	Au	Bi	Cu	Fe	Ni	Pb	S	Sb	Sn	Ti	W	Zn	Total
11-15A 240-2 -49	0.01	0.03	18.93			0.04								0.02	18.94
11-15A 240-2 -50	0.05	0.04				0.11									0.10
11-15A 240-2 -51					0.02	33.39								0.01	32.15
11-15A 240-2 -52	0.03		0.01		30.73	30.53		0.18	31.88						93.18
11-15A 240-2 -53	0.03	42.03	0.02			34.80	0.22		21.87					0.01	98.96
11-15A 240-2 -54	0.02	42.98			0.01	34.63		0.19	20.68						98.49
11-15A 240-2 -55		43.70			0.01	33.89	0.10	0.01	20.53						98.16
11-15A 240-2 -56		43.50			0.01	34.54		0.06	20.38					0.01	98.50
11-15A 240-2 -57		0.03	0.02			46.18	0.04	0.09	53.21						99.56
11-15A 240-2 -58	0.03	0.02			33.57	29.60	0.01	0.06	34.73						97.79
11-15A 240-2 -59	0.04	0.04	0.03		0.01	46.28		0.02	53.02					0.03	99.46
11-15A 240-2 -60		0.02	0.01		33.57	29.62		0.20	34.28						97.54
11-15A 240-2 -61	0.01		0.01			46.24	0.06	0.03	53.44						99.78
11-15A 240-2 -62					0.01	38.69			0.01						38.61
11-15A 240-2 -63	0.01	0.02	0.01			46.30	0.04	0.10	54.03						100.50
11-15A 240-1 -64		0.03				0.07	0.01	85.97	13.71					0.01	99.56
11-15A 240-1 -65		0.03	0.05			46.06	0.05	0.16	53.67					0.01	100.03
11-15A 240-1 -66					0.02	33.53								0.01	32.56
11-15A 240-1 -67		0.23			0.01	46.12		0.10	53.03						99.41
11-15A 240-1 -68	0.01	0.01				46.03	0.35	0.14	53.34						99.82
11-15A 240-1 -69		40.90	0.01			34.94		0.09	22.51					0.01	98.44
11-15A 240-1 -70	0.01	41.27				34.77	0.02	0.06	22.26						98.35
11-15A 240-1 -71		42.52				33.04	0.32	0.01	20.97						96.78
11-15A 240-1 -72	0.06	0.01				46.13	0.01	0.13	53.15						99.43

Sulfide Data -continued

Sample ID	Ag	As	Au	Bi	Cu	Fe	Ni	Pb	S	Sb	Sn	Ti	W	Zn	Total
11-15A 240-1 -73	0.03	42.40				34.71	0.17	0.03	21.76					0.02	99.09
11-15A 240-1 -74	0.01	0.04	0.01			0.09		0.05							0.20
11-10A 95.45 -75	0.02	41.93				34.98	0.01	0.02	21.73						98.66
11-10A 95.45 -76	0.04	0.08	0.03		33.89	29.34			34.81						97.99
11-10A 95.45 -77						22.48								0.04	21.01
11-10A 95.45 -78		0.01				0.09	0.01		0.01					0.01	0.02
11-10A 95.45 -79		41.26				35.05	0.01	0.12	22.14						98.52
11-10A 95.45 -80	0.03	0.04			0.01	46.41		0.15	53.24					0.01	99.89
11-10A 95.45 -81		0.05			2.47	5.23	0.01	0.07	33.39					48.22	89.35
11-10A 95.45 -82		0.02				57.85	0.01	0.19	38.55					0.01	96.60
11-10A 95.45 -83	0.05	1.22	0.04			46.01		0.06	52.37					0.01	99.74
11-10A 95.45 -84	0.02	0.57	0.01			46.11	0.01	0.15	52.85						99.70
11-10A 95.45 -85		42.83				33.10	0.65	0.05	20.71						97.28
11-10A 46.34 -86		0.03				0.01		77.10	11.83						88.71
11-10A 46.34 -87		0.01				0.06		86.58	13.28						99.72
11-10A 46.34 -88		0.02	0.01		0.01	0.03		86.26	13.35						99.52
11-10A 46.34 -89		0.01	0.02			46.62		0.15	52.87						99.61
11-10A 46.34 -90	0.02	0.08			0.01	46.47		0.15	53.04					0.01	99.77
11-10A 46.34 -91		0.04				46.49	0.01	0.17	53.34						100.02
11-11 81.75 -92	2.84	0.04	92.28		0.03	0.05			0.06						95.00
11-11 81.75 -93	2.82	0.01	88.95		0.03	0.06			0.07						91.62
11-11 81.75 -94	3.01	0.07	90.10		0.04	0.15			0.07						93.24
11-11 81.75 -95	3.09	0.04	90.95		0.02	0.06	0.01		0.04						93.91
11-11 81.75 -96	2.89	0.01	86.52		0.02	0.10			0.08						89.01

Sulfide Data -continued

Sample ID	Ag	As	Au	Bi	Cu	Fe	Ni	Pb	S	Sb	Sn	Ti	W	Zn	Total
11-11 81.75 -97	2.80		84.69		0.01	0.12			0.15						87.58
11-11 81.75 -98		42.94	0.03			33.79			20.57					0.01	97.27
11-11 81.75 -99		43.10	0.03		0.01	33.74		0.08	20.77					0.02	97.73
11-11 81.75 -100	3.11	0.05	91.89			0.04	0.01		0.04						95.04
11-11 81.75 -101		40.42			0.03	34.33		0.68	21.35						96.78
11-11 81.75 -102		41.74	0.02			34.31	0.01	0.08	21.44					0.01	97.59
11-11 81.75 -103	0.03	42.59	0.03			34.47	0.01	0.02	21.73					0.01	98.90
11-11 81.75 -104	3.33	0.05	90.74			0.01	0.02		0.03						94.04
11-11 81.75 -105		27.33	0.05		0.03	22.79	0.01	0.23	0.02						50.41
11-11 81.75 -106		0.03	0.02			0.46		0.06							0.57
11-11 81.75 -107	0.01	28.58	0.03		0.03	25.45		0.32	0.06						54.47
11-11 81.75 -108		29.06	0.06		0.02	25.87		0.08	0.05						55.13
11-11 81.75 -109	0.05	28.04	0.02		0.02	27.58			0.08						55.79
11-11 81.75 -110		41.97			0.01	34.59	0.01		22.16					0.01	98.72
11-11 81.75 -111		31.09	0.02		0.03	26.74		0.15	0.08						58.09
11-11 81.75 -112	3.32	0.05	90.85		0.01	0.04			0.03						94.30
11-11 81.75 -113	0.01	29.30			0.01	21.63	0.02	2.94	0.02						53.91
11-11 81.75 -114	2.52	0.05	91.76		0.02	0.03	0.01		0.07						94.32
11-11 81.75 -115		42.14	0.04		0.01	35.29			21.40						98.84
11-11 81.75 -116	0.02	41.93				34.61		0.08	21.42						98.03
11-11 81.75 -117		37.96	0.01		0.09	21.99		0.07							60.08
11-11 81.75 -118		41.55			0.03	34.86		0.03	21.90						98.33
11-11 143.82 -119		0.02				46.14	0.01	0.06	52.88						99.08
11-11 143.82 -120		0.05			0.01	0.55		85.68	13.57					0.02	99.75

Sulfide Data -continued

Sample ID	Ag	As	Au	Bi	Cu	Fe	Ni	Pb	S	Sb	Sn	Ti	W	Zn	Total
11-11 143.82 -121		0.04			0.01	46.14		0.15	53.13					0.01	99.44
11-11 143.82 -122		0.04			0.02	1.20		85.53	13.66					0.03	100.32
11-11 143.82 -123		0.05			0.01	45.86		0.24	52.26						98.33
11-11 143.82 -124		0.02				0.87		85.69	13.36						99.70
11-11 143.82 -125	0.02	0.32			0.01	48.50		0.56	0.12					0.72	50.24
11-11 143.82 -126	0.02	0.01			0.01	40.57	0.01		0.05						40.62
11-11 143.82 -127	0.03	0.64	0.02		0.01	39.75		0.18	45.42						86.05
11-11 143.82 -128	0.02	0.08			0.01	44.06	0.01	0.14	54.45						98.74
11-11 143.82 -129	0.02	0.09	0.01		0.02	44.58		0.10	53.36						98.16
11-11 143.82 -130		0.05			33.76	28.85		0.05	34.11						96.56
11-11 143.82 -131	0.05	0.04				46.15		0.12	52.80						99.12
11-11 143.82 -132	0.01	0.05			33.72	28.87		0.07	34.71						97.26
11-11 143.82 -133		0.01			0.01	0.35		86.17	13.33						99.60
11-11 143.82 -134						36.47									36.03
11-11 143.82 -135			0.04			31.61		0.02							31.30
11-11 143.82 -136		0.06			11.80	1.47	0.01	71.17	15.53						99.89
11-11 143.82 -137					0.01	36.78		0.01	0.02					0.01	36.56
11-11 143.82 -138		0.01	0.04		0.02	46.04		0.23	52.20						98.52
11-11 143.82 -139		0.18			0.01	41.51		0.22	47.74						89.63
11-11 143.82 -140		0.17				45.88		0.19	52.44						98.62
11-11 143.82 -141		0.07	0.01			46.29		0.12	52.79						99.26
11-15A 227.75-1 -142		28.90	0.03			17.15		0.09	21.65						67.80
11-15A 227.75-1 -143						23.71		0.01							23.68
11-15A 227.75-1 -144		40.41	0.01			32.20	0.01	0.11	20.39					0.02	93.12

Sulfide Data -continued

Sample ID	Ag	As	Au	Bi	Cu	Fe	Ni	Pb	S	Sb	Sn	Ti	W	Zn	Total
11-15A 227.75-1 -145		0.06	0.01			57.67	0.35	0.20	38.73						96.96
11-15A 227.75-1 -146	0.03	43.35			0.01	33.90	0.15	0.11	20.64						98.18
11-15A 227.75-1 -147	0.01	0.06				58.03	0.42	0.14	38.16						96.75
11-15A 227.75-1 -148	0.01		0.04		0.01	29.01	0.01								27.85
11-15A 227.75-1 -149		0.10				7.39	0.05	28.38	13.50						49.33
11-15A 227.75-1 -150			0.02		0.02	23.64			0.01					0.01	23.65
11-15A 227.75-1 -151		42.61				35.05		0.06	21.44						99.09
11-15A 227.75-1 -152		0.18				1.44		88.17	13.08						102.65
11-15A 227.75-1 -153		42.56				34.90	0.03	0.21	21.17						98.83
11-15A 227.75-1 -154						29.76			0.01						28.61
11-15A 227.75-1 -155	0.03	43.63				34.70	0.02	0.09	20.55						98.95
11-10A 78.94-1 -156		0.48	0.02			46.27		0.04	52.15					0.01	98.96
11-10A 78.94-1 -157	0.01	0.29	0.04		0.02	46.26	0.01	0.18	51.84					0.01	98.65
11-10A 78.94-1 -158	0.05	0.73	0.04		0.01	45.08	0.19	0.10	51.31						97.50
11-10A 78.94-1 -159						34.24		0.01	0.02					0.01	32.82
11-10A 78.94-1 -160	0.01	0.65	0.02			46.34		0.15	51.79						98.92
11-10A 78.94-1 -161	0.02	0.28				46.24	0.02	0.10	52.10						98.74
11-10A 78.94-1 -162		0.51	0.01		0.01	46.24		0.09	52.05					0.02	98.91
11-10A 78.94-1 -163	0.01					30.31		0.04	0.06					0.01	30.39
11-10A 78.94-1 -164		0.28				36.32	0.01	0.21	31.78						68.56
11-10A 78.94-1 -165		0.21	0.02			37.25		0.18	32.51						70.13
11-10A 78.94-1 -166	0.01	0.04			27.04	22.40		0.09	21.45						71.00
11-10A 78.94-1 -167	0.01					22.60	0.01		0.02					0.01	22.00
11-10A 78.94-1 -168	0.01	0.02				36.80	0.01	0.31	33.90						71.03

Sulfide Data -continued

Sample ID	Ag	As	Au	Bi	Cu	Fe	Ni	Pb	S	Sb	Sn	Ti	W	Zn	Total
11-11 81.75 -169	3.12		90.74			0.04			0.05						93.58
11-11 81.75 -170	2.94	0.02	86.71			0.13			0.17						89.35
11-11 81.75 -171	2.99	0.06	90.47		0.01	0.05			0.07						93.23
11-11 81.75 -172	3.06	0.05	88.93		0.03	0.31			0.06						92.25
11-11 81.75 -173	3.14	0.02	87.03		0.02	0.09			0.11						90.15
11-15A 227.75ii_A -134	0.01			0.06	0.02	45.86		0.29	52.67	0.04					98.94
11-15A 227.75ii_A -135	0.05				0.04	45.16	0.02	0.19	43.83			0.01			89.31
11-15A 227.75ii_A -136	0.02				0.07	45.33		0.21	51.18						96.81
11-15A 227.75ii_A -137						45.78		0.25	52.80			0.01			98.83
11-15A 227.75ii_A -138						45.90	0.01	0.19	52.97						99.07
11-15A 227.75ii_A -139						45.39		0.23	52.50	0.04			0.01	0.01	98.18
11-15A 227.75ii_A -140						45.55	0.01	0.18	52.76	0.02		0.02			98.54
11-15A 227.75ii_A -141						45.40	0.01	0.21	52.62	0.02			0.05	0.02	98.32
11-15A 227.75ii_A -142				0.03	0.02	45.44		0.14	52.86				0.01		98.50
11-15A 227.75ii_A -144	0.01					44.62	0.01	0.15	52.40	0.02				0.06	97.26
11-15A 227.75ii_A -145						45.04		0.17	52.59				0.01		97.80
11-15A 227.75ii_B -143						45.31		0.29	52.94					0.01	98.55
11-15A 227.75ii_B2 -146		2.18				44.96	0.01	0.05	51.37			0.01		0.02	98.59
11-15A 227.75ii_B2 -147		2.17			0.01	44.85		0.29	51.26			0.01		0.02	98.60
11-15A 227.75ii_B2 -148		1.98			0.04	44.80		0.18	51.01				0.01		98.01
11-15A 227.75ii_C -149	0.21					0.15		80.32	12.70	0.06		0.01			93.44
11-15A 227.75ii_C -150	0.20	0.33				0.08		80.53	13.00			0.02		0.05	94.21
11-15A 227.75ii_C -155		0.11			0.02	45.49		0.16	52.72			0.01	0.02	0.03	98.56
11-15A 227.75ii_C -156	0.02				0.03	45.43	0.01	0.22	52.65			0.02		0.03	98.42

Sulfide Data -continued

Sample ID	Ag	As	Au	Bi	Cu	Fe	Ni	Pb	S	Sb	Sn	Ti	W	Zn	Total
11-15A 227.75ii_C -157	0.06					1.90		82.54	13.42	0.08					98.01
11-15A 227.75ii_C -158						45.66	0.02	0.18	52.76			0.01	0.04	0.01	98.67
11-15A 227.75ii_C -159				0.08		45.47	0.02	0.18	52.77	0.02		0.02	0.01		98.56
11-15A 227.75ii_C -160	0.06					45.42		0.21	52.78			0.01	0.01		98.49
11-15A 227.75ii_C -161						45.49		0.20	53.12				0.03		98.83
11-15A 227.75ii_C -162					0.01	45.45	0.02	0.16	52.95	0.01			0.02		98.63
11-15A 227.75ii_C -163	0.01	0.41				45.39	0.02	0.16	52.77				0.02		98.79
11-15A 227.75ii_C -164						45.52		0.23	53.07			0.01		0.02	98.86
11-15A 227.75ii_D -165		42.57			0.01	33.47	0.02	0.08	21.33	0.02		0.01	0.04		97.54
11-15A 227.75ii_D -166		0.16				45.46		0.16	53.18	0.01		0.01		0.01	98.98
11-15A 227.75ii_D -167	0.06	0.03			0.03	45.21	0.01	0.20	53.05			0.01		0.02	98.60
11-15A 227.75ii_D -168	0.01	42.22				34.81	0.02	0.11	21.27				0.04	0.05	98.52
11-15A 227.75ii_D -169	0.03				0.01	45.53		0.21	52.95				0.03	0.03	98.79
11-15A 227.75ii_F -170	0.03	0.33			0.05	45.51		0.15	52.80			0.01			98.88
11-15A 227.75ii_F -171						45.62		0.16	53.25						99.03
11-15A 227.75ii_F -172					0.05	45.81	0.01	0.18	53.46	0.01			0.01		99.52
11-15A 227.75ii_F -173					0.03	39.71		0.04	0.01				0.01	0.05	39.85
11-15A 227.75ii_F -174	0.05				32.53	30.28	0.01	0.09	34.75				0.03	0.01	97.74
11-15A 227.75ii_F -175	0.13				32.95	30.23	0.01		34.38				0.01		97.72
11-15A 227.75ii_G -176	0.03					45.59		0.19	53.27					0.04	99.12
11-15A 227.75ii_G -177	0.04					46.74		0.23	52.46			0.01		0.04	99.51
11-15A 227.75ii_G -178				0.07		45.48		0.11	53.12				0.02		98.81
11-15A 227.75ii_G -179	0.05				0.01	45.57	0.01	0.14	53.22			0.01	0.03		99.05
11-15A 227.75ii_G -180	0.14					0.09		83.37	13.41	0.02		0.01			97.04

Sulfide Data -continued

Sample ID	Ag	As	Au	Bi	Cu	Fe	Ni	Pb	S	Sb	Sn	Ti	W	Zn	Total
11-15A 227.75ii_G -181	0.01				0.01	45.67		0.13	53.52						99.33
11-15A 227.75ii_G -182		0.03				45.68	0.01	0.16	53.16			0.01			99.04
11-15A 227.75ii_G -183	0.03				0.01	45.65		0.23	54.98				0.03		100.92
11-15A 227.75ii_G -184				0.03		45.78		0.32	55.59					0.03	101.74
11-15A 227.75ii_G -185					0.04	45.46		0.25	53.43	0.04		0.02		0.02	99.26
11-15A 227.75ii_G -186						45.61		0.21	55.00						100.82
11-15A 227.75ii_I -187						45.53		0.19	54.07	0.02		0.02			99.84
11-15A 227.75ii_I -188	0.05		0.01			45.51		0.25	54.26				0.01		100.08
11-15A 227.75ii_I -189	0.05			0.01		45.29	0.04	0.17	53.42					0.02	99.00
11-15A 227.75ii_I -190						45.33	0.24	0.21	54.46	0.01				0.03	100.28
11-15A 227.75ii_I -191					0.13	44.96	0.07	0.19	53.07				0.02	0.03	98.48
11-15A 227.75ii_I -192						45.50		0.22	52.75				0.01		98.48
11-15A 227.75ii_I -193					0.07	44.92		0.20	49.28						94.48
11-15A 227.75ii_I -194					0.07	44.93		0.22	49.52	0.02			0.01		94.77
11-15A 227.75ii_I -195	0.03					44.67	0.01	0.18	48.16						93.05
11-15A 227.75ii_I -196					0.10	45.25	0.01	0.18	51.88				0.01		97.43
11-15A 227.75ii_I -197					0.04	45.40		0.19	53.89	0.02			0.08		99.61
11-15A 227.75ii_I -198					0.08	45.52		0.18	52.94				0.03		98.75
11-15A 227.75ii_I -199						45.06	0.01	0.20	47.34						92.60
11-15A 227.75ii_I -200					0.01	45.28		0.26	49.95			0.02		0.07	95.58
11-15A 227.75ii_I -201						43.22		0.14	38.19					0.01	81.56
11-15A 227.75ii_I -202					0.02	45.50	0.01	0.18	44.25	0.03					89.98
11-15A 227.75ii_I -203	0.01				0.06	44.86	0.01	0.21	47.28	0.02			0.01		92.46
11-15A 227.75ii_I -204					0.08	45.40		0.21	53.61	0.01			0.08		99.39

Sulfide Data -continued

Sample ID	Ag	As	Au	Bi	Cu	Fe	Ni	Pb	S	Sb	Sn	Ti	W	Zn	Total
11-15A 227.75ii_I -205					0.07	45.78	0.01	0.23	54.88	0.01		0.01	0.02	0.04	101.05
11-15A 227.75ii_I -206	0.02					45.79		0.23	54.98					0.04	101.06
11-11 81.75ii_B -110	5.89		83.16	0.61	0.02	0.10			0.09						89.86
11-11 81.75ii_B -111		4	0.17			34.78		0.06	22.18	0.01		0.01	0.03	0.02	97.25
11-11 81.75ii_B -112	6.12		92.43	0.77	0.01	0.02			0.03						99.37
11-11 81.75ii_B -113		42.95				34.85	0.02	0.09	21.40	0.04				0.04	99.39
11-11 81.75ii_B -114	0.03	41.49	0.20	0.08		34.56		0.07	21.29			0.02			97.75
11-11 81.75ii_B -115	5.96		82.78	0.71	0.02	0.17	0.01		0.12	0.05		0.02			89.83
11-11 81.75ii_B -116		41.01	0.33		0.03	34.38	0.01	0.10	22.18	0.01				0.01	98.07
11-11 81.75ii_B -117	5.77		82.52	0.78		0.15			0.11			0.05			89.37
11-11 81.75ii_B -118		41.58	0.22		0.03	34.76		0.08	21.89			0.01			98.56
11-11 81.75ii_B -119	6.44		91.90	0.97		0.10			0.05			0.02			99.48
11-11 81.75ii_B -120	6.30		89.44	0.66	0.03	0.02			0.02			0.01	0.04		96.52
11-11 81.75ii_B -121	0.02	42.25	0.73			34.29	0.01	0.06	21.16	0.03		0.01		0.09	98.63
11-11 81.75ii_B -122		41.81	0.05	0.17	0.01	34.82	0.01	0.09	21.78						98.74
11-11 81.75ii_B -123	5.86		89.30	0.62	0.02	0.01									95.81
11-11 81.75ii_B -124	6.05		81.54	0.81	0.03	0.17	0.02		0.10			0.01			88.73
11-11 81.75ii_B -125	0.01	43.17				34.93		0.01	21.31	0.04		0.01	0.04	0.02	99.53
11-11 81.75ii_B -126		42.84		0.02		35.10		0.09	21.96	0.03				0.01	100.05
11-11 81.75ii_B -127	0.03	43.78				34.95		0.10	21.49	0.02		0.01			100.37
11-11 81.75ii_B -128		39.97				31.86		5.30	21.65	0.05			0.01	0.01	98.85
11-11 81.75ii_B -129	0.04	38.82				32.03	0.02	8.09	21.63	0.06			0.01	0.05	100.74
11-11 81.75ii_B -130	0.01	42.44				35.22	0.01	0.01	22.46	0.02			0.06		100.22
11-11 81.75ii_C -131		40.78	0.21			34.58		0.06	22.15	0.06		0.01			97.84

Sulfide Data -continued

Sample ID	Ag	As	Au	Bi	Cu	Fe	Ni	Pb	S	Sb	Sn	Ti	W	Zn	Total
11-11 81.75ii_C -132		43.14				34.91		0.17	21.03	0.02				0.04	99.32
11-11 81.75ii_C -133	5.11		84.70	0.85		0.15			0.11						90.91
MF035-1_A -10	0.01	42.73			0.02	35.15		0.11	21.62	0.02		0.01		0.01	99.67
MF035-1_A -5	0.03	42.68		0.08		35.72		0.10	22.03	0.01					100.64
MF035-1_A -6	0.04	42.76				34.95		0.06	21.07	0.05				0.01	98.95
MF035-1_A -7		42.83				35.71		0.17	22.32	0.01		0.02			101.06
MF035-1_A -8	0.05	42.98				35.26			21.81					0.03	100.12
MF035-1_A -9	0.02	43.38			0.03	35.34		0.07	21.46	0.07			0.01	0.03	100.40
MF035-1_B -11		21.93				29.62		0.01	2.57	0.06					54.18
MF035-1_B -12	0.06	42.86				35.01	0.01	0.10	20.74	0.03					98.82
MF035-1_B -13	0.08	41.89			0.02	35.54	0.01	0.17	22.03	0.04				0.01	99.79
MF035-1_B -14		21.49			0.01	30.32		0.01	3.09	0.04				0.02	54.97
MF035-1_B -15		42.50			0.02	35.25	0.01	0.12	22.38			0.01		0.01	100.31
MF035-1_B -16		41.31			0.01	35.34		0.06	22.75				0.02		99.49
MF035-1_B -17	0.06	42.59			0.04	35.29		0.05	21.69	0.04				0.01	99.76
MF035-1_B -18	0.02	21.78			0.02	28.52	0.01		2.49	0.06		0.01		0.01	52.91
MF035-1_C -19	0.06	40.87		0.08	0.02	35.02		0.18	22.20			0.01			98.44
MF035-1_C -20		42.95		0.28		35.23		0.03	21.27	0.01		0.01		0.01	99.79
MF035-1_C -21		43.15	0.06			34.89		0.07	20.92						99.09
MF035-1_C -22	0.03	42.96			0.01	35.23		0.10	21.46	0.07		0.01	0.01	0.02	99.89
MF035-1_C -23		42.22	0.14			35.04	0.01	0.01	21.54	0.04			0.04		99.03
MF035-1_C -24	7.34		91.75	1.27		0.03			0.04						100.42
MF035-1_C -25	7.26		91.52	0.97		0.09			0.03				0.02		99.90
MF035-1_C -26	7.39		91.98	0.76	0.01	0.08	0.02		0.04						100.26

Sulfide Data -continued

Sample ID	Ag	As	Au	Bi	Cu	Fe	Ni	Pb	S	Sb	Sn	Ti	W	Zn	Total
MF035-1_C -27	0.01	43.21		0.02	0.02	35.20		0.14	21.37	0.03		0.01			100.02
MF035-1_C -28		44.72			0.02	34.95		0.06	20.29			0.01			100.05
MF035-1_C -29	0.04	43.53			0.01	35.16		0.09	21.64	0.02			0.03		100.52
MF035-1_C -30		42.88			0.03	35.29		0.01	21.97	0.01					100.19
MF035-1_C -31	0.01	43.31				35.36	0.01	0.10	21.71	0.06			0.03		100.58
MF035-1_C -32	7.38		91.43	0.39		0.04			0.06						99.30
MF035-1_C -33	7.44		91.68	1.27	0.06	0.06	0.01		0.03						100.56
MF035-1_C -34	7.61		91.51	1.25	0.02	0.06	0.01		0.02				0.01		100.48
MF035-1_C -35	0.05	43.30	0.04	0.14		35.14	0.02	0.02	20.94	0.04		0.01	0.01		99.73
MF035-1_C -36	0.02	41.74				35.68		0.03	22.56			0.01	0.02	0.04	100.10
MF035-1_C -37		43.44			0.02	35.38		0.10	22.26	0.03		0.01			101.24
MF035-1_C -38		42.31			0.01	34.80	0.01	0.15	22.63				0.08		99.98
MF035-1_C -39	0.01	43.38			0.02	35.17	0.01	0.05	20.90						99.53
MF035-1_C -40	7.36		91.62	1.09	0.05	0.24	0.02		0.04			0.01			100.42
MF035-1_C -41	7.45		91.82	0.75	0.06	0.01			0.04			0.02			100.15
MF035-1_C -42	7.57		92.44	0.97	0.05	0.03			0.04			0.02			101.12
MF035-1_C -43	7.55		92.02	0.86		0.03			0.04						100.52
MF035-1_D-44	0.01	42.33		0.01		35.49	0.01	0.14	22.17	0.03		0.01	0.07		100.25
MF035-1_D-45		42.98				35.39	0.01	0.08	21.69					0.06	100.21
MF035-1_D-46	0.02	43.19		0.07		35.19		0.15	21.80	0.01					100.43
MF035-1_D-47	0.02	42.88				35.49		0.07	21.71	0.01			0.07		100.25
MF035-1_D-48	0.02	43.26				34.91	0.02	0.16	21.32	0.02					99.71
MF035-1_D-49	0.01	42.34				35.30		0.07	22.07	0.01			0.06	0.02	99.88
MF035-1_E -55		42.08		0.01	0.04	35.41		0.08	22.41	0.03		0.02			100.06

Sulfide Data -continued

Sample ID	Ag	As	Au	Bi	Cu	Fe	Ni	Pb	S	Sb	Sn	Ti	W	Zn	Total
MF035-1_E -56		43.49			0.01	34.98		0.14	21.47	0.08				0.03	100.19
MF035-1_E -57	0.04	42.35				35.17	0.22	0.14	22.64						100.57
MF035-1_E -58		43.98			0.03	34.87		0.13	21.39					0.01	100.41
MF035-1_E -59		42.14				35.16	0.04	0.03	22.38						99.74
MF035-1_E -60	0.05	42.49			0.04	35.19		0.12	22.15				0.01	0.06	100.11
MF035-1_E -61	0.01	42.84			0.04	34.69	0.01	0.41	21.98	0.02		0.02		0.01	100.01
MF035-1_E -62		42.51				34.89		0.10	21.91	0.05			0.03	0.02	99.52
MF035-1_E -63		43.64				35.05		0.12	21.73	0.10		0.03		0.01	100.68
MF035-1_E -64		39.50		0.06	0.01	34.88	0.01	0.04	21.24			0.04		0.03	95.80
MF035-1_F -65	0.02	42.41			0.01	34.85		0.07	16.80						94.17
MF035-1_F -66	0.02	43.55			0.02	34.52	0.01	0.01	11.72			0.01			89.87
MF035-1_F -67		43.05				34.53		0.04	12.80				0.01		90.44
MF035-1_F -68	0.01	40.90		0.01		34.77		0.05	15.71			0.01			91.45
MF035-1_F -69		27.29				33.80	0.01	0.08	19.64	0.03		0.17			81.02
MF035-1_F -70		36.25			0.04	27.06		0.03	5.25						68.63
MF035-1_F -71	0.02	36.27				30.96		0.05	10.40			0.02		0.09	77.81
MF035-1_F -72		21.20			0.01	18.49		0.12	0.01			0.01	0.02		39.84
MF143_B-78	0.03	0.10				40.64	0.01	0.17	50.37	0.02					91.32
MF143_B-79		0.03			0.01	43.60	0.01	0.29	51.67	0.03		0.01	0.05	0.02	95.72
MF143_B-80	0.01					43.46		0.27	51.49	0.02					95.24
MF143_B1-73	0.01	0.83				43.08		0.22	50.96						95.10
MF143_B1-74	0.04	1.20			0.04	42.93		0.18	50.79	0.01		0.01		0.07	95.27
MF143_B1-75	0.02	0.73			0.01	43.30		0.14	51.00				0.03		95.22
MF143_B1-76					0.02	29.21	0.01	38.47	34.87					0.01	102.59

Sulfide Data -continued

Sample ID	Ag	As	Au	Bi	Cu	Fe	Ni	Pb	S	Sb	Sn	Ti	W	Zn	Total
MF143_B2 -77	0.01				0.08	41.72	0.01	0.17	50.74				0.03	0.02	92.77
MF143_C -81		0.62		0.08		44.63	0.01	0.22	51.61						97.16
MF143_C -82		0.06				44.36		0.26	51.61				0.01		96.31
MF143_C -83	0.05					44.46		0.19	51.88				0.01		96.58
MF143_C -84		42.50		0.01	0.04	34.04	0.01	0.06	20.34					0.03	97.03
MF143_C -85	0.03	0.03				44.20		0.23	48.61	0.02		0.01		0.03	93.16
MF143_C -86	0.02			0.03		44.88	0.04	0.19	51.70			0.01			96.86
MF143_C -87	0.05	1.12			0.01	43.94		0.17	50.10	0.03		0.01	0.05		95.47
MF143_C -88		0.03				44.99	0.01	0.18	51.93						97.14
MF143_C -89		0.36				44.14		0.17	50.65				0.02		95.34
MF143_C -90		42.70			0.01	34.36		0.12	20.51	0.02					97.72
MF143_C -91		42.76			0.05	34.38		0.06	20.38				0.06		97.69
MF143_C -92		41.03			0.02	34.39	0.01	0.10	21.67	0.03		0.01		0.04	97.30
MF143_C -93		42.11				34.16		0.13	21.18	0.02				0.02	97.62
MF143_C -94		42.10			0.01	34.09		0.08	21.19			0.01		0.04	97.51
MF143_C -95	0.01	41.50			0.01	34.65	0.02	0.03	21.03					0.01	97.25
MF143_D -105		0.79				43.70	0.03	0.20	51.40						96.11
MF143_D -106		0.47			0.05	43.98	0.01	0.16	51.85	0.02				0.01	96.53
MF143_D -107	0.06	41.18				34.22	0.01	0.10	21.21						96.76
MF143_D -108		42.31			0.02	34.11		0.15	20.82			0.01	0.02		97.43
MF143_D -109	0.02	40.58				34.24	0.01		21.66						96.51
MF143_D -96					0.05	44.23		0.27	51.08			0.01	0.01	0.01	95.66
MF143_D -97	0.05	0.33			0.06	44.42		0.17	51.46			0.02	0.01	0.05	96.56
MF143_D -98					0.01	43.76	0.04	0.20	51.65			0.01	0.01		95.67

Sulfide Data -continued

Sample ID	Ag	As	Au	Bi	Cu	Fe	Ni	Pb	S	Sb	Sn	Ti	W	Zn	Total
MF143_D -99		0.89				38.97		0.15	42.68			0.01	0.03		82.72
11-11 143.82_A -28			0.06			45.85	0.02	0.10	54.72			0.01		0.02	100.77
11-11 143.82_A -29		1.33				43.90	0.01	0.21	53.56					0.06	99.08
11-11 143.82_A -30		1.05				45.32		0.17	54.07	0.01		0.01			100.64
11-11 143.82_A -31	0.02	1.08				45.07		0.25	53.48					0.02	99.93
11-11 143.82_A -32					0.02	45.47		0.18	54.82					0.04	100.54
11-11 143.82_A -33	0.01	0.67			0.26	47.32	0.03	2.11	0.13	0.06				2.27	52.86
11-11 143.82_A -34					0.03	43.65		0.20	49.03	0.01				0.03	92.94
11-11 143.82_A -35	0.04				0.05	44.25	0.01	0.13	5				0.01	0.04	94.51
11-11 143.82_A -36						45.63	0.03	0.19	55.02	0.01				0.10	100.98
11-11 143.82_A -37	0.01	0.59			0.25	46.98	0.04	1.64	0.21	0.06				3.26	53.03
11-11 143.82_A -38	0.01			0.15	0.01	38.60	0.01	0.02	0.03					0.02	38.85
11-11 143.82_A -39	0.01					45.13		0.23	54.84					0.01	100.22
11-11 143.82_A -40	0.01				0.01	45.45		0.25	55.07			0.01	0.02	0.01	100.82
11-11 143.82_A -41	0.01					45.60	0.01	0.19	55.56						101.37
11-11 143.82_A -42	0.02					45.18		0.17	54.90						100.27
11-11 143.82_A -43				0.03		41.53		0.05	0.01	0.01		0.01	0.02		41.64
11-11 143.82_A -44		0.08				49.40		0.75	0.16					0.71	51.10
11-11 143.82_A -45		0.11				45.36		0.16	54.20						99.83
11-11 143.82_A -46	0.02	0.54				45.29		0.17	54.00	0.02			0.04		100.08
11-11 143.82_A -47		0.19			0.04	45.37		0.19	54.26	0.01		0.01	0.03		100.09
11-11 143.82_A -48	0.01	0.08				45.57		0.23	54.85			0.01			100.76
11-11 143.82_A -49					0.01	45.35		0.20	54.85	0.01					100.43
11-11 143.82_B -90						0.50		83.80	13.51	0.10					97.90

Sulfide Data -continued

Sample ID	Ag	As	Au	Bi	Cu	Fe	Ni	Pb	S	Sb	Sn	Ti	W	Zn	Total
11-11 143.82_B -91	0.12				0.04	0.01		84.26	13.63	0.19		0.01			98.25
11-11 143.82_B -92						0.04	0.02	65.13				0.01			65.20
11-11 143.82_B -53	0.04							83.79	13.45	0.15					97.44
11-11 143.82_B -54	0.02					0.01	0.01	82.79	13.23	0.09		0.02			96.18
11-11 143.82_C -55					0.03	45.15	0.01	0.18	52.58			0.01	0.03	0.01	97.99
11-11 143.82_D -56						45.46		0.19	52.92						98.57
11-11 143.82_D -57						45.22	0.02	0.15	52.33	0.02		0.01			97.74
11-11 143.82_D -58	0.12					2.86		84.21	13.93	0.28					101.40
11-11 143.82_D -59			0.01	0.06		0.01		0.06		0.04		0.01			0.20
11-11 143.82_D -60						45.26		0.21	52.36				0.02	0.05	97.90
11-11 143.82_D -61						45.40		0.19	52.61					0.01	98.20
11-11 143.82_E -62		0.24				45.42		0.20	52.65	0.01					98.52
11-11 143.82_E -59						45.58		0.20	52.71				0.02	0.01	98.52
11-11 143.82_E -64						44.51	0.01	0.19	52.82			0.01			97.54
11-11 143.82_E -65		0.81			0.01	45.25	0.02	0.22	52.35	0.01					98.66
11-11 143.82_E -66				0.03	0.03	45.35	0.01	0.14	52.85	0.02			0.04		98.47
11-11 143.82_E -67						45.42	0.06	0.13	53.05						98.66
F140a_A -4	0.03	43.10			0.03	35.34	0.08	0.06	22.33	0.01		0.01	0.04		101.02
F140a_A -5	0.02	43.80				35.29	0.02	0.15	22.49	0.08		0.01		0.03	101.88
F140a_A -6	0.02	43.38			0.01	35.16	0.01	0.12	22.26	0.04		0.02			101.01
F140a_A -7		43.40			0.01	35.09	0.01	0.14	22.19	0.02		0.01	0.02		100.86
F140a_A -8	0.01	43.84		0.08		35.03	0.01	0.07	21.97	0.02		0.01			101.04
F140a_A -13	0.03	43.81				34.82	0.01	0.15	22.04			0.02	0.01	0.01	100.90
F140a_B-14		41.33				35.58		0.11	24.09			0.01	0.04	0.01	101.18

Sulfide Data -continued

Sample ID	Ag	As	Au	Bi	Cu	Fe	Ni	Pb	S	Sb	Sn	Ti	W	Zn	Total
F140a_B-15	0.04	40.18				35.62	0.01	0.10	24.53	0.04		0.01	0.02	0.04	100.58
F140a_B-16	0.05	44.03				34.90	0.01	0.13	22.14	0.01		0.01			101.28
F140a_B-17	0.05	44.01			0.03	34.94		0.10	22.20				0.04		101.38
F140a_B-18	0.04	33.51			0.09	22.49	0.01	0.05	0.16	0.02			0.02	0.02	56.42
F140a_B-19	0.04	42.11				35.48	0.01	0.10	23.83	0.03					101.59
F140a_B-20	0.03	21.20			0.18	17.30		0.04	0.35				0.05	0.01	39.17
F140a_B-21		26.93		0.09	0.30	21.77	0.01	0.04	0.35	0.04			0.01	0.01	49.55
F140a_B-22	0.03	42.37				35.39	0.01	0.05	23.86			0.01	0.02		101.74
F140a_B-23		44.19				35.11	0.01	0.04	22.33	0.02			0.04		101.74
F140a_B-24		42.92				35.17	0.01	0.13	22.92	0.02				0.04	101.21
F140a_B-25		43.92				35.13		0.14	22.44			0.03			101.66
F140a_B-26		43.73		0.12		33.06	0.72	0.11	21.67	0.04		0.01	0.02		99.48
F140a_B-27	0.01	32.45				22.99			0.10	0.03			0.03		55.62
F140a_B -9		44.93			0.04	34.99		0.08	21.90	0.02					101.96
F140a_B -10	0.01	44.58				34.78	0.02		21.75	0.02		0.01		0.03	101.19
F140a_B -11		44.18			0.03	34.52	0.01	0.10	21.44			0.01			100.28
F140a_B -12	0.03	42.16			0.03	34.59		0.05	22.53			0.01			99.40
F171_A -68		0.49			0.01	45.18		0.28	52.52						98.48
F171_A -69		0.03		0.03		45.32	0.02	0.23	53.16					0.03	98.82
F171_A -70	0.04					45.37		0.17	53.12	0.01			0.01	0.02	98.73
F171_A -71	0.03	0.34				45.43		0.21	52.93						98.94
F171_A -72		0.04				45.49		0.23	53.33			0.01	0.02		99.10
F171_A -73	0.02	0.40				45.12	0.01	0.18	52.84				0.03	0.10	98.71
F171_A -74	0.05	42.69				35.13		0.11	22.03	0.01					100.02

Sulfide Data -continued

Sample ID	Ag	As	Au	Bi	Cu	Fe	Ni	Pb	S	Sb	Sn	Ti	W	Zn	Total
F171_A -75		43.96		0.10	0.02	34.85		0.08	21.78				0.02	0.01	100.82
F171_A -76	0.04	42.86			0.01	35.01		0.06	22.09			0.01	0.04		100.11
F171_A -77		43.10			0.01	35.02		0.05	21.83	0.03			0.10		100.14
F171_A -78		45.20				34.71		0.14	20.72						100.77
F171_A -79		43.56				34.88	0.01	0.11	21.43				0.02		100.01
F171_A -80	0.08	32.84			0.02	20.68		0.08	0.02					0.04	53.76
F171_A -81		30.18		0.01	0.03	20.71	0.01	0.06	0.03				0.04	0.03	51.09
F171_A -82		43.21				35.08			21.88			0.02	0.02	0.02	100.23
F171_A -83		0.38		0.07	0.03	45.45		0.21	52.66			0.01			98.81
F171_A -84	0.03	1.19			0.02	45.07		0.15	52.19			0.02			98.68
F171_A -85	0.04	1.19			0.03	45.20		0.31	52.83			0.01			99.60
F171_A -86		43.36				34.90		0.10	21.31	0.01		0.01	0.01	0.01	99.71
F171_A -87		34.31			0.01	21.12		0.03	0.02				0.02		55.52
F171_A -88	0.03	44.36		0.06	0.02	34.51		0.03	21.16				0.03	0.03	100.23
F171_A -89	0.04	39.16				34.65		0.10	21.49			0.02		0.09	95.53

APPENDIX C

Microthermometry Data

Microthermometric Data

AREA	SAMPLE ID	TYPE	FIA No.	PHASE	FILL	TmCO ₂	Tfm	Tmi	Tmclath	wt. % NaCl. Eq.	Th _{CO2}	Th _{TOT}
GZ	50.6 Ai	H ₂ O+CO ₂ +NaCl	24	Apy	50							228.5
GZ	50.6 Ai	H ₂ O+CO ₂ +NaCl	24	Apy	65		-6.7	-1.3		2.2		234.1
GZ	50.6 Ai	H ₂ O+CO ₂ +NaCl	24	Apy	65			-0.2		0.4		236.0
GZ	50.6 Ai	H ₂ O+CO ₂ +NaCl	24	Apy	65			-0.2		0.4		236.0
GZ	50.6 Aii	H ₂ O+CO ₂ +NaCl	25	Apy	60	216.0		-2.1		3.5		217.8
GZ	50.6 Aii	H ₂ O+CO ₂ +NaCl	26	Apy	80		-4.6	-2.8		4.6		196.0
GZ	50.6 Aii	H ₂ O+CO ₂ +CH ₄ +NaCl	27	Apy	50	-58.2			9.3	1.4	24.9	280+
GZ	50.6 Bi	H ₂ O+CO ₂ +CH ₄ +NaCl	28	Apy	50	-58.2			7.6	4.7	24.0	276.0
GZ	50.6 Bi	H ₂ O+CO ₂ +CH ₄ +NaCl	28	Apy	50	-57.6			8.9	2.2	24.0	288.0
GZ	50.6 Bi	H ₂ O+CO ₂ +CH ₄ +NaCl	28	Apy	50				9.8	0.4	24.0	303.0
GZ	50.6 Bi	H ₂ O+CO ₂ +CH ₄ +NaCl	28	Apy	50				9.8	0.4	24.0	
GZ	50.6 Bi	H ₂ O+CO ₂ +CH ₄ +NaCl	29	Apy	50	-58.0			9.8	0.4	23.3	310+
GZ	153.12ii C QA	H ₂ O+CO ₂ +NaCl	45	Apy	75		-2.1	-1.4		2.4		351.0
GZ	153.12ii C QB	H ₂ O+CO ₂ +CH ₄ +NaCl	46	Apy	65	-57.2			9.7	0.6	24.0	280.5
GZ	153.12ii C QB	H ₂ O+CO ₂ +CH ₄ +NaCl	46	Apy	50	-57.2			9.7	0.6	24.2	285.1
MZ	49.3 A	H ₂ O+CO ₂ +NaCl	1	veinlet	75							244.0
MZ	49.3 A	H ₂ O+CO ₂ +NaCl	2	veinlet	95						258.6	244.0
MZ	49.3 A	H ₂ O+CO ₂ +NaCl+CH ₄	3	veinlet	60						24.2	160.0
MZ	49.3 A	H ₂ O+CO ₂ +CH ₄ +NaCl	4	veinlet	60				9.9	0.2	26.0	250+
MZ	49.3 A	H ₂ O+CO ₂ +CH ₄ +NaCl	5	veinlet	50			-0.9		1.6	24.0	

Microthermometric Data -continued

MZ	49.3 A	H ₂ O+CO ₂ +CH ₄ +NaCl	6	veinlet	60						24.0	
MZ	49.3 A	H ₂ O+CO ₂ +CH ₄ +NaCl	6	veinlet	60						24.0	
MZ	49.3 A	H ₂ O+CO ₂ +NaCl	6	veinlet	80							140.0
MZ	F028-1 Ai	H ₂ O+CO ₂ +CH ₄ +NaCl	7	vug	50			-1.0	8.5	3.0	23.0	281.0
MZ	F028-1 Ai	H ₂ O+CO ₂ +CH ₄ +NaCl	7	vug	50						23.0	281.0
MZ	F028-1 Ai	H ₂ O+CO ₂ +CH ₄ +NaCl	7	vug	50	-62.4			9.8	0.4	23.0	297.0
MZ	F028-1 Ai	H ₂ O+CO ₂ +CH ₄ +NaCl	7	vug	75	-74.0		-1.0	8.5	3.0		250+
MZ	F028-1 Ai	H ₂ O+CO ₂ +NaCl	8	vug	70	-57.9		-4.8		7.6		247.0
MZ	F028-1 Ai	H ₂ O+CO ₂ +CH ₄ +NaCl	8	vug	75			-1.0	8.5	3.0		247.0
MZ	F028-1 Ai	H ₂ O+CO ₂ +NaCl+CH ₄	8	vug	80				10.7	0.0		230.0
MZ	F028-1 Ai	H ₂ O+CO ₂ +NaCl+CH ₄	8	vug	80	-78.8			10.7	0.0		237.0
MZ	F028-1 Ai	H ₂ O+CO ₂ +NaCl+CH ₄	8	vug	80				10.7	0.0		237.0
MZ	F028-1 Ai	H ₂ O+CO ₂ +NaCl	8	vug	80			-1.0			1.7	240.0
MZ	F028-1 Aiii	H ₂ O+CO ₂ +NaCl+CH ₄	9	vug	90				8.2	3.6		201.5
MZ	F028-1 Aiii	H ₂ O+CO ₂ +NaCl+CH ₄	9	vug	90				8.2	3.6		237.0
MZ	F028-1 Aiii	H ₂ O+CO ₂ +CH ₄ +NaCl	10	vug	60		-4.0	-1.4	10.8	0.0		299.0
MZ	F028-1 Aiii	H ₂ O+CO ₂ +CH ₄ +NaCl	10	vug	50		-3.1	-1.0	10.8	0.0		250+
MZ	F028-1 C	H ₂ O+CO ₂ +NaCl	11	vug	85			-4.5			7.2	171.2
MZ	F028-1 E	H ₂ O+CO ₂ +NaCl+CH ₄	12	Au	90			-2.9	10.0	4.8		190.0
MZ	F028-1 E	H ₂ O+CO ₂ +NaCl	12	Au	90		-2.9	-2.7			4.5	190.0
MZ	F028-1 E	H ₂ O+CO ₂ +NaCl	12	Au	90			-4.0			6.4	190.0
MZ	F028-1 E	H ₂ O+CO ₂ +NaCl	13	Au	90			-2.9			4.8	227.0

Microthermometric Data -continued

MZ	F028-1 E	H ₂ O+CO ₂ +NaCl	13	Au	90							227.0
MZ	F028-1 E	H ₂ O+CO ₂ +NaCl	13	Au	90							227.0
MZ	F028-1 E	H ₂ O+CO ₂ +NaCl+CH ₄	14	Au	90				3.0	11.9		157.0
MZ	F028-1 E	H ₂ O+CO ₂ +NaCl+CH ₄	14	Au	90			-2.5	0.6	4.2		167.0
MZ	F028-1 E	H ₂ O+CO ₂ +NaCl+CH ₄	15	Au	80			-6.8	-2.7	9.1	4.5	221.5
MZ	F028-1 E	H ₂ O+CO ₂ +CH ₄ +NaCl	16	Au	65	-58.4			8.6	2.8	20.9	297.0
MZ	F026-1 A	H ₂ O+CO ₂ +NaCl+CH ₄	17	Au	90				9.5	1.0		237.3
MZ	F026-1 A	H ₂ O+CO ₂ +NaCl	17	Au	90			-2.8		4.6		237.3
MZ	F026-1 A	H ₂ O+CO ₂ +NaCl+CH ₄	17	Au	75				9.5	1.0		247.0
MZ	F026-1 A	H ₂ O+CO ₂ +NaCl+CH ₄	17	Au	90				9.0	2.0		247.0
MZ	F026-1 A	H ₂ O+CO ₂ +NaCl	18	Au	95			0.0		0.0		144.5
MZ	F026-1 A	H ₂ O+CO ₂ +CH ₄ +NaCl	19	Au	50				9.4	1.2		250+
MZ	99.66-1 B	H ₂ O+CO ₂ +NaCl	20	Apy	70			-8.5	-2.8		4.6	206.9
MZ	99.66-1 B	H ₂ O+CO ₂ +NaCl+CH ₄	20	Apy	70			-11.5	-2.4	7.2	4.0	210.7
MZ	F030-1 C	H ₂ O+CO ₂ +NaCl+CH ₄	30	Au	60				-0.9	10.8	1.6	265.0
MZ	F030-1 C	H ₂ O+CO ₂ +NaCl+CH ₄	30	Au	60	-64.0	-5.4	-1.8	10.8	3.1		265.0
MZ	F030-1 C	H ₂ O+CO ₂ +NaCl+CH ₄	30	Au	60				10.8	0.0		265.0
MZ	F030-1 C	H ₂ O+CO ₂ +NaCl+CH ₄	30	Au	60				10.8	0.0		265.0
MZ	F030-1 C	H ₂ O+CO ₂ +NaCl	31	Au	60			-5.5	-1.8		3.1	202.1
MZ	F030-1 C	H ₂ O+CO ₂ +NaCl	31	Au	60			-4.6	-2.1		3.5	213.1
MZ	F030-1 C	H ₂ O+CO ₂ +NaCl+CH ₄	32	Au	60				-1.4	10.5	2.4	234.3
MZ	F030-1 C	H ₂ O+CO ₂ +NaCl+CH ₄	32	Au	60				-1.8	9.8	3.1	238.9
MZ	F030-1 C	H ₂ O+CO ₂ +NaCl	33	Au	60				-1.1		1.9	250.0

Microthermometric Data -continued

MZ	F030-2 A	H ₂ O+CO ₂ +NaCl	34	Au	80							250.0
MZ	F030-2 A	H ₂ O+CO ₂ +CH ₄ +NaCl	35	Au	60	-57.4		-2.1	10.2	0.0	23.4	250+
MZ	F030-2 A	H ₂ O+CO ₂ +CH ₄ +NaCl	36	Au	45	-57.6					24.3	250+
MZ	F030-2 A	H ₂ O+CO ₂ +CH ₄ +NaCl	36	Au	50	-57.6					24.3	250+
MZ	F030-2 A	H ₂ O+CO ₂ +CH ₄ +NaCl	36	Au	60	-57.6					24.3	250+
MZ	F030-2 A	H ₂ O+CO ₂ +CH ₄ +NaCl	36	Au	60	-57.6					24.3	250+
MZ	F030-2 A	H ₂ O+CO ₂ +CH ₄ +NaCl	36	Au	60	-57.2					24.3	250+
MZ	F030-2 A	H ₂ O+CO ₂ +CH ₄ +NaCl	36	Au	65	-57.2					24.3	250+
MZ	F030-2 A	H ₂ O+CO ₂ +CH ₄ +NaCl	36	Au	70	-57.6					24.3	250+
MZ	F030-2 A	H ₂ O+CO ₂ +NaCl	37	Au	75							200.6
MZ	F030-2 A	H ₂ O+CO ₂ +NaCl	37	Au	80		-5.1	-2.7		4.5		204.5
MZ	F030-2 A	H ₂ O+CO ₂ +NaCl	37	Au	80			-3.2		5.3		204.5
MZ	F026-1ii A QD	H ₂ O+CO ₂ +CH ₄ +NaCl	37	vug	50	-57.3			9.7	0.6	20.1	291.0
MZ	F026-1ii A QD	H ₂ O+CO ₂ +CH ₄ +NaCl	37	vug	60	-58.6			9.7	0.6	20.1	291.0
MZ	F026-1ii A QD	H ₂ O+CO ₂ +CH ₄ +NaCl	37	vug	60	-58.6			9.7	0.6	19.3	295.0
MZ	F026-1ii A QA	H ₂ O+CO ₂ +CH ₄ +NaCl	37	vug	60	-57.4			9.6	0.8	21.9	250+
MZ	F026-1ii A QA	H ₂ O+CO ₂ +CH ₄ +NaCl	37	vug	65	-57.4			9.6	0.8	21.9	250+
MZ	F026-1ii A QC	H ₂ O+CO ₂ +CH ₄ +NaCl	37	vug	50				9.7	0.6	24.0	250+
MZ	F026-1ii A QC	H ₂ O+CO ₂ +CH ₄ +NaCl	37	vug	60	-57.5			10.2	0.0	21.3	250+
MZ	F026-1ii A QD	H ₂ O+CO ₂ +CH ₄ +NaCl	37	vug	65				8.7	2.6		d280.2
MZ	F026-1ii A QC	H ₂ O+CO ₂ +CH ₄ +NaCl	37	vug	60	-57.5			11.0	0.0	21.8	
MZ	F026-1ii A QA	H ₂ O+CO ₂ +NaCl+CH ₄	38	vug	90			-1.6	10.2	2.7		187.0
MZ	F026-1ii A QD	H ₂ O+CO ₂ +NaCl	39	vug	95							214.6

Microthermometric Data -continued

MZ	F026-1ii B QB	H ₂ O+CO ₂ +NaCl	40	Au	80			-3.6		5.9		232.0
MZ	F026-1ii B QB	H ₂ O+CO ₂ +NaCl	41	Au	80			-2.1		3.5		193.0
MZ	F026-1ii B QB	H ₂ O+CO ₂ +NaCl	41	Au	80			-2.1		3.5		207.0
MZ	F026-1ii C QA	H ₂ O+CO ₂ +NaCl	42	vug	85			-0.8		1.4		217.0
MZ	F026-1ii C QA	H ₂ O+CO ₂ +CH ₄ +NaCl	43	vug	60				9.8	0.4	23.0	298.0
MZ	F026-1ii C QA	H ₂ O+CO ₂ +NaCl	44	vug	70			-0.2		0.4		238.0
MZ	227.75ii A QA	H ₂ O+CO ₂ +CH ₄ +NaCl	47	Py	50	-62.9			10.1	0.0	12.5	311.0
MZ	227.75ii A QA	H ₂ O+CO ₂ +CH ₄ +NaCl	47	Py	50	-58.4			10.1	0.0	12.5	311.0
MZ	227.75ii A QA	H ₂ O+CO ₂ +CH ₄ +NaCl	47	Py	50	-58.4			10.1	0.0	12.5	311.0
MZ	227.75ii A QA	H ₂ O+CO ₂ +CH ₄ +NaCl	47	Py	60	-62.0			10.1	0.0	12.5	311.0
MZ	F028-1ii A QA	H ₂ O+CO ₂ +NaCl+CH ₄	48	vug	70	-57.5		-1.1	8.7	1.9		231.0
MZ	F028-1ii A QA	H ₂ O+CO ₂ +NaCl+CH ₄	48	vug	70				9.3	1.4		236.0
MZ	F028-1ii A QA	H ₂ O+CO ₂ +NaCl+CH ₄	48	vug	70	-57.5	-5.3	-1.1	9.3	1.9		245.0
MZ	F028-1ii A QA	H ₂ O+CO ₂ +CH ₄ +NaCl	49	vug	70	-57.4			9.8	0.4	24.3	270.0
MZ	F028-1ii A QA	H ₂ O+CO ₂ +CH ₄ +NaCl	49	vug	60				9.8	0.4	24.3	295.0
MZ	F028-1ii A QA	H ₂ O+CO ₂ +NaCl	50	vug	80							220.0
MZ	F028-1ii A QA	H ₂ O+CO ₂ +NaCl	51	vug	65			-2.6		4.3		
MZ	F028-2ii A QA	H ₂ O+CO ₂ +CH ₄ +NaCl	52	Au	50	-58.3			9.6	0.8	22.9	298.0
MZ	F028-2ii A QA	H ₂ O+CO ₂ +CH ₄ +NaCl	52	Au	50	-58.3			9.6	0.8	23.1	298.0
MZ	F028-2ii A QA	H ₂ O+CO ₂ +CH ₄ +NaCl	52	Au	50	-58.3			9.6	0.8	23.1	298.0
MZ	F028-2ii A QA	H ₂ O+CO ₂ +CH ₄ +NaCl	52	Au	50	-58.2			9.6	0.8	23.1	298.0
MZ	F028-2ii A QA	H ₂ O+CO ₂ +CH ₄ +NaCl	52	Au	50	-57.5			9.8	0.4	24.0	d290.2
MZ	F028-2ii B QB	H ₂ O+CO ₂ +CH ₄ +NaCl	53	Au	50	-58.2			9.5	1.0	18.6	296.0

Microthermometric Data -continued

MZ	F028-2ii B QB	H ₂ O+CO ₂ +CH ₄ +NaCl	53	Au	60	-58.2			9.5	1.0	18.6	296.0
MZ	F028-2ii B QB	H ₂ O+CO ₂ +CH ₄ +NaCl	53	Au	60	-58.2			9.5	1.0	18.6	296.0
MZ	F028-2ii B QB	H ₂ O+CO ₂ +CH ₄ +NaCl	53	Au	50	-58.2			9.5	1.0	20.4	296.0
MZ	F028-3ii C	H ₂ O+CO ₂ +NaCl	54	Au	85	-57.1		-2.6		4.3		188.2
MZ	F028-3ii C	H ₂ O+CO ₂ +NaCl	54	Au	90	-57.1		-2.6		4.3		207.2
MZ	F028-3ii C	H ₂ O+CO ₂ +CH ₄ +NaCl	55	Au	75	-56.6			10.1	0.0	22.5	304.0
MZ	F028-3ii C	H ₂ O+CO ₂ +CH ₄ +NaCl	55	Au	45	-56.6			10.1	0.0	22.6	304.0
MZ	F028-3ii C	H ₂ O+CO ₂ +CH ₄ +NaCl	55	Au	75	-56.6			10.1	0.0	22.6	304.0
MZ	F028-3ii C	H ₂ O+CO ₂ +CH ₄ +NaCl	56	Au	80	-58.2		-2.9		1.2		253.0
SG	F140a-1 A	H ₂ O+CO ₂ +CH ₄ +NaCl	21	vug	60	-58.6	-5.8		10.6	0.0	15.1	305.0
SG	F140a-1 A	H ₂ O+CO ₂ +CH ₄ +NaCl	21	vug	50	-60.1			7.8	4.3	16.0	306.0
SG	F140a-1 A	H ₂ O+CO ₂ +CH ₄ +NaCl	22	vug	75	-58.6	-5.2	-1.8	10.2	3.1		245.7
SG	F140a-1 A	H ₂ O+CO ₂ +NaCl	23	vug	90							188.2
SG	F140a-1 A	H ₂ O+CO ₂ +NaCl	23	vug	90			-2.9		4.8		199.4
SG	F140a-2ii E	H ₂ O+CO ₂ +CH ₄ +NaCl	57	vug	60	-58.2			10.6	0.0	17.8	292.0
SG	F140a-2ii E	H ₂ O+CO ₂ +CH ₄ +NaCl	57	vug	50	-58.2			10.6	0.0	19.4	292.0
SG	F140a-2ii E	H ₂ O+CO ₂ +CH ₄ +NaCl	57	vug	60	-58.2			10.6	0.0	19.4	292.0
SG	F140a-2ii E	H ₂ O+CO ₂ +CH ₄ +NaCl	57	vug	50	-58.0			10.6	0.0	20.7	292.0
SG	F140a-2ii E	H ₂ O+CO ₂ +CH ₄ +NaCl	57	vug	75	-60.1			9.7	0.6	15.6	301.0
SG	F140a-2ii E	H ₂ O+CO ₂ +CH ₄ +NaCl	57	vug	70	-58.2			10.6	0.0	17.8	306.0
SG	F140a-2ii E	H ₂ O+CO ₂ +NaCl	58	vug	70			-0.4		0.7		358.0

APPENDIX D

Oxygen Isotope Data

Summary of oxygen stable isotope data obtained using the SIMS technique (QX = quartz generation).

Sample ID	$\delta^{18}\text{O}$ (SMOW)	2 σ (‰) inter- session	QX	Sample ID	$\delta^{18}\text{O}$ (SMOW)	2 σ (‰) inter- session	QX	Sample ID	$\delta^{18}\text{O}$ (SMOW)	2 σ (‰) inter- session	QX	Sample ID	$\delta^{18}\text{O}$ (SMOW)	2 σ (‰) inter- session	QX
3A-10-01 95.1	16.25	0.23	1	3A-10-01 95.1	16.59	0.14	4	3A-11-11 81.94	16.22	0.19	4	SCW_11_F027	17.92	0.17	4
3A-10-01 95.1	16.64	0.14	1	3A-10-01 95.1	16.69	0.18	4	3A-11-11 81.94	16.79	0.20	4	SCW_11_F027	17.93	0.19	4
3A-10-01 95.1	16.82	0.18	1	3A-10-01 95.1	16.69	0.15	4	3A-11-11 81.94	17.04	0.17	4	SCW_11_F027	17.95	0.16	4
3A-10-01 95.1	16.95	0.18	1	3A-10-01 95.1	16.72	0.17	4	3A-11-11 81.94	17.23	0.16	4	SCW_11_F027	18.04	0.17	4
3A-10-01 95.1	17.42	0.17	1	3A-10-01 95.1	16.75	0.16	4	3A-11-11 81.94	17.52	0.17	4	SCW_11_F027	18.09	0.17	4
3A-10-01 95.1	16.82	0.16	2	3A-10-01 95.1	16.79	0.16	4	3A-11-11 81.94	17.64	0.22	4	SCW_11_F027	18.23	0.21	4
3A-10-01 95.1	16.84	0.19	2	3A-10-01 95.1	16.93	0.17	4	3A-11-11 81.94	20.28	0.14	5	SCW_11_F028-2	17.57	0.16	1
3A-10-01 95.1	16.85	0.16	2	3A-10-01 95.1	16.95	0.15	4	SCW_11_F027	17.54	0.16	2	SCW_11_F028-2	17.63	0.15	1
3A-10-01 95.1	16.85	0.16	2	3A-10-01 95.1	16.95	0.17	4	SCW_11_F027	17.67	0.17	2	SCW_11_F028-2	17.65	0.16	1
3A-10-01 95.1	16.90	0.18	2	3A-10-01 95.1	16.96	0.15	4	SCW_11_F027	17.84	0.14	2	SCW_11_F028-2	17.67	0.16	1
3A-10-01 95.1	16.93	0.14	2	3A-10-01 95.1	17.05	0.18	4	SCW_11_F027	17.86	0.15	2	SCW_11_F028-2	17.70	0.17	1
3A-10-01 95.1	17.00	0.17	2	3A-10-01 95.1	17.07	0.15	4	SCW_11_F027	17.95	0.17	2	SCW_11_F028-2	17.74	0.14	1
3A-10-01 95.1	17.03	0.16	2	3A-10-01 95.1	17.08	0.17	4	SCW_11_F027	18.04	0.17	2	SCW_11_F028-2	17.78	0.16	1
3A-10-01 95.1	17.06	0.15	2	3A-10-01 95.1	17.11	0.18	4	SCW_11_F027	18.08	0.17	2	SCW_11_F028-2	17.81	0.18	1
3A-10-01 95.1	17.24	0.16	2	3A-10-01 95.1	17.15	0.18	4	SCW_11_F027	18.08	0.17	2	SCW_11_F028-2	18.06	0.17	1
3A-10-01 95.1	17.32	0.17	2	3A-10-01 95.1	17.30	0.15	4	SCW_11_F027	18.10	0.18	2	SCW_11_F028-2	17.66	0.15	2
3A-10-01 95.1	17.33	0.17	2	3A-10-01 95.1	17.30	0.15	4	SCW_11_F027	17.75	0.18	3	SCW_11_F028-2	17.80	0.16	2
3A-10-01 95.1	16.72	0.18	3	3A-10-01 95.1	17.35	0.18	4	SCW_11_F027	17.93	0.18	3	SCW_11_F028-2	17.58	0.21	3
3A-10-01 95.1	16.78	0.14	3	3A-10-01 95.1	17.61	0.15	4	SCW_11_F027	17.96	0.21	3	SCW_11_F028-2	17.67	0.19	3
3A-10-01 95.1	16.85	0.18	3	3A-11-11 81.94	17.03	0.15	2	SCW_11_F027	17.98	0.19	3	SCW_11_F028-2	17.87	0.19	3
3A-10-01 95.1	16.86	0.17	3	3A-11-11 81.94	17.14	0.16	2	SCW_11_F027	16.91	0.17	4	SCW_11_F028-2	17.32	0.17	4
3A-10-01 95.1	17.00	0.17	3	3A-11-11 81.94	17.20	0.20	2	SCW_11_F027	17.29	0.19	4	SCW_11_F028-2	17.96	0.15	4
3A-10-01 95.1	17.05	0.16	3	3A-11-11 81.94	17.16	0.18	3	SCW_11_F027	17.53	0.17	4	SCW_11_F028-2	18.01	0.17	4
3A-10-01 95.1	17.11	0.16	3	3A-11-11 81.94	17.20	0.17	3	SCW_11_F027	17.61	0.18	4	SCW_11_F028-2	18.06	0.18	4
3A-10-01 95.1	16.38	0.17	4	3A-11-11 81.94	17.39	0.17	3	SCW_11_F027	17.68	0.15	4	SCW_11_F028-2	18.22	0.16	4
3A-10-01 95.1	16.45	0.17	4	3A-11-11 81.94	17.42	0.16	3	SCW_11_F027	17.75	0.18	4				
3A-10-01 95.1	16.57	0.17	4	3A-11-11 81.94	17.58	0.21	3	SCW_11_F027	17.83	0.16	4				

APPENDIX E

Monazite U-Pb isotope data, EDS
spectra, and BSE images

Monazite U-Pb isotope data

Sample ID	^{206}Pb (cps)	^{204}Pb (cps)	$^{207}\text{Pb}/^{206}\text{Pb}$	2σ	$^{207}\text{Pb}/^{235}\text{U}$	2σ	$^{206}\text{Pb}/^{238}\text{U}$	2σ	ρ
816-1A	3965	142	0.352	0.019	2.070	0.210	0.043	0.004	0.840
816-1B	14093	155	0.105	0.015	0.383	0.058	0.027	0.002	0.377
816-1C	12157	201	0.164	0.024	0.591	0.094	0.026	0.002	0.389
816-1D	4774	175	0.224	0.035	0.937	0.167	0.030	0.003	0.488
816-1E	13474	543	0.502	0.075	4.129	1.004	0.060	0.011	0.787
816-1F	16346	301	0.155	0.021	0.565	0.100	0.026	0.003	0.635
22775-1A	152499	10170	0.811	0.011	40.167	3.042	0.359	0.027	0.983
22775-1B	193792	11474	0.823	0.014	51.725	7.575	0.456	0.066	0.993
22775-1C	182180	11913	0.824	0.011	43.184	7.344	0.380	0.064	0.997
395-1A	16894	570	0.470	0.015	3.286	0.213	0.051	0.003	0.874
395-1B	11184	381	0.409	0.023	2.519	0.245	0.045	0.004	0.810
395-1C	8349	141	0.129	0.018	0.448	0.067	0.025	0.002	0.404
395-1D	15557	434	0.383	0.017	2.113	0.152	0.040	0.002	0.776
395-1E	13827	283	0.281	0.020	1.196	0.128	0.031	0.003	0.763
395-1F	7910	104	0.193	0.023	0.722	0.095	0.027	0.001	0.397
395-1G	1490	118	0.576	0.075	7.549	2.163	0.095	0.024	0.891
7894-1A	46748	2545	0.794	0.013	16.964	2.783	0.155	0.025	0.995
7894-1B	19068	1061	0.784	0.013	24.493	2.663	0.226	0.024	0.989

Monazite U-Pb isotope data –continued

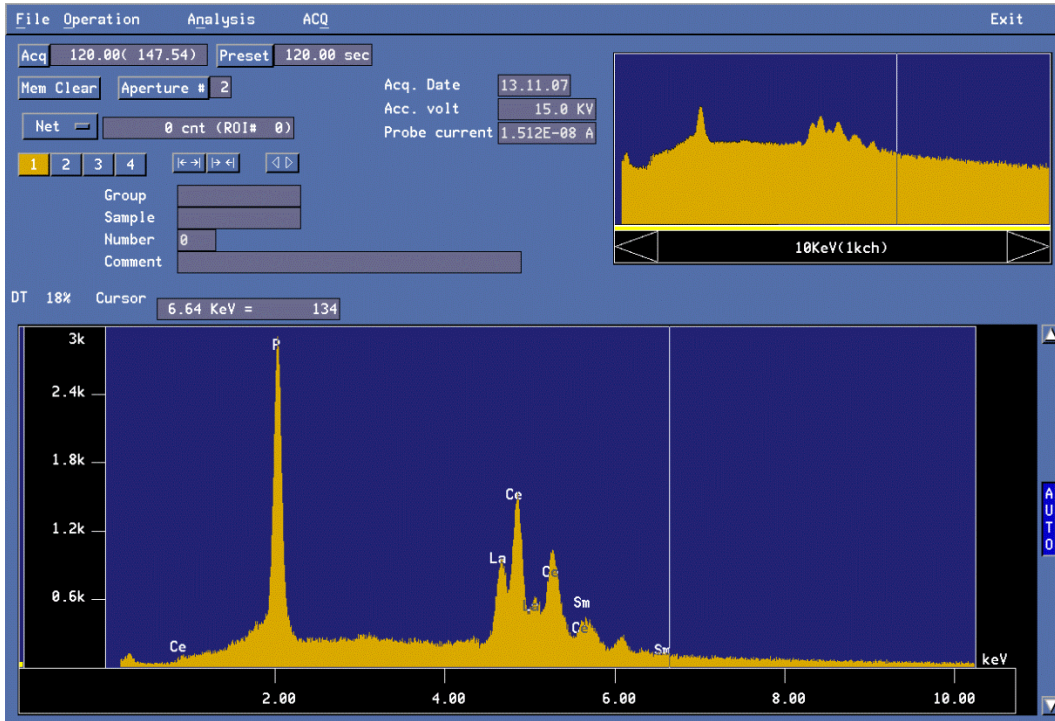
Sample ID	$^{207}\text{Pb}^*/^{206}\text{Pb}^*$	2σ	$^{207}\text{Pb}^*/^{235}\text{U}$	2σ	$^{206}\text{Pb}^*/^{238}\text{U}$	2σ	% discordance
	age (Ma)	error (Ma)	age (Ma)	error (Ma)	age (Ma)	error (Ma)	
816-1A	3717	81	1139	67	269	22	94.5
816-1B	1708	238	329	42	169	9	91.3
816-1C	2499	228	471	58	166	10	94.5
816-1D	3008	230	671	84	193	17	94.9
816-1E	4246	205	1660	182	374	69	93.6
816-1F	2403	216	455	63	168	19	94.2
22775-1A	4942	20	3775	72	1978	126	68.8
22775-1B	4962	24	4026	136	2421	287	60.7
22775-1C	4964	19	3847	156	2076	294	67.2
395-1A	4149	46	1478	49	319	18	94.4
395-1B	3942	83	1278	68	282	22	94.7
395-1C	2080	223	376	46	161	10	93.4
395-1D	3842	67	1153	48	253	14	95.1
395-1E	3369	104	799	58	196	16	95.5
395-1F	2770	185	552	54	172	9	95.0
395-1G	4449	177	2179	229	585	141	90.4
7894-1A	4911	23	2933	146	929	140	86.4
7894-1B	4894	23	3288	101	1316	127	80.1

Monazite U-Pb isotope data –continued

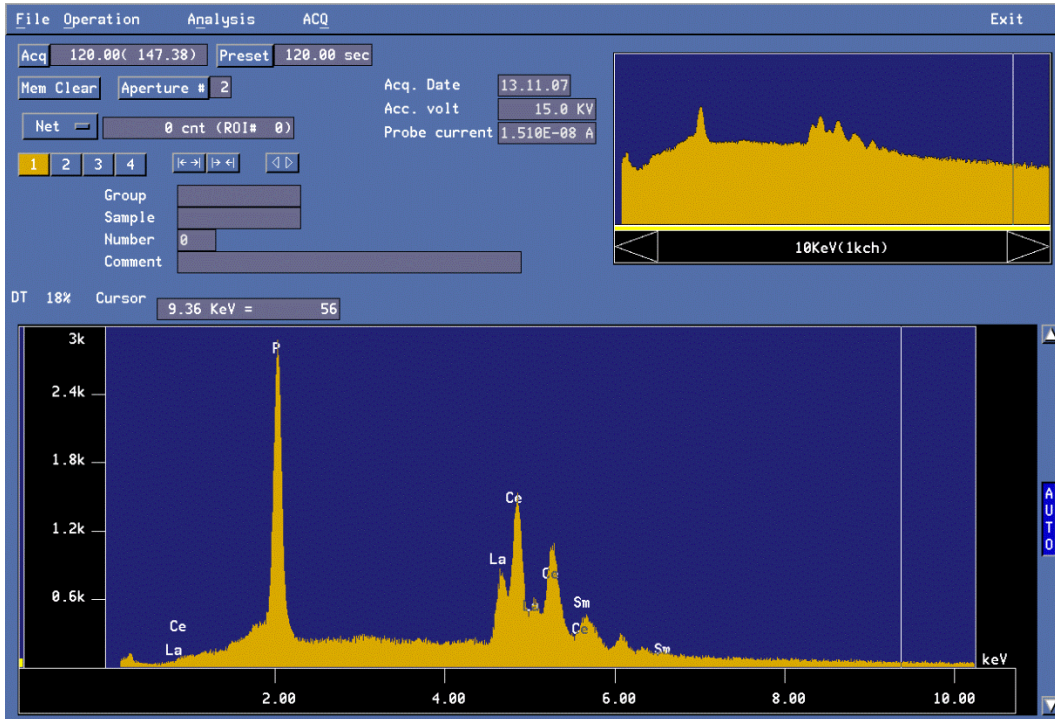
Sample ID	$^{238}\text{U}/^{206}\text{Pb}$	2 σ	$^{207}\text{Pb}/^{206}\text{Pb}$	2 σ
816-1A	23.462	1.999	0.352	0.019
816-1B	37.684	2.149	0.105	0.015
816-1C	38.296	2.367	0.164	0.024
816-1D	32.917	2.869	0.224	0.035
816-1E	16.749	3.206	0.502	0.075
816-1F	37.857	4.259	0.155	0.021
22775-1A	2.785	0.207	0.811	0.011
22775-1B	2.194	0.319	0.823	0.014
22775-1C	2.632	0.446	0.824	0.011
395-1A	19.711	1.114	0.470	0.015
395-1B	22.372	1.764	0.409	0.023
395-1C	39.590	2.391	0.129	0.018
395-1D	24.964	1.397	0.383	0.017
395-1E	32.422	2.654	0.281	0.020
395-1F	36.915	1.925	0.193	0.023
395-1G	10.522	2.687	0.576	0.075
7894-1A	6.454	1.053	0.794	0.013
7894-1B	4.416	0.475	0.784	0.013

Monazite EDS Spectra with labelled peaks

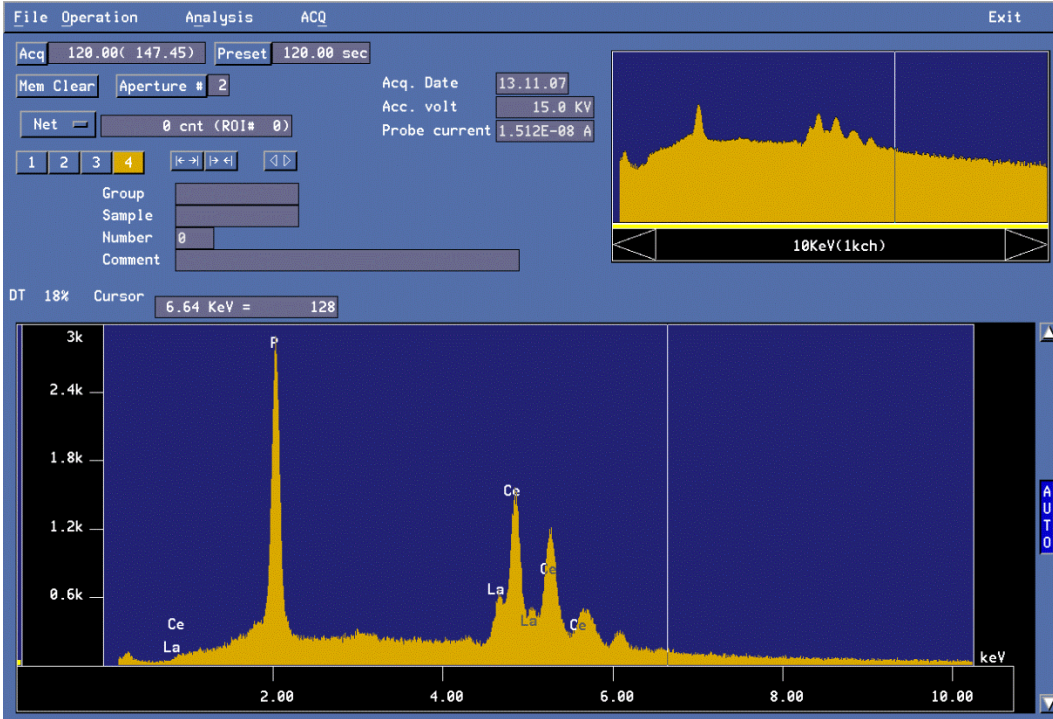
3A-10-03 3.95



3A-11-11 81.6

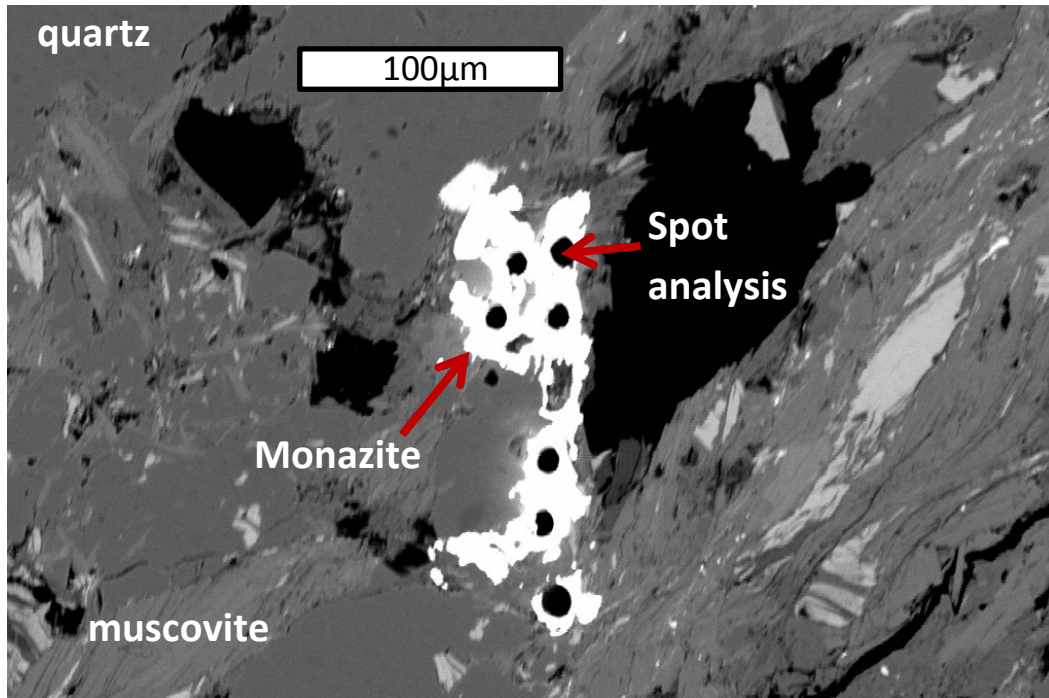


3A-11-15A 227.75

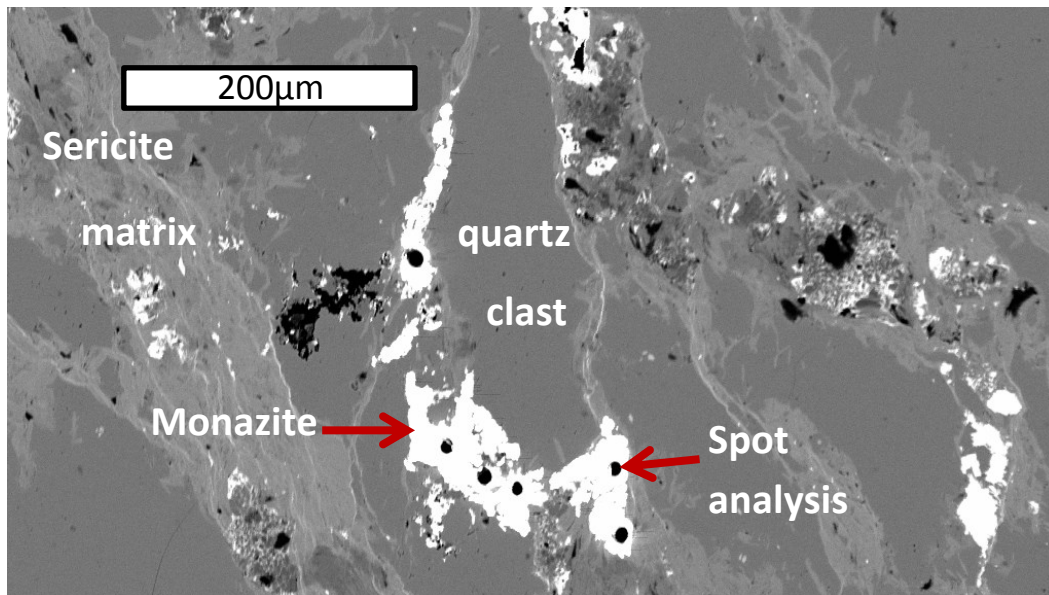


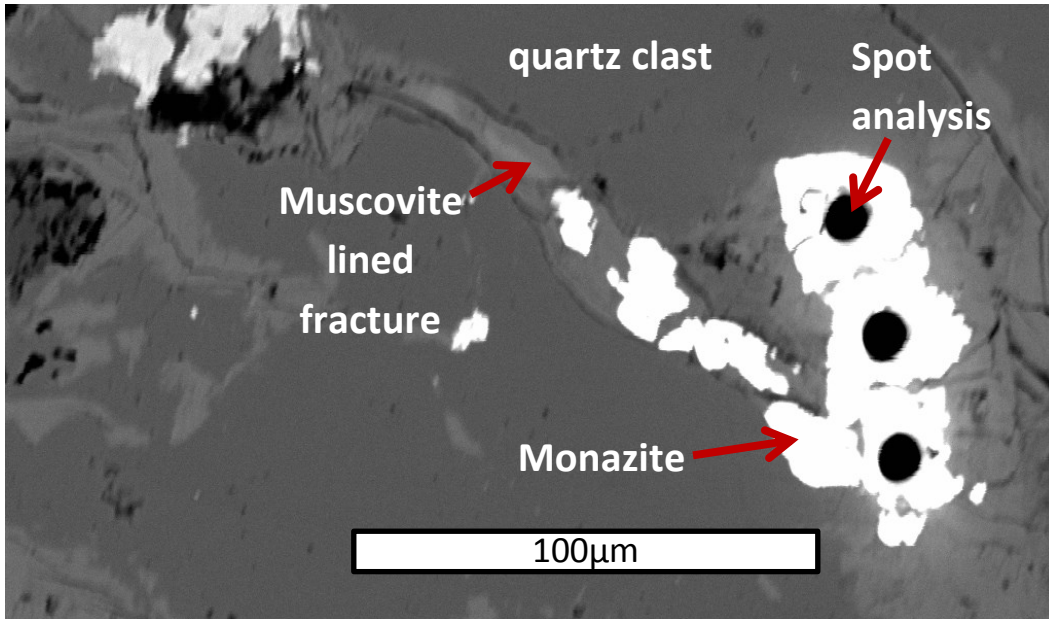
Monazite BSE images

3A-10-03 3.95



3A-11-11 81.6





APPENDIX F

Sprogge zircon U-Pb isotope data,
Inverse Concordia diagrams, and
weighted average plots

U-Pb isotope data used in Isoplot for age determination (strike-through indicates rejected data)

Sample ID	²⁰⁶ Pb (cps)	²⁰⁴ Pb (cps)	²⁰⁷ Pb/ ²⁰⁶ Pb	2 σ	²⁰⁷ Pb/ ²³⁵ U	2 σ	²⁰⁶ Pb/ ²³⁸ U	2 σ	ρ
212-8A	532379	355	0.050	0.001	0.101	0.004	0.015	0.001	0.855
212-1B	183512	134	0.049	0.001	0.103	0.004	0.015	0.001	0.899
212-4B	114777	427	0.047	0.001	0.100	0.005	0.015	0.001	0.905
212-6A	154980	164	0.049	0.001	0.104	0.005	0.015	0.001	0.852
212-4A	160760	353	0.048	0.001	0.103	0.005	0.016	0.001	0.901
212-4D	383461	352	0.048	0.001	0.102	0.004	0.016	0.001	0.906
212-5A	220050	197	0.048	0.001	0.102	0.005	0.016	0.001	0.913
212-5B	237300	180	0.048	0.001	0.102	0.004	0.016	0.001	0.898
212-9A	333849	278	0.049	0.001	0.105	0.005	0.016	0.001	0.907
212-1	198462	101	0.049	0.001	0.106	0.006	0.016	0.001	0.937
212-1C	77417	110	0.049	0.001	0.107	0.005	0.016	0.001	0.816
212-4C	160669	304	0.048	0.001	0.105	0.004	0.016	0.001	0.873
212-3	238446	127	0.048	0.001	0.107	0.005	0.016	0.001	0.919
212-3B	203590	144	0.048	0.001	0.108	0.005	0.016	0.001	0.889
212-8B	1695084	362	0.049	0.001	0.110	0.005	0.016	0.001	0.908
212-5C	292350	219	0.052	0.002	0.117	0.006	0.016	0.001	0.777
212-10A	112788	263	0.046	0.001	0.110	0.006	0.017	0.001	0.909
165-1A	276236	315	0.049	0.001	0.106	0.005	0.016	0.001	0.905
165-1B	944409	388	0.160	0.003	4.290	0.529	0.199	0.024	0.986
165-2A	84664	277	0.048	0.001	0.106	0.006	0.016	0.001	0.862
165-3A	239676	347	0.048	0.001	0.102	0.004	0.015	0.001	0.899
165-4A	529802	376	0.049	0.001	0.106	0.006	0.016	0.001	0.936
165-5A	186626	311	0.049	0.001	0.101	0.004	0.015	0.001	0.892
165-5B	195169	312	0.048	0.001	0.098	0.004	0.015	0.001	0.909
165-6A	74922	342	0.050	0.001	0.103	0.004	0.015	0.001	0.848
165-7A	254050	440	0.053	0.001	0.108	0.005	0.015	0.001	0.897
165-8A	100552	526	0.084	0.006	0.168	0.013	0.015	0.001	0.469
165-9A	432060	500	0.053	0.001	0.107	0.005	0.015	0.001	0.887
165-10A	1035514	550	0.103	0.002	1.898	0.152	0.134	0.010	0.970
165-10B	1097399	704	0.098	0.002	1.104	0.106	0.082	0.008	0.969
165-11A	116345	607	0.076	0.002	0.167	0.008	0.016	0.001	0.882
165-12A	243007	580	0.074	0.002	0.217	0.024	0.021	0.002	0.959
165-12B	352687	569	0.091	0.003	0.417	0.047	0.033	0.004	0.950
165-13A	206952	570	0.064	0.001	0.137	0.006	0.016	0.001	0.895
165-14A	242535	582	0.065	0.002	0.146	0.008	0.016	0.001	0.771
165-14B	315074	496	0.058	0.002	0.131	0.007	0.016	0.001	0.851
165-15A	447891	237	0.048	0.001	0.102	0.005	0.015	0.001	0.916
165-16A	351375	271	0.048	0.001	0.102	0.005	0.015	0.001	0.924
165-17A	163357	320	0.049	0.001	0.101	0.004	0.015	0.001	0.903
165-18A	250380	283	0.050	0.001	0.112	0.005	0.016	0.001	0.856
165-19A	395130	287	0.048	0.001	0.103	0.004	0.016	0.001	0.896
165-20A	223431	308	0.048	0.001	0.099	0.004	0.015	0.001	0.888

U-Pb isotope data used in Isoplot for age determination – continued

Sample ID	²⁰⁶ Pb (cps)	²⁰⁴ Pb (cps)	²⁰⁷ Pb/ ²⁰⁶ Pb	2 σ	²⁰⁷ Pb/ ²³⁵ U	2 σ	²⁰⁶ Pb/ ²³⁸ U	2 σ	ρ
165-21A	159950	309	0.075	0.001	1.767	0.078	0.170	0.007	0.906
165-21B	166182	280	0.075	0.001	1.820	0.079	0.176	0.007	0.902
165-22A	1433011	392	0.068	0.001	0.784	0.032	0.084	0.003	0.892
165-23A	301642	330	0.052	0.001	0.128	0.009	0.018	0.001	0.937
165-24A	424359	334	0.048	0.001	0.096	0.004	0.015	0.001	0.884
168-1A	300180	293	0.048	0.001	0.105	0.004	0.016	0.001	0.886
168-2A	1426992	248	0.090	0.002	2.383	0.145	0.192	0.011	0.955
168-3A	244844	203	0.047	0.001	0.102	0.004	0.016	0.001	0.901
168-4A	236745	256	0.047	0.001	0.100	0.004	0.015	0.001	0.899
168-5A	253683	160	0.047	0.001	0.096	0.004	0.015	0.001	0.879
168-6A	199390	131	0.047	0.001	0.100	0.004	0.016	0.001	0.892
168-7A	101876	125	0.045	0.001	0.091	0.004	0.015	0.001	0.849
168-8A	318528	134	0.047	0.001	0.097	0.004	0.015	0.001	0.893
168-9A	629272	158	0.118	0.002	2.227	0.163	0.137	0.010	0.968
168-10A	164656	112	0.047	0.001	0.093	0.004	0.015	0.001	0.891
168-11A	302110	155	0.047	0.001	0.095	0.004	0.015	0.001	0.886
168-12A	812175	180	0.123	0.002	4.838	0.212	0.285	0.011	0.909
168-13A	148805	180	0.050	0.001	0.103	0.005	0.015	0.001	0.910
168-14A	154315	177	0.050	0.001	0.101	0.004	0.015	0.001	0.871
168-14B	143685	128	0.050	0.001	0.102	0.005	0.015	0.001	0.897
168-15A	166937	197	0.050	0.001	0.097	0.005	0.014	0.001	0.890
168-16A	48825	164	0.050	0.001	0.101	0.004	0.015	0.001	0.843
168-17A	139948	182	0.052	0.001	0.108	0.005	0.015	0.001	0.911
180-1A	151001	123	0.052	0.001	0.115	0.006	0.016	0.001	0.914
180-2A	159517	155	0.049	0.001	0.106	0.005	0.016	0.001	0.909
180-3A	1228840	133	0.152	0.003	5.092	0.328	0.243	0.015	0.944
180-4A	169945	160	0.049	0.001	0.100	0.005	0.015	0.001	0.912
180-5A	1093989	148	0.161	0.003	5.738	0.426	0.259	0.019	0.968
180-5B	91913	107	0.049	0.001	0.102	0.005	0.015	0.001	0.870
180-6A	254208	160	0.049	0.001	0.110	0.005	0.016	0.001	0.934
180-7A	184895	210	0.050	0.001	0.107	0.004	0.016	0.001	0.904
166-1A	232702	169	0.049	0.001	0.109	0.005	0.016	0.001	0.937
166-2A	288298	166	0.049	0.001	0.109	0.004	0.016	0.001	0.924
166-3A	214704	127	0.049	0.001	0.110	0.005	0.016	0.001	0.941
166-4A	201509	163	0.049	0.001	0.111	0.005	0.016	0.001	0.910
166-5A	86593	176	0.052	0.001	0.113	0.005	0.016	0.001	0.866
166-6A	291713	157	0.049	0.001	0.106	0.005	0.016	0.001	0.946
166-7A	272084	155	0.049	0.001	0.106	0.005	0.016	0.001	0.945
166-8A	338831	198	0.049	0.001	0.112	0.004	0.017	0.001	0.907
166-9A	36707	139	0.057	0.001	0.120	0.006	0.015	0.001	0.834

U-Pb isotope data used in Isoplot for age determination – continued

Sample ID	²⁰⁶ Pb (cps)	²⁰⁴ Pb (cps)	²⁰⁷ Pb/ ²⁰⁶ Pb	2 σ	²⁰⁷ Pb/ ²³⁵ U	2 σ	²⁰⁶ Pb/ ²³⁸ U	2 σ	ρ
166-9B	167063	103	0.051	0.001	0.112	0.005	0.016	0.001	0.915
166-10A	308119	161	0.049	0.001	0.108	0.004	0.016	0.001	0.929
166-10B	146099	100	0.050	0.001	0.112	0.006	0.016	0.001	0.923
166-11A	129284	132	0.050	0.001	0.106	0.004	0.015	0.001	0.909
166-11B	103112	150	0.051	0.001	0.107	0.006	0.015	0.001	0.930
166-12A	462736	160	0.048	0.001	0.111	0.005	0.017	0.001	0.935
166-13A	480580	148	0.097	0.003	1.064	0.119	0.080	0.009	0.973
166-14A	384603	68	0.049	0.001	0.107	0.004	0.016	0.001	0.934
166-16A	286078	129	0.049	0.001	0.108	0.004	0.016	0.001	0.930
172-1A	423463	210	0.048	0.001	0.107	0.004	0.016	0.001	0.939
172-2A	137679	242	0.050	0.001	0.111	0.004	0.016	0.001	0.920
172-2B	52180	214	0.053	0.001	0.118	0.005	0.016	0.001	0.867
172-3A	330703	278	0.102	0.002	1.445	0.107	0.102	0.007	0.979
172-4A	97220	220	0.052	0.001	0.112	0.004	0.016	0.001	0.893
211-1A	176393	109	0.049	0.001	0.106	0.006	0.016	0.001	0.959
211-2A	21381	124	0.047	0.002	0.103	0.006	0.016	0.001	0.734
211-3A	60275	91	0.049	0.001	0.101	0.005	0.015	0.001	0.863
211-3B	481539	117	0.080	0.004	2.119	0.091	0.191	0.008	0.942
211-4A	258377	148	0.048	0.001	0.104	0.004	0.016	0.001	0.911
211-5A	647997	608	0.058	0.002	0.099	0.005	0.012	0.001	0.824
211-6A	205083	163	0.049	0.001	0.101	0.004	0.015	0.000	0.896
211-7A	153517	105	0.048	0.001	0.103	0.004	0.016	0.001	0.917
211-8A	135605	100	0.048	0.001	0.104	0.004	0.016	0.001	0.915
211-9A	298258	117	0.048	0.001	0.104	0.004	0.016	0.001	0.922
211-10A	98823	175	0.050	0.001	0.108	0.005	0.016	0.001	0.803
211-11A	278717	285	0.049	0.001	0.112	0.004	0.017	0.001	0.926
211-12A	223462	282	0.049	0.001	0.109	0.006	0.016	0.001	0.953
211-13A	861961	236	0.084	0.004	1.942	0.145	0.167	0.012	0.981
211-14A=F- 1A									
211-14A	146065	178	0.047	0.004	0.107	0.004	0.016	0.001	0.918
211-15A	348252	148	0.048	0.001	0.107	0.005	0.016	0.001	0.942
211-16A	160855	191	0.047	0.004	0.102	0.005	0.016	0.001	0.931
211-17A	295865	206	0.047	0.001	0.104	0.004	0.016	0.001	0.925
211-18A	86188	238	0.051	0.001	0.110	0.005	0.016	0.001	0.795
211-19A	311583	253	0.048	0.001	0.101	0.004	0.015	0.000	0.900
211-20A	426856	185	0.048	0.001	0.103	0.004	0.016	0.001	0.915
211-21A	180678	245	0.047	0.004	0.102	0.004	0.016	0.001	0.918
211-22A	234229	228	0.047	0.001	0.102	0.004	0.016	0.001	0.914
211-23A	250597	221	0.048	0.001	0.103	0.004	0.016	0.001	0.907
211-24A	300280	230	0.048	0.001	0.101	0.004	0.015	0.001	0.936
211-25A	187413	258	0.063	0.003	0.173	0.017	0.020	0.002	0.842
211-26A	251059	260	0.049	0.001	0.103	0.004	0.015	0.001	0.908

U-Pb isotope data used in Isoplot for age determination – continued

Sample ID	²⁰⁶ Pb (cps)	²⁰⁴ Pb (cps)	²⁰⁷ Pb/ ²⁰⁶ Pb	2 σ	²⁰⁷ Pb/ ²³⁵ U	2 σ	²⁰⁶ Pb/ ²³⁸ U	2 σ	ρ
211-27A	72052	468	0.049	0.001	0.095	0.005	0.014	0.001	0.932
211-28A	263718	396	0.048	0.001	0.097	0.005	0.014	0.001	0.942
211-29A	458626	724	0.060	0.001	0.098	0.004	0.012	0.000	0.816
211-30A	400926	405	0.048	0.001	0.104	0.004	0.016	0.001	0.933
211-31A	146449	348	0.048	0.001	0.105	0.005	0.016	0.001	0.926
211-32A	132162	304	0.048	0.001	0.102	0.005	0.015	0.001	0.932
211-33A	219112	269	0.048	0.001	0.104	0.004	0.016	0.001	0.924
211-34A	68625	277	0.048	0.001	0.110	0.006	0.017	0.001	0.814
211-35A	127118	207	0.047	0.001	0.106	0.005	0.016	0.001	0.944
211-36A	365409	638	0.066	0.002	0.100	0.007	0.011	0.001	0.863
211-37A	180551	266	0.050	0.001	0.114	0.006	0.016	0.001	0.847
211-38A	174762	219	0.049	0.001	0.110	0.005	0.016	0.001	0.934
211-39A	245517	273	0.060	0.001	0.186	0.010	0.023	0.001	0.885
211-40A	268785	217	0.048	0.001	0.103	0.004	0.016	0.001	0.934
211-41A	290324	259	0.048	0.001	0.109	0.005	0.016	0.001	0.944
211-42A	163505	199	0.063	0.002	0.180	0.011	0.021	0.001	0.839
211-43A	375687	236	0.048	0.001	0.104	0.004	0.016	0.001	0.918
211-44A	327963	294	0.050	0.001	0.115	0.007	0.017	0.001	0.966
211-45A	484475	284	0.111	0.002	3.325	0.284	0.216	0.018	0.986
211-46A	382343	257	0.076	0.005	0.292	0.044	0.028	0.004	0.880
211-47A	960044	183	0.109	0.002	3.882	0.224	0.257	0.014	0.962
211-48A	400063	254	0.049	0.001	0.108	0.004	0.016	0.001	0.918
211-49A	222037	220	0.048	0.001	0.110	0.005	0.017	0.001	0.932
211-50A	253670	209	0.048	0.001	0.111	0.006	0.017	0.001	0.956
211-51A	355518	190	0.048	0.001	0.107	0.005	0.016	0.001	0.943
215-1A	244524	215	0.049	0.001	0.104	0.004	0.016	0.001	0.924
215-2A	231167	205	0.048	0.001	0.103	0.004	0.015	0.001	0.926
215-3A	202182	183	0.049	0.001	0.104	0.004	0.016	0.001	0.924
215-4A	206686	171	0.050	0.001	0.102	0.004	0.015	0.001	0.898
215-5A	197991	250	0.049	0.001	0.101	0.004	0.015	0.001	0.901
215-6A	186337	221	0.048	0.001	0.104	0.005	0.016	0.001	0.936
215-7A	158645	329	0.049	0.001	0.106	0.005	0.015	0.001	0.905
215-8A	121852	295	0.050	0.001	0.104	0.005	0.015	0.001	0.903
215-9A	48969	261	0.050	0.001	0.104	0.005	0.015	0.001	0.802
215-10A	133584	246	0.048	0.001	0.105	0.005	0.016	0.001	0.927
215-11A	141596	277	0.048	0.001	0.103	0.004	0.015	0.001	0.931
215-12A	186301	260	0.049	0.001	0.100	0.004	0.015	0.000	0.901
215-13A	194142	289	0.049	0.001	0.103	0.004	0.015	0.001	0.907
215-14A	134913	289	0.048	0.001	0.104	0.005	0.016	0.001	0.941
215-15A	216543	293	0.048	0.001	0.101	0.004	0.015	0.001	0.935

U-Pb isotope data used in Isoplot for age determination – continued

Sample ID	$^{207}\text{Pb}^*/^{206}\text{Pb}^*$ age (Ma)	2 σ error (Ma)	$^{207}\text{Pb}^*/^{235}\text{U}$ age (Ma)	2 σ error (Ma)	$^{206}\text{Pb}^*/^{238}\text{U}$ age (Ma)	2 σ error (Ma)	% discordance
212-8A	192	50	98	4	94	3	51.3
212-1B	155	44	100	4	97	4	37.3
212-4B	59	50	97	5	99	4	68.6
212-6A	125	58	100	5	99	4	21.1
212-4A	97	49	99	5	99	4	-2.3
212-4D	80	44	99	4	100	4	-24.2
212-5A	76	45	99	4	100	4	-31.1
212-5B	80	44	99	4	100	4	-23.9
212-9A	138	45	101	4	100	4	27.7
212-1	141	44	102	5	101	5	28.6
212-1C	149	63	103	5	101	4	32.3
212-4C	83	49	101	4	102	4	-23.9
212-3	99	44	103	5	103	4	-4.5
212-3B	106	45	104	4	104	4	1.7
212-8B	154	43	106	4	104	4	32.8
212-5C	280	72	112	5	104	4	63.3
212-10A	10	53	106	5	111	5	1057.5
165-1A	152	43	102	4	100	4	34.6
165-1B	2454	34	1711	95	1171	126	57.0
165-2A	104	62	102	5	102	5	2.5
165-3A	113	45	98	4	98	4	13.9
165-4A	140	44	102	5	100	5	28.4
165-5A	124	45	98	4	97	4	22.5
165-5B	98	44	95	4	95	4	3.4
165-6A	208	52	99	4	95	3	54.8
165-7A	340	43	104	4	94	4	72.8
165-8A	1285	132	158	12	93	3	93.4
165-9A	344	43	103	4	93	3	73.4
165-10A	1680	36	1080	52	808	59	55.2
165-10B	1582	44	755	50	507	45	70.5
165-11A	1105	46	157	7	101	4	91.5
165-12A	1041	61	200	20	136	14	87.8
165-12B	1448	65	354	33	211	22	86.8
165-13A	743	40	131	5	99	4	87.3
165-14A	788	75	138	7	103	5	87.6
165-14B	542	61	125	6	104	5	81.5
165-15A	91	43	98	4	99	4	-8.6
165-16A	118	43	98	5	98	4	17.3
165-17A	159	44	97	4	95	4	40.5
165-18A	203	50	108	4	104	4	49.2
165-19A	101	44	99	4	99	4	1.6
165-20A	98	44	96	4	96	3	2.4

U-Pb isotope data used in Isoplot for age determination – continued

Sample ID	$^{207}\text{Pb}^*/^{206}\text{Pb}^*$ age (Ma)	2 σ error (Ma)	$^{207}\text{Pb}^*/^{235}\text{U}$ age (Ma)	2 σ error (Ma)	$^{206}\text{Pb}^*/^{238}\text{U}$ age (Ma)	2 σ error (Ma)	% discordance
165-21A	1080	37	1033	28	1011	38	6.9
165-21B	1069	37	1053	28	1045	38	2.4
165-22A	855	38	588	18	521	18	40.7
165-23A	304	56	122	8	113	8	63.4
165-24A	89	45	93	4	93	3	-4.8
168-1A	101	46	101	4	101	4	0.2
168-2A	1426	34	1238	42	1132	60	22.4
168-3A	69	45	99	4	100	4	-46.2
168-4A	65	45	97	4	98	4	-52.0
168-5A	69	45	93	4	94	3	-37.5
168-6A	39	44	97	4	99	4	-156.1
168-7A	53	55	88	4	94	3	277.4
168-8A	68	44	94	4	95	4	-39.4
168-9A	1921	32	1189	50	829	55	60.5
168-10A	26	47	90	4	93	4	-266.4
168-11A	64	44	92	4	93	3	-44.8
168-12A	1999	32	1792	36	1619	57	21.5
168-13A	206	45	99	4	95	4	54.4
168-14A	196	47	98	4	94	3	52.7
168-14B	189	46	99	4	95	4	50.3
168-15A	188	51	94	4	91	4	52.2
168-16A	181	54	98	4	95	3	48.3
168-17A	273	45	104	5	97	4	64.8
180-1A	284	48	111	5	103	5	64.3
180-2A	165	44	102	4	100	4	40.1
180-3A	2371	36	1835	53	1400	76	45.4
180-4A	144	49	97	5	95	4	34.2
180-5A	2461	31	1937	62	1486	95	44.2
180-5B	164	52	99	4	96	4	41.9
180-6A	163	36	106	4	104	4	36.6
180-7A	192	37	103	4	99	3	48.8
166-1A	163	35	105	4	103	4	37.3
166-2A	149	34	105	4	104	4	30.7
166-3A	152	34	106	4	104	4	31.7
166-4A	164	43	107	5	104	4	36.8
166-5A	286	49	109	5	101	4	65.2
166-6A	131	33	102	4	101	4	23.0
166-7A	124	34	103	4	102	4	18.3
166-8A	132	35	107	4	106	3	19.7
166-9A	474	57	115	5	98	4	79.9

U-Pb isotope data used in Isoplot for age determination – continued

Sample ID	$^{207}\text{Pb}^*/^{206}\text{Pb}^*$ age (Ma)	2 σ error (Ma)	$^{207}\text{Pb}^*/^{235}\text{U}$ age (Ma)	2 σ error (Ma)	$^{206}\text{Pb}^*/^{238}\text{U}$ age (Ma)	2 σ error (Ma)	% discordance
166-9B	223	39	108	4	102	4	54.5
166-10A	144	35	105	4	103	4	28.6
166-10B	214	44	108	5	103	5	52.3
166-11A	200	35	102	4	98	3	51.4
166-11B	255	45	104	5	97	5	62.5
166-12A	122	34	107	4	106	4	13.0
166-13A	1567	48	736	57	494	52	71.1
166-14A	134	34	104	4	102	4	23.7
166-16A	146	34	104	4	102	4	30.3
172-1A	116	33	104	4	103	4	11.0
172-2A	199	35	107	4	103	4	48.5
172-2B	334	44	113	4	103	3	69.8
172-3A	1670	28	908	43	627	43	65.4
172-4A	268	40	108	4	101	4	62.8
211-1A	141	37	102	6	100	5	29.1
211-2A	37	90	99	5	102	4	179.4
211-3A	153	53	98	4	96	4	37.9
211-3B	1206	28	1155	29	1128	42	7.0
211-4A	111	37	101	4	100	3	10.1
211-5A	539	62	96	5	79	3	85.8
211-6A	125	36	97	3	96	3	23.3
211-7A	85	38	99	4	100	4	-17.2
211-8A	81	40	100	4	101	4	-24.5
211-9A	85	35	100	4	101	4	-18.0
211-10A	176	65	104	5	101	4	42.8
211-11A	163	35	108	4	106	4	35.7
211-12A	137	37	105	5	104	5	24.4
211-13A	1297	28	1096	49	997	67	25.0
211-14A	57	38	103	4	105	4	85.1
211-15A	77	35	103	4	105	4	-36.4
211-16A	48	40	99	4	101	4	112.9
211-17A	65	35	101	4	102	4	-57.9
211-18A	239	63	106	5	100	4	58.6
211-19A	88	36	97	3	98	3	-11.0
211-20A	75	35	100	3	101	3	-35.4
211-21A	53	36	99	4	101	4	88.7
211-22A	67	35	98	3	100	3	-49.6
211-23A	106	36	100	3	99	3	6.0
211-24A	107	35	98	4	98	4	8.6
211-25A	692	110	162	15	128	11	82.3
211-26A	129	39	99	4	98	3	24.3

U-Pb isotope data used in Isoplot for age determination – continued

Sample ID	$^{207}\text{Pb}^*/^{206}\text{Pb}^*$ age (Ma)	2 σ error (Ma)	$^{207}\text{Pb}^*/^{235}\text{U}$ age (Ma)	2 σ error (Ma)	$^{206}\text{Pb}^*/^{238}\text{U}$ age (Ma)	2 σ error (Ma)	% discordance
211-27A	140	43	92	5	90	4	35.8
211-28A	120	39	94	4	93	4	22.9
211-29A	586	50	95	4	77	3	87.4
211-30A	92	34	101	4	101	4	-9.9
211-31A	85	39	101	4	102	4	-19.9
211-32A	104	40	99	4	98	4	5.8
211-33A	86	35	101	4	101	4	-17.6
211-34A	84	69	106	5	107	4	-27.5
211-35A	71	37	102	5	104	5	-46.9
211-36A	820	75	96	7	70	4	92.0
211-37A	217	60	110	5	105	4	52.1
211-38A	157	37	106	5	104	4	33.8
211-39A	589	54	173	9	144	7	76.3
211-40A	81	34	99	4	100	4	-24.3
211-41A	116	35	105	4	105	4	9.3
211-42A	711	70	168	10	132	7	82.3
211-43A	85	35	100	4	101	3	-17.9
211-44A	177	35	111	6	107	6	39.7
211-45A	1823	26	1487	65	1263	96	33.8
211-46A	1087	139	260	34	178	23	84.8
211-47A	1789	29	1610	46	1477	73	19.5
211-48A	164	34	104	4	102	3	38.5
211-49A	106	36	106	4	106	4	0.5
211-50A	104	35	106	5	107	5	-2.4
211-51A	95	34	103	4	104	4	-8.8
215-1A	133	36	101	4	99	4	25.4
215-2A	117	37	100	4	99	4	15.5
215-3A	130	37	101	4	99	4	23.9
215-4A	180	44	99	4	96	4	47.3
215-5A	135	38	98	3	97	3	28.6
215-6A	84	37	101	4	102	4	-20.8
215-7A	168	43	102	4	99	4	41.4
215-8A	204	43	100	4	96	4	53.5
215-9A	189	66	100	5	97	4	49.3
215-10A	88	41	101	4	102	4	-16.0
215-11A	114	37	99	4	99	4	13.7
215-12A	124	37	97	3	95	3	23.4
215-13A	149	41	100	4	98	4	34.7
215-14A	90	38	101	5	101	4	-12.4
215-15A	92	35	98	4	98	4	-7.0

U-Pb isotope data used in Isoplot for age determination – continued

Sample ID	$^{238}\text{U}/^{206}\text{Pb}$	2 σ	$^{207}\text{Pb}/^{206}\text{Pb}$	2 σ	Sample ID	$^{238}\text{U}/^{206}\text{Pb}$	2 σ	$^{207}\text{Pb}/^{206}\text{Pb}$	2 σ
212-8A	68.007	2.445	0.050	0.001	165-4A	63.792	3.242	0.049	0.001
212-1B	65.671	2.563	0.049	0.001	165-5A	66.270	2.516	0.049	0.001
212-4B	64.924	2.930	0.047	0.001	165-5B	67.522	2.773	0.048	0.001
212-6A	64.528	2.615	0.049	0.001	165-6A	67.350	2.470	0.050	0.001
212-4A	64.452	2.788	0.048	0.001	165-7A	67.799	2.642	0.053	0.001
212-4D	64.251	2.547	0.048	0.001	165-8A	68.767	2.592	0.084	0.006
212-5A	64.246	2.760	0.048	0.001	165-9A	68.738	2.569	0.053	0.001
212-5B	64.215	2.474	0.048	0.001	165-10A	7.489	0.582	0.103	0.002
212-9A	64.034	2.668	0.049	0.001	165-10B	12.209	1.131	0.098	0.002
212-1	63.492	3.239	0.049	0.001	165-11A	63.063	2.772	0.076	0.002
212-1C	63.115	2.426	0.049	0.001	165-12A	46.946	4.905	0.074	0.002
212-4C	62.620	2.342	0.048	0.001	165-12B	30.074	3.186	0.091	0.003
212-3	61.908	2.685	0.048	0.001	165-13A	64.295	2.456	0.064	0.001
212-3B	61.589	2.287	0.048	0.001	165-14A	61.870	2.762	0.065	0.002
212-8B	61.536	2.464	0.049	0.001	165-14B	61.522	2.841	0.058	0.002
212-5C	61.315	2.436	0.052	0.002	165-15A	64.862	2.703	0.048	0.001
212-10A	57.835	2.826	0.046	0.001	165-16A	65.494	2.960	0.048	0.001
165-1A	64.143	2.545	0.049	0.001	165-17A	67.481	2.721	0.049	0.001
165-1B	5.020	0.597	0.160	0.003	165-18A	61.605	2.220	0.050	0.001
165-2A	62.796	2.840	0.048	0.001	165-19A	64.491	2.458	0.048	0.001
165-3A	65.384	2.595	0.048	0.001	165-20A	66.867	2.427	0.048	0.001
					165-21A	5.886	0.237	0.075	0.001

U-Pb isotope data used in Isoplot for age determination – continued

Sample ID	$^{238}\text{U}/^{206}\text{Pb}$	2 σ	$^{207}\text{Pb}/^{206}\text{Pb}$	2 σ	Sample ID	$^{238}\text{U}/^{206}\text{Pb}$	2 σ	$^{207}\text{Pb}/^{206}\text{Pb}$	2 σ
165-21B	5.682	0.222	0.075	0.001	168-17A	65.811	2.863	0.052	0.001
165-22A	11.888	0.435	0.068	0.001	180-1A	62.101	2.959	0.052	0.001
165-23A	56.631	3.814	0.052	0.001	180-2A	64.275	2.700	0.049	0.001
165-24A	68.544	2.477	0.048	0.001	180-3A	4.122	0.251	0.152	0.003
168-1A	63.277	2.358	0.048	0.001	180-4A	67.560	3.202	0.049	0.001
168-2A	5.208	0.301	0.090	0.002	180-5A	3.857	0.277	0.161	0.003
168-3A	63.916	2.524	0.047	0.001	180-5B	66.594	2.685	0.049	0.001
168-4A	64.972	2.577	0.047	0.001	180-6A	61.740	2.502	0.049	0.001
168-5A	67.919	2.403	0.047	0.001	180-7A	64.470	2.194	0.050	0.001
168-6A	64.470	2.395	0.047	0.001	166-1A	62.145	2.526	0.049	0.001
168-7A	68.205	2.528	0.045	0.001	166-2A	61.742	2.183	0.049	0.001
168-8A	67.276	2.504	0.047	0.001	166-3A	61.554	2.537	0.049	0.001
168-9A	7.286	0.516	0.118	0.002	166-4A	61.337	2.531	0.049	0.001
168-10A	68.860	2.675	0.047	0.001	166-5A	63.386	2.412	0.052	0.001
168-11A	68.728	2.477	0.047	0.001	166-6A	63.273	2.649	0.049	0.001
168-12A	3.503	0.139	0.123	0.002	166-7A	62.907	2.688	0.049	0.001
168-13A	67.549	2.892	0.050	0.001	166-8A	60.126	1.949	0.049	0.001
168-14A	68.365	2.505	0.050	0.001	166-9A	65.137	2.586	0.057	0.001
168-14B	67.492	2.755	0.050	0.001	166-9B	62.461	2.434	0.051	0.001
168-15A	70.678	3.098	0.050	0.001	166-10A	62.166	2.335	0.049	0.001
168-16A	67.696	2.517	0.050	0.001					

U-Pb isotope data used in Isoplot for age determination – continued

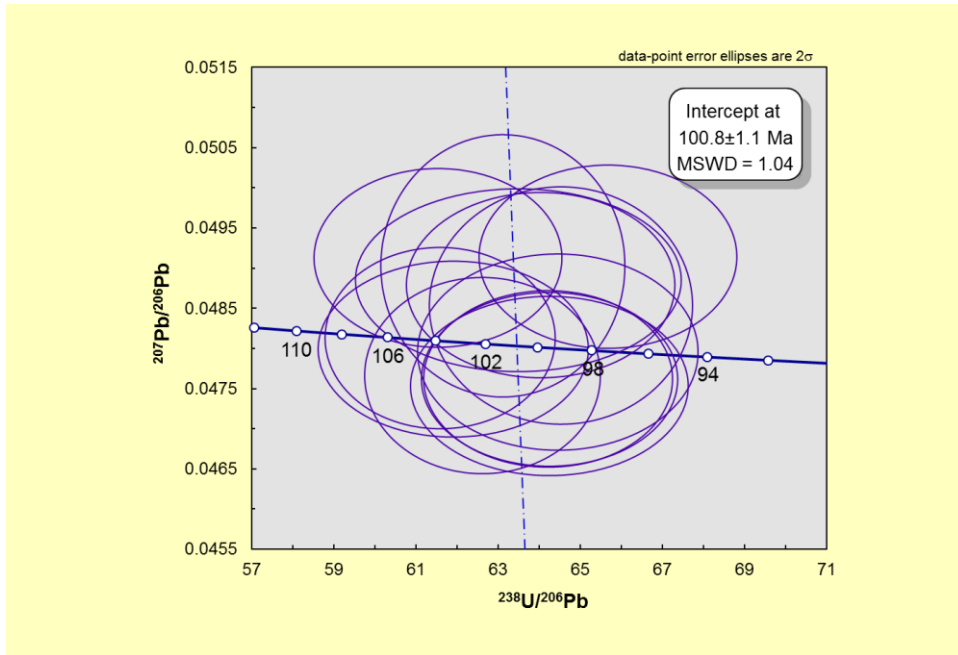
Sample ID	$^{238}\text{U}/^{206}\text{Pb}$	2 σ	$^{207}\text{Pb}/^{206}\text{Pb}$	2 σ
166-10B	62.211	2.884	0.050	0.001
166-11A	65.272	2.184	0.050	0.001
166-11B	65.937	3.322	0.051	0.001
166-12A	60.114	2.289	0.048	0.001
166-13A	12.561	1.372	0.097	0.003
166-14A	62.485	2.425	0.049	0.001
166-16A	62.480	2.314	0.049	0.001
172-1A	62.018	2.424	0.048	0.001
172-2A	61.970	2.243	0.050	0.001
172-2B	62.184	2.125	0.053	0.001
172-3A	9.782	0.708	0.102	0.002
172-4A	63.281	2.229	0.052	0.001
211-1A	63.705	3.490	0.049	0.001
211-2A	62.849	2.618	0.047	0.002
211-3A	66.876	2.636	0.049	0.001
211-3B	5.230	0.212	0.080	0.001
211-4A	63.878	2.216	0.048	0.001
211-5A	80.921	3.405	0.058	0.002
211-6A	66.530	2.085	0.049	0.001
211-7A	64.040	2.400	0.048	0.001
211-8A	63.363	2.483	0.048	0.001
211-9A	63.476	2.277	0.048	0.001
211-10A	63.238	2.410	0.050	0.001
211-11A	60.540	2.244	0.049	0.001
211-12A	61.764	3.070	0.049	0.001
211-13A	5.978	0.439	0.084	0.001
-	-	-	-	-
211-14A	60.934	2.285	0.047	0.001
211-15A	61.133	2.592	0.048	0.001
211-16A	63.202	2.762	0.047	0.001
211-17A	62.646	2.285	0.047	0.001
211-18A	63.927	2.323	0.051	0.001
211-19A	65.388	2.049	0.048	0.001
211-20A	63.487	2.122	0.048	0.001
211-21A	63.634	2.254	0.047	0.001
211-22A	64.228	2.144	0.047	0.001
211-23A	64.422	2.115	0.048	0.001
211-24A	65.459	2.619	0.048	0.001
211-25A	49.972	4.173	0.063	0.003
211-26A	65.276	2.342	0.049	0.001
211-27A	71.015	3.410	0.049	0.001
211-28A	69.149	3.287	0.048	0.001

U-Pb isotope data used in Isoplot for age determination – continued

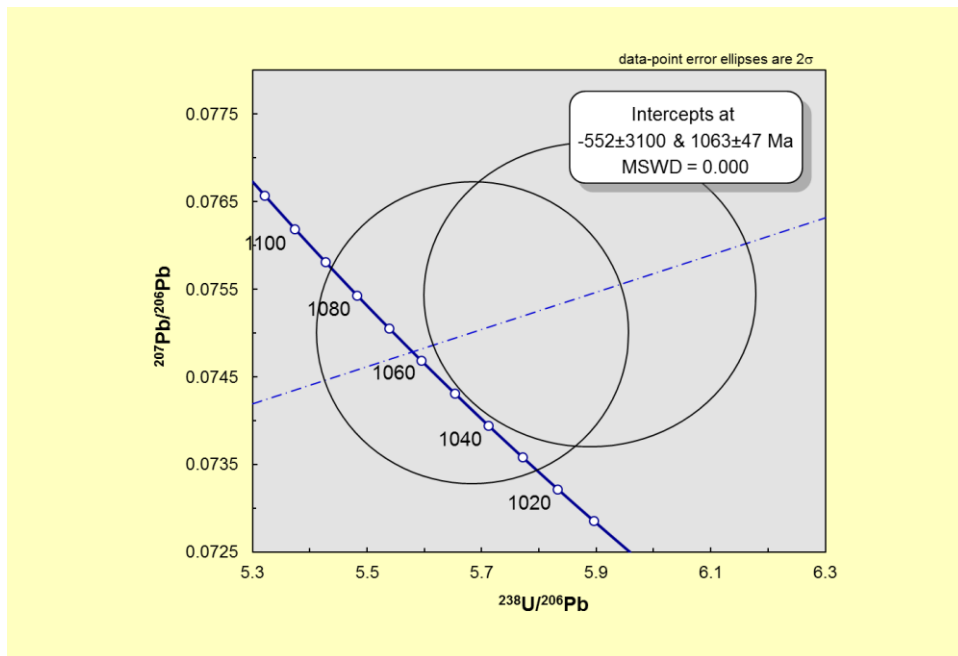
Sample ID	$^{238}\text{U}/^{206}\text{Pb}$	2 σ	$^{207}\text{Pb}/^{206}\text{Pb}$	2 σ	Sample ID	$^{238}\text{U}/^{206}\text{Pb}$	2 σ	$^{207}\text{Pb}/^{206}\text{Pb}$	2 σ
211-29A	83.623	2.748	0.060	0.001	211-51A	61.741	2.541	0.048	0.001
211-30A	63.173	2.378	0.048	0.001	215-1A	64.353	2.439	0.049	0.001
211-31A	62.689	2.556	0.048	0.001	215-2A	64.732	2.528	0.048	0.001
211-32A	65.002	2.865	0.048	0.001	215-3A	64.339	2.450	0.049	0.001
211-33A	63.031	2.276	0.048	0.001	215-4A	66.962	2.591	0.050	0.001
211-34A	59.898	2.490	0.048	0.001	215-5A	66.303	2.236	0.049	0.001
211-35A	61.572	2.794	0.047	0.001	215-6A	62.937	2.628	0.048	0.001
211-36A	91.919	5.746	0.066	0.002	215-7A	64.558	2.530	0.049	0.001
211-37A	61.016	2.559	0.050	0.001	215-8A	66.867	2.651	0.050	0.001
211-38A	61.373	2.559	0.049	0.001	215-9A	66.122	2.589	0.050	0.001
211-39A	44.127	2.103	0.060	0.001	215-10A	62.930	2.681	0.048	0.001
211-40A	63.909	2.452	0.048	0.001	215-11A	64.750	2.588	0.048	0.001
211-41A	60.976	2.585	0.048	0.001	215-12A	67.010	2.224	0.049	0.001
211-42A	48.411	2.527	0.063	0.002	215-13A	65.445	2.518	0.049	0.001
211-43A	63.533	2.181	0.048	0.001	215-14A	63.257	2.837	0.048	0.001
211-44A	59.499	3.359	0.050	0.001	215-15A	65.044	2.547	0.048	0.001
211-45A	4.620	0.389	0.111	0.002					
211-46A	35.785	4.802	0.076	0.005					
211-47A	3.884	0.216	0.109	0.002					
211-48A	62.978	2.164	0.049	0.001					
211-49A	60.602	2.423	0.048	0.001					
211-50A	59.985	2.897	0.048	0.001					

Inverse Concordia

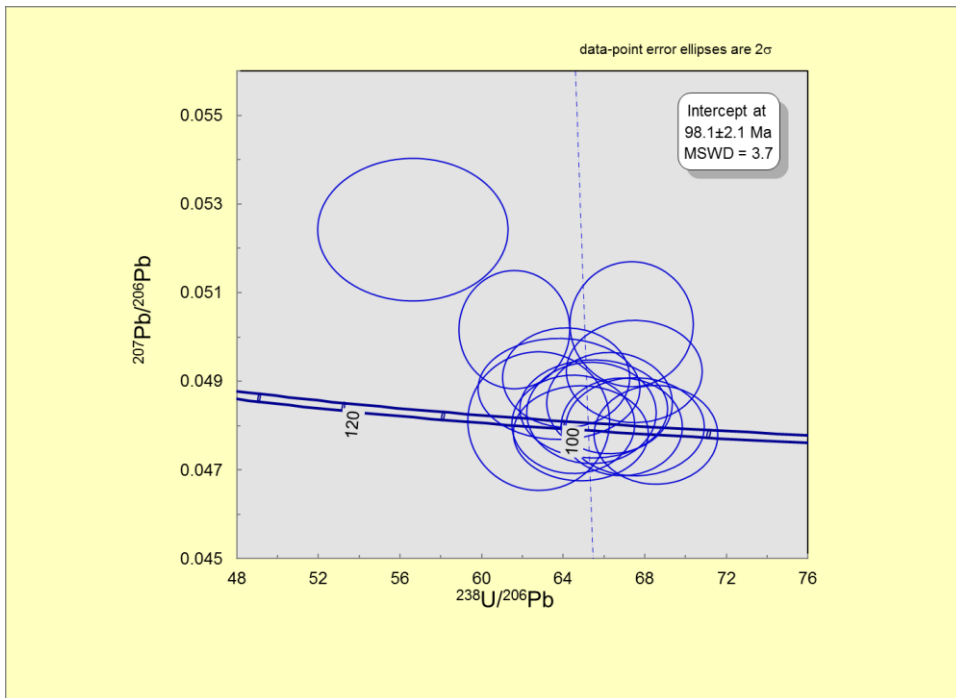
SCW 11 F212



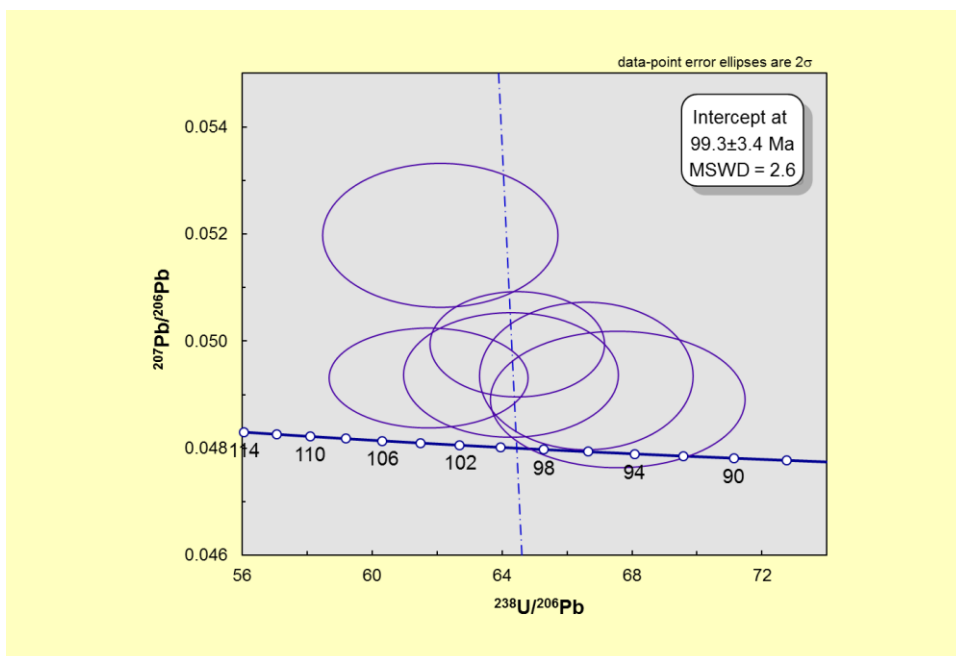
SCW 11 F165 – inherited cores



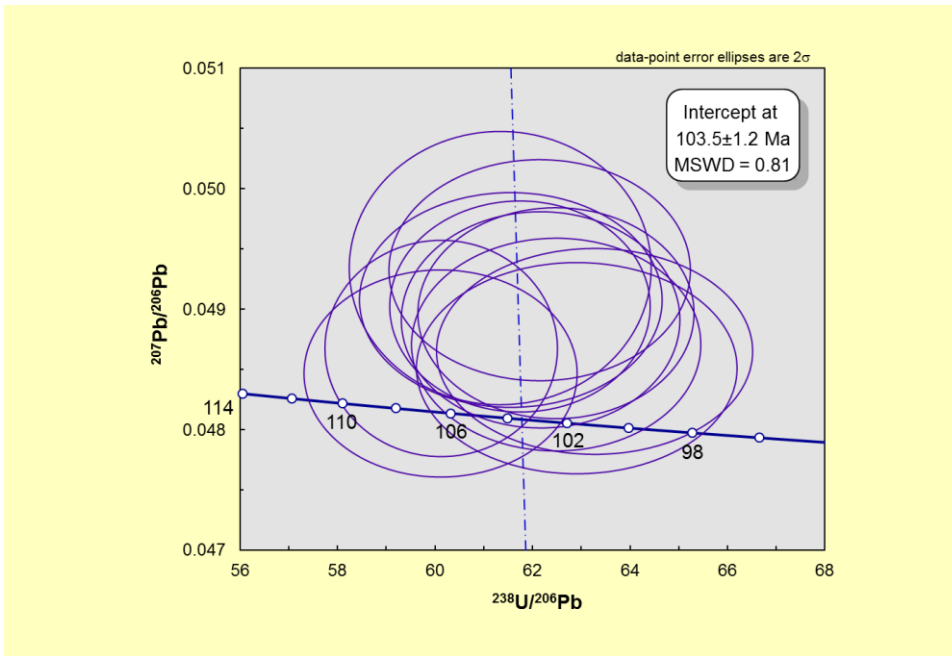
SCW 11 F165 – growth zone



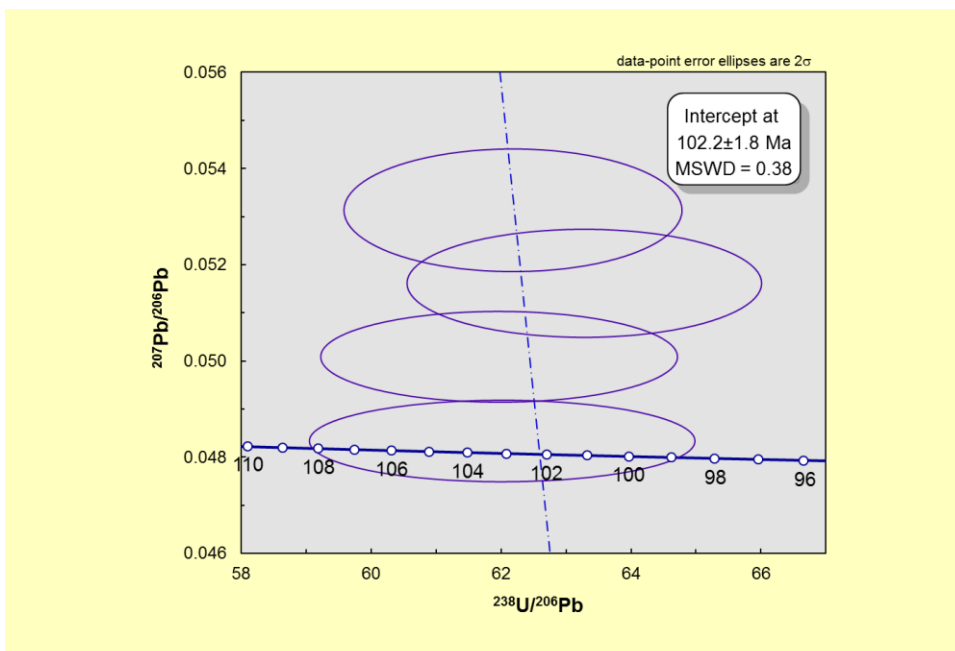
SCW 11 F180



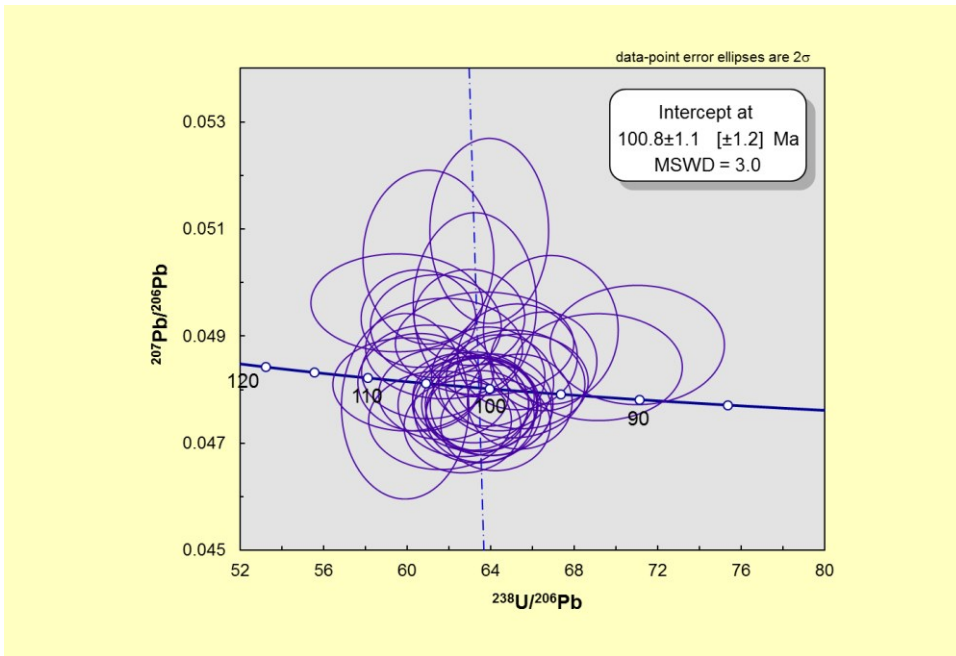
SCW 11 F166



SCW 11 F172

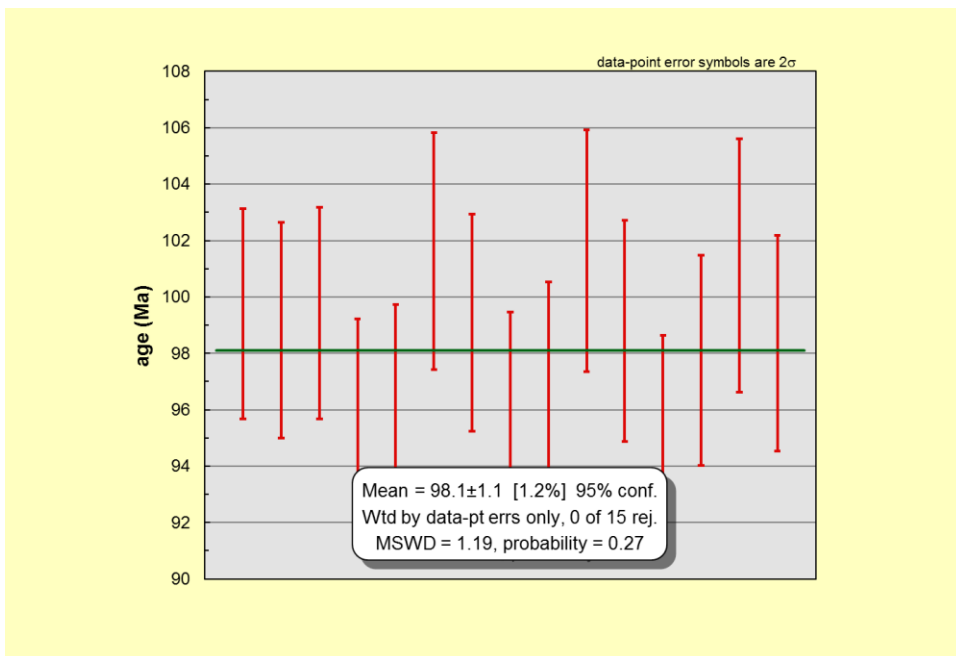


SCW 11 F211

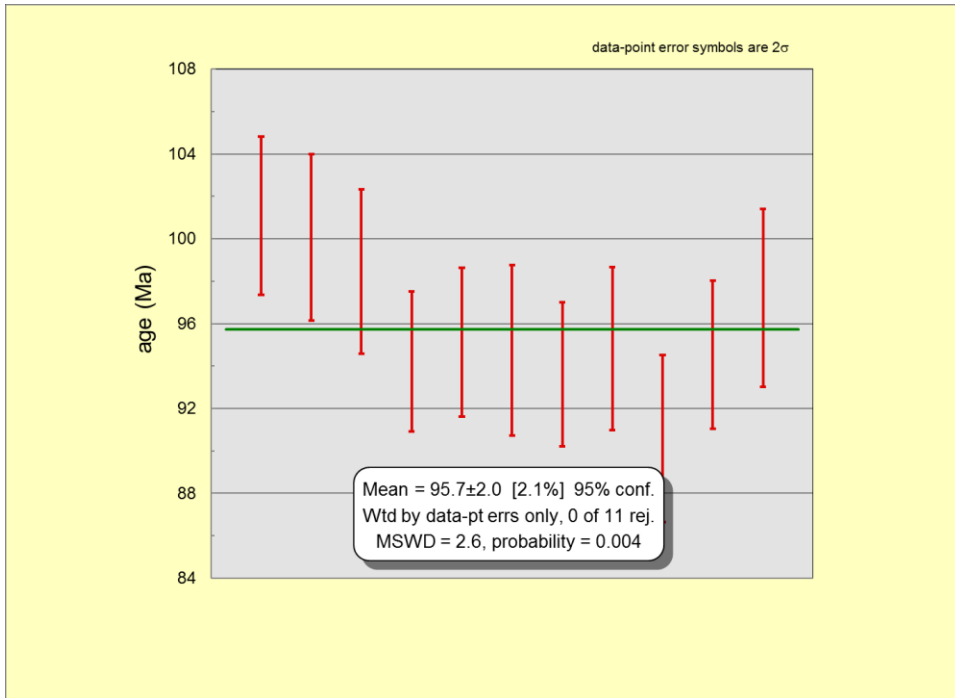


Weighted Average Diagrams

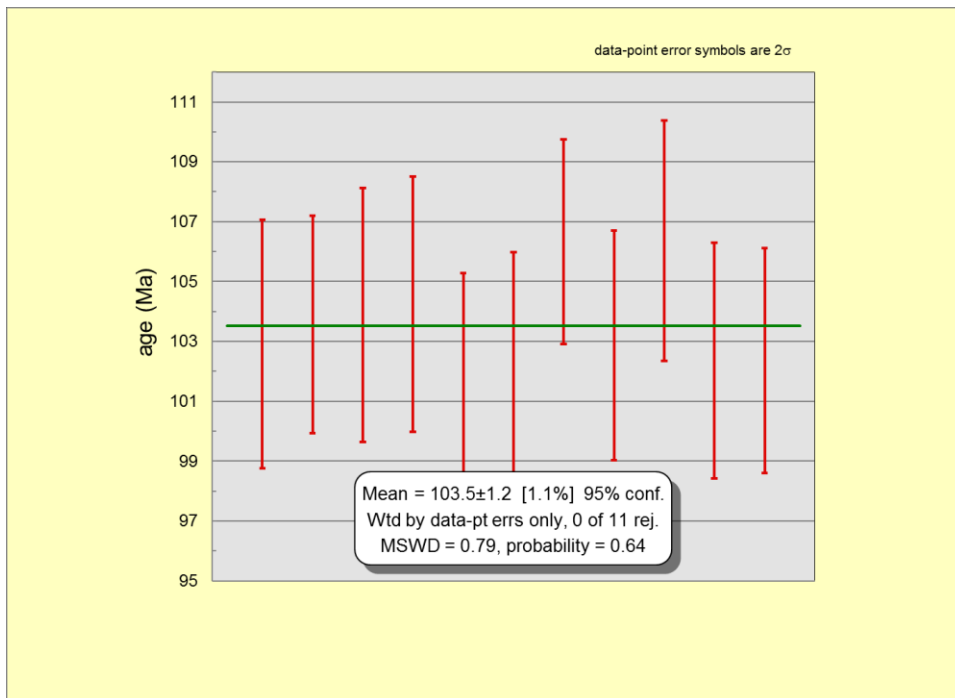
SCW 11 F215



SCW 11 F168



SCW 11 F166



APPENDIX G

Sprogge Whole-Rock Geochemical Data

Whole-rock geochemical data for Sprogge quartz-monzonite dike samples

Method	Pulp	4X	4X	4X	4X	4X	4X	4X	4X	4X	4X	4X	4X	4X	4X	2A	2A
Analyte	Wgt	SiO2	Al2O3	Fe2O3	CaO	MgO	Na2O	K2O	MnO	TiO2	P2O5	Cr2O3	Ba	LOI	SUM	Leco	Leco
Unit	KG	%	%	%	%	%	%	%	%	%	%	%	%	%	%	TOT/C	TOT/S
MDL	0.01	0.01	0.01	0.01	0.01	0.01	0.01	0.01	0.01	0.01	0.01	0.001	0.01	5.11	0.01	0.02	0.02
Sample																	
F165	0.06	72.37	15.26	2.38	0.99	0.54	2.84	3.63	0.02	0.32	0.1	0.019	0.08	2.15	100.7	0.03	<0.02
F168	0.05	66.22	15.9	4.84	1.78	1.9	2.49	2.86	0.14	0.47	0.11	0.02	0.07	3.53	100.34	0.19	0.03
F172	0.04	72.1	14.84	2.17	1.03	0.3	2.75	3.84	0.01	0.26	0.08	0.02	0.11	2.35	99.87	0.03	0.13
F180	0.05	66.04	14.86	4.46	2.72	1.67	2.6	2.71	0.08	0.41	0.11	0.016	0.07	4.08	99.85	0.4	0.22
F211	0.08	73.07	15.25	1.45	1.31	0.41	2.94	3.64	0.01	0.31	0.1	0.011	0.08	1.74	100.34	<0.02	<0.02
F212	0.04	72.57	15.07	2.25	1	0.48	2.75	3.82	0.01	0.32	0.11	0.018	0.08	2.04	100.52	<0.02	0.19
F215	0.1	69.66	14.59	2.85	2.32	0.6	2.61	3.84	0.07	0.31	0.1	0.011	0.08	2.64	99.68	0.29	0.31
Duplicates																	
F215	0.1	69.66	14.59	2.85	2.32	0.6	2.61	3.84	0.07	0.31	0.1	0.011	0.08	2.64	99.68	0.29	0.31
F165	0.06	72.37	15.26	2.38	0.99	0.54	2.84	3.63	0.02	0.32	0.1	0.019	0.08	2.15	100.7	0.03	<0.02
F172	0.04	72.1	14.84	2.17	1.03	0.3	2.75	3.84	0.01	0.26	0.08	0.02	0.11	2.35	99.87	0.03	0.13
Standards																	
STD GS311-1																0.98	2.45
STD GS910-4																2.63	8.32
STD SY-4(D)		50.04	20.74	6.17	7.94	0.5	7.19	1.61	0.1	0.28	0.13	0.005	0.04	4.56	99.32		
STD OREAS72B		51.71	9.01	9.76	3.93	16.26	1.39	1.32	0.13	0.35	0.06	0.151	0.04	5.39	99.51		
BLK																<0.02	<0.02
BLK		<0.01	<0.01	<0.01	<0.01	<0.01	0.04	<0.01	<0.01	<0.01	<0.01	<0.001	<0.01	0	<0.01		
G1		67.54	15.75	3.47	3.41	1.24	3.73	3.56	0.1	0.41	0.18	0.018	0.1	0.79	100.31	<0.02	<0.02

Whole-rock geochemical data for Sprogge quartz-monzonite dike samples – continued

Method	4B	4B	4B	4B	4B	4B	4B	4B	4B	4B	4B	4B	4B	4B	4B	4B	4B
Analyte	Ba	Be	Co	Cs	Ga	Hf	Nb	Rb	Sn	Sr	Ta	Th	U	V	W	Zr	Y
Unit	PPM	PPM	PPM	PPM	PPM	PPM	PPM	PPM	PPM	PPM	PPM	PPM	PPM	PPM	PPM	PPM	PPM
MDL	1	1	0.2	0.1	0.5	0.1	0.1	0.1	1	0.5	0.1	0.2	0.1	8	0.5	0.1	0.1
Sample																	
F165	832	<1	1.4	2	16.1	4.6	11	89.3	4	264.1	0.9	11.7	4	40	0.7	136.6	16
F168	725	3	5.4	3.9	17.1	3.5	8.7	92.7	9	258.1	0.7	9.6	2.6	88	1.4	128.1	20.6
F172	980	3	1.5	2.6	15.7	4	10.9	97	6	295.3	0.9	11.9	4.1	26	1.1	146.6	18.4
F180	728	5	5.5	3.1	15.6	4	9	87	7	281.1	0.8	10.1	3.4	69	1.9	132.4	20.9
F211	802	<1	1.2	1.8	15.8	4.6	10.4	89.9	4	302.3	1.1	13.4	4.6	33	0.7	138.4	16
F212	803	1	2	2.5	15.9	3.8	10.4	106	8	270.9	0.8	13.8	3.6	33	1.1	148.8	17.4
F215	733	1	6.5	2.7	15.6	3.7	10.7	116.8	11	294.9	1	13.2	3	34	0.9	141.4	18.4
Duplicates																	
F215	733	1	6.5	2.7	15.6	3.7	10.7	116.8	11	294.9	1	13.2	3	34	0.9	141.4	18.4
F165	832	<1	1.4	2	16.1	4.6	11	89.3	4	264.1	0.9	11.7	4	40	0.7	136.6	16
F172	980	3	1.5	2.6	15.7	4	10.9	97	6	295.3	0.9	11.9	4.1	26	1.1	146.6	18.4
F172	1081	2	1.5	2.3	14.9	4.4	11.2	96.4	6	293.3	0.9	12.5	4.1	23	0.7	152.6	19.3
Standards																	
STD SO-18	531	<1	25	6.9	15.8	9.8	18.9	26.2	14	382.9	6.7	9.3	16.5	208	14.6	280.3	29.2
BLK	8	<1	<0.2	<0.1	<0.5	<0.1	<0.1	<0.1	<1	<0.5	<0.1	<0.2	<0.1	<8	<0.5	<0.1	<0.1
G1	1087	3	5	4.4	17.1	3.8	22.1	118.6	1	834.1	1.4	7.9	3.3	66	<0.5	133	15.9

Whole-rock geochemical data for Sprogge quartz-monzonite dike samples – continued

Method	4B	4B	4B	4B	4B	4B	4B	4B	4B	4B	4B	4B	4B	4B	1DX	1DX	1DX
Analyte	La	Ce	Pr	Nd	Sm	Eu	Gd	Tb	Dy	Ho	Er	Tm	Yb	Lu	Mo	Cu	Pb
Unit	PPM	PPM	PPM	PPM	PPM	PPM	PPM	PPM	PPM	PPM	PPM	PPM	PPM	PPM	PPM	PPM	PPM
MDL	0.1	0.1	0.02	0.3	0.05	0.02	0.05	0.01	0.05	0.02	0.03	0.01	0.05	0.01	0.1	0.1	0.1
Sample																	
F165	28.7	57.8	5.85	20.2	3.93	0.76	3.56	0.53	2.83	0.55	1.62	0.23	1.55	0.25	2.4	10.2	7.1
F168	33	60.6	6.75	25.3	4.6	0.96	4.38	0.64	3.94	0.81	2.21	0.33	2.3	0.34	1.2	9.8	7.9
F172	31.4	62.8	6.25	23.8	4.08	0.78	3.89	0.56	3.33	0.66	1.88	0.32	2.29	0.34	2.4	20.4	6.9
F180	34.5	69.5	7.63	26.8	5.29	0.88	5.15	0.73	4.05	0.78	2.08	0.3	1.87	0.34	1.4	10.9	7.1
F211	23.3	53.5	5.7	21.3	3.92	0.76	3.53	0.53	3.13	0.63	1.45	0.24	1.64	0.25	1	12.9	16.4
F212	30.4	59.7	6.27	23.2	4.43	0.62	3.86	0.58	3.09	0.6	1.55	0.24	1.49	0.25	1.6	17.4	16.5
F215	30.5	60	6.38	23.5	4.66	0.9	4.09	0.63	3.44	0.73	1.69	0.28	1.72	0.28	0.8	8.1	11.2
Duplicates																	
F215	30.5	60	6.38	23.5	4.66	0.9	4.09	0.63	3.44	0.73	1.69	0.28	1.72	0.28	0.8	8.1	11.2
F215															0.9	8.1	11.3
F165	28.7	57.8	5.85	20.2	3.93	0.76	3.56	0.53	2.83	0.55	1.62	0.23	1.55	0.25	2.4	10.2	7.1
F172	31.4	62.8	6.25	23.8	4.08	0.78	3.89	0.56	3.33	0.66	1.88	0.32	2.29	0.34	2.4	20.4	6.9
F172	32.5	61.6	6.39	22.2	4.26	0.74	3.8	0.58	3.51	0.76	2.12	0.32	2.31	0.33			
Standards																	
STD DS10															14	154.4	158.7
STD OREAS45EA															1.5	734.1	15
STD SO-18	13.7	28.8	3.32	13.6	2.71	0.84	2.95	0.49	2.94	0.62	1.76	0.28	1.77	0.27			
BLK															0.1	0.3	<0.1
BLK	<0.1	<0.1	<0.02	<0.3	<0.05	<0.02	<0.05	<0.01	<0.05	<0.02	<0.03	<0.01	<0.05	<0.01			
G1	29.3	58.1	5.65	20.7	3.54	1.08	3.04	0.49	2.67	0.6	1.62	0.26	1.55	0.29	1	4.7	3.2

Whole-rock geochemical data for Sprogge quartz-monzonite dike samples – continued

Method	1DX	1DX	1DX	1DX	1DX	1DX	1DX	1DX	1DX	1DX	1DX	G806
Analyte	Zn	Ni	As	Cd	Sb	Bi	Ag	Au	Hg	Tl	Se	FeO
Unit	PPM	PPM	PPM	PPM	PPM	PPM	PPM	PPB	PPM	PPM	PPM	%
MDL	1	0.1	0.5	0.1	0.1	0.1	0.1	0.5	0.01	0.1	0.5	0.01
Sample												
F165	14	3.5	7.9	<0.1	0.2	0.2	<0.1	0.7	<0.01	<0.1	<0.5	1.54
F168	55	8.4	20.5	0.2	0.4	0.6	<0.1	7.2	<0.01	0.1	<0.5	3.4
F172	11	2.6	17.4	<0.1	0.3	0.5	<0.1	1.1	<0.01	<0.1	<0.5	1.01
F180	34	4.5	7.8	<0.1	0.2	0.7	<0.1	2.1	<0.01	0.1	<0.5	3.93
F211	9	3.2	22.6	<0.1	0.2	0.2	<0.1	46.8	<0.01	<0.1	<0.5	1.02
F212	12	2.5	13.9	<0.1	0.2	0.2	<0.1	2.7	<0.01	0.1	<0.5	1.3
F215	17	2.1	1908	<0.1	1.1	0.3	<0.1	19.3	<0.01	0.1	<0.5	1.33
Duplicates												
F215	17	2.1	1908	<0.1	1.1	0.3	<0.1	19.3	<0.01	0.1	<0.5	1.33
F215	17	2.1	1936.7	<0.1	1	0.3	<0.1	18	<0.01	0.1	<0.5	
F165	14	3.5	7.9	<0.1	0.2	0.2	<0.1	0.7	<0.01	<0.1	<0.5	1.54
F165												1.59
F172	11	2.6	17.4	<0.1	0.3	0.5	<0.1	1.1	<0.01	<0.1	<0.5	1.01
Standards												
STD DS10	366	69.9	47.6	2.9	9	12.2	2.3	70.4	0.27	5.4	2.2	
STD OREAS45EA	32	410.5	11	<0.1	0.3	0.2	0.2	53.3	<0.01	<0.1	<0.5	
STD FER-2												15.42
STD SY-4												2.85
BLK	<1	<0.1	<0.5	<0.1	<0.1	<0.1	<0.1	<0.5	<0.01	<0.1	<0.5	
G1	53	5.3	<0.5	<0.1	<0.1	<0.1	<0.1	1.3	<0.01	0.4	<0.5	1.95